VOLUME 118 NUMBER 3

THE ASTROPHYSICAL JOURNAL

AN INTERNATIONAL REVIEW OF SPECTROSCOPY AND ASTRONOMICAL PHYSICS

NOVEMBER 1953

THE BRIGHTEST VARIABLE STARS IN EXTRAGALACTIC NEBULAE. I. M31 AND M33 — *Edwin Hubble and Allan Sandage* 353
A CATALOGUE OF EMISSION NEBULAE NEAR THE GALACTIC PLANE — *Stewart Sharpless* 362
SPECTROGRAPHIC OBSERVATIONS OF GALACTIC EMISSION REGIONS AND NEBULAE — *Hugh M. Johnson* 370
THE SOLAR MAGNETOGRAPH — *Horace W. Babcock* 387
CARBON MONOXIDE IN THE SUN — *Leo Goldberg and Edith A. Müller* 397
SPECTRA AND INTENSITY OF LIGHT FROM SOLAR CRESCENTS NEAR TOTALITY OF ECLIPSE OF FEBRUARY 25, 1952 — *F. J. Heyden, S.J., C. A. Beck, D. J. Lovell, W. B. Fussell, J. H. Hancock, and E. O. Hulburt* 412
ISOPHOTAL PHOTOMETRY OF A SOLAR FLARE — *Donald E. Billings and Walter Orr Roberts* 429
A STUDY OF THE MOTIONS OF SOLAR PROMINENCES — *Lewis Larmore* 436
THE SPECTRUM OF CHI CYGNI NEAR MINIMUM LIGHT — *Paul W. Merrill* 453
LINE INTENSITIES IN THE SPECTRA OF COOL CARBON STARS. I. R STARS IN THE VIOLET — *William Buscombe* 459
A STUDY OF LINE PROFILES: THE SPECTRUM OF RHO LEONIS — *Su-Shu Huang and Otto Struve* 463
THE SPECTROSCOPIC BINARY 12 COMAE BERENICES — *George H. Herbig and Beverly A. Turner* 477
THE LIGHT-VARIATIONS OF HD 217050 — *Merle F. Walker* 481
LIGHT-VARIATIONS OF PECULIAR A STARS — *Sanford S. Provin* 489
RED AND INFRARED MAGNITUDES FOR 138 STARS OBSERVED AS PHOTOMETRIC STANDARDS — *Gerald E. Kron, Howard S. White, and S. C. B. Gascoigne* 502
RED AND INFRARED MAGNITUDES FOR 27 SOUTHERN HEMISPHERE STARS OF EARLY SPECTRAL TYPE — *Gerald E. Kron and S. C. B. Gascoigne* 511
ON THE FRAGMENTATION OF GAS CLOUDS INTO GALAXIES AND STARS — *F. Hoyle* 513
THE INTERNAL STRUCTURE OF RED DWARF STARS — *Donald E. Osterbrock* 529
THERMAL EFFECTS OF COLLISIONAL LINE EXCITATION IN GASEOUS NEBULAE — *Lawrence H. Aller* 547
THE PHYSICAL THEORY OF METEORS. IV. INQUIRY INTO THE RADIATION PROBLEM—A LABORATORY MODEL — *Richard N. Thomas and William C. White* 555

NOTES

THE NEBULAR SPECTRUM OF NOVA PUPPIS 1942 — *Livio Gratton* 568
NOTE ON THE SPECTRUM OF β DORADUS — *Livio Gratton* 570
NOTE ON SPECTRA OF COOL STARS IN THE 1μ REGION — *Freeman D. Miller* 572
INTERSTELLAR POLARIZATION AND MAGNETIC FIELDS — *G. R. Burbidge* 575
SIRIUS AND THE CARBON CYCLE — *Thomas L. Swihart* 577

INDEX 581

THE UNIVERSITY OF CHICAGO PRESS
CHICAGO, ILLINOIS, U.S.A.

November 1953 Vol. 118, No. 3

THE ASTROPHYSICAL JOURNAL

AN INTERNATIONAL REVIEW OF SPECTROSCOPY AND ASTRONOMICAL PHYSICS

Founded in 1895 by George E. Hale and James E. Keeler

Published in Collaboration with the American Astronomical Society

S. CHANDRASEKHAR
Managing Editor

GERARD P. KUIPER
Associate Editor

Yerkes Observatory of the University of Chicago

EDITORIAL BOARD

H. W. BABCOCK (1953-57)
Mount Wilson Observatory of the Carnegie Institution of Washington

G. HERZBERG (1952-56)
National Research Council, Ottawa

FRED L. WHIPPLE (1952-54)
Harvard College Observatory

C. D. SHANE (1952-55)
Lick Observatory, University of California

LYMAN SPITZER, JR. (1952-53)
Princeton University Observatory

The Astrophysical Journal is published bimonthly by the University of Chicago at the University of Chicago Press, 5750 Ellis Avenue, Chicago 37, Illinois, during January, March, May, July, September, and November. ¶Two volumes are published per year, one beginning with the January issue and the other beginning with the July issue. The subscription price is $6.00 per volume or $12.00 per year; the price of single copies is $3.00. (Orders for service of less than a volume will be charged at the single copy rate.) ¶Postage is prepaid by the publishers on all orders from the United States and its possessions. No extra charge is made for postage to countries in the Pan American Postal Union. ¶Postage is charged extra as follows: for Canada, 20 cents per volume, 40 cents per year (total $6.20 per volume, $12.40 per year); on single copies 5 cents (total $3.05); for all other countries in the Postal Union, 40 cents per volume, 75 cents per year (total $6.40 per volume, $12.75 per year), on single copies 10 cents (total $3.10). ¶Subscriptions are payable in advance. Please make all remittances payable to The University of Chicago Press, in United States currency or its equivalent by postal or express money orders or bank drafts.

The following is an authorized agent:

For the British Empire, except North America and Australasia: The Cambridge University Press, Bentley House, 200 Euston Road, London, N.W. 1, England. Prices of yearly subscriptions and of single copies may be had on application.

Claims for missing numbers should be made within the month following the regular month of publication. The publishers expect to supply missing numbers free only when losses have been sustained in transit, and when the reserve stock will permit.

Business correspondence should be addressed to The University of Chicago Press, Chicago 37, Illinois.

Communications for the editors and manuscripts should be addressed to: S. Chandrasekhar, Editor of THE ASTROPHYSICAL JOURNAL, Yerkes Observatory, Williams Bay, Wisconsin.

Line drawings and photographs should be made by the author, and all marginal notes such as co-ordinates, wave lengths, etc., should be included in the cuts. It will not be possible to set up such material in type.

One copy of the corrected galley proof should be returned as soon as possible to the editor, Yerkes Observatory, Williams Bay, Wisconsin. Authors should take notice that the manuscript will not be sent to them with the proof.

The cable address is "Observatory, Williamsbay, Wisconsin."

The articles in this journal are indexed in the *International Index to Periodicals*, New York, N.Y.

Applications for permission to quote from this journal should be addressed to The University of Chicago Press, and will be freely granted.

Microfilms of complete journal volumes are available to regular subscribers only and may be obtained at the end of the year. Orders and inquiries should be addressed to University Microfilms, 313 North First Street, Ann Arbor, Michigan.

Notice to subscribers: If you change your address, please notify us and your local postmaster immediately.

Entered as second-class matter, July 31, 1940, at the Post-Office at Chicago, Ill., under the Act of March 3, 1879.
Acceptance for mailing at special rate of postage provided for in United States Postal Act of October 3, 1917, Section 1103, amended February 28, 1925.
Copyright 1953 by the University of Chicago.

[PRINTED IN U.S.A.]

THE ASTROPHYSICAL JOURNAL

AN INTERNATIONAL REVIEW OF SPECTROSCOPY AND ASTRONOMICAL PHYSICS

VOLUME 118 NOVEMBER 1953 NUMBER 3

THE BRIGHTEST VARIABLE STARS IN EXTRAGALACTIC NEBULAE. I. M31 AND M33

EDWIN HUBBLE AND ALLAN SANDAGE

MOUNT WILSON AND PALOMAR OBSERVATORIES
CARNEGIE INSTITUTION OF WASHINGTON
CALIFORNIA INSTITUTE OF TECHNOLOGY

Received June 27, 1953

ABSTRACT

Light-curves are obtained for five irregular variables: one in M31 and four in M33. Observations extend continuously from 1916 to the present. Spectra are available for four of the five variables. The light-curves, color indices, and spectra show that a new class of variable star has been isolated. This class is characterized by (1) high luminosity, (2) blue color indices, and (3) intermediate F-type spectra.

The absolute magnitude at maximum for these stars is a quantity of small dispersion. If $m - M = 22.4$ for M31 and $m - M = 22.3$ for M33, the observations give M_{pg} (max.) $= -6.9 \pm 0.2$ (A.D.). If the provisional revision to the cosmic distance scale of $\delta M = -1.5$, suggested by Baade, is adopted, these five variables have an absolute magnitude M_{pg} (max.) $= -8.4 \pm 0.2$ (A.D.). The small dispersion in this value shows the usefulness of this group of blue irregular variables as distance indicators. Additional stars of this type are known in other nebulae and provide a larger sample for future study.

I. INTRODUCTION

A study of the brightest individual objects in extragalactic nebulae is important for two reasons: (1) Statistical studies of the objects themselves are unhampered by the large selection effects present in similar studies in the galactic system, and (2) the recognizable individual objects in extragalactic nebulae provide the only means of obtaining a calibration of the cosmic-distance scale. The group of recognizable individual objects consists of (*a*) globular clusters, (*b*) normal novae, (*c*) the brightest variable stars (usually irregular), (*d*) the brightest nonvariable stars, and (*e*) cepheid variables.[1] These are listed in the order of their absolute luminosities and hence in the inverse order in which these objects fade and can no longer be recognized as the nebular distances increase. It is important that the group characteristics of any of these objects be known before that group can be used as a distance criterion.

Only a few nebulae are so close that all or most of the six groups can be studied simultaneously. Such a study is essential for a calibration of the relative luminosity function of each group. It is this small sample of nebulae which must be used to calibrate the distance scale. Previous work[2] with the 100-inch telescope at Mount Wilson had given the best absolute-magnitude calibration available for most of these groups. With the

[1] Also visible as individual objects in nebulae are supernovae and emission patches. Supernovae are so rare in a given nebula that they are of little use as distance indicators. Emission patches vary widely in size and magnitude and hence are difficult objects to use.

[2] E. P. Hubble, *Ap. J.*, **69**, 103, 1929; **76**, 44, 1932; **84**, 158, 1936.

200-inch Hale telescope now in operation and with the revisions to the magnitude scale at the faint end now under way, a complete re-examination of the individual distance criteria in all close resolvable nebulae must be undertaken in an effort to improve the accuracy of the first reconnaissance of nearly 20 years ago.

Among the individual objects which might be used as distance indicators are the brightest variable stars occurring in nebulae. Owing to their variability, they are the easiest objects to recognize. Furthermore, they are among the brightest objects in spiral systems and hence can be seen as individuals to large distances. To be of use, however, these variables must have group attributes with dispersions small enough to provide characteristics capable of calibration. This paper is a report of the study of the brightest variable stars in M31 and M33, with particular attention directed to those group characteristics which may prove useful as distance indicators.

II. IDENTIFICATION AND MAGNITUDE STANDARDS

The first variable stars recorded in extragalactic nebulae are the three found in M33 by J. C. Duncan[3] in 1922. The brightest of the three was later found independently by Max Wolf[4] working at Heidelberg. These historic variables are Nos. 1, 2, and 3 identified on prints published in this *Journal* in 1926.[5] Numbers 1 and 2 are irregular variables, while No. 3 (the faintest of the three) is a cepheid of period 41.7 days. During the course of routine examination of many plates of M33 in the years following the initial work on this system in 1926, three additional bright irregular variables have been found. These are assigned letters—A, B, and C—and are identified in Figure 1. Each of these five irregular variables has rivaled or exceeded the brightness of the most luminous nonvariable stars in M33. One additional bright variable, discovered by Baade while at the Hamburg Observatory, is near the edge of most of the plates of M33 in the Mount Wilson collection, so extensive data are not available. This star is not shown in Figure 1.

No additional bright variables have been found in M31 since the list of 1929 was published.[6] Variable No. 19, identified in Figure 2, is the brightest of the variables known in M31.

The five stars whose characteristics are reported in this paper are: in M33, var. No. 2, A, B, and C; and in M31, var. No. 19.[7]

New magnitude standards in the vicinity of each of the variables were determined by intercomparisons between the nebular fields and Selected Area 68. All magnitudes are based upon Stebbins, Whitford, and Johnson's photoelectric standards[8] in SA 68. One sequence near the center of M33 was determined in the photographic spectral region, while a sequence near variable A in M33 and a sequence near variable 19 in M31 were determined in both the photographic and the photovisual spectral regions. The stars for each of these sequences are identified in Figures 2, 3, and 4. Eastman 103*a*-O plates behind a Schott GG1 filter were used to obtain the photographic magnitudes, while Eastman 103*a*-D plates behind a Schott GG11 filter were used for the photovisual magnitudes. The color equations converting magnitudes obtained with these plate and filter combinations (m_{pg} and m_{pv}), to **P** and **V** of the SWJ system, are[9]

$$\mathbf{P} = m_{pg} - 0.09\,(\mathbf{P} - \mathbf{V}) + 0.05\,, \tag{1}$$

$$\mathbf{V} = m_{pv}\,, \tag{2}$$

$$\mathbf{P} - \mathbf{V} = 0.92\,(m_{pg} - m_{pv}) + 0.05\,. \tag{3}$$

[3] *Pub. A.S.P.*, **34**, 290, 1922.

[4] *A.N.*, **217**, 475, 1923.

[5] E. P. Hubble, *Ap. J.*, **63**, 83, 1926.

[6] *Ibid.*, **69**, 103, 1929.

[7] Variable 1 in M 33, which attained its maximum magnitude of 17.3 in 1911, has been fainter than $m_{pg} = 18.5$ since 1925. Data for this star are not discussed in this paper.

[8] *Ap. J.*, **112**, 469, 1950.

[9] A. R. Sandage, *A.J.*, **58**, 61, 1953.

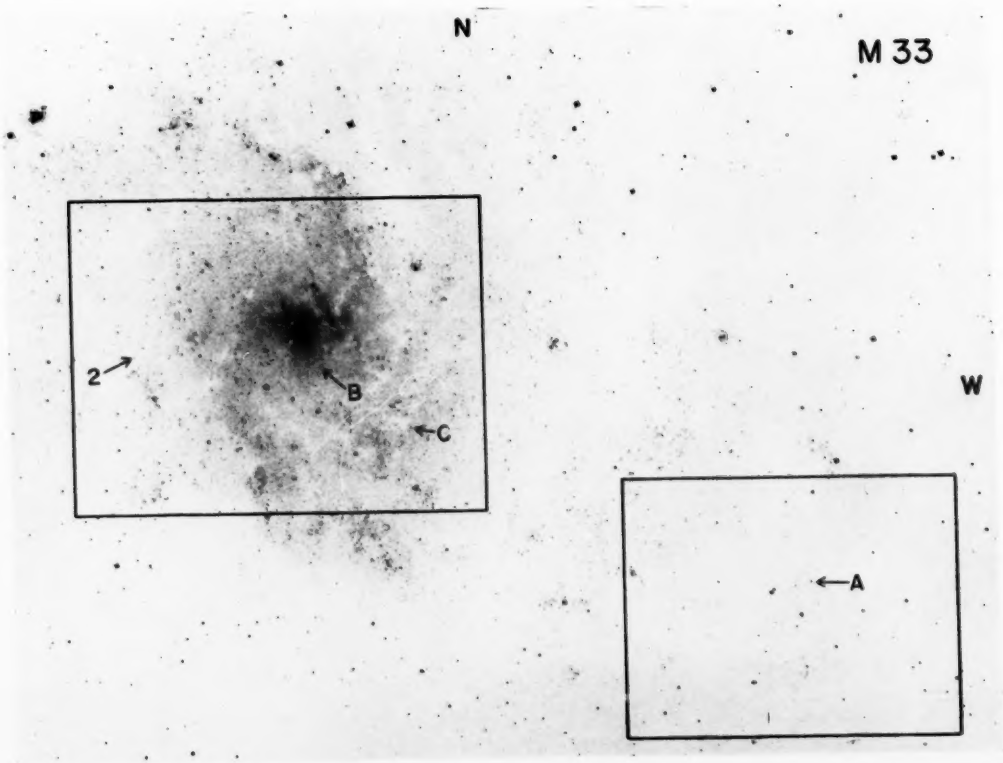

FIG. 1.—Identification chart for variables A, B, C, and 2 in M33. The two areas outlined are shown in Figures 3 and 4 with the sequence stars identified.

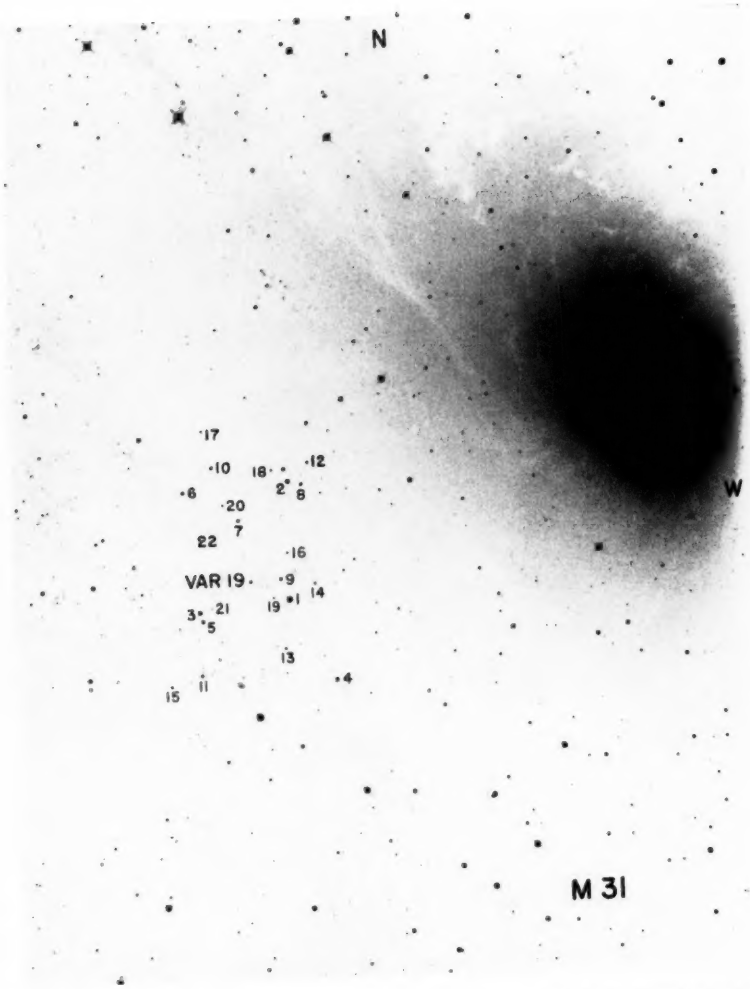

FIG. 2.—Identification chart for the sequence stars for variable 19 in M31. Magnitudes for these stars are given in Table 1.

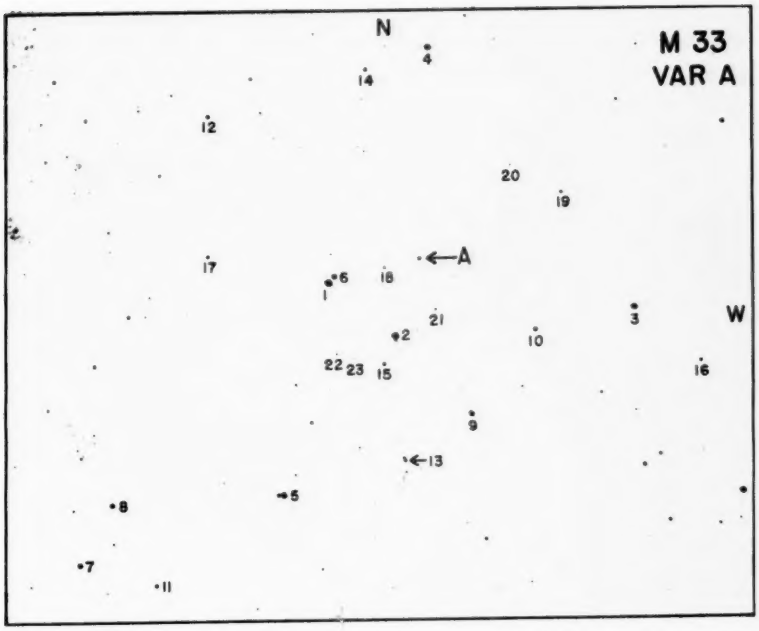

FIG. 3.—Identification chart for the sequence stars for variable A in M33. Magnitudes for these stars are given in Table 1.

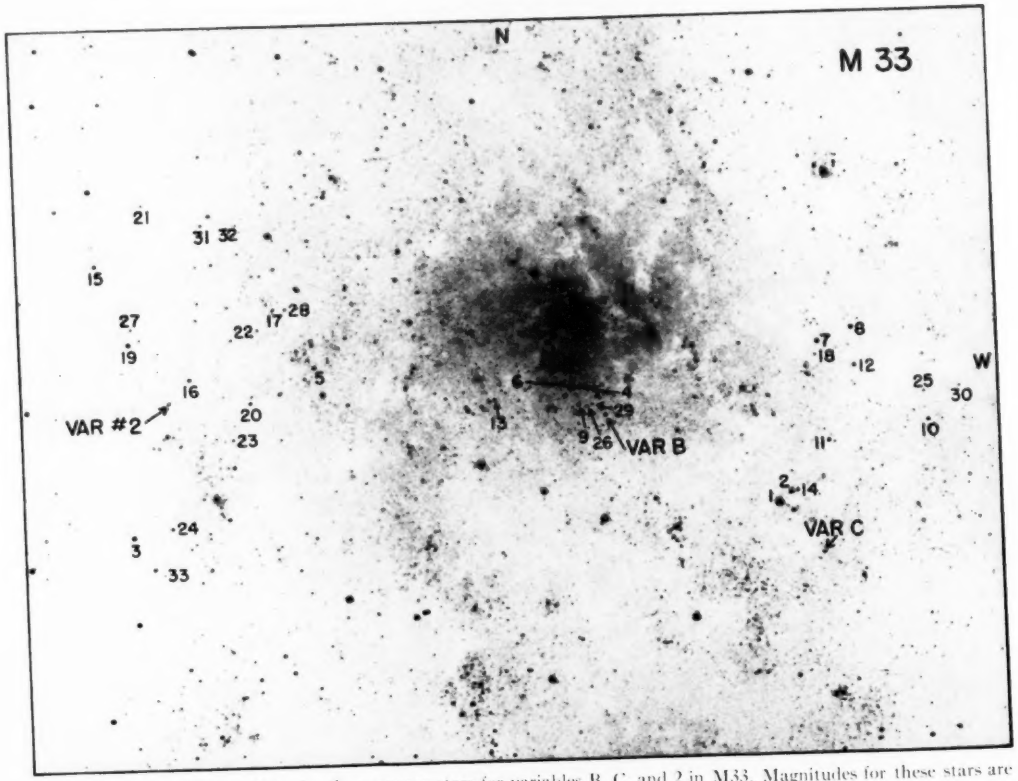

FIG. 4.—Identification chart for the sequence stars for variables B, C, and 2 in M33. Magnitudes for these stars are given in Table 1.

All data reported in this paper are on the m_{pg} and m_{pv} system. Equations 1 and 2 may be used to transform to the **P**, **V** system, although the accuracy of the data presented ($\delta m \cong 0.1$) hardly warrants such transformation. The intercomparisons between SA 68 and the three sequence fields were reduced by H. F. Weaver's Q_0 method[10] and by the more common direct-comparison method. No significant difference was found between these methods of reduction. The adopted magnitudes of the sequence stars are given in Table 1. The sequence in M33 (center) is the most uncertain, owing to the background of the unresolved nuclear region. Although the systematic effect of this background is probably small,[11] the random error is larger than for the clear regions encountered in the other two sequences. The number of intercomparisons for each sequence is as follows: M33, center, three for m_{pg}; M33, A, five for m_{pg} and three for m_{pv}; M31, 19, five for m_{pg} and three for m_{pv}. The internal agreement indicates that the final magnitudes are reliable to $\delta m \cong \pm 0.1$.

TABLE 1

MAGNITUDES OF THE STANDARD STARS

M31; VAR. 19			M33 CENTER		M33; VAR. A		
No.	m_{pg}	m_{pv}	No.	m_{pg}	No.	m_{pg}	m_{pv}
1	13.13	11.56	1	13.79	1	13.67	13.23
2	14.65	13.83	2	15.46	2	14.39	13.72
3	14.68	13.94	3	15.72	3	15.00	13.92
4	15.04	14.28	4	15.93	4	15.05	14.20
5	15.40	14.25	5	16.04	5	15.15	14.22
6	15.55	14.63	6	16.07	6	15.27	14.89
7	15.71	14.99	7	16.35	7	15.53	14.91
8	15.89	15.30	8	16.41	8	15.68	15.02
9	16.20	15.08	9	16.49	9	15.99	15.15
10	16.23	15.31	10	16.52	10	15.99	15.64
11	16.30	16.18	11	16.77	11	16.16	15.94
12	16.33	15.63	12	16.88	12	16.37	16.13
13	16.65	16.06	13	16.90	13	16.62	16.46
14	16.83	16.00	14	16.93	14	17.02	16.57
15	16.96	16.79	15	16.96	15	17.17	16.71
16	17.03	16.39	16	17.01	16	17.23	17.03
17	17.05	15.99	17	17.24	17	17.35	16.98
18	17.07	16.69	18	17.49	18	17.42	.....
19	17.47	17.56	19	17.50	19	17.69	16.92
20	17.61	17.62	20	17.58	20	18.02	.....
21	17.98	17.18	21	17.66	21	18.06	.....
22	18.62	18.28	22	17.69	22	18.35	.....
			23	17.71	23	18.37	.....
			24	17.71			
			25	17.71			
			26	17.75			
			27	17.91			
			28	17.97			
			29	18.01			
			30	18.04			
			31	18.11			
			32	18.21			
			33	18.38			

[10] *Ap. J.*, **106**, 366, 1947.

[11] See Seyfert and Nassau, *Ap. J.*, **101**, 179, 1945, for an evaluation of the background effect.

III. THE LIGHT-CURVES, ABSOLUTE MAGNITUDES, AND COLORS

The extensive observational material on M33 and M31 available in the Mount Wilson plate collection from 1920 to the present (1953) permitted a rather complete coverage of the photographic light-curves of these variables.

Fast photovisual plates have come into general use only in the last five years. Color indices for these stars are therefore available from 1950. The photographic light-curves

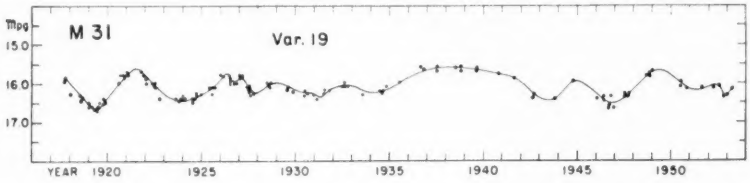

FIG. 5.—The light-curve for variable 19 in M31 from 1917 to 1953. The apparent photographic magnitude is plotted as ordinate.

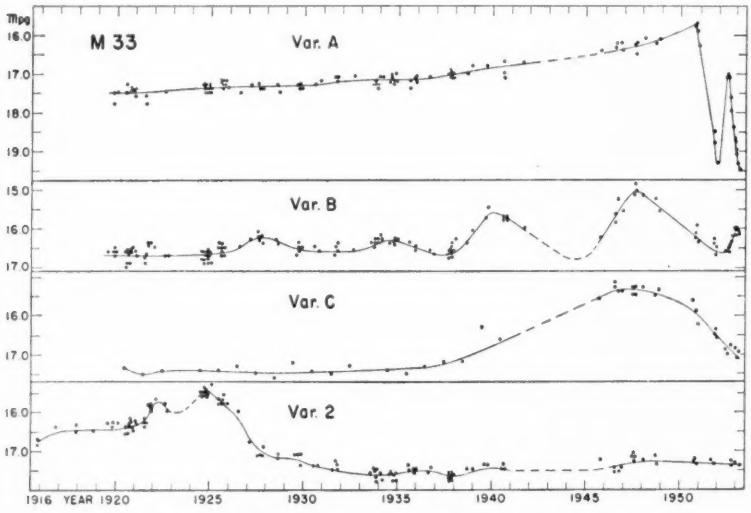

FIG. 6.—Photographic light-curves for the four variables in M33

for all five stars are shown in Figures 5 and 6.[12] The individual points were obtained by eye-estimates of the variables compared with the appropriate sequence stars. The accuracy of this method is somewhat less than one-tenth of a magnitude but is entirely sufficient to show the characteristics of the light-curves.[13]

Magnitude estimates are available for the variables in M33 prior to 1920 from two

[12] It is of interest to inspect the distribution of points in Figs. 5 and 6. The lack of points in the interval 1941–1945 shows the imprint of the last war on observational activity at Mount Wilson.

[13] Variable C in M33 is crowded by a close optical companion which makes magnitude estimates difficult when the variable is fainter than $m_{pg} = 16.5$. Yearly means are given in Fig. 6 for this star while it was fainter than 16.5 mag. Only plates of the best seeing were used to establish the mean values shown.

sources: (1) Table III in Hubble's[5] paper gives Duncan's[3] and Wolf's[4] published magnitudes reduced to the photographic International System plus a few additional data obtained from existing early plates, and (2) early plates taken with the 36-inch Crossley reflector at Lick (mostly by Keeler) were made available through the kindness of Director Shane and Dr. N. U. Mayall, and a few additional plates taken at Mount Wilson by

TABLE 2

ADDITIONAL PHOTOGRAPHIC MAGNITUDES FOR VARIABLES IN M33

DATE	VARIABLES IN M33				OBSERVER
	2	A	B	C	
1899 Sept. 12	17.6	18.1	16.4	17.1	Lick
1903 Jan. 16	17.4	17.6	.....	(16.7)	Isaac Roberts
1908 Nov. 17	17.7	17.6	16.3	.....	Lick
1909 Sept. 10	17.5	17.7	16.3	.....	Ritchey
1910 Oct. 24	17.4	.....	16.2	17.3	Lick
1914 Dec. 14	17.4	17.6	16.0	.....	Lick
1915 Aug. 5, 6, 7	17.4	17.4	16.3	17.7	Ritchey
1915 Nov. 5	17.2	17.5	16.1	.....	Lick

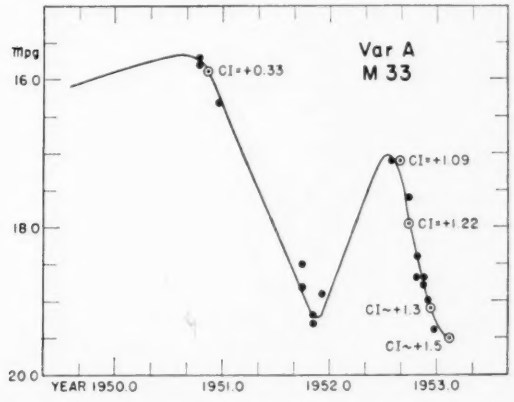

FIG. 7.—Details of the light-curve of variable A in M33 from 1950 to 1953. Color indices were determined on five dates and are indicated in the figure.

Ritchey were examined. The additional magnitudes obtained from these old plates are given in Table 2. These points are not plotted in Figure 6.

Figures 5 and 6 show the irregular character of the variations of these stars. The light-curves for M33, A, and M33, B, have unique characteristics. The light-curve for M33, A, together with the additional observations in Table 2, shows that the magnitude of this star increased since the early observation in 1899 from $m_{pg} = 18.1$ mag. to the peak value of 15.7 mag. in 1950.9. At its maximum light, the star's color index was 0.33 mag. The very sudden drop in brightness with the corresponding change in the color index is shown in detail in Figure 7. The large light-variation is partially a result of the finite spectral response of the detector. The change in the bolometric luminosity is much

smaller. Since data for the color-index variation are available (shown in Fig. 7), the bolometric corrections may be inferred.[14] The amplitude of δM_{bol} is 1.4 mag., compared with a range of 3.5 mag. in the photographic region. This bolometric range is correct only if the color index is a measure of the effective temperature, an assumption which is near the truth if (1) the Planck function approximates the true energy-distribution-curve and (2) if the light-changes are internal to the star, i.e., not caused by changing amounts of obscuration in the light-path due, for example, to drifting interstellar clouds in M33. This hypothesis of drifting obscuring clouds can be checked from the absorption-to-reddening coefficient obtained from the data of Figure 7. The average value derived from these data is $\Delta m/\Delta(CI) = 2.5$, which is somewhat less than the value of 4.0 currently adopted.[15] For this reason the obscuration hypothesis is probably invalid. The light-variations are most likely internal to the stars themselves.

Perhaps the most interesting of the five stars is M33, B. The undamped, oscillatory character of the light-curve is unique among variables. Careful watch of this star is

TABLE 3

SUMMARIZED DATA

	M31, 19	M33, 2	M33, A	M33, B	M33, C
1. m_{pg} (max.)	15.6	15.4	15.7	15.1	15.3
2. Date at max.	1921.5, 1938.2	1925.0	1950.9	1947.7	1947.5
3. m_{pg} (min.)	16.7	17.6	19.6	16.7	17.5
4. Date at min.	1919.4, 1946.9	1934	1953	Many	1921–1935
5. CI	0.07	−0.4	0.33	−0.3	−0.2
Date	1950.9	1952.6	1950.9	1952.6	1952.6
6. M_{pg} (max.) old distance scale	−6.8	−6.9	−6.6	−7.2	−7.0
7. M_{pg} (max.) new provisional scale	−8.3	−8.4	−8.1	−8.7	−8.5

desirable. The next maximum should occur in 1954 if the present trend of light-variation continues.

Although these five stars show little similarity in their light-variations, they do show a strong similarity in their maximum magnitudes. The summarized data are given in Table 3. Rows 1–5 of this table are self-explanatory, while rows 6 and 7 are discussed later.

Two conclusions are evident from Table 3: (1) The similarity of the maximum apparent magnitudes indicates that the peak luminosities of this group of bright variables have a rather small dispersion; this is precisely the characteristic which makes this class of stars important as distance indicators. (2) The color indices in row 5 show that these are blue variables—a surprising result for which there is no known galactic analogue.

It therefore seems that a new class of variables has been isolated. The members of this class are exceedingly luminous and have quite blue color indices. This type of luminous, blue, irregular variable is rather rare in extraglactic nebulae, since only one is known in M31 and five in M33 (including Baade's star, which is also blue and very bright). Hence it is not strange that analogous stars are not known in our galaxy. The chance of discovery of such rare objects is small.

Additional stars of this type are known in the extragalactic nebulae which have been surveyed in some detail. The Sb spiral M81 has six blue variables which have become at least as bright at maximum as the brightest stars associated with the nebula. NGC 2403, M101, NGC 4486, and others in the Virgo cluster have similar bright variables.

[14] G. P. Kuiper, *Ap. J.*, **88**, 492, 1938.

[15] See *Statistical Astronomy* by Trumpler and Weaver (Berkeley: University of California Press, 1953), p. 450, for a summary of the determination of this value.

Although these systems have not yet been studied in sufficient detail, the similarities with the stars in M31 and M33 are evident.[16]

The absolute magnitudes to be assigned to the stars in Table 3 depend upon the apparent distance moduli of M31 and M33. The values which have been adopted in recent years are $m-M = 22.4$ for M31 and $m-M = 22.3$ for M33. The M_{pg} (max.) corresponding to these moduli are given in row 6 of Table 3. The corresponding mean for the five stars is

$$\bar{M}_{pg}\,(\text{max.}) = -6^{M}.9 \pm 0^{M}.2\ (\text{A.D.})\,.$$

Recent work on the Andromeda nebula with the 200-inch Hale telescope by W. Baade,[17] together with the new[9] color-magnitude diagram of M3, has provided evidence that the modulus of M31 of $m - M = 22.4$ is incorrect by about $\delta M = -1^{M}.5$. If this value is eventually substantiated, the apparent modulus of M31 is $m-M = 23.9$, and that of M33 is $m - M = 23.8$. The absolute magnitudes of the blue variables discussed would then be those in row 7 of Table 3, with a mean of

$$\bar{M}_{pg}\,(\text{max.}) = -8.4 \pm 0.2\ (\text{A.D.})\,.$$

The present study provides no information for a decision on a new distance scale. The only conclusion which may be drawn from the present study is that this new class of variable stars will provide rough distances to other nebulae containing such stars in terms of the distance to M31 and M33. The calibration of this unit of distance is proceeding along lines described elsewhere;[17] the preliminary value of the correction to the scale being $\delta M = -1^{M}.5$, as already quoted.

IV. SPECTRA

Spectra for four of the five variables are available from plates taken with the 100-inch telescope, largely by R. Minkowski, who has generously placed these at our disposal for discussion. Dr. George Herbig, of the Lick Observatory, has obtained spectra of variables B and C with the nebular spectrograph at the Crossley reflector which gives 430 A/mm at $H\gamma$ and has sent his results for inclusion in the present discussion.

A summary of the available plates is shown in Table 4. The phase of light-variation corresponding to the dates given may be found from Figures 5 and 6. Most of the 100-inch prism plates were obtained with a dispersion of 220 A/mm at $H\gamma$. Nearly the same normal dispersion applies to the grating material. Discussion of these plates follows.

The one available plate of variable A in M33 was taken near the star's peak luminosity in 1950.9. This particular plate is the best of the group. Many faint metal lines are just at the limit of visibility. The most prominent feature is strong H and K of *Ca* II in absorption. The lines $H\gamma$ and $H\delta$ are very weak in absorption, while $H\beta$ is weakly in emission. There is, however, a suggestion of P Cygni characteristics in the hydrogen lines, i.e., very weak emission to the red of the absorption components of $H\gamma$ and $H\delta$ may be present. The high-luminosity criteria lines of *Fe* II at λ 4171 and λ 4177 are clearly present. The *Mg* I triplet at $\lambda\lambda$ 3890, 3892, and 3896 is just visible. The spectrum matches that of ϵ Aurigae fairly well (class F0 I*a* by the MKK atlas), except for the weakness of the hydrogen lines. This may be due to weak emission partially filling the absorption

[16] The star S Doradus in the Large Magellanic Cloud may also be of the type discussed here. Its P Cygni characteristics and color show this. The maximum absolute magnitude to be assigned to this star, with the new provisional modulus to the Magellanic Clouds of $m - M \approx 19.0$, is $M_{pg} = -10.8$, which is considerably brighter than the M31 and M33 stars. S. Gaposchkin has, however, found that most of the light-variation of S Doradus may be explained by an eclipse. If this is true, classification with the intrinsic variables in M31 and M33 is doubtful.

[17] Annual Report of the Director, Mount Wilson and Palomar Observatories, *Carnegie Institution of Washington Yearbook, 1950–51,* and *1952–53.*

cores. Judging by the weakness of the hydrogen lines, the class may be as late as F8, with extreme supergiant characteristics. The dispersion is too small and the spectrum insufficiently wide (the magnitude of this star was $m_{pg} = 15.8$ when the spectrogram was taken) to give a more detailed match. The best compromise classification is probably intermediate F, I*a*. The color index of variable A in M33 at this time was $CI = +0.3$, which is normal for this spectral class.

Six spectrograms of variable B in M33 are available: four from Mount Wilson and two by Herbig. The Mount Wilson plate of August 10, 1940, is near the peak luminosity of variable B in 1940.0. This plate shows $H\beta$ and possibly $H\gamma$ in emission, with H and K of equal strength weakly in absorption. No other features are clearly visible. The class

TABLE 4

SPECTROGRAMS AVAILABLE

Variable Star	Date	Optics	Observer
Var A, M33	Nov. 7, 1950	100″ prism	Minkowski
	Aug. 10, 1940	100″ prism	Hubble
	Aug. 22, 1950	36″ Crossley	Herbig
Var B, M33	Oct. 31, 1951	36″ Crossley	Herbig
	Nov. 28, 1951	100″ grating	Minkowski
	Sept. 28, 1952	100″ grating	Sandage
	Nov. 21, 1952	100″ grating	Minkowski
	Nov. 30, 1946	100″ prism	Minkowski
	Aug. 23, 1947	100″ prism	Humason
	July 24, 1949	36″ Crossley	Herbig
	July 25, 1949	36″ Crossley	Herbig
Var C, M33	Sept. 22, 1949	36″ Crossley	Herbig
	Aug. 3, 1951	36″ Crossley	Herbig
	Oct. 28, 1951	36″ Crossley	Herbig
	Oct. 31, 1951	36″ Crossley	Herbig
	Nov. 29, 1951	100″ grating	Minkowski
Var 19, M31	Nov. 5, 1951	100″ prism	Minkowski

cannot be earlier than F0 judged by the H and K lines. The next spectra of this star, obtained by Herbig, were taken on the descending part of the light-curve. Herbig writes:

> The spectrum of B is quite featureless except for a rather weak emission at $H\beta$, and faint absorption H and K. From comparison with galactic supergiants I believe the strength of H and K, their ratio and the weakness of the hydrogen lines indicate that the spectral type cannot be earlier than F0, and may be considerably later. . . . I estimated the color index on these two plates as +0.3 and 0.0 respectively, so [the star] can hardly be a very late type.

(The somewhat uncertain color index from the Mount Wilson photometric data is −0.3 at this time.) Herbig's first plate, on August 22, 1950, was taken about midway between maximum light in 1947 and minimum light in 1952. His second plate was near minimum phase. Apparently, no great change occurred in the spectrum in this interval.

A plate by Minkowski of variable B on November 28, 1951, shows that a change had occurred since Herbig's last plate of October 31, 1951. The hydrogen lines $H\beta$, $H\gamma$, $H\delta$, and $H\zeta$ were visible in emission together, with the two strongest *He* lines at λ 3889 and λ 4471 also weakly in emission. No other lines were visible. H and K were not seen, but they may have been lost in the grain, since the spectrum could not be widened at the telescope, owing to the faintness of the source. This plate was obtained near minimum light, which occurred in February, 1952. The two remaining plates were taken on the ascending branch of the light-curve in 1952. The plate of November 21, 1952, shows very weak $H\beta$ and $H\gamma$ in emission. Furthermore, P Cygni characteristics are rather pro-

nounced, especially for $H\beta$. The H and K lines are possibly visible but of much weaker intensity than on September 28, 1952. The pronounced P Cygni characteristics on November 21 and their absence on September 28 clearly indicate that a change in the spectrum had occurred in this interval.

With the exception of the plate of November 28, 1951, which showed only hydrogen and helium in emission, the spectra of variable B in M33 are, in general, characterized by weak $H\beta$ and $H\gamma$ in emission (with P Cygni characteristics some of the time) and with H and K in absorption. No other features are prominent. The H and K lines, together with the blue color index, point to an F spectral type.

Three Mount Wilson spectrograms of star C are available. Two of these occur at the phase of maximum light. Both show H and K in absorption of nearly equal strength,

TABLE 5

SUMMARY OF SPECTRAL FEATURES

Star	Date	Light-Phase	Hydrogen Lines	H and K Ca II
Var A, M33	Nov. 7, 1950	Max. light	β in em.; γ, δ with P Cyg	Strong
	Aug. 10, 1940	Near max.	β and γ in em.	Present
	Aug. 22, 1950	Decreasing light	β in em.	Present
	Oct. 31, 1951	Near min.	β in em.	Present
Var B, M33	Nov. 28, 1951	Near min.	$\beta, \gamma, \delta, \zeta$, and *He* 3889 *He* 4471 in em.	Not seen
	Sept. 28, 1952	Increasing light	β and γ in em.	Strong
	Nov. 21, 1952	Increasing light	β and γ in em; P Cyg	Just visible
	Nov. 30, 1946	At max.	γ and δ in abs.	Strong
	Aug. 23, 1947	At max.	None seen	Present
Var C, M33	July–Sept. 1949	Decreasing light	β in em.	Not seen
	Aug.–Oct. 1951	Decreasing light	β and γ in em.	Present
	Nov. 29, 1951	Decreasing light	β and γ in em.	Not seen
Var 19, M31	Nov. 5, 1951	.....	β and γ in em.	Present

indicating that the spectral class is at least later than F0. Lines of $H\gamma$ and $H\delta$ are weakly in absorption. Herbig's 1949 spectra occur just after maximum light on the slow decline to minimum. He writes: "The 1949 plates of Variable C show a faint emission at $H\beta$ and little else. The 1951 spectra show that the $H\beta$ emission is considerably stronger and emission is present at $H\gamma$; H and K appear in absorption." Minkowski's spectrogram of November 29, 1951, deep on the descending light-curve toward minimum, shows $H\beta$ and $H\gamma$ in emission, with little else clearly seen. H and K are not visible.

Only one plate of variable 19 in M31 is available. This plate of November 5, 1951, shows bright $H\beta$. The line $H\gamma$ is also weakly in emission. H and K may be faintly visible. The continuous spectrum of this star extends far into the ultraviolet—again showing that this class of object is quite blue.

The characteristics of the spectra of these stars are summarized in Table 5. In general, the spectra now available for these variable stars show sufficient similarities to indicate that we are dealing with a group of objects which may be classed together as a unit. The spectra usually show the hydrogen lines weakly in emission, with H and K in absorption. The strength of the H and K lines, together with the blueness of the continuum, indicate that the spectral class may be intermediate F. Furthermore, the spectrum of variable A in M33 showed sufficient detail to indicate the supergiant nature of these objects.

A CATALOGUE OF EMISSION NEBULAE NEAR THE GALACTIC PLANE

STEWART SHARPLESS*

MOUNT WILSON AND PALOMAR OBSERVATORIES
CARNEGIE INSTITUTION OF WASHINGTON
CALIFORNIA INSTITUTE OF TECHNOLOGY

Received April 23, 1953

ABSTRACT

A catalogue is given of 142 emission nebulae within several degrees of the galactic equator and between galactic longitudes 315° and 105°. Known early-type stars associated with these nebulae are listed.

The 48-inch Schmidt telescope of the Mount Wilson and Palomar Observatories has the greatest resolving power of existing wide-field instruments and thus provides the most complete material available at the present time for a survey of distant emission nebulae. The 48-inch plates on which this survey is based were kindly put at the author's disposal by Drs. Baade and Minkowski. The survey extends between galactic longitudes 315° and 105°. The limits in galactic latitude vary between 1° and 5°, averaging about 3°, on either side of the galactic equator. Red plates were taken on Eastman 103*a*-E emulsion behind a red Plexiglas filter, and blue plates on 103*a*-O emulsion. The exposures

TABLE 1

PLATE CENTERS

α	δ	α	δ	α	δ	α	δ
17h10m	−39°	18h20m	−10°	19h45m	+25°	22h10m	+58°
17 20	−33	18 35	− 5	20 00	+30	23 00	+60
17 35	−29	18 45	0	20 10	+35	23 40	+61
17 55	−24	18 55	+ 6	20 35	+40	0 20	+62
18 05	−19	19 05	+11	20 45	+45	1 00	+62
18 10	−15	19 15	+16	21 15	+50	1 50	+61
18 15	−26	19 30	+21	21 45	+53	2 25	+60

were such as to produce a background density of several tenths. The plate centers are listed in Table 1. Each plate covers 40 square degrees of the sky, with a scale of approximately 2 inches per degree.

In listing the nebulous objects on these plates, an attempt was made to exclude all planetary and reflection nebulae. The latter were identified on the basis of their blue color as revealed by a comparison of the red and blue plates. The doubtful cases are indicated as such in the notes following the catalogue.

The nebulae are listed in Table 2. The co-ordinates of the center of each nebula were measured to 1 minute of arc with respect to a near-by star and, for ease in identification, are given for the same epoch as the corresponding section of the BD or CD catalogue. The angular diameters are given in the third column. Owing to the diffuse nature of many of these nebulae, their diameters cannot be defined with an accuracy of better than about 20 per cent. The maximum diameters of irregular objects are given. In the fifth, sixth, and seventh columns the nebulae are classified according to their form (1 = cir-

* Now at the U.S. Naval Observatory, Washington, D.C.

TABLE 2

CATALOGUE OF EMISSION NEBULAE

No.	α	δ	Diameter	Form	Structure	Brightness	Stars	Notes
1	16h 54m3	−37° 56′	60′	3	2	2	1	NGC 6281*
2	17 3.8	−38 19	12	2	3	2–3	.....	
3	17 5.3	−36 56	4	3	2	3	.....	NGC 6302
4	17 9.4	−33 56	60	3	2	1–2	1	
5	17 9.8	−39 11	5	2	3	3	.....	
6	17 10.1	−38 16	100	3	2	2	9	NGC 6337
7	17 11.7	−35 51	50	3	3	3	4	NGC 6334*
8	17 16.9	−34 4	90	3	3	2–3	2	NGC 6357*
9	17 21.0	−30 9	2	3	1	2	.....	
10	17 21.1	−31 26	40	2	2	2	1	
11	17 26.5	−32 30	120	1	2	2	9	NGC 6383*
12	17 36.9	−28 47	25	3	2	2	.....	
13	17 38.6	−29 15	20	3	2	2	.....	*
14	17 39.5	−29 12	4	1	2	2	.....	
15	17 40.0	−28 37	10	3	2	2	.....	
16	17 40.1	−29 4	12	1	1	2	.....	
17	17 41.2	−31 13	30	2	2	2	3	
18	17 42.4	−28 51	5	3	2	2	.....	
19	17 46.1	−25 0	60	3	2	2	5	S 181
20	17 50.2	−23 18	20	3	2	1	.....	
21	17 53.9	−23 35	40	1	2	1	.....	
22	17 54.8	−23 1	20	3	3	3	1	NGC 6514
23	17 56.8	−24 24	90	3	3	3	14	NGC 6523*
24	17 57.7	−21 40	90	3	2	2	1	S 186
25	17 57.9	−14 10	25	2	2	2	1	S 185
26	18 0.3	−18 17	3	3	2	1	.....	
27	18 1.7	−24 1	40	3	2	2	3	NGC 6559*
28	18 1.9	−16 50	3	3	1	2	.....	
29	18 2.1	−23 40	8	1	2	2	2	IC 1274
30	18 2.5	−23 49	8	1	1	2	1	IC 1275
31	18 3.6	−17 46	15	3	2	2	.....	
32	18 7.2	−20 18	20	3	1	2	5	
33	18 7.4	−18 17	90	3	2	2	6	
34	18 8.0	−17 27	15	2	1	2	.....	
35	18 8.1	−16 47	60	3	2	2	2	IC 4701*
36	18 8.3	−19 50	2	3	2	2	1	NGC 6589*
37	18 8.3	−18 42	3	3	1	2	.....	
38	18 8.5	−19 55	2	3	2	3	1	NGC 6590*
39	18 9.1	−19 43	20	3	2	2	3	IC 1284
40	18 9.4	−15 40	5	1	2	2	1	*
41	18 9.8	−11 47	40	3	3	2–3	7	NGC 6604*
42	18 10.5	−14 0	25	3	3	3	10	NGC 6611*
43	18 12.4	−16 14	60	3	3	3	6	NGC 6618*
44	18 14.1	−14 39	10	3	2	2	1	S 194*
45	18 17.1	−13 18	15	3	2	2	.....	S 195*
46	18 17.2	−14 47	35	3	2	2	1	*
47	18 22.6	− 8 43	2	3	2	1	1	
48	18 23.1	− 9 49	7	1	2	1	.....	
49	18 23.5	− 8 34	8	3	2	2	.....	
50	18 24.1	−11 52	5	3	2	1	1	
51	18 25.2	− 5 8	2	3	2	2–3	.....	
52	18 28.9	− 6 49	20	3	2	2	.....	S 198
53	18 29.9	− 7 27	20	3	2	1	.....	
54	18 36.8	− 3 16	25	3	1	1	.....	
55	18 37.0	− 0 25	20	2	2	2	1	*
56	18 38.0	− 2 8	8	3	2	2	.....	
57	18 39.3	− 3 54	7	3	2	2	.....	
58	18 49.4	+ 7 38	7	1	2	1	.....	*
59	18 52.2	+ 6 56	10	1	2	1	.....	*
60	18 56.5	+13 55	12	1	1	1	.....	
61	19 1.7	+ 5 23	3	3	2	2	.....	*
62	19 5.0	+16 38	2	3	2	3	.....	
63	19 16.6	+13 42	40	3	2	1	.....	
64	19 18.3	+20 31	2	1	2	2	.....	*
65	19 37.0	+22 57	40	1	2	1–2	3	NGC 6823*

TABLE 2—*Continued*

No.	α	δ	Diameter	Form	Structure	Brightness	Stars	Notes
66	19h39m9	+25° 0′	25′	3	2	2	1	S 43
67	19 40.3	+24 17	10	3	1	1	1	
68	19 40.8	+27 54	50	1	1	1	4	S 44
69	19 43.2	+26 30	6	3	2	2	.....	S 45
70	19 44.0	+26 7	5	1	2	1	.....	
71	19 49.0	+26 50	1	3	2	3	.....	
72	19 49.2	+28 55	1	1	2	2	.....	*
73	19 50.2	+29 49	10	1	2	1	.....	
74	19 53.0	+31 2	15	1	1	1	1	
75	19 54.5	+34 54	20	3	2	2	1	
76	20 6.8	+37 55	18	2	3	3	1	NGC 6888*
77	20 12.3	+36 18	7	1	2	2	.....	*
78	20 17.0	+39 48	180	3	3	2–3	.....	*
79	20 26.2	+43 31	60	3	2	2	1	S 73
80	20 27.7	+46 52	2	1	2	2	.....	S 76
81	20 29.0	+45 10	15	1	2	2	1	
82	20 29.8	+46 23	50	3	2	2	.....	S 78*
83	20 33.9	+41 41	30	3	2	1	.....	S 217*
84	20 37.7	+38 58	50	3	2	1–2	.....	S 220*
85	20 39.9	+40 27	40	3	2	1–2	.....	*
86	20 51.5	+44 23	240	3	3	2	1	NGC 7000, IC 5067–8
87	20 58.8	+49 18	1	1	1	1	.....	
88	21 0.4	+49 4	1	3	2	1	.....	
89	21 9.0	+47 9	2	3	2	3	.....	
90	21 33.2	+49 42	15	1	2	2	.....	S 92
91	22 13.4	+55 24	90	3	3	2	3	*
92	22 16.9	+58 0	15	3	2	2	.....	S 94*
93	22 27.2	+57 44	1	3	2	2	.....	
94	22 29.5	+57 28	10	3	2	1	.....	S 96
95	22 39.3	+59 8	4	3	2	1	.....	
96	22 41.8	+57 18	30	3	3	2–3	3	NGC 7380
97	22 43.7	+59 10	2	3	2	2	.....	S 97
98	22 44.4	+56 57	4	3	1	1	.....	S 98
99	22 45.7	+60 25	60	3	2	2	.....	
100	22 49.6	+57 42	2	1	1	1	.....	
101	22 50.3	+57 45	2	3	2	3	.....	
102	22 50.5	+57 46	1	1	1	2	.....	
103	22 51.0	+61 51	60	3	2	2	9	
104	22 52.7	+58 1	2	3	2	3	.....	
105	22 53.2	+57 58	5	1	2	2	.....	S 11
106	22 59.1	+59 28	2	1	2	3	.....	
107	23 7.5	+60 43	10	2	3	3	.....	NGC 7538*
108	23 9.5	+60 21	7	3	2	2	.....	
109	23 9.8	+59 15	90	3	3	2–3	5	S 13, 14*
110	23 14.3	+60 24	40	3	3	2–3	2	NGC 7635*
111	23 26.6	+59 59	10	3	2	2	.....	S 102
112	23 31.6	+59 10	3	3	2	2	.....	S 273
113	23 33.0	+61 8	10	2	2	2	1	S 103*
114	23 35.3	+60 10	10	1	1	1	1	
115	23 45.9	+59 40	7	2	2	2	.....	S 104
116	23 46.8	+59 34	5	1	1	1	1	
117	23 54.3	+63 49	20	1	2	2	1	S 105*
118	0 0.0	+64 9	2	3	2	1	.....	
119	0 7.1	+63 6	15	3	1	1	.....	
120	0 7.8	+60 27	1	1	1	1	.....	*
121	0 14.0	+60 56	30	1	2	2	1	S 21
122	0 19.2	+63 54	2	1	2	2	.....	*
123	0 19.6	+60 35	15	3	1	1	.....	
124	0 23.4	+61 40	40	3	1	1	2	
125	0 28.6	+62 42	2	3	2	1	.....	
126	0 32.0	+62 4	1	1	1	1	.....	
127	0 40.2	+62 8	15	3	1	1	.....	
128	0 40.5	+64 25	15	3	1	1	.....	
129	0 41.5	+63 57	2	3	1	1	.....	
130	0 51.2	+60 12	120	3	2	2	1	IC 63, 59*
131	0 52.2	+62 7	2	1	1	1	.....	

TABLE 2—*Continued*

No.	α	δ	Diameter	Form	Structure	Brightness	Stars	Notes
132	$0^h59^m.7$	+62°21′	1′	3	2	2	.....	
133	1 13.7	+61 6	10	3	3	2	.....	*
134	1 21.3	+57 37	9	3	3	2	.....	S 22*
135	2 1.3	+63 29	2	1	1	1	.....	
136	2 22.5	+60 48	150	3	3	2–3	8	IC 1805*
137	2 25.9	+59 0	2	3	1	3	.....	
138	2 29.3	+59 0	3	3	1	1	.....	
139	2 31.1	+59 0	5	3	2	1	.....	
140	2 36.0	+61 17	2	1	1	2	.....	
141	2 36.0	+61 20	1	1	1	1	.....	
142	2 36.3	+61 21	2	2	2	1	.....	*

NOTES TO TABLE 2

1 Cluster of A stars southeast of center.
7 Several detached portions; lane of emission extending about 2° toward west.
8 Very bright central portion.
11 Cluster around central O-star.
13 May contain faint cluster.
23 M8; appears to be connected with M20 = NGC 6514.
27 Appears to be connected with M8.
35 May be connected with NGC 6618.
36 May be connected with IC 1284.
38 May be connected with IC 1284.
40 May be connected with NGC 6618.
41 Very bright central portion; cluster.
42 Appears to be connected with NGC 6604 and NGC 6618.
43 Very bright central portion, about 25′ in diameter.
44 May be connected with NGC 6611.
45 About six detached portions.
46 May be connected with NGC 6611.
55 Contains faint cluster.
58, 59, 61 May be reflection nebulae.
64 Very small faint cluster in center.
65 Cluster in center.
72 Faint star in center.
76 Peculiar filamentary structure.
77 May be very compact cluster in center.
78 γ Cygni nebula; consists of several bright condensations, including NGC 6914, NGC 6910, IC 1318 and condensations at 20^h14^m, +38°45′, and 20^h22^m, +39°20′.
82 Cluster near brightest part.
83, 84, 85 These appear to be condensations in a connecting lane between the P Cygni nebulae and NGC 7000.
91 Very small cluster around HD 211853.
92 Appears to be small cluster around +57°2513.
107 Peculiar turbulent structure.
109 Small cluster in center.
110 Very bright central portion containing +60°2522; appears to be small cluster around this star.
113 Small cluster in center.
117 Small cluster in center.
120 Two detached circular regions, each with star in center.
122 Star in center.
130 γ Cas nebulosity; in addition to bright nebulae to north and east of γ Cas, there is also a faint arc about 2° to the east.
133 Small cluster in center.
134 Crescent-shaped; filamentary.
136 Extends northwest as far as 3° from center; cluster in central part; bright condensations at $1^h49^m.1$, +60°7′.
142 Very small cluster in center.

In addition to the discrete nebulae listed above, there are several extended regions of faint emission:

A. 17^h00^m to 17^h30^m, −35° to −33°. This region also contains NGC 6383 and Nos. 4 and 8.
B. 18^h10^m to 18^h20^m, −18° to −12°. This region also contains NGC 6611, NGC 6618, and Nos. 34, 35, 40, 41, and 44.
C. 19^h35^m to 20^h35^m, +32° to +44°. This is the P Cygni nebulosity and is probably ionized by the Cygnus concentration of early-type stars.
D. 20^h20^m to 20^h40^m, +45° to +48°. This consists of faint emission to north and southeast of No. 82.
E. 22^h00^m to 22^h20^m, +58° to +60°. This consists of faint emission to north and west of No. 92.
F. 22^h50^m to 23^h15^m, +61° to +63°. This consists of faint emission between Nos. 103 and 110.

TABLE 3

CATALOGUE OF ASSOCIATED O- AND B-TYPE STARS

Nebulae	Star	Mag.	Spectral Type
1	153919	6.73	Od
4	156327	9.4	Oa
6	156468	8.0	B3
	156688	7.14	B3
	157038	6.3	B8p
	E323015	.....	B
	E323016	9.5	B2
	E323019	10.7	B0
	E323025	.....	B0
	E323110	10.7	B0
	E323117	.....	B5
7	E319699	10.2	B0
	E319701	.....	B
	E319702	9.5	B
	E319703	10.4	B5
8	157504	11.8	Oa
	E319881	10.7	B
10	158186	6.81	B3
11	159176	5.71	Oe5
	E317828	.....	B5
	E317837	.....	B5
	E317842	.....	B5
	E317844	8.7	B5
	E317845	9.5	B5
	E317846	.....	B5
	E317858	10.4	B
	E317861	10.7	B
17	161839	10.2	B5
	161853	8.0	B3
	E318406	.....	B0
19	162718	9.0*	B0
	162978	6.13	B2
	E314700	.....	B5
	E314701	10.2	B5
	E314704	.....	B
22	164492	6.91	Oe5, OB
23	164794	5.86	Oe5
	164816	7.9	B0
	164865	8.3	B
	164906	9.0	B
	164947	10.0	B5
	165052	6.79	Oe5
	E315023	.....	B3
	E315024	10.2	B5
	E315026	10.9	B5
	E315031	9.0	B3
	E315032	.....	B5
	E315033	.....	B3
	E315034	.....	B5
	E315035	10.2	B3
24	165516	6.22	B1, OB
25	165319	8.1	B0, OB
27	165921	7.7	B0, OB
	166056	9.7	B
	166192	8.9	B5
29	166033	9.0	B
	E314031	.....	B5
30	166107	7.64	B5
32	167263	6.02	B1, OB
	167379	8.7	B9
	E312973	9.4	(B0)
	E312974	9.7	B5
	E312989	10.6	B3
33	167336	9.4	B5, OB
	167411	8.6	B3, OB
	167412	9.4	B5
	167478	10.3	B5
	167771	6.37	Oe5, OB
	E312875	11.0	B0
35	167633	8.7	Oe5, OB
	167657	9.4	B3
36	167638	10.3	B5
38	E313094, 5	10.3	B5
39	167722	10.1	B5
	167815	7.59	B2
	E313098	.....	B5
40	−15°4914†	10.7	.....
41	167834	9.2	B
	167971	7.34	B0, OB
	168112	8.7	B0, OB
	168206	8.87	Oa
	−11°4586	9.2	OB
	−12°4970	8.9	OB
	−12°4982	9.4	OB
42	167451	7.9	B2, OB
	167497	9.4	B3, OB
	167519	10.1	B
	167543	8.8	B2, OB
	168015	8.9	B8, OB
	168075, 6	8.5	B, OB
	168137	9.4	B, OB
	168183	8.3	B0, OB
	168207	10.1	B0
	168504	9.2	B, OB
43	168163	9.1	B3
	168302	9.9	B5
	168607	8.9	B, OB
	168625	9.2	B
	168726	9.7	B5
	168987	8.3	B
44	168894	9.7	B
46	−14°5037	8.3	OB
47	−8°4623†	10.1	.....
50	−11°4665†	9.7	.....
55	173371	6.80	B9
65	E344775	10.0	B, OB
	E344776	8.8	B
	E344783, 4	9.5	B, OB
66	E338916	10.0	B
67	E338936	9.8	B2
68	186943	9.98	Oa
	E332737	.....	B5
	E332755	9.0	B0, OB
	E332757	8.7	B5, OB
74	E331626	.....	B9

* Variable Star.
† Central Star.

TABLE 3—*Continued*

Nebulae	Star	Mag.	Spectral Type	Nebulae	Star	Mag.	Spectral Type
75.....	E227018	9.5	B		219460	9.2	Oa
76.....	192163	7.44	Ob		E240234	9.1	B0
79.....	195592	7.15	B, OB		E240250	8.6	B0, OB
81.....	+45°3216	8.9	OB	110.....	220057	6.8	B5
86.....	199579	6.01	Oe5, OB		+60°2522	8.0	OB
91.....	211564	11.07	Oc	113.....	+61°2494†	10.2	.....
	211853	9.0	Ob	114.....	+60°2607†	10.2	.....
	+54°2726	9.4	OB	116.....	+59°2786†	9.7	.....
96.....	215605	9.5	B, OB	117.....	+63°2093†	9.4	.....
	215806	9.4	B, OB	121.....	+60°39	9.4	OB
	215835	8.6	B, OB	124.....	+61°105	8.9	B, OB
103.....	216532	8.0	B3, OB		2928	8.7	G, OB
	216658	8.6	B, OB	130.....	γCas	1.6–2.3	B0p
	216711	9.4	B, OB	136.....	15558	7.82	B, OB
	216898	8.0	B2, OB		15570	8.0	B, OB
	217035	7.76	B5, OB		15629	8.4	B, OB
	217061	9.0	B		+60°493	8.5	OB
	217086	7.70	B0, OB		+60°497	8.7	OB
	217312	7.7	B8, OB		+60°498	10.2	OB
	217463	8.9	B2		+60°501	9.5	OB
109.....	219286	8.6	B		+60°512	10.2	OB
	219287	8.5	B, OB				

cular, 2 = elliptical, 3 = irregular); the amount of inherent structure (ranging from 1 = amorphous to 3 = filamentary); and the surface brightness (on an arbitrary scale of 1–3, ranging, respectively, from the faintest perceptible images to the densest). The eighth column gives the number of known early-type stars associated with the nebula. The true number may be considerably in excess of this. The last column lists previous designations, including those of the recent survey of Hase and Shain.[1]

The stars associated with these nebulae are listed in detail in Table 3. Most of the stars of type B listed here cannot contribute appreciably to the ionization. Their concentration within the boundaries of a nebula, however, leaves little doubt of their physical connection with it. The visual magnitudes and spectral types in Table 3 are taken from the *Henry Draper Catalogue* and its extensions.[2] For stars not contained in these catalogues, the corrected[3] BD magnitude is given. Those stars which appear in the Case survey[4] of O and B stars of high luminosity are indicated as OB in the last column.

Figure 1 shows the apparent distribution of these nebulae with respect to the galactic equator. The scarcity of nebulae north of the equator between longitudes 315° and 30° is clearly due to the obscuring effects of the Great Rift and the Ophiuchus nebulosities. The scarcity of nebulae between longitudes 60° and 70°, however, is evidently real, since the number of faint O and B stars[5] of high luminosity in this region is appreciable. This suggests a rather spotty distribution of interstellar hydrogen along the more remote spiral arms of our galaxy, similar to the distribution found by Baade[6] for emission regions in the outer arms of M31.

[1] *Simeis Izvestiya*, **7**, 93, 1951; **9**, 52, 1952.

[2] *Harvard Ann.*, Vol. **100**, 1936; Vol. **112**, 1949.

[3] *Harvard Ann.*, Vol. **78**, 1916.

[4] Nassau and Morgan, *Ap. J.*, **113**, 141, 1951.

[5] Nassau and Morgan, *Pub. Michigan U. Obs.*, **10**, 43, 1951.

[6] Private communication.

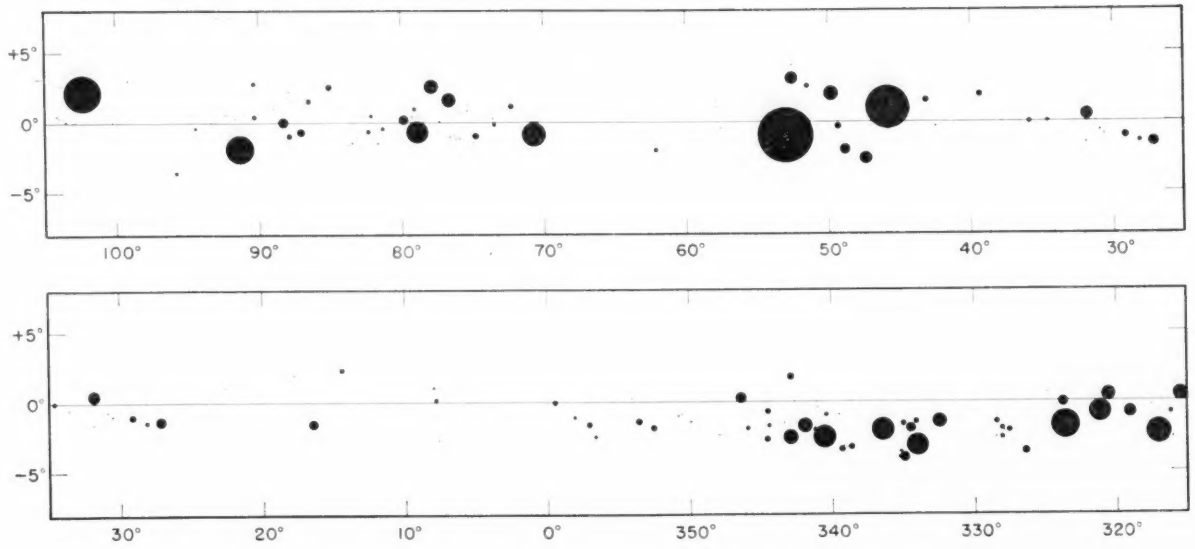

FIG. 1.—The distribution of emission nebulae between $l = 315°$ and $l = 105°$

While reliable distances for these objects cannot be obtained from their average characteristics, nevertheless certain qualitative information on their spacial distribution can be inferred from Figure 1. The gradual decrease in the angular sizes of the nebulae from $l = 315°$ to $l = 360°$ is consistent with the suggestion[7] of an inner spiral arm going off in perspective in the direction of Scutum. Similarly, the difference in the angular sizes of the nebulae near $l = 50°$ and $l = 30°$, respectively, is qualitatively in keeping with the curvature of the arms, as illustrated by Oort[8] on the basis of observations of the 21-cm line of hydrogen.

Individual spectroscopic parallaxes of the stars associated with these objects will be necessary in order to obtain further information on the details of their distribution in space. Such programs are now in progress at the United States Naval Observatory and the Yerkes Observatory.

The author is indebted to Drs. Baade and Minkowski for the observational material upon which this paper is based. An appointment as Carnegie Fellow permitted him to make use of the facilities of the Mount Wilson and Palomar Observatories.

[7] Morgan, Sharpless, and Osterbrock, *A.J.*, **57**, 3, 1952.

[8] *Sky and Telescope*, **12**, 60, 1953.

SPECTROGRAPHIC OBSERVATIONS OF GALACTIC EMISSION REGIONS AND NEBULAE

HUGH M. JOHNSON
Yerkes Observatory
Received June 22, 1953

ABSTRACT

Sixty-three spectrograms of interstellar regions near O stars have been analyzed. Interstellar emission is nearly always present near O stars within 250 psc of the galactic plane; emission is not observed at greater distances from the galactic plane. Emission lines of *H*, *He* I, [*N* II], [*O* II], [*O* III], [*S* II], and [*Ne* III] have been recorded and measured for extents and relative intensities. The stellar sources of excitation of each region and their distances from the sun and from the galactic plane have been tabulated. The *EM* of many regions has been derived from the *Hα* line intensity and the known *EM* of one region. The *EM* and the corresponding linear extent of each measured region have been combined to find the hydrogen density. The positive values of the *EM* range from 400 to 63,000, while the densities range from 0.7 cm^{-3} in Cassiopeia and Cepheus to 65 cm^{-3} in Orion. The most frequent type of emission line is one with an intense core and faint extensions. The extensions may refer to the intercloud medium.

INTRODUCTION

The work of Struve and his colleagues in 1937–1939, first with the Yerkes 58-foot slit spectrograph[1] and then with the McDonald 150-foot slit spectrograph,[2] established the existence of large areas where *Hα* appears in emission. Until 1938, practically all observations had been confined to bright emission nebulae, but the spectrograms of Struve and Elvey revealed faint extended emission regions in the Milky Way. These regions showed little concentration toward individual stars of early spectral type, although they were found at low galactic latitudes; other conclusions to be drawn from this series of 80 observations have been summarized by Struve.[3] Interstellar emissions in the range λλ 3727–6563 over many areas along the Milky Way were thus known by 1939. But the dispersion of the 150-foot McDonald spectrograph became very low at *Hα*. The [*N* II] 6584–6548 doublet was blended with *Hα*, and the [*S* II] 6731–6717 doublet was not detected. There is little doubt that *He* I 5876 would have blended with the airglow *Na* I 5890–5896 doublet if it had been present in McDonald regions. The important question of the purity of *Hα* emission remained open until 1948, when Page[4] used the B spectrograph at the McDonald Observatory to resolve *Hα* and [*N* II] 6584 and to measure their intensity ratio in seven emission nebulae. He found that [*N* II] 6584 was weak compared with *Hα*.

In 1951–1953 the writer made a series of spectrographic observations of galactic emission regions and nebulae with the B spectrograph at the Yerkes Observatory. The B spectrograph has been described by Page,[5] and its application to the present series of observations has been reported.[6] Altogether, there are sixty-three exposures on emission regions or suspected emission regions. They were planned to give new information on

[1] O. Struve, *Ap. J.*, **86**, 613, 1937; J. L. Greenstein and L. G. Henyey, *Ap. J.*, **86**, 620, 1937; **87**, 79, 1938.

[2] O. Struve, G. Van Biesbroeck, and C. T. Elvey, *Ap. J.*, **87**, 559, 1938; O. Struve and C. T. Elvey, *Ap. J.*, **88**, 364, 1938; **89**, 119, 517, 1939; **90**, 301, 1939; and J. L. Greenstein and L. G. Henyey, *Ap. J.*, **89**, 647, 653, 1939.

[3] *J. Washington Acad. Sci.*, **31**, 217, 1941.

[4] *Ap. J.*, **108**, 157, 1948.

[5] *La Physique des comètes* (Louvain: Imprimerie Ceuterick, 1953), p. 49.

[6] H. M. Johnson, *Ap. J.*, **117**, 235, 1953; **118**, 162, 1953.

(*a*) the frequency of occurrence of interstellar emission in the presence of O stars, (*b*) the extent of emission regions near O stars, (*c*) the relative intensities of the emission lines in many regions, and (*d*) the emission measure and hydrogen density of various emission regions. We may assume that the B spectrograph, which isolates a few angstroms and which utilizes an $f/0.65$ camera with modern 103*a*-F film, will be more efficient than other means heretofore used to pick up nebular emissions against night-sky radiations. It follows that points *a* and *b* may be investigated more certainly than in the past, while very little has been published about points *c* and *d*. However, the sensitivity of the B spectrograph is somewhat offset by the disadvantage of scanning the sky with a slit, albeit a long one.

OBSERVATIONAL PROCEDURE

The spectra were obtained on Eastman 103*a*-F emulsion, dated November, 1951, except where otherwise noted. Since a 14-mm square film loads the spectrograph, sheets from only two boxes supplied the entire program, including tests and calibration exposures. All emulsion was continuously refrigerated until a few hours or days before cutting and loading. Inherent fog remained light and uniform on all pieces of film, and they were considered to be homogeneous enough for photometric use. Rocked-tray development was given to each plate for 3 minutes in Eastman developer.

Owing to their small size, plates which had been exposed to the sky could not also be exposed for calibration or standardization. For calibration a special sensitometer was designed to duplicate the conditions of sky observation. A diffusing screen in this sensitometer was placed in front of the object glass of the spectrograph and illuminated by a neon lamp in six known steps of intensity. Six corresponding plates were taken and developed to match the conditions of developing a group of plates of interstellar emissions. Measures of peak densities of selected neon lines in such a series were made on the tracing of a Brown recorder attached to the Yerkes microdensitometer. The results were combined to make characteristic curves in the range of wave lengths λλ5945–6717. Several series of sensitometer exposures were made to match all the conditions imposed on sky plates and to test variations among the characteristic curves. The exposure times of these series ranged from 2 to 5 hours per plate so as to stay within a factor of 2 of sky-exposure times. In addition to its neon lamp, the sensitometer was provided with a tungsten lamp and Corning Daylite filter. In this way a continuous spectrum approximating the night-sky continuum could be exposed together with the neon line spectrum. The effect of background continuum on line intensities was investigated, and it was found that moderate background intensity could be subtracted from line plus background intensities to leave only line intensity if the microdensitometer slit were made sufficiently narrow. To keep the night-sky continuum at a minimum, to exclude as many stars as possible, and to resolve emissions as close as 14 A, the slit of the spectrograph was set (except where noted) 0.10 mm wide = 16μ on the emulsion = 6 A in the spectrum = 8′ on the sky. On an average exposure the night-sky continuum has a density of about 0.05 near λ 6600 or λ 4900.

Characteristic curves were constructed in particular for the *Ne* I 5945, 6599, and 6717 lines, because they are free of gross blending at our resolution and are nearly extremes of wave length in the recorded neon spectrum. Uniform contrast over a wide range of wave lengths is typical of a fast, low-contrast emulsion.[7] Indeed, the characteristic curves varied so slightly in the range λλ 5945–6717 that, within the accuracy of about 15 per cent shown by different characteristic curves at any one wave length, it was assumed that a common curve might be used for all emissions on a plate in the range λλ 3727–6731.

The variation in the response of the whole spectrographic apparatus to light of different wave lengths in the range λλ 3727–6731 was determined with a General Electric

[7] G. R. Harrison, *J. Opt. Soc. Amer.*, **19**, 267, Fig. 4, 1929.

standard lamp. Its radiation was measured by the manufacturer at several wave lengths from λ 3998 to λ 6563. Interpolations and extrapolations of the intensity to the wave lengths listed in Table 1 were made. The factor S_λ is inversely proportional to the intensity required to produce unit density in unit time. Therefore, a plate intensity at any wave length relative to one at λ 6563 must be divided by the relative sensitivity factor S_λ in order to reduce it to the true intensity outside the object glass. The object glass used with the spectrograph does not focus equally well at all wave lengths. This will not appreciably affect the relative line intensities at two wave lengths of an emission region which is large compared with the projected width of the slit.

The sensitivity of the spectrograph is nearly uniform along much of the length of the slit. Table 2 gives the relative sensitivity as a function of angular distance from the center

TABLE 1

RELATIVE SENSITIVITY OF THE B SPECTROGRAPH WITH OBJECT GLASS AND 103*a*-F EMULSION

λ (A)	S_λ	λ (A)	S_λ	λ (A)	S_λ	λ (A)	S_λ
6731	1.0	6584	1.0	5876	1.0	4861	1.7
6717	1.0	6563	1.0	5007	1.2	3727	2.4:
6678	1.0	6548	1.0	4959	1.4		

TABLE 2

SENSITIVITY AND CURVATURE CORRECTION ALONG THE SLIT

		Distance from Center of Spectrum (Degrees)				
		0	1.5	3.0	4.5	6.0
Relative sensitivity		1.0	1.0	1.0	1.0	0.9
Corrections to the declination of the center of the slit (minutes of arc)	$\delta = -20°$	0	+1	+2	+ 4	+ 7
	$\delta = +20°$	0	−1	−2	− 4	− 7
	$\delta = +40°$	0	−1	−4	− 9	−16
	$\delta = +50°$	0	−2	−6	−13	−23
	$\delta = +60°$	0	−2	−8	−18	−33

of the slit. Strong emissions are recorded for several degrees beyond the 6° limit tabulated; but there the sensitivity is lowered rapidly, the images become of poor quality, and the scale becomes very compressed. Within the central 12° of the slit the scale is very nearly linear and equal to 0.141 mm/degree on the sky. Table 2 also gives corrections to the declination of the center of the slit for points away from the center. The slit was tested to run accurately east-west by keeping a bright equatorial star centered in it with a periscope (built in the spectrograph) while turning the mounting on its polar axis through several degrees. The same device made it easy to check the mutual alignment of the slit, setting circles and finder on the mounting within a minute of arc. The mounting of the 6-inch UV telescope on the roof of the Yerkes Observatory was used. Setting and guiding were estimated to be accurate to ± 2′ arc.

Exposures were made only during hours with no astronomical twilight. The occasional presence of moonlight is noted in Table 3. An exposure of at least 4 hours in a quite clear sky was standard. However, exposures shortened by clouds have not been discarded from

TABLE 3

THE SPECTROGRAMS AND O STAR REGIONS

No.	Center of slit (1900) α	δ	Date	U.T. mid. exp.	Length exp.	Sky	Exciting star(s)	Spectral type	r (pc)	z (pc)	Nebula(e) on slit
(1)	(2)	(3)	(4)	(5)	(6)	(7)	(8)	(9)	(10)	(11)	(12)
1	17^h48^m	$-18°31'$	Jul.25,'52	5^h24^m	4^h08^m	c	167659 167771	08 08	2300	-110	....
2	17 53	-24 29	Jul.24,'52	5 30	4 00	c	164794 165052	05 07	1300	- 60	NGC 6523
3	18 51	-20 33	Aug.22,'52	4 29	4 03	c-(h)	(175876)	06	1900	-400	....
4	19 22	+23 04	Aug.24,'52	5 35	5 50	c	+22°3782	06	1800	- 40	....
5	19 46	+31 51	Jul.27,'52	5 55	5 00	c	186980	08	1500	+ 70	....
6[a]	19 49	+46 54	Aug.18,'52	6 27	5 19	c-(sh)	188209	09.5 III	1000	+160	+45°3216
7[a]	19 55	+18 26	Aug.17,'52	5 20	5 11	sh	188001	08 f	1800	-170	....
8	19 55	+38 00	Aug.23,'52	5 38	6 15	c	192281 192639 193322 193443 193514 193595 193682 228841	05 f 08 f 08 09 III 07 f 07 05 06.5	1500	+ 30	NGC 6888
9	20 07	+35 16	Jun.27,'52	5 59	4 02	sh-h	190864 190918 191612	06 09.5 I+WR 08	2300	+ 40	McD 12
10	20 48	+34 12	Aug.25,'52	6 21	6 02	c-(sh)	198846	BO IV	1800	-220	....
11	21 12	+43 31	Dec. 2,'51	2 33	3 04	sh	199579	06	900	- 10	NGC 7000
12	21 23	+59 25	Sep.15,'52	5 03	5 22	c	202214 206267 207198 209481 209975 210839	BO V 06 09 II 09 V 09.5 Ib 06 f	700	+ 60	McD 19 Ced 190
13	21 27	+57 17	Sep.16,'52	5 44	6 17	c	Same as No. 12		700	+ 60	IC 1936b
14	21 38	+61 52	Sep.17,'52	6 19	7 21	c	Same as No. 12		700	+ 60	....
15	21 49	+51 59	Sep.19,'52	6 14	6 32	c	210809	09 Ib	3600	-210	....
16	22 04	+59 02	Sep.20,'52	5 54	5 22	c	Same as No. 12		700	+ 60	McD 19
17[a]	22 06	+55 30	Sep.21,'52	6 18	5 45	c	214419 215835 235673 235825 +55°2840 +53°2843	07+WR 06 nn 07 09 V 07 08	3600	-120	McD 16
18	22 32	+39 32	Nov.12,'52	1 41	2 38	c	214680	09 V	460	-140	10 Lac
19	22 32	+39 00	Nov.22,'52	4 07	5 36	sh	Same as No. 18		460	-140	10 Lac
20	22 32	+38 40	Nov.13,'52	4 06	6 19	sh	Same as No. 18		460	-140	10 Lac
21	22 32	+38 27	Oct.22,'52	5 01	7 26	c	Same as No. 18		460	-140	10 Lac
22	22 32	+38 25	Nov.11,'52	3 28	6 19	c	Same as No. 18		460	-140	10 Lac
23	22 32	+38 02	Dec. 8,'52	2 18	4 25	c	Same as No. 18		460	-140	10 Lac
24	22 32	+37 32	Oct.24,'52	5 49	7 08	c	Same as No. 18		460	-140	10 Lac
25	23 10	+52 23	Oct.25,'52	6 33	6 20	sh	(218915)	09	3600	-430	....
26	23 40	+61 35	Oct.21,'52	7 09	6 50	c	108 225160 +61°2559	08 fp 08 f 09 V	2500	+ 20	NGC 7538 NGC 7635 IC 59 IC 63

TABLE 3 (Continued)

THE SPECTROGRAMS AND O STAR REGIONS

No.	Center of slit (1900) α	δ	Date	U.T. mid. exp.	Length exp.	Sky	Exciting star(s)	Spectral type	r (psc)	z (psc)	Nebula(e) on slit
(1)	(2)	(3)	(4)	(5)	(6)	(7)	(8)	(9)	(10)	(11)	(12)
27[a]	23^h53^m	+59°05'	Dec.17,'52	3^h38^m	7^h05^m	c	Same as No. 26		2500	+ 20	NGC 7538
28	0 01	+63 11	Oct.12,'52	3 16	4 26	c	Same as No. 26		2500	+ 20	....
29	0 12	+50 57	Oct.13,'52	3 21	4 28	sh-c	(1337)	09 III	2300	-430	....
30	1 05	+56 05	Oct.23,'52	6 22	4 37	sh-c	5005	06	2500	-260	NGC 281
31	2 09	+40 57	Dec.18,'52 Dec.19,'52 Jan. 6,'53	3 37 3 33 2 33	5 00 2 25 3 25 10 50	c-h c-h c	(44633)	08 V	2300	-690	....
32[b]	3 44	+23 53	Jan.12,'53	4 12	7 45	c	23862	B8 p	150	- 60	Pleiades
33	3 57	+36 24	Sep.25,'52	6 35	6 30	sh-h	24912	07	300	- 60	NGC 1499
34[a]	3 57	+36 16	Sep.24,'52	4 37	3 07	(sh)-c	Same as No. 33		300	- 60	NGC 1499
35	3 57	+36 20	Sep.23,'52	4 35	3 00	c	Same as No. 33		300	- 60	NGC 1499
36	3 57	+35 46	Dec. 1,'51	10 00	2 33	sh	Same as No. 33		300	- 60	NGC 1499
37	4 55	+43 41	Jan. 3,'52	9 45	3 40	c	....	....	....	....	....
38[c]	5 12	+34 20	Oct.13,'52	8 07	4 43	c-sh	34078	09.5 V	580	- 10	IC 405
39[a,d]	5 12	+34 18	Sep.27,'52	7 26	5 32	c-sh	Same as No. 38		580	- 10	IC 405
40	5 12	+34 16	Sep.23,'52	8 14	3 40	c	Same as No. 38		580	- 10	IC 405
41[a]	5 12	+34 12	Sep.24,'52	8 13	3 50	c	Same as No. 38		580	- 10	IC 405
42[e]	5 12	+34 04	Oct.12,'52	8 05	4 47	c	Same as No. 38		580	- 10	IC 405
43[a]	5 17	+37 21	Sep.28,'52	7 57	4 26	c-sh	(34656) (35921)	07 09.5 III	1200	+ 40	....
44	5 28	+ 9 58	Feb. 9,'53	3 50	5 12	c	36861	08	600	-110	λ Ori
45[a]	5 30	- 5 28	Jan.31,'52	6 39	1 11	sh	37022	06 p	500	-150	NGC 1976
46	5 30	- 5 33	Oct.22,'52	9 29	1 01	c	Same as No. 45		500	-150	NGC 1976
47	5 30	- 5 38	Oct.24,'52	10 07	1 10	c	Same as No. 45		500	-150	NGC 1976
48	5 30	- 5 43	Mar.11,'53 Apr. 7,'53	2 23 2 33	1 00 1 14 2 14	sh-h c-sh	Same as No. 45		500	-150	NGC 1976
49[f]	5 33	- 2 34	Nov. 5,'51	8 41	4 00	c	37468 37742	09.5 V 09.5 Ib	360	-100	IC 434 Orion Loop
50[g]	6 06	+48 10	Dec. 9,'52 Dec.14,'52 Dec.15,'52	3 54 1 52 5 39	3 38 3 17 1 49 8 44	sh-c sh-h c	(41161)	09 n	1300	+320	....
51	6 24	+20 36	Jan.13,'53	5 34	8 03	h	42088	06	2100	+ 70	NGC 2175
52[a]	6 29	+11 27	Feb.27,'52	3 38	4 30	c	47839	07	700	+ 50	NGC 2264
53	6 29	+10 08	Feb.25,'52	3 42	4 45	c	Same as No. 52		700	+ 50	NGC 2264
54	6 29	+ 9 11	Feb.23,'52	3 48	5 00	c	Same as No. 52		700	+ 50	NGC 2264
55	6 29	+ 7 47	Feb.26,'52	3 37	4 35	c-(h)	46056 46149 46150 46223 46485 46573 46966 47129 48099	08 08 06 05 08 07 08 08 06	1400	0	NGC 2237

TABLE 3 (Continued)

THE SPECTROGRAMS AND O STAR REGIONS

No.	Center of slit (1900) α	δ	Date	U.T. mid. exp.	Length exp.	Sky	Exciting star(s)	Spectral type	r (psc)	z (psc)	Nebula(e) on slit
(1)	(2)	(3)	(4)	(5)	(6)	(7)	(8)	(9)	(10)	(11)	(12)
56[a]	6^h29^m	+ 6°03'	Jan.27,'52	4^h58^m	6^h00^m	(h)-sh	Same as No. 55		1400	0	NGC 2237
57	6 29	+ 5 03	Jan.21,'52	2 34	3 22	c-(h)	Same as No. 55		1400	0	NGC 2237-9
58[a]	6 29	+ 4 59	Jan.30,'52	5 28	6 00	c	Same as No. 55		1400	0	NGC 2237-9
59[a,h]	6 32	+10 07	Nov. 3,'51	10 17	1 04	c-sh	Same as No. 52		700	+ 50	NGC 2264
60	7 14	-24 35	Feb.18,'53	5 38	3 00	c	57060 57061	07 f var. 09 III	830	- 60	McD 44
61[i]	7 24	-10 00	Feb.15,'53 Feb.15,'53 Feb.17,'53	1 40 4 25 4 14	1 20 2 00 6 08 9 28	sh sh c	54662 57682	06 09 V	1100	+ 40	IC 2177 McD 45 McD 46
62[a]	7 34	-14 13	Mar. 7,'53 Mar. 9,'53	3 25 3 49	3 00 4 56 7 56	c-h c	(61347)	09 Ib	5000	+440	....
63[a]	7 47	+17 02	Dec.15,'52 Dec.16,'52	9 16 7 22	4 47 8 26 13 13	c c	(60848)	08 V:pe	1900	+620	....

NOTES TO TABLE 3

a Aurora Borealis present during part of exposure.
b Value for r from H. Shapley, Star Clusters (New York: McGraw-Hill Book Co., 1930).
c 24.1-day moon during 3^h40^m of exposure.
d Eastman 103a D emulsion.
e 23.1-day moon throughout exposure.
f Eastman 103a F emulsion dated 1949; slit width = 9' arc.
g Value for r and spectrum for HD 41161 from Stebbins, Whitford and Huffer.
h Eastman 103a O emulsion; slit width = 11' arc.
i 3.1-day moon during 2^h03^m of exposure.

our list of data when they showed interstellar emission. Neither did the intervention of perceptible visual haze stop an observation. At many declinations an observation made with the 6-inch UV telescope mounting must start or stop near the meridian, and when an exposure lasts several hours one cannot be too critical about constant quality of the sky or about the altitude at the beginning or end of the exposure.

OBSERVATIONAL DATA

The regions of observation were based chiefly on the O stars north of $\delta = -25°$ in the catalogue of 1332 B stars by Stebbins, Whitford, and Huffer.[8] This catalogue includes nearly all the O–B2 stars north of $\delta = -40°$ to the limit of magnitude of the *Henry Draper Catalogue*. The center of the slit was set within a few minutes of arc of the declination of an O star (but not necessarily so closely in right ascension). Brighter O stars were kept out of the slit to avoid their spectra for the photometry of the nebular lines. The attempt to keep all bright stars out of the slit was the reason, in fact, for displacements from O stars of more than half a slit-width (or more than 4′ on the sky). However, displacements of the slit by more than half its width from some stars did not always prevent their spectra from appearing.

A few reference points were chosen from *Hα*-emission areas on a set of prints from photographs taken by C. Fehrenbach and B. Strömgren, although there is an obvious advantage in searching for emissions which depend on stars with known color excesses. Several spectrograms were obtained within a few minutes of arc of one another for more detailed results in certain regions. Except for these spectrograms, the series was made independently of the known nebulae.

Table 3 lists the data for the spectrograms and the O-star regions. The 1900 right ascension and declination of the center of the slit are given in the second and third columns. The fourth and fifth columns record the date and U.T. of the middle of the exposure. In some cases exposures were continued over more than one night; individual durations and totals are set down in the sixth column. The visual sky is described in the seventh column by means of the symbols c = clear, h = hazy, or sh = slightly hazy. The use of the parentheses indicates that the h or sh condition lasted a negligible part of the exposure.

The eighth column of Table 3 identifies the stars which excite each *H* II region. Parenthetical identifications are used when no emission was detected in the vicinity of the star(s). Strömgren's[9] theory of *H* II regions shows that a single O star outweighs many B stars in exciting an emission region. For this reason few B stars appear in Table 3, although it must be remembered that O and B stars (and emission nebulae) often form an apparently physical group. W stars and P Cygni stars also may belong to such a group, but few of them have been included in Table 3. The distances r of emission nebulae must be taken from the corresponding distances of the exciting stars. Since these stars are preferentially of early O type, it is exceptionally difficult to obtain accurate values of r. The ninth column lists W. W. Morgan's spectral type, the tenth column lists distances based on his spectroscopic parallaxes, and the eleventh column lists the distance from the galactic plane, $z = r \sin b$, where $\sin b$ is the average sine of the Lund galactic latitude of the exciting stars. Whenever the spectrograph slit fell on or near an emission nebula in Cederblad's[10] catalogue of bright diffuse galactic nebulae, the nebula is named in the twelfth column of Table 3.

Table 4 gives the data for the emission lines. Corresponding index numbers in the first column of Tables 3 and 4 refer to the same plates. "Line type" in the second column classifies the appearance of the *Hα* emission as it extends along the slit. The symbols are:

[8] *Ap. J.*, **91**, 20, 1940; *Mt. W. Contr.*, No. 621, 1940.

[9] *Ap. J.*, **89**, 526, 1939; **108**, 242, 1948.

[10] *Lund Medd.* Ser. II, **12**, No. 119, 1946.

TABLE 4

THE EMISSION LINES

No.	Line type	Trac. slit length and α (1900)	Angular extent on slit (σ) and reduced relative intensities of the lines: [SII] 6731	[SII] 6717	[NII] 6584	Hα 6563	[NII] 6548	[OIII] 5007	[OIII] 4959	Hβ 4861	Hγ 4340	[OII] 3727	10^{-2} x EM	s (pc)	N_H
(1)	(2)	(3)	(4)	(5)	(6)	(7)	(8)	(9)	(10)	(11)	(12)	(13)	(14)	(15)	(16)
1	s	0.9	...	...	2.3	3.1	...	...	...	...	...	...	...	62	...
		$17^h55.9$	...	.35	.26	1	...	...	...	...	...	...			
2	b,g ce-b	0.4	0.6	0.6	2.4	$2.4_{+1.0}$	0.7	0.6	0.5	0.7	0.6	...	...	27 +11	...
		17 57.7	.062	.11	.42	1	.16	.16	.043	.11	...	...			
3	...	...	...	...	...	...	...	...	...	...	...	...	(0)	...	(0)
		...	...	...	...	...	...	...	...	...	...	...			
4	ce	0.4	...	0.5	0.4	1.6	...	...	...	...	...	...	22	25	7
		19 38.9	.12	.15a	.29	1	...	...	...	...	...	...			
5	s	2.2	...	...	...	7.3	...	...	...	...	...	...	...	95	...
		19 36.0	...	...	...	...	...	...	...	...	...	...			
6	ce	0.4	...	...	...	8.5	...	...	...	...	...	...	...	74	...
		20 28.6	...	...	...	...	...	...	...	...	...	...			
7	s	0.5	...	...	...	0.5	...	...	...	...	...	...	...	8	...
		19 44.0	...	...	...	...	...	...	...	...	...	...			
8	ce	0.4	5.4	5.7	6.4	>10.5	...	1.6	pres.	1.6	1.6	1.6	19	>140	<3
		20 00.0	.17	.21	.38	1	...	.075	...	.022	...	.081	16	>140	<2
		0.9													
		20 04.0	.11	.16	.24	1	...	.089	.059	.078	...	.13			
9	b	1.0	...	pres.	pres.	>12.6	...	...	...	...	...	...	...	>250	...
		20 03.1	...	.30	.21	1	...	...	...	...	...	...			
10	s	2.5	...	...	pres.	10.5	...	...	...	...	...	...	5	170	1
		20 48.1	<.15	<.15	...	1	...	...	...	...	...	...			
11	b-nce	0.5	7.7	7.7	9.2	>13.3	pres.	2.4	pres.	2.5	0.7	...	...	>100	...
		20 48.5	...	.070	.18	1	...	.029	.017	.045	...	...	...	>100	...
		0.5													
		20 56.9	.046	.049	.15	1	...	.023	.009	.041	...	...			
12	s-b	1.2	...	...	pres.	>11.1	pres.	...	...	...	...	...	6	>68	<2
		21 11.6	...	...	.45	1	...	...	...	...	...	...	4	>68	<2
		2.5													
		21 57.1	...	<.21	.42	1	...	...	...	...	...	...			
13	2ce	0.6	...	2.5	7.0	7.1	2.2	1.7	1.7	1.9	1.9	1.7	49	43	8
		21 39.3	...	.064	.13	1	...	.045	...	.041	...	.025			
14	s	0.8	pres.	pres.	10.0	>12.7	...	...	...	...	...	...	5	>77	<2
		22 06.6	...	...	.29	1	...	...	...	...	...	...			
15	s	0.8	...	...	0.9	1.3	...	...	...	...	...	...	4	41	2
		22 07.0	...	...	.60	1	...	...	...	...	...	...			
16	s	1.3	pres.	pres.	7.5	10.6	...	...	...	...	...	...	5	65	2
		22 00.5	.25	...	.21	1	...	...	...	...	...	...			
17	2ce	0.9	pres.	pres.	8.1	9.8	...	...	...	...	...	...	13	310	1
		22 33.1	.14	.12	.23	1	...	...	...	...	...	...			
18	s	0.8	...	...	...	1.7	...	...	...	...	...	...	8	7	7
		22 34.0	...	...	...	...	...	...	...	...	...	...			
19	ce	0.4	...	pres.	pres.	1.4	...	...	...	...	...	...	>11	6	>10
		22 29.1	...	.18a	.15	1	...	...	...	...	...	...			
20	ce	0.3	...	...	0.8	2.2	...	...	...	...	...	...	13	9	9
		22 27.0	...	...	.31	1	...	...	...	...	...	...	5	9	5
		0.3													
		22 30.8	...	...	...	...	...	...	...	...	...	...			

TABLE 4 (Continued)

THE EMISSION LINES

No.	Line type	Trac. slit length and α (1900)	Angular extent on slit (σ″) and reduced relative intensities of the lines [SII] 6731	[SII] 6717	[NII] 6584	Hα 6563	[NII] 6548	[OIII] 5007	[OIII] 4959	Hβ 4861	Hγ 4340	[OII] 3727	10^{-2} x EM	s (pc)	N_H
(1)	(2)	(3)	(4)	(5)	(6)	(7)	(8)	(9)	(10)	(11)	(12)	(13)	(14)	(15)	(16)
21	ce	0.″6 22^{h}26.^{m}9	pres. .14	0.″7 .17	2.″8 .39	2.″8 1	... ...	... ...	... ...	pres? ...	pres? ...	... ...	11	11	7
22	ce	0.″4 22 26.9 0.″4 22 30.8	pres. ... .45	pres. .22 .50	2.″4 .28 .34	3.″9 1 1	... ...	... ...	... ...	... ...	... ...	... ...	13 4	16 16	6 4
23	b	0.″4 22 27.0	pres. .19	pres. .22	pres. .44	2.″1 1	... ...	... ...	... ...	... ...	... ...	... ...	10	8	8
24	s	1.″7 22 33.5	... ...	... .33[a]	1.″6 .34	2.″7 1	... ...	... ...	... ...	... ...	... ...	... ...	5	11	5
25	...	... ...	... ...	... ...	... ...	... ...	... ...	... ...	... ...	... ...	... ...	... ...	(0)	...	(0)
26	nce	0.″6 23 12.3 2.″2 23 24.6 1.″0 0 15.7	10.″7 .11 .28 .14	10.″7 .13 .21[a] .12	pres. .22 .43 .29	≥19.″3 1 1 1	pres?	... ...	... ...	pres.	... ...	pres. .061 ... .15	19 4 9	≥420 ≥420 ≥420	≤2 ≤0.7 ≤1
27	s	0.″7 23 07.0	... ...	pres. .29	pres. .24	≥19.″7 1	... ...	... ...	... ...	... ...	... ...	... ...	4	≥430	≤0.7
28	s	0.″7 0 00.9	... ...	... ...	... ...	pres. ...	... ...	... ...	... ...	... ...	... ...	... ...	5	...	≥0
29	...	... ...	... ...	... ...	... ...	... ...	... ...	... ...	... ...	... ...	... ...	... ...	(0)	...	(0)
30	c	0.″3 0 46.7	... ...	0.″4 .081[a]	0.″3 .22	0.″5 1	... ...	0.″3 .075	... ...	0.″4 .070	0.″4 ...	pres. .033	≥49	11	≥15
31	...	... ...	... ...	... ...	... ...	... ...	... ...	... ...	... ...	... ...	... ...	... ...	(0)	...	(0)
32	(s)	0.″4 3 43.2	... ...	pres? ...	pres? ...	pres? ...	... ...	... ...	... ...	... ...	... ...	... ...	≤7	...	...
33	s	0.″4 3 56.9	1.″2 .085	1.″2 .10	5.″2 .31	5.″4 1	1.″3 ...	... ...	... ...	1.″5 .056	1.″7 ...	1.″7 .018	≥55	14	≥14
34	2ce	1.″1 3 56.9	pres? .12	1.″1 .10	1.″6 .27	2.″0 1	1.″4 .097	... ...	... ...	1.″3 .060	1.″2 ...	... ...	73	5	26
35	ce	0.″9 3 56.9	1.″1 .063	1.″3 .080	1.″7 .29	1.″8 1	1.″6 ...	... ...	... ...	1.″3 .060	1.″4 ...	0.″9 .029	107	5	31
36	ce	0.″5 3 57.4	1.″2 .070	1.″2 .083	1.″7 .30	2.″1 1	0.″9 ...	... ...	... ...	1.″2 .053	1.″8 ...	... ...	...	6	...
37	...	... ...	... ...	... ...	... ...	... ...	... ...	... ...	... ...	... ...	... ...	... ...	(0)	...	(0)
38[c]	ce	0.″6 5 09.7	pres. .096	pres. .10	≥2.″4 .36	≥2.″4 1	pres. ...	... ...	... ...	pres. .060	pres. ...	pres. .046	≥45	≥12	14:
39	ce	... ...	... ...	... ...	... ...	... ...	... ...	... ...	... ...	1.″5 ...	0.″8 ...	0.″9 ...	...	...	...
40	ce	0.″4 5 09.4	pres. ...	0.″4 .16	4.″5 .37	4.″7 1	pres. ...	... ...	... ...	0.″7 .051	1.″1 ...	0.″5 .053	61	24	11

TABLE 4 (Continued)

THE EMISSION LINES

No.	Line type	Trac. slit length and α (1900)	Angular extent on slit (σ″) and reduced relative intensities of the lines [SII] 6731	[SII] 6717	[NII] 6584	Hα 6563	[NII] 6548	[OIII] 5007	[OIII] 4959	Hβ 4861	Hγ 4340	[OII] 3727	10^{-2} x EM	s (pc)	N_H
(1)	(2)	(3)	(4)	(5)	(6)	(7)	(8)	(9)	(10)	(11)	(12)	(13)	(14)	(15)	(16)
41	ce	0.″4 5 09.4	pres. .063	1.″5 .081	4.″5 .29	5.″2 1	pres. .11	pres. .083	... ...	0.″5 .044	... ...	1.″0 .053	63	26	11
42[c]	nce	0.″7 5 09.7	pres. .084	pres. .13	≥2.″4 .22	≥2.″4 1	≥2.″4 ...	... ...	... ...	pres. .044	... ...	pres. .067	34	≥12	<12
43	...	... ...	... ...	... ...	... ...	... ...	... ...	... ...	... ...	... ...	... ...	... ...	(0)	...	(0)
44	s	1.″1 5 25.9	6.″7 .098	6.″7 .085[a]	7.″0 .21	7.″4 1	pres? ...	... ...	... ...	5.″6 .098	5.″5 ...	6.″3 .078	31	39	6
		1.″1 5 33.3	.071	.10	.17	1	...	...	...	.10	...	.058	30	39	6
45[b,d]	ce	0.″4 5 30.4	0.″6 .23	0.″6 .17	0.″8 .88	2.″8 1	0.″6 ...	0.″5 .36	0.″4 .14	0.″4 .076	0.″5 ...	0.″5 .13	...	12	...
46[b,c,d,e]		0.″4 5 30.4	0.″8 .094	0.″8 .13	1.″7 .68	≥1.″7 1	0.″6 .27	0.″7 .40	0.″5 .16	0.″7 .27	0.″7 ...	0.″7 .15	630	≥7	<65
47[b,c,e,f]		0.″4 5 30.4	0.″5 .074	0.″5 .085	0.″7 .41	1.″1 1	0.″5 ...	0.″4 .17	0.″3 .068	0.″6 .20	0.″6 ...	0.″7 .068	380	5	62
48[g]	ce	0.″4 5 30.4	0.″7 .059	0.″7 .070	2.″4 .34	8.″0 1	0.″5 .12	0.″4 .16	0.″2 .059	0.″7 .17	0.″4 ...	pres. .14	≥200	35	≥17
49	ce	... ...	... ...	... ...	0.″7 ...	6.″9 ...	pres. ...	... ...	... ...	1.″9 ...	4.″9 ...	0.″9 ...	...	22	...
50	...	... ...	... ...	... ...	... ...	... ...	... ...	... ...	... ...	... ...	... ...	... ...	(0)	...	(0)
51	c	0.″4 6 03.7	0.″6 .066	0.″6 .072	0.″6 .29	0.″8 1	pres. ...	0.″4 .077	pres. .020	0.″7 .049	0.″7 ...	0.″9 .024	≥49	15	≥13
52	s	1.″0 6 36.9	pres. .18	5.″3 .24	2.″3 .25	6.″1 1	pres. ...	... ...	... ...	2.″0 .11	pres. ...	2.″0 .17	...	37	...
53	nce	0.″6 6 33.3	pres. .050	3.″9 .080	4.″6 .14	4.″6 1	3.″6 .052	0.″8 .047	... ...	3.″6 .065	2.″7 ...	4.″0 .061	...	28	...
54	2ce	0.″6 6 31.5	3.″8 .095	3.″8 .15	4.″1 .34	5.″1 1	4.″3 .16	pres. ...	pres. ...	3.″7 .099	1.″6 ...	3.″2 .086	...	31	...
		0.″6 6 38.2	.036	.064[a]	.16	1	.072	.037	...	.075	...	.066	...	31	...
55	nce	0.″6 6 33.4	pres. .14	1.″8 .25	4.″8 .22	7.″7 1	... ...	... ...	... ...	pres. .088	pres. ...	3.″2 .077	...	94	...
56[b]	2ce	0.″5 6 39.3	5.″8 .084	5.″8 .13[a]	4.″8 .20	4.″8 1	pres. ...	... ...	... ...	3.″8 ...	... ...	6.″8 .058	...	59	...
57[b]	ce	0.″5 6 25.4	2.″4 .063	3.″5 .093	3.″4 .26	5.″1 1	1.″3 ...	0.″9 .060	0.″6 .017	2.″4 .050	1.″0 ...	1.″3 .043	...	62	...
		0.″5 6 34.3	.13	.12[a]	.31	1	...	...	...	...	...	...	...	62	...
58	ce	0.″4 6 28.4	5.″6 .14	5.″6 .16	4.″2 .37	5.″9 1	5.″2 ...	1.″0 .045	0.″8 .014	1.″4 .071	1.″0 ...	4.″0 .042	...	72	...
		0.″4 6 36.5	...	.32[a]	.64	1	...	...	...	...	...	.27	...	72	...
59	ce	... ...	... ...	... ...	... ...	... ...	... ...	... ...	... ...	... ...	... ...	4.″4 ...	...	...	...
60	s	1.″3 7 14.5	... ...	... ...	3.″7 .29	5.″6 1	... ...	... ...	... ...	... ...	... ...	... ...	27	41	6

TABLE 4 (Continued)

THE EMISSION LINES

No.	Line type	Trac. slit length and α (1900)	Angular extent on slit (σ) and reduced relative intensities of the lines: [SII] 6731	[SII] 6717	[NII] 6584	Hα 6563	[NII] 6548	[OIII] 5007	[OIII] 4959	Hβ 4861	Hγ 4340	[OII] 3727	10^{-2} x EM	s (psc)	N_H
(1)	(2)	(3)	(4)	(5)	(6)	(7)	(8)	(9)	(10)	(11)	(12)	(13)	(14)	(15)	(16)
61	ce	0.″5 7h01.m6	5.″6 .11	5.″6 .15	4.″0 .31	5.″1 1	1.″5 ...	2.″3 .067	pres. .030	3.″3 .063	1.″8 ...	5.″3 .075	≥35	49	≥6
62	...	... ...	... ...	... ...	... ...	... ...	... ...	... ...	... ...	... ...	... ...	... ...	(0)	...	(0)
63	...	... ...	... ...	... ...	... ...	... ...	... ...	... ...	... ...	... ...	... ...	... ...	(0)	...	(0)

NOTES TO TABLE 4

a Correction for Ne I 6717 intensity ≈ 30 per cent of [S II] 6717 intensity.
b See Table 8 for data on helium.
c Slit length = 2.″4 arc.
d σ = 0.″5 for Hδ, σ = 0.″3 for Hε, H8 pres., [Ne III] 3869 pres.
e σ = 0.″6 for Hδ, σ = 0.″5 for Hε, σ = 0.″3 for H8, σ = 0.″3 for [Ne III] 3869.
f Hδ and Hε pres.
g Hδ pres.

c = a line consisting only of a "core"; *ce* = a line with a dense core and fainter extensions; *2ce* or *nce* = the same but with two or more cores; *b* = a broken or noncontinuous line; *s* = a smooth or featureless line. This classification discounts apparent photographic effects at the junction of *Hα* emission with the continuum of any star spectrum. The third column lists the length of the recording slit of the Yerkes microdensitometer in degrees on the sky and the right ascension of the center of the slit. The fourth to thirteenth columns give the measured lengths of the observed emissions on the east-west slit, converted into degrees on the sky. The measures are estimated to be accurate to a few tenths of a degree. Where a line was present on the spectrogram with too indefinite an extension to measure, *pres.* is tabulated. Where a line extends more than about 6° from the center of the slit in one or both directions, the inequality sign is used. The inequality sign is also used in those few cases where the slit was shortened below 12° and the emission appears bounded by it. Measures of the angular extents of the interstellar emission lines [*S* II] 6717 and *He* I 6678 may be affected by the frequent presence of neon emissions at very nearly the same wave lengths. Where there was doubt that [*S* II] 6717 was spuriously extended by a superposed *Ne* I 6717 line, the extension of [*S* II] 6717 was written equal to that of [*S* II] 6731, although the latter line usually appeared shorter on plates judged free of *Ne* I 6717. Measures of the extents of the nebular lines [*N* II] 6548, *Hα*, and [*N* II] 6548 may likewise suffer from the partial superposition of the *P* branch of the (6, 1) band of *OH* in the airglow. Measures of its wave lengths[11] on spectrograms give λλ 6533, 6554, and 6575. There is also a neon line at λ 6599. However, these lines are separated by several angstroms from interstellar emissions near them, and they are usually very weak. Indeed, their presence has been adopted as a criterion for sufficient exposure when no *Hα* appears. The negative observations of hydrogen emission in Table 4 depend on this rough criterion.

The fourth to thirteenth columns of Table 4 also list the "reduced relative intensities" of several interstellar emission lines. These reduced relative intensities are the result of three operations: the conversion of densities on the plate into relative intensities, division by the factor $6563 \times \lambda^{-1} S_\lambda$, and the application of corrections for atmospheric absorption. The first and last of these operations remain to be discussed.

The reproducibility of the tracings of the Brown recorder attached to the microdensitometer was tested and found to be good. Spectrograms were carefully adjusted to cross the microdensitometer slit at a constant right ascension. The slit was always shortened so that there was no obvious gradient of density of the emission line along the length of the slit. In the case of an object like the Orion Nebula, where the intensity is known to fall off very rapidly from the central square minute of arc, it is clear that there will be a gradient when the slit must extend at least several tenths of a degree in order to integrate a sufficient number of grains of emulsion. But the effect of this failing on *relative* line intensities derived from densities should be of the second order. The microdensitometer slit was also set to avoid star spectra and obvious plate defects at interstellar lines. These conditions largely determined where tracings might be taken, but tracings were not taken at every suitable place. The absence of an intensity in the fourth to thirteenth columns does not always mean the definite absence of a line. In some cases it means that the line was not definitely measurable.

Relative intensities on the emulsion were derived from the appropriate characteristic curves. The factor $6563 \times \lambda^{-1} S_\lambda$ was then applied, leaving a factor for atmospheric transmission, T_λ, at each wave length. The time average of T_λ is given by the expression

$$(t_2 - t_1)\,\bar{T}_\lambda = \int_{t_1}^{t_2} \exp \frac{-2.303 \times 0.4\, m_\lambda}{\sin\phi \sin\delta + \cos\phi \cos\delta \cos t}\, dt \qquad (1)$$

[11] Cf. J. Cabannes, J. Dufay, and M. Dufay, *C.R.*, **230**, 1233, 1950, who observed the first two lines and report the same wave lengths.

where δ, t_1, and t_2 are the declination and hour angles at the beginning and end of an exposure, respectively, ϕ is the latitude, and m_λ is the zenithal extinction in magnitudes. It is obviously difficult to select mean extinction coefficients to use for these observations, but Table 5 has been made up from existing photometric data at the Yerkes Observatory and other places of comparable altitude. Equation (1) was integrated in all necessary cases by Gauss's numerical method with three points and weights. It was tested to have ample accuracy in an extreme case. Finally, then, the factor $\bar{T}_{6563}/\bar{T}_\lambda$ was multiplied into all relative intensities at the object glass to give the relative intensities reduced to outside the atmosphere.

It should be noted that these intensities remain uncorrected for interstellar reddening. Such reddening should never have an appreciable effect on the relative intensities within the range of wave lengths λλ 6548–6731 or λλ 4861–5007. The smallest photometric errors will occur in the ratio of two red lines of moderate density and of nearly equal wave

TABLE 5

ADOPTED ZENITHAL EXTINCTION

λ (A)	m_λ (Mag.)	λ (A)	m_λ (Mag.)	λ (A)	m_λ (Mag.)	λ (A)	m_λ (Mag.)
6731	0.23	6584	0.24	5876	0.26	4861	0.36
6717	.23	6563	.24	5007	.33	3727	0.80
6678	0.23	6548	0.24	4959	0.34		

lengths exposed at large altitudes on the clearest night. All sources of error grow with departure from these conditions. In particular, the relative intensity of [*O* II] 3727 is scarcely more than a rough estimate, while the relative intensities of the [*S* II] doublet would often be the best on a plate, were it not for the coincidence of the *Ne* I 6717 and [*S* II] 6717 lines. In order to get the intensity of [*S* II] 6717 from the sum of the intensities of these two lines, half of the intensity of the neighboring *Ne* I 6678 was subtracted from the sum whenever it appeared in a tracing. This procedure was adopted after the intensity ratio *Ne* I 6717 : *Ne* I 6678 was found equal to about $\frac{1}{2}$ in spectra free of interstellar emission. When this correction amounts to more than 30 per cent of the intensity of [*S* II] 6717, it has been noted in Table 4. In the case of No. 57 of Table 4, where *He* I 6678 may be superposed on *Ne* I 6678 in one tracing, the *Ne* I 6678 intensity of the other tracing has been used to correct the intensities of both *He* I 6678 and [*S* II] 6717. It is believed that neon intensity varies with position on the slit, so that this alternative was used only once. Terrestrial neon does not appear in short exposures such as those of the Orion Nebula.

There are very few published values of the emission measure[9] *EM* or surface brightness[12, 13] of galactic emission nebulae and extended emission regions. To get at least rough values for some of the areas observed in this survey, the relative intensities of the *Hα* line in a homogeneous group of the spectrograms have been utilized. The largest group of spectrograms in Table 4 developed in the same way are those beginning August 23, 1952. It is also the group which contains the best material for a calibration according to the measures of B. Strömgren,[14] by referring Nos. 38–42 in Table 4 to his *EM* = 7200 over the central 1′.3 of IC 405. The law of the drop of *EM* from that center is not known. The integrated relative *EM*'s along the projection of the slit of the spectrograph show that there is a decrease of interstellar density from the center of the nebula: the relative

[12] V. Ambarzumian, *Zs. f. Ap.*, **6**, 107, 1933.

[13] R. Minkowski, *Pub. A.S.P.*, **61**, 151, 1949.

[14] *Problems of Cosmical Aerodynamics* (Dayton, Ohio: Central Air Documents Office, 1951), p. 7.

EM decreases much faster than does the length of the chord parallel to the line-of-sight diameter which corresponds to the measured angular extent. It should be fairly accurate to set the $EM = 6300$ over the central $8' \times 24'$ of IC 405, corresponding to the *Hα* intensity of No. 41. Then, in the fourteenth column of Table 4, we have

$$EM = \frac{6300\,I}{\sum_{i=1}^{n} \bar{T}_i x_i^{0.9}}, \tag{2}$$

where I is the plate intensity of the *Hα* line, x_i is the length of the ith of n exposures per plate (in two cases $n > 1$), and $\bar{T}_i$ is the corresponding ith mean atmospheric transmission at *Hα* according to equation (1), all variables being relative to their values in plate No. 41. Failure of the reciprocity law should be well compensated by the exponent 0.9 in equation (2), because of the relatively small variation of x in the series. Other sources of error are probably greater. They include variability in the sensitivity of the emulsion and in the atmospheric extinction. An inequality sign is attached to an *EM* whenever atmospheric haze is suspected of affecting its value. The first-order effect of differences of the gradient along the microdensitometer slit from one region to another is another source of error. For example, the *EM* integrated photographically over an $8' \times 18'$ area near the center of the Orion Nebula is nearly meaningless. However, the center of the Orion Nebula is an extreme case, and the results for fainter and more uniform areas may be considerably more accurate than for it. Plates showing no *Hα* emission have been tabulated $EM = (0)$. The lowest *EM* tabulated is $EM = 400$, which must be close to the lower limit measurable on these spectrograms. This is about equal to the *EM* of the faintest emission region measured by Strömgren[14] with another technique. An error by a factor of 2 seems easily possible in the present *EM*'s, and they are uncorrected for interstellar absorption. The *EM*'s of Table 4 do tend to have the smallest values at large r, where there is the greatest interstellar absorption.

The definition of the *EM* of an emission region may be used to derive a mean density of atoms and ions in the region,

$$N_H = \left(\frac{EM}{2\,s}\right)^{1/2}, \tag{3}$$

where $s = r \sin \sigma/2$, and is tabulated in the fifteenth column. This expression assumes that the depth of the emission region equals its apparent breadth. When the *EM* refers to a condensation in the general extent, such a mean N_H will be smaller than the density in the condensation but larger than the density outside it.

Of 63 plates, 62 were exposed in or near 35 sources of excitation. Each source is composed of one or more early-type stars supposed to be acting to produce a separate *H* II region. Table 6 assembles the results so as to answer the question: What is the frequency of occurrence of interstellar emission in the presence of O stars? The conclusions reached from Table 6 are that interstellar emission is present in 27 out of 28 "sources of excitation" which are within 250 psc of the galactic plane, but it is absent whenever a source is more than 300 psc from the galactic plane. These conclusions would not hold for sources surrounded by small, dense *H* II regions.

The *Hα* line in almost every case equals or exceeds other emissions in angular extent. This may be explained simply by the greater intensity of *Hα*. The extent should nearly equal that of a sharply bounded *H* II region unless a cloud of denser gas in the region is mistaken for it. The angular extents reported in Table 4 are generally larger than those determined by *Hα*-filter photography.[13, 15, 16] An example is No. 33 of NGC 1499 with

[15] V. F. Hase and G. A. Shajn, *Pub. Crimean Ap. Obs.*, **6**, 3, 1950; **7**, 93, 1951; **9**, 52, 1952.

[16] S. Sharpless and D. Osterbrock, *Ap. J.*, **115**, 89, 1952.

$\sigma = 5^\circ.4$. The excess over the $200' \times 60'$ dimension given by Hase and Shajn[15] or the $2^\circ.4 \times 0^\circ.8$ dimension given by Sharpless and Osterbrock[16] is a very faint extension to the east of the core of emission usually observed. This extension is apparently emission of a general stratum of interstellar gas in which NGC 1499 is a dense "cloud." Another example is the Monoceros region, with centers at NGC 2237 and NGC 2264. Minkowski[13] found a fairly sharp-edged disk of emission 80′ in diameter extending around the cluster NGC 2244. The data of Table 4 indicate that an entire region of at least $5^\circ \times 6^\circ$ around NGC 2237 and NGC 2264 is filled with emission. A part of one spectrogram of this region has been published.[6] It appears that the brighter photographic disk is a dense core or cloud immersed in a rarer stratum rather than the *H* II sphere of the hot stars near its center. The classification of line type in Table 4 most frequently is *ce* ("core with extensions"): similar, perhaps, to the examples just cited. It is possible that sometimes a large *H* II region is in the line of sight with a smaller and brighter *H* II region. For example, nebula S 126 in the list of Hase and Shajn[15] appears to be projected on part of IC 405.

The mean true intensity ratios between various pairs of emission lines are shown in Table 7. The number of ratios in the table is simply the total number of microdensitometer tracings measured for both lines. They are supposed to be the true ratios except for interstellar reddening. Such reddening will not be important for the ratios of lines within

TABLE 6

PRESENCE OF INTERSTELLAR EMISSION NEAR O STARS

z (Psc)	Excitation Sources	Interstellar Emission	Remarks
0–50	10	9	*Hα* probably absent on No. 43 in Auriga
50–100	9	9	Complete correspondence
100–150	4	4	Complete correspondence
150–200	2	2	Complete correspondence
200–250	2	2	Complete correspondence
250–300	1	1	NGC 281; $r = 2.5$ kpc; $z = 260$ psc
300–700	7	0	See criterion for negative observations

TABLE 7

MEAN LINE-INTENSITY RATIOS

Lines	Mean Ratio	No. of Ratios	Remarks
[*S* II] 6731:*Hα*	0.12	36	
[*S* II] 6717:*Hα*	0.16	47	See remarks on *Ne* I 6717
He I 6678:*Hα*	0.05	2	See Table 8 and discussion of *He* I
[*N* II] 6584:*Hα*	0.31	54	
[*N* II] 6548:*Hα*	0.14	8	
He I 5876:*Hα*	0.05	5	See Table 8 and discussion of *He* I
[*O* III] 5007:*Hα*	0.15	18	
[*O* III] 4959:*Hα*	0.070	12	
Hβ:*Hα*	0.11	30	See mention of Balmer decrement
[*O* II] 3727:*Hα*	0.14	29	The [*O* II] 3726–3729 doublet is unresolved
[*S* II] 6731:[*S* II] 6717	0.84	36	Theoretical ratios* are 0.55 and 0.86
[*N* II] 6548:[*N* II] 6584	0.40	8	A theoretical ratio* is 0.34
[*O* III] 4959:[*O* III] 5007	0.40	12	A theoretical ratio* is 0.34
[*O* III] 5007:*Hβ*	1.3	18	

* R. H. Garstang, *M.N.*, **111**, 115, 1951; *Ap. J.*, **115**, 506, 195[illegible]

a few hundred angstroms of each other, but it may introduce a large depression and dispersion into the $H\beta$: $H\alpha$ and [O II] 3727 : $H\alpha$ ratios. The $H\beta$: $H\alpha$ ratio differs considerably from the predicted ratio[17] (or Balmer decrement), in the sense of interstellar reddening.

The He : H intensity ratio is of interest in questions of the interstellar abundance of helium. He I 5876 emission was discovered in the Orion Nebula by Copeland,[18] but He I 5876 or He I 6678 has since been detected with certainty in only one or two other galactic nebulae.[6] According to Table 8, He I 5876 : $H\alpha$ is lower in NGC 2237 (the ratio is 0.022)

TABLE 8

DATA FOR HELIUM

No. in Tables 3–4	σ and True Intensity Relative to $H\alpha$			Nebula
	He I 6678	He I 5876	He I 4472	
2	.....	0?4	.....	NGC 6523
	.....	.029	.....	
39	No D_3 line despite a strong exposure on 103*a*-D emulsion near λ 5876			IC 405
45	0?4	.4	Pres.	NGC 1976
	.060	.10	.....	
46	.....	.2	Pres.	NGC 1976
	.....	.059	.....	
47	.....	Pres.	.....	NGC 1976
	.....	.037	.....	
51	.....	Pres.?	.....	NGC 2175
	.....	.....	.....	
56	.....	Pres.?	.....	NGC 2237
	.....	.....	.....	
57	.9	.4	.....	NGC 2237–2239
	0.038	0.022	.....	

and NGC 6523 (the ratio is 0.029) than in NGC 1976 (where the ratio decreases from 0.10 near the center to 0.037 about 10′ from the center). The ratio He I 6678 : He I 5876 = 0.6 in Orion is much more certain than this ratio in NGC 2237, because of the relatively bright neon mixed in the spectrum of the latter.

Within a given emission region there is a slight correlation between the intensity ratio [N II] 6584 : $H\alpha$ and the intensity of $H\alpha$. It is in the sense of a decrease in [N II] 6584 : $H\alpha$ for a substantial increase in the intensity of $H\alpha$. This correlation may be real, for there is no correlation of [N II] 6584 : $H\alpha$ with the intensity of $H\alpha$ among different nebulae with one tracing each.

There is a slight correlation between forbidden line: $H\alpha$ intensity and spectral type of the nearest exciting stars. It is in the sense that the highest intensity ratios go with the hottest stars

The result for the Pleiades Nebula (No. 32) requires an explanation. The slit passes so near Electra, Alcyone, and Pleione that their light raises the background continuum strongly. Spectrograms of several Pleiades taken by Dr. E. M. Burbidge with the 40-inch on February 18, 1953, show Alcyone and Pleione with $H\alpha$ in emission. This emission may be present on the B spectrograms and may account for all of it there. The order of the *EM* expected for a cluster of such B stars is very low. The use of a narrow slit on the B

[17] J. G. Baker and D. H. Menzel, *Ap. J.*, **88**, 52, 1938.

[18] *M.N.*, **48**, 360, 1888.

spectrograph has apparently excluded the continua of reflection nebulae as well as some other sources of night-sky continua.

The positive values of mean N_H in the last column of Table 4 range from 0.7 in Cassiopeia and Cepheus to 65 near the center of the Orion Nebula. The smaller value is probably representative of the general interstellar medium in the direction of observation. Since the values of N_H in Table 4 usually exceed the density of 1 H atom/cm^3 found by Oort[19] in H I regions, we have some evidence for excess densities near O stars in H II regions.

SUMMARY

Observations with the B spectrograph at the Yerkes Observatory have resulted in new information on (*a*) the occurrence of interstellar emission near O stars, (*b*) the extent of such emission, (*c*) the relative intensities of several emission lines, and (*d*) the emission measure and corresponding density of hydrogen atoms and ions. The probability of finding interstellar emission near O stars within 250 psc of the galactic plane is very high, and the extent of the emission is generally greater than that indicated by previous measures.

I wish to thank Dr. B. Strömgren for his advice and encouragement throughout, Dr. W. W. Morgan for his special aid, Dr. C. Y. Fan for the use of his standard lamp, and Drs. L. H. Aller, A. B. Meinel, and O. Struve for comments about this work.

[19] *Ap. J.*, **116**, 233, 1952.

THE SOLAR MAGNETOGRAPH

HORACE W. BABCOCK

MOUNT WILSON AND PALOMAR OBSERVATORIES
CARNEGIE INSTITUTION OF WASHINGTON
CALIFORNIA INSTITUTE OF TECHNOLOGY

Received July 10, 1953

ABSTRACT

A new instrument for measuring and recording weak magnetic fields on the surface of the sun has been developed for use with the 150-foot solar telescope and 75-foot spectrograph of the Hale Solar Laboratory. Principal features include: a superior grating of high resolving power for use in the fifth-order spectrum; an electro-optic analyzer for polarization; a double-slit detector for the longitudinal Zeeman effect; and a self-synchronous system by which the disk of the sun is scanned in a raster of parallel traces, the results as to magnetic intensity and polarity being presented conformally on the screen of a cathode-ray tube and recorded by a camera. The noise level (about 0.1 gauss) is such that fields of the order of 1 gauss can be recorded readily. The method of calibration is described, and the possibility is pointed out of using the instrument, with a slight optical modification, for studying small Doppler shifts in the sun's atmosphere.

INTRODUCTION

The first attempts to apply photoelectric methods to the measurements of the general magnetic field of the sun were by G. E. Hale in collaboration with Dunham, Strong, Stebbins and Whitford, about 1933.[1] Essentially, the method is as follows: A powerful spectrograph, equipped with an analyzer for circular polarization, receives light from a selected part of the sun's image. At the focus of the spectrograph, an exit slit is placed on a wing of a Fraunhofer line chosen for sensitivity to the Zeeman effect. Radiation transmitted by the second slit enters a phototube that is connected to an amplifier having a meter or other means of indicating the intensity of the light. If the longitudinal Zeeman effect now occurs, owing to a magnetic field in the sun's atmosphere, a change of the analyzer from the right-handed to the left-handed condition will produce a slight shift in the position of the line and, because of the sloping profile of the wing, will result in a corresponding change in the indication of the output meter.

For a magnetic field of 1 gauss the line shift to be expected in the green region is only 8×10^{-5} A, even for a line having a Zeeman pattern (0) 3. Owing to the weakness of the sun's field and to the difficulty of eliminating systematic errors, Hale and his collaborators did not achieve positive results with the photoelectric method. Later, however, variations of this method have been employed by G. Thiessen,[2] by K. O. Kiepenheuer,[3] and by H. D. and H. W. Babcock.[4] It is the purpose of this paper to describe the magnetograph in the form in which it is now employed daily for recording weak magnetic fields on the surface of the sun. The instrument is designed primarily for measuring and mapping solar fields of from 1 to 20 gauss; the much stronger fields of sunspots have for several decades been adequately observed on Mount Wilson by visual measurements of the Zeeman effect.

The unique features of the magnetograph include: (1) a large plane grating of unusually high resolving power; (2) an oscillating optical analyzer without moving parts, incorporating an electrically excited retardation plate; (3) a detector for Zeeman dis-

[1] "Annual Report of the Director, Mount Wilson Observatory," *Carnegie Institution of Washington Yearbook*, No. 32 (1933), p. 143.

[2] *Ann. d'ap.*, **9**, 101, 1946; *Zs. f. Ap.*, **30**, 185, 1952.

[3] *Ap. J.*, **117**, 447, 1953.

[4] *Pub. A.S.P.*, **64**, 282, 1952.

placements employing not one but two exit slits and two photomultiplier tubes connected to a difference amplifier, as well as other means to avoid systematic errors; and (4) a system for automatically scanning the sun's disk, with conformal recording by means of a cathode-ray tube and a camera.

Observations with this apparatus have already shown that the scanning technique is practically indispensable because of the complex and detailed nature of the changing magnetic effects to be observed on the sun. It is apparent that considerable new and significant information should be obtainable by continuing such observations throughout the solar cycle.

OPTICAL EQUIPMENT

The telescope of the Hale Solar Laboratory[5] in Pasadena has a coelostat and a second flat mirror followed by a compact off-axis Cassegrain reflecting system with a focal length of 150 feet. The 17-inch image of the sun is formed in a convenient basement laboratory in which is located the head of the spectrograph. The latter is a vertical Littrow instrument in a deep pit. A large plane grating is used in the fifth order, with a lens of 75-foot

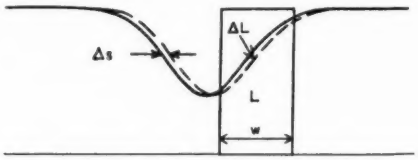

FIG. 1.—Slit on one wing of line transmits varying light to phototube as line shifts in response to reversal of circular analyzer when longitudinal Zeeman effect is present.

focus. This yields a dispersion of 11 mm/A. The grating, ruled at the Mount Wilson Observatory,[6] has a ruled area of $5\frac{1}{4} \times 8$ inches, with 600 grooves per millimeter. It was designed to throw as much of the light as possible into the fifth order, where the available resolving power, measured photographically, is 600,000. This figure was obtained by measurements on close groups of the very sharp absorption lines artificially produced in the solar spectrum by placing in front of the slit a cold tube of iodine vapor. This resolving power, hitherto unavailable without an interferometer, is sufficient to resolve sharp lines in the green region of the spectrum only 0.009 A apart; it thereby ensures that the spectrograph will render nearly perfect profiles of solar lines having half-widths of about 0.1 A. Because of the intrinsic width of Fraunhofer lines, a further increase of resolving power would accomplish very little; an appreciable decrease, on the other hand, would impair the ability of the instrument to measure weak fields.

The reason for this dependence on resolving power may be seen by reference to Figure 1, in which an exit slit of width w is placed on one wing of the line profile. The line now shifts a distance Δs (small compared to its half-width) in response to a reversal of the polarizing analyzer. The resulting change in light, ΔL, is the "signal" to be measured by the phototube and amplifier in the presence of the much larger constant light L under the wing of the line. The small signal has necessarily to be measured in the presence of noise, which in this case, where the light-level is moderate, is almost entirely due to shot effect in the photocurrent and is proportional to $\sqrt{L}$. The signal-to-noise ratio, which sets a lower limit to the field than can be measured, is then $\Delta L/\sqrt{L}$. Now if the optical resolution is inferior, the line profile becomes broader and shallower (usually also asymmetrical), so that if ΔL is to be accepted without loss, the slit width, w, must be increased. But

[5] "Annual Report of the Director, Mount Wilson Observatory," *Carnegie Institution of Washington Year Book*, No. 25 (1926), p. 135.

[6] H. D. Babcock and H. W. Babcock, *J. Opt. Soc. Amer.*, **41**, 776, 1951.

this at once increases the constant component of the light and the noise, with a consequent reduction in the signal-to-noise ratio. It is evident that high resolution is needed and that the width and position of the exit slit, as well as the width of the entrance slit, should be so chosen that $\Delta L/\sqrt{L}$ is a maximum. Also, the optical system should be as efficient as possible if weak fields are to be measured with a short instrumental time constant, as is desirable when scanning the sun's image.

Calculation shows that with a slit length of 2 cm on the 40-cm image of the sun, the light reaching the photocathode will be of the order of 10^{-7} lumens, whereas the dark current of a typical photomultiplier tube is equivalent to about 10^{-9} lumens. Shot effect is therefore the only important source of noise, and nothing is to be gained by refrigerating the tube. Quantum efficiency of the photocathode is important, however, and selection of tubes with this characteristic in mind is worth while.

ANALYZER

The analyzer for circular polarization in front of the entrance slit is required to alternate its sign at a fixed frequency. While a rotating retardation plate in combination with a fixed plane polarizer will fulfil this requirement, it has been found practically impossible to eliminate reliably and completely all traces of false modulation of the light when moving optical elements are used. Trouble may arise from flickering secondary reflections from the moving surfaces, from small imperfections, or from mechanical vibration. A satisfactory solution to the problem is the use of an electro-optic retardation plate in the form of a Z-cut crystal of ammonium dihydrogen phosphate (ADP).[7] Such plates, of good optical quality and with transparent electrodes affixed, may be obtained commercially.[8] Upon the application of an alternating voltage (about 9 kv), the retardation oscillates between plus and minus a quarter-wave at the applied frequency—in this case 120 cycles/sec. A Nicol prism follows the ADP plate, the two fixed elements constituting an oscillating circular analyzer.

DETECTOR

The arrangement of a single slit and phototube as in Figure 1 is subject to a severe drawback, in that any slight false modulation of the whole spectrum at the signal frequency is a source of systematic error. It produces a spurious signal that may be confused with the true Zeeman effect. And, with a tower telescope using oblique reflections, some slight false modulation is almost unavoidable because these reflections result in a slight general elliptical polarization of all the light. This effect varies with the hour angle of the sun, so that compensation of it by a tilted-glass polarizing plate between the retardation plate and the Nicol is hardly practicable.

The detector shown in Figure 2, having two slits and two phototubes, has several advantages. The two slits are placed symmetrically on opposite wings of the line and the corresponding phototubes are connected to a difference amplifier such that their response to a shift in position of the line is additive, but a small change of intensity of the whole spectrum has no effect. Since the useful light is doubled by this method, the signal-to-noise ratio is multiplied by $\sqrt{2}$, but, more important, the detector rejects the effect of elliptical polarization by the telescope mirrors, and the system operates without systematic error.

The width of each exit slit is about 0.56 mm, and they are separated by 0.45 mm. The solar line ordinarily used is *Fe* I λ 5250.218, (0) 3, which has a central intensity of 0.40 and a half-width of about 0.1 A or 1.1 mm. As a check on the performance of the instrument, it is convenient to make control observations using the magnetically unaffected line *Fe* I λ 5123.723 (0) 0.

[7] B. H. Billings, *J. Opt. Soc. Amer.*, **39**, 797, 1949.

[8] Baird Associates, Inc., 33 University Road, Cambridge, Mass.

AMPLIFIER

The signal frequency chosen for this system is 120 cycles/sec. Obviously, the amplifier should have narrow-band characteristics in order to reject noise in so far as possible. The amplifier, phase-sensitive demodulator, and filter circuits are shown schematically in Figure 3. Essentially, these elements are similar to those described by Kiepenheuer,[3] except that we have added a band-pass wave filter in addition to using a peaked amplifier

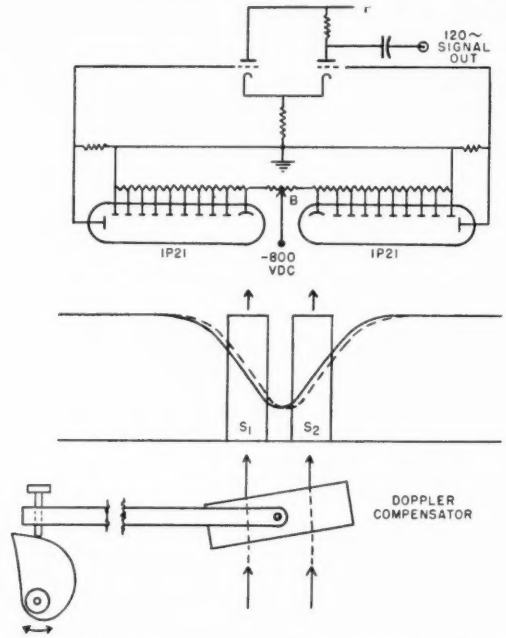

FIG. 2.—Schematic diagram of detector, showing Doppler compensator at bottom, line profile on the two exit slits, photomultipliers, and difference amplifier. This detector rejects the effect of any slight general intensity modulation of the spectrum and is insensitive to a small decentering of the line or to a slight imbalance of phototube sensitivity.

and that a cathode-follower is used to provide a low-impedance source for the demodulator.

The peaked amplifier of Figure 3 is a commercial 2-stage plug-in unit having a 120-cycle twin-*T* filter in its feedback loop. The driver amplifier likewise is a plug-in unit of two stages with cathode-follower output.[9] It has been found that the amplifier is nearly linear for weak fields up to about 20 gauss but that it saturates above this level. In order to provide for recording a greater range of signal intensity, provision is being made for optional use of a logarithmic attenuator.

The phase of the vibrator-type demodulator must be adjusted with respect to the phase of the electro-optic retardation plate. These units are driven by the 60-cycle line through separate frequency doublers; the vibrator is provided with a phase shifter. By rotating the retardation plate 90° in azimuth, its effective electrical phase may be reversed. This provides a useful check on the response to weak fields.

[9] Kalbfell Laboratories, Inc., P.O. Box 1578, San Diego, Calif.

The two parallel filter circuits with balanced cathode-follower output provide a choice of time constants of 1, 3, and 10 seconds. The d.c. potential appearing across the output terminals is a measure of the polarity and amplitude of the field being investigated. It has been found that, with a time constant of 10 seconds, the root-mean-square amplitude of the noise is equivalent to about 0.1 gauss. With this time constant, a scanning rate of about 3 minutes for the sun's diameter is sufficiently slow to permit recording of all prominent magnetic features. With a longer time constant, the noise is, of course, further reduced, but a slower scanning rate is desirable.

Provided that the instrument is totally free of systematic errors, the limiting field that can be detected is set by the signal-to-noise ratio, and this is a fundamental limit that can be lowered only by presenting a brighter spectrum to the detector, by using photocathodes of higher quantum efficiency, or by working on more than one spectrum line at

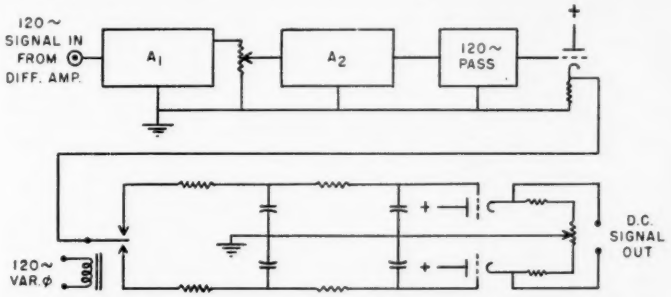

FIG. 3.—Signal amplifier and filter circuits. A_1, two-stage, 120 cycle/sec peaked amplifier (Kalbfell model 107); A_2 two-stage driver amplifier (model 106A). The phase of the demodulator is adjusted with respect to the phase of the analyzer. Parallel resistors in the filter circuits are switched to provide time constants of 1, 3, and 10 seconds.

a time. A new detector, now under consideration, is designed to exploit all three of these possibilities, thereby improving the signal-to-noise ratio by a factor of at least 2.

SCANNING SYSTEM

The foregoing parts of the instrument constitute a "gaussmeter" capable of indicating the polarity and intensity of the magnetic field at any chosen point on the disk of the sun. In order to record the available data in a convenient manner, a scanning system is required which will cause the image to move across the slit in a pattern or raster of parallel traces (usually about 25 in number). This controlled motion of the image is accomplished by two micrometer drives which move the second flat mirror that directs light into the telescope. A cathode-ray tube is well adapted to display the signal as a function of position on the disk. Potentials for the deflection plates of the tube are provided by direct-coupled precision potentiometers. The electron spot on the screen of the cathode-ray tube is thus made to move in a manner conforming to the effective motion of the spectrograph slit on the sun's image. By superposition of the gaussmeter signal voltage on the vertical deflection plates, in a manner to be described, the electron spot is divided into two parts: a fiducial spot that produces a straight trace, and a signal spot that fluctuates in position above or below the fiducial line. A camera, making a time exposure, records the results as in Figure 5.

In scanning the image, a minor complication enters in the form of Doppler effect due to the sun's axial rotation. In passing from the east to the west limb, the velocity difference of 4 km/sec is sufficient to shift the line about 0.07 A, which is comparable to its half-width. Compensation for the Doppler shift is readily accomplished by the device shown

in Figure 2. A plane-parallel plate of glass is mounted on a shaft a short distance in front of the exit slits of the spectrograph. By means of a lever and cam, the glass plate is tilted during scanning in such a way as to keep the line centered between the two exit slits. The range of tilt of the half-inch-thick plate is about 9°. Tests have shown that Zeeman measurements are not extremely sensitive to this adjustment and that the equatorial acceleration of the sun may be neglected. Therefore, the required tilt varies linearly with distance (x) from the sun's axis and is independent of heliographic latitude.

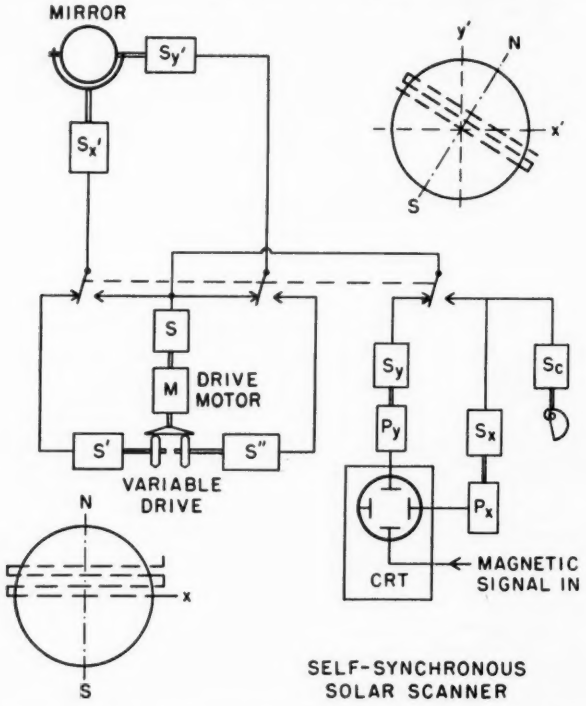

FIG. 4.—Schematic diagram of the scanning system, using synchros. By driving the flat mirror in two co-ordinates, the traces are made perpendicular to the sun's axis. Automatic switching circuits, not shown, govern the scanning of the entire disk.

The scanning operation requires a coupling of the motions of the second flat mirror in the dome with the deflection potentiometers of the cathode-ray tube and with the Doppler compensating cam in the laboratory. It was decided that the coupling of these motions with the desired degree of flexibility and ease of adjustment would be best accomplished by the use of a self-synchronous system employing synchros (Selsyns) of the type ordinarily used in pairs as torque transmitters. A single motor that can be operated over a wide range of speed drives a synchro that serves as a transmitter. Several other synchros connected in parallel to the transmitter may be driven together at the same speed, and any one of the synchro repeaters may have its direction of rotation reversed by the interchange of any two of its three field connections. A system using, altogether, eight synchros with the necessary controls and switching circuits was developed and put into operation early in 1953. The synchro system is shown schematically in Figure 4.

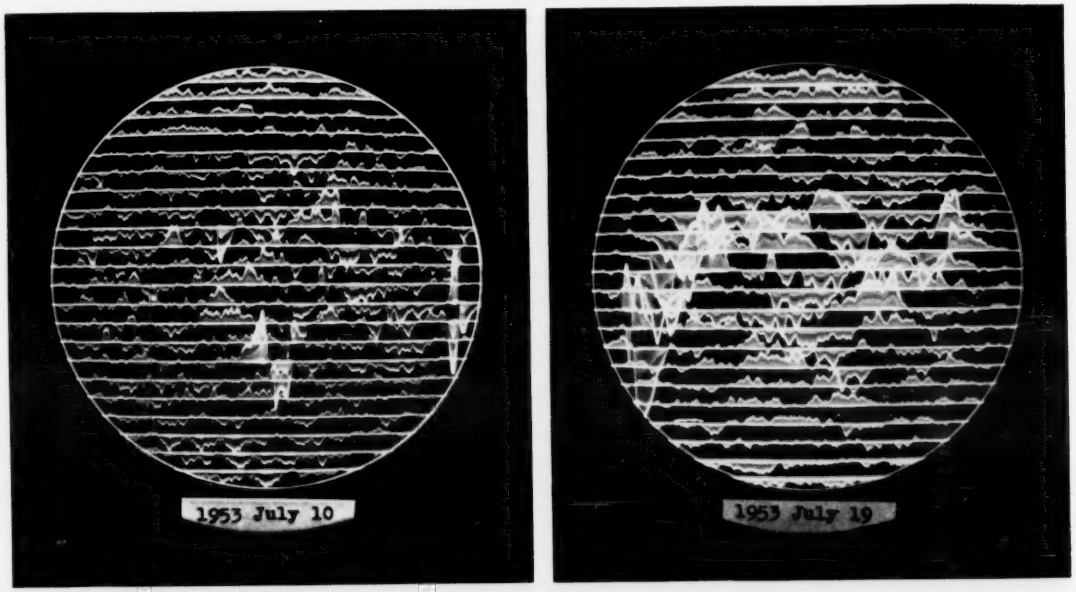

FIG. 5.—Magnetograms of the sun. The axis is vertical, with north at the top. East is at the right. For each trace there is a straight fiducial line. A deflection equal to the interval between traces indicates that $H \cos \gamma$ is about 1 gauss at the center of the disk, 2 gauss at the limb. For upward deflections $H \cos \gamma$ is toward the observer. Evidence for the sun's general magnetic field is shown by the opposite deflections on the traces nearest the north and south poles. The only visible sunspot group on July 19 was at 54° W., 8° S. The length of the slit (0.04 of the sun's diameter) is approximately equal to the interval between traces.

Approximately 300 turns of the primary synchro are required for one traverse of the sun's image. By varying the speed of the driving motor, the time required for one traverse may be varied from about 30 seconds (for making adjustments) to 10 minutes. At the normal speed of about 3 minutes per trace, the complete disk is scanned in about 60 minutes. Once the scan has been started, the entire operation is carried out automatically. Switching from one trace to the next, with appropriate time delay and overrun, is initiated by a monitoring phototube which detects the passage of the sun's limb from the slit. The interval between horizontal traces (Δy) is controlled by a notched disk that is coupled to the y-potentiometer and its driving synchro.

For ready interpretation of the resulting magnetograms, it is highly desirable that the parallel traces should all be perpendicular to the sun's axis, which we take as the y-coordinate, or vertical on the magnetograms. The traces all run in the x-direction, so that,

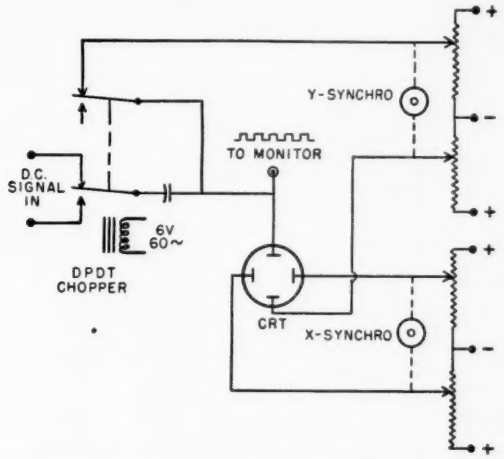

FIG. 6.—Deflection circuits. The d.c. signal indicating the polarity and amplitude of the magnetic field is chopped at 60 cycles/sec to produce a square wave that is superimposed on the y-deflection voltage of the potentiometer.

in making each trace, only the x-potentiometer is rotated by its synchro, the y-synchro being disconnected. The motion of the sun's image, however, requires simultaneous rotation of the second flat mirror about its two axes (x' and y') at different rates. Furthermore, owing to the seasonal changes in the position angle of the sun's axis and the changes in the position of the coelostat caused by the varying declination, the ratio of the two mirror-drive rates must be adjusted almost daily. The system provides, therefore, for driving the x'-motion of the second flat at the primary-synchro rate while making an x-trace, but at the same time for driving the y'-motion at a predetermined slower rate, this y'-rate being developed by an additional transmitting synchro that is driven through a variable-ratio friction transmission by the primary-drive motor. At the end of each x-trace, relays interchange the connections to the x'- and y'-synchros, thus producing a stepwise y-motion of the image. But since, in general, the directions of motion of the image produced by rotation of the second flat about its two axes are not orthogonal, a second variable transmission and transmitter synchro have to be provided for producing the x'-component of motion in making the y-steps.

A standard 5-inch laboratory oscillograph (DuMont type 304A) with its screen masked down to 4 inches is used with a 35-mm camera for recording. For maximum

stability, the internal d.c. amplifiers are not used, but push-pull deflection potentials are applied directly to the plates of the cathode-ray tube from precision multiturn potentiometers connected to well-regulated d.c. power supplies, as indicated in Figure 6. This figure also shows how, by means of a DPDT chopper, the d.c. magnetic signal from the gaussmeter is converted to a 60-cycle/sec square-wave whose base is clamped to the y-deflection potential established by the y-synchro. With normal scanning in the x-co-ordinate, the time-collapsed square-wave appears as two slowly moving dots, one tracing a straight fiducial line (y = const.) and the other fluctuating in position to indicate the magnetic polarity and field intensity with respect to this line.

In order to improve the visibility of the records, intensity modulation of the cathode-ray tube is provided so that the recording spot is brightened in proportion to signal intensity, regardless of polarity. This is accomplished through a balanced modulator

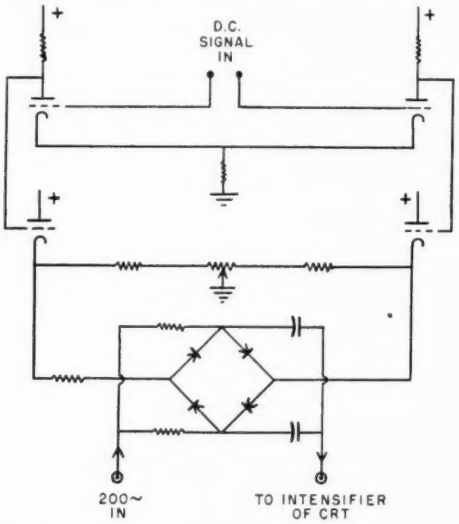

FIG. 7.—Balanced modulator for intensifying record trace in proportion to signal amplitude

(Fig. 7), by which the amplitude of the magnetic signal governs the amplitude of a sine wave (of frequency incommensurate with 60 cycles/sec) that is applied to the control grid of the cathode-ray tube.

Figure 8 is a general view of the equipment in the solar laboratory.

OPERATION

Adjustment of the scanning system involves the following steps:

1. The east-west direction of drift on the image screen (Fig. 8) is established, and the azimuth of the screen is corrected for the position angle of the sun's axis, so that guide lines on the screen are perpendicular to the y-axis.

2. The friction rollers controlling the x'- and y'-drive rates of the second flat are adjusted so that the two motions of the image on the screen occur in the x- and y-directions, respectively.

3. The number of turns (to the nearest 0.01 turn) of the x and y ten-turn potentiome-

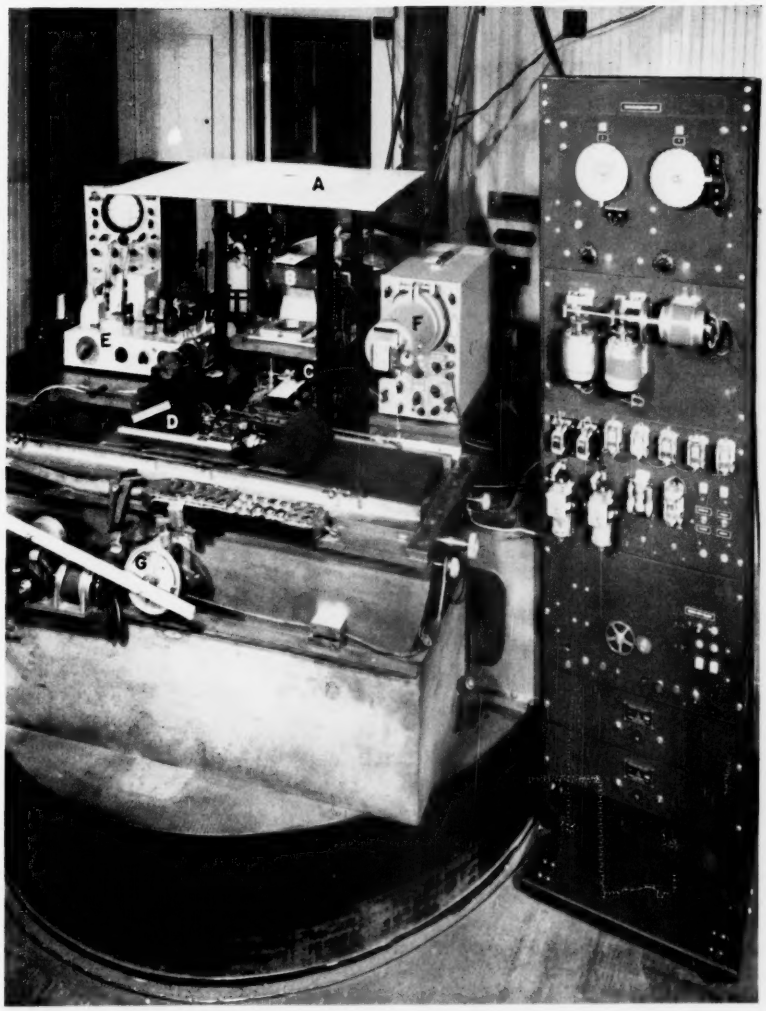

FIG. 8.—The head of the spectrograph, showing (*A*) image screen, (*B*) electro-optic retardation plate, (*C*) Nicol prism above slit, (*D*) detector, (*E*) amplifier, (*F*) recording oscilloscope with camera, and (*G*) Doppler compensator. At right is rack holding scanning controls and switching circuits. The grating and collimator are at the bottom of the 75 foot pit.

ters is determined that corresponds to motion of the image through its own diameter, in each co-ordinate.

4. Supply voltages and potentiometer settings are so adjusted that the visible limits of spot traverse on the screen of the cathode-ray tube correspond to the appropriate position of the sun's image with respect to the slit.

5. With the axis of the sun ($x = 0$) on the slit, the Doppler compensating cam is placed at mid-range and, by means of a micrometer adjustment, the exit slits are placed symmetrically on the spectrum line. This adjustment requires further elaboration.

A circular polarizer, consisting of a Polaroid sheet followed by a mica quarter-wave plate is so mounted that it may be swung temporarily into the light-beam just above the oscillating circular analyzer (*B*, Fig. 8). With this in place, the intensity of the transmitted light varies sinusoidally between zero and a maximum at a frequency of 120 cycles/sec, i.e., the light is 100 per cent modulated. This is a condition in which the detector is exceedingly sensitive to inequality of illumination at the two exit slits, and it thereby facilitates the following adjustments.

a) By tilting the glass compensating plate, the two exit slits are exposed to the modulated light of the continuous spectrum, and the relative sensitivity of the two photomultipliers is equalized by adjustment of the applied voltages using potentiometer *B* (Fig. 2).

b) Still using the modulated spectrum, the chosen line is centered between the slits with high precision. Only when it is precisely centered will the output signal of the gaussmeter be zero. If the circular polarizer is then removed from the beam, the instrument is ready to measure the Zeeman effect.

CALIBRATION

The circular polarizer offers a means of calibrating the sensitivity of the gaussmeter. With the modulated spectrum, a slight controlled displacement of the line from its centered position results in an artificial signal whose equivalent in magnetic intensity can be evaluated.

Let the artificial displacement of the line be $\delta\lambda_c$ and let the actual transmission of the circular polarizer be f for circularly polarized light of its own sign. Then the amplitude of the difference signal developed by the two phototubes is proportional to $f\delta\lambda_c$. For the longitudinal Zeeman effect, without the circular polarizer, the amplitude of displacement of the line is

$$\delta\lambda_z = \pm 4.67 \times 10^{-5}\,\lambda^2\,Hz\,;$$

and this results in a difference signal proportional to $2\,\delta\lambda_z$. For equal signals we then have

$$\delta\lambda_c = \frac{2}{f}\,\delta\lambda_z\,, \qquad \text{or} \qquad \frac{H}{\delta\lambda_c} = 3.9\,f/z \text{ gauss/milliangstrom}\,.$$

The factor f is readily determined and is about 0.3, while, for the line λ 5250.218, $z = 3$. Therefore, approximately, a shift of the line of 0.001 A or 0.011 mm, by tilting the plane-parallel plate while using the circular polarizer, would produce an artificial signal equivalent to 4 gauss. In observing, calibration is customarily done by repeatedly inserting and retracting a standard 5-gauss shim under the end of the lever that tilts the Doppler compensating plate; this operation, carried out with the image stationary, results in a square-wave pattern that is recorded in the usual manner.

With the circular polarizer in the beam, the instrument can be used for measuring radial velocities at various points on the sun. The signal introduced by the standard shim would in this case be equivalent to a velocity of 70 m/sec. In this mode of operation the instrument is exceedingly sensitive to slight line displacements due to turbulence both in the atmosphere of the sun (through the Doppler effect) and in the spectrograph (through refraction). This leads to a certain amount of drift and irregularity in the cali-

bration records, but it may be overcome by using a larger artificial line displacement for calibrating and by switching to correspondingly smaller load resistors for the photomultiplier tubes. It should be emphasized that this extreme sensitivity to small displacements at low random frequencies does not occur in the course of normal Zeeman measurements, as then the spectrum is essentially unmodulated. In this condition there does remain a very great sensitivity of the spectrograph to vibration at the signal frequency, and every precaution should be taken to see that this does not occur.

INTERPRETATION OF MAGNETOGRAMS

When the Zeeman effect is observed in the manner described here, the displacements measured are proportional to $H \cos \gamma$, the component of the field in the line of sight.[10] Particularly near the limb, the projection factor is unfavorable. Furthermore, the gaussmeter really measures the product of magnetic intensity and light-intensity, so that deflections near the limb are further reduced by limb darkening. Also, when atmospheric transparency is low, the sensitivity suffers. On typical records a deflection equal to the interval between traces is equivalent to 1 gauss near the center of the disk and to 2 gauss at the limb. The root-mean-square noise is about 0.1 gauss.

The magnetic polarity is readily checked on sunspots. In the solar cycle now approaching a minimum, leading spots in the northern hemisphere have negative polarity (the magnetic vector is away from the observer) and the phasing of the instrument has been set so that such deflections are downward.

Some preliminary results obtained with the magnetograph have already been reported.[4] Evidence confirming the existence of a weak general field of the sun, in high latitudes only, was found with this apparatus by Harold D. Babcock in August, 1952. Subsequent observations on nearly every clear day show this persistent field in heliographic latitudes above about $\pm 65°$, with positive polarity in the north, negative in the south. This is opposite to the magnetic polarity of the earth and opposite to the polarity of the leading sunspots in the respective hemispheres in the cycle now drawing to a close. It is also opposite to the polarity of the sun's general field reported by G. E. Hale[11] for the year 1912, which refers to nearly the same phase in the sunspot cycle. The polar fields of the sun are frequently observed without scanning, but with the image fixed with respect to the slit; this permits the use of a longer instrumental time constant. The effective intensity of the field is found to vary from point to point on the surface. The signal reverses polarity when the phasing of the analyzer is reversed by changing the azimuth of the ADP crystal 90°, and it disappears when the exciting voltage is removed from the crystal. These and other tests confirm the reality of the weak fields. The component of these high-latitude fields in the line of sight is of the order of 1 gauss; if allowance is made for the obliquity of the lines of force, the actual intensity may be 2 gauss or more. The lower limit in latitude of these polar fields is variable and rather indefinite; on a few occasions they could be found in one hemisphere only. As yet we have no evidence for systematic changes or for obliquity between the sun's magnetic axis and the axis of rotation.

In heliographic latitudes below $\pm 65°$ a great deal of rather transient solar magnetic activity is found, as previously reported. Extensive areas of weak magnetic intensity, varying somewhat from day to day and of limited duration, are not uncommon. It appears quite plausible that chance distribution of such magnetic areas may have been the source of the difficulty of earlier observers in obtaining consistent results. Further reports on the rather voluminous data regarding magnetic effects on the sun's surface will be postponed for subsequent discussion.

[10] F. H. Seares, *Ap. J.*, **38**, 99, 1913.

[11] G. E. Hale, *Ap. J.*, **38**, 27, 1913.

CARBON MONOXIDE IN THE SUN*

LEO GOLDBERG AND EDITH A. MÜLLER
McMath-Hulbert Observatory, University of Michigan, Pontiac, Michigan
Received May 1, 1953

ABSTRACT

Nearly 300 lines of carbon monoxide have been identified in the spectrum of the solar limb between 2.29 and 2.50 μ. The lines belong to the overtone bands 2–0, 3–1, 4–2, 5–3, 6–4, and 7–5. Analysis of the solar wave lengths has led to a new determination of the vibrational and rotational constants of the *CO* molecule.

The measured absorption coefficients of Penner and Weber and the theoretical values of Scholz have been applied to the measured equivalent widths at the center of the disk. The resulting equivalent abundance of *CO* is 1.45×10^{19} molecules per square centimeter above the photosphere, and the excitation temperature is 4300° K. It is shown from model-atmosphere calculations that solar *CO* is concentrated near the top of the photosphere and hence that the derived excitation temperature is consistent, since it agrees with the boundary temperature. At present, it is not known whether the dissociation energy of *CO* is 9.6 or 11.1 e.v. If the lower value is correct, the solar-line intensities suggest that the boundary temperature is less than 4500° K. The exact value of the temperature depends on the choice of atomic abundances for *O* and *C*.

The low intensities of the fundamental band lines of *CO* in the 4.6 μ region are explained as a consequence of (1) the high opacity of the solar atmosphere at long wave lengths, (2) the importance of stimulated emissions in the infrared, and (3) the small collisional line widths in the sun's outer layers.

INTRODUCTION

The recent discovery of carbon monoxide, both in the earth's atmosphere[1] and in the sun,[2] has been made possible by advances in infrared spectroscopy. The electronic bands of *CO* occur in the neighborhood of λ 1600 and are therefore not yet accessible to observation in the sun and stars. The fundamental vibration-rotation band falls at 4.6 μ, however, and this region and that of the first overtone at 2.3 μ are favorably located for observation with photoconductive cells and improved thermocouples.

At the temperature of the earth's atmosphere an insignificant fraction of the *CO* molecules are in excited vibrational states, and the only bands observed are two that originate from the ground state, namely, the fundamental 1–0 band at 4.6 μ, discovered by Migeotte,[1] and the extremely faint first overtone at 2.3 μ. The solar bands of *CO* differ in three important respects from the telluric bands, the differences arising as a consequence of the sun's high temperature. First, the excited vibrational states are highly populated in the sun, and hence bands arising from excited states are comparable in intensity with those starting from the ground state. Second, the intensity maximum in the solar bands occurs at about $J = 28$, instead of at $J = 7$, as in the telluric bands. Third, the rotational levels of high energy are so well populated that lines up to about $J = 70$ in the overtone bands are observed in the spectrum of the solar limb. Since the convergence limits fall near $J = 50$, both sides of the overtone band parabolas appear in the spectrum, an effect that, in the laboratory, is usually restricted to electronic bands.

The Fraunhofer spectrum of carbon monoxide presents many interesting problems. First, since the lines of very high J value have been observed only in the sun, analysis of the measured wave lengths can lead to improvement of the molecular constants of *CO*. Second, the existence of very accurate absorption coefficients, measured in the laboratory by Penner and Weber,[3] makes possible the determination of the solar abundance of *CO*

* Supported in part by Contract N6-ONR-232-V with the Office of Naval Research.

[1] M. Migeotte, *Phys. Rev.*, **76**, 1108, 1949.

[2] L. Goldberg, R. R. McMath, O. C. Mohler, and A. K. Pierce, *Phys. Rev.*, **85**, 140, 1952.

[3] *J. Chem. Phys.*, **19**, 1351, 1951.

and of the excitation temperature for the region of the solar atmosphere in which the lines are formed. It will be shown later that the *CO* molecules are concentrated at very small optical depths and that analysis of the line intensities not only may yield information on the temperatures in the sun's outer layers but may also assist in choosing between competing values of the dissociation energy of *CO*. Third, the relative intensities of the solar and telluric lines are strikingly different in the overtone and fundamental bands. This apparent anomaly is caused mainly by differences in the solar and terrestrial curves of growth and by the wave-length dependence of the solar continuous opacity.

The observational data upon which this investigation is based consist of tracings of the solar spectrum in the region 2.3–2.5 μ, made with the infrared spectrometer and Cashman *PbS* cell attached to the Snow telescope of the Mount Wilson Observatory.[4] The tracings, each about 80 A in length, were made in groups of three, i.e., tracings of the east limb, disk center, and west limb were made consecutively on each region.

The overtone bands of solar *CO* in the spectrum of the center of the disk are relatively weak, the equivalent widths of the strongest unblended lines not exceeding about 0.050 A. Despite the fact that some 125 lines, belonging to six bands, appear in the spectrum,[5] the arrangement of the lines into band series is not at all obvious, owing to overlapping of the solar lines by strong telluric lines of H_2O and CH_4. At the limb, however, the lines are strengthened by a factor of 2–3; the number of lines that can be recognized is doubled; and the band structure is plainly apparent. It was, in fact, on the first tracings of the limb spectrum at 2.3 μ that the *CO* bands were discovered.[2] Figure 1 shows a portion of the 3–1 band as observed at the center of the disk and at the limb.

Identifications

Two criteria were employed in the identification of the lines: (1) strengthening at the limb and (2) coincidences between the solar wave lengths and laboratory or calculated values. The original identifications were on the basis of wave lengths calculated with the constants derived by Rao[6] from analysis of the ultraviolet Cameron bands. In this way the bands 2–0, 3–1, 4–2, and 5–3 were recognized. Almost simultaneously, Plyler, Benedict, and Silverman[7] published their accurate wave-length measures on the same four bands, observed in emission in the laboratory. These wave lengths made possible the identification of additional lines, especially in the negative branches. The solar wave lengths were then employed in the calculation of a new set of molecular constants (see following section), from which wave lengths were calculated and solar lines identified in the 6–4 and 7–5 bands.

The complete list of *CO* lines observed in the solar limb spectrum is given in Table 1, which is arranged in order of increasing wave length. The observed wave lengths in column 1 were measured on the limb tracings with the aid of a smoothed wave-length scale, previously established by the method of overlapping orders.[8] Whenever possible, the wave lengths were measured on pairs of tracings made at the east and west limbs and then averaged. Measurements made on only one limb were corrected for the Doppler effect of the sun's rotation; hence the observed wave lengths in Table 1 refer to the center of the disk. The calculated wave lengths in column 2 were derived in the manner described in the next section. Columns 3 and 4 give the vibrational and rotational transi-

[4] R. R. McMath and O. C. Mohler, *J. Opt. Soc. Amer.*, **39**, 903, 1949; O. C. Mohler, A. K. Pierce, R. R. McMath, and L. Goldberg, *Photometric Atlas of the Near Infra-red Solar Spectrum* λ *8465–*λ *25,242* (Ann Arbor: University of Michigan Press, 1950).

[5] O. C. Mohler, A. K. Pierce, R. R. McMath, and L. Goldberg, *Ap. J.*, **117**, 41, 1953.

[6] *Ap. J.*, **110**, 304, 1949.

[7] *J. Chem. Phys.*, **20**, 175, 1952.

[8] L. Goldberg, O. C. Mohler, R. R. McMath, and A. K. Pierce, *Phys. Rev.*, **76**, 1848, 1949.

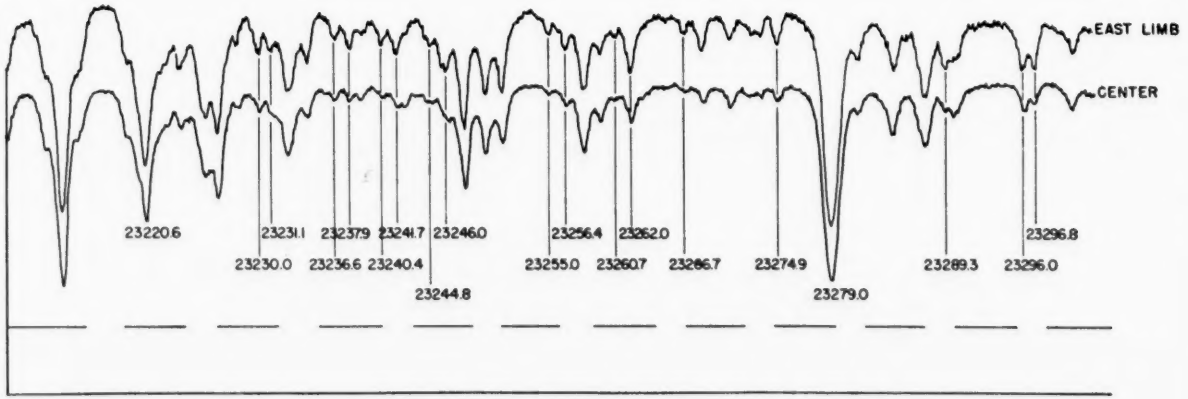

FIG. 1.—Region of the positive branch of the 3–1 band of *CO* in the solar spectrum, showing enhancement of lines in the limb

Table 1

CARBON MONOXIDE LINES IN THE SPECTRUM OF THE SOLAR LIMB

Asterisks denote unblended lines used in the derivation of molecular constants.

λ_{obs}	λ_{calc}	Band	Line	Blends
22929.3	22929.38	2-0	R50	CH_4
	22929.34	2-0	R51	
22930.7	22930.69	2-0	R48	CH_4
	22930.47	2-0	R53	
22935.5	22935.70	2-0	R45	CH_4
	22935.26	2-0	R56	
22937.8	22937.68	2-0	R57	CH_4
22938.5	22938.18	2-0	R44	CH_4
22940.4*	22940.51	2-0	R58	
22941.3*	22941.06	2-0	R43	
22944.4	22944.35	2-0	R42	CH_4, H_2O
22947.5*	22947.42	2-0	R60	
22948.2*	22948.03	2-0	R41	
22956.2	22956.62	2-0	R39	CH_4
	22956.00	2-0	R62	
22960.8	22960.92	2-0	R63	CH_4
22961.6	22961.52	2-0	R38	CH_4
22966.1*	22966.26	2-0	R64	
22967.0*	22966.82	2-0	R37	
22971.9	22972.02	2-0	R65	CH_4
22972.7	22972.52	2-0	R36	CH_4
22984.5	22984.82	2-0	R67	CH_4
22992.2	22992.03	2-0	R33	CH_4
22999.8	22999.33	2-0	R32	CH_4
23007.0*	23007.03	2-0	R31	
23023.9*	23023.65	2-0	R29	
23041.9*	23041.88	2-0	R27	
23051.8	23051.59	2-0	R26	CH_4, H_2O
23062.1	23061.70	2-0	R25	CH_4
23072.6*	23072.22	2-0	R24	
23083.6	23083.14	2-0	R23	CH_4
23094.8	23094.47	2-0	R22	CH_4
23106.6*	23106.19	2-0	R21	
23118.7*	23118.32	2-0	R20	
23131.2*	23130.85	2-0	R19	
23144.0	23143.80	2-0	R18	H_2O
23199.8	23199.61	2-0	R14	CH_4
23214.7	23214.58	2-0	R13	CH_4, H_2O
23222.0	23222.19	3-1	R53	CH_4, H_2O
23223.5*	23223.58	3-1	R54	
23225.7	23226.08	3-1	R45	CH_4, H_2O
	23225.40	3-1	R55	
23227.1	23227.64	3-1	R56	CH_4, H_2O
23228.1	23228.45	3-1	R44	CH_4, H_2O
23230.0	23229.96	2-0	R12	
	23230.30	3-1	R57	
23231.1*	23231.22	3-1	R43	
23234.2	23234.40	3-1	R42	H_2O
23236.6	23236.90	3-1	R59	CH_4
23237.9*	23238.01	3-1	R41	
23240.5*	23240.85	3-1	R60	
23241.9*	23242.01	3-1	R40	
23244.8*	23245.21	3-1	R61	
23246.1	23245.75	2-0	R11	CH_4, H_2O
	23246.44	3-1	R39	
23249.6	23250.00	3-1	R62	CH_4
23251.0	23251.28	3-1	R38	CH_4
23255.0	23255.23	3-1	R63	CH_4
23256.4*	23256.53	3-1	R37	
23260.7	23260.89	3-1	R64	CH_4
23262.0	23261.95	2-0	R10	CH_4, H_2O
	23262.19	3-1	R36	
23266.8*	23266.98	3-1	R65	
23268.3*	23268.26	3-1	R35	
23273.2*	23273.50	3-1	R66	
23274.7*	23274.75	3-1	R34	
23281.7	23281.63	3-1	R33	CH_4
23287.1	23287.86	3-1	R68	CH_4, H_2O
23289.1	23288.94	3-1	R32	CH_4
23295.6	23295.58	2-0	R8	CH_4, H_2O
	23295.70	3-1	R69	
23296.6	23296.66	3-1	R31	CH_4
23304.8	23304.79	3-1	R30	CH_4
23312.9	23313.02	2-0	R7	CH_4, H_2O
	23313.32	3-1	R29	

Table 1 - Continued

λ_{obs}	λ_{calc}	Band	Line	Blends
23331.6*	23331.63	3-1	R27	
23341.6	23341.41	3-1	R26	CH_4
23348.8	23349.13	2-0	R5	H_2O
23351.8*	23351.59	3-1	R25	
23362.4	23362.18	3-1	R24	CH_4
23367.9	23367.81	2-0	R4	CH_4, H_2O
23373.1*	23373.19	3-1	R23	
23384.6	23384.61	3-1	R22	CH_4
23386.9*	23386.91	2-0	R3	
23396.4	23396.45	3-1	R21	CH_4, H_2O
23408.7	23408.70	3-1	R20	CH_4
23421.3	23421.36	3-1	R19	CH_4
23434.4*	23434.44	3-1	R18	
23448.1	23447.92	3-1	R17	CH_4
23476.1	23476.15	3-1	R15	CH_4
23488.6	23488.70	2-0	P1	CH_4
23506.4*	23506.06	3-1	R13	
23521.5	23521.63 23521.34	3-1 4-2	R12 R46	H_2O
23522.4*	23522.26	4-2	R54	
23523.4*	23523.15	4-2	R45	
23524.6*	23524.32	4-2	R55	
23526.0	23525.39	4-2	R44	CH_4
23527.0	23526.80	4-2	R56	CH_4
23531.3	23531.12	4-2	R42	CH_4
23533.2*	23533.07	4-2	R58	
23534.7	23534.63	4-2	R41	CH_4
23536.9	23536.86	4-2	R59	CH_4
23538.5	23538.55	4-2	R40	CH_4
23541.3	23541.08	4-2	R60	CH_4
23546.0	23545.75	4-2	R61	CH_4
23547.7*	23547.68	4-2	R38	
23558.4*	23558.49	4-2	R36	
23564.4*	23564.52	4-2	R35	
23569.0*	23568.83	4-2	R65	
23571.0	23570.88 23570.98	3-1 4-2	R9 R34	
23576.0	23575.71	4-2	R66	CH_4
23585.1*	23585.16	4-2	R32	
23588.0*	23588.14	3-1	R8	
23590.9*	23590.82	4-2	R68	
23592.9*	23592.89	4-2	R31	
23599.1*	23599.04	4-2	R69	
23601.1	23601.11 23601.03	2-0 4-2	P6 R30	
23605.9*	23605.83	3-1	R7	
23618.7*	23618.59	4-2	R28	
23624.3	23624.88 23623.93	2-0 3-1	P7 R6	
23627.6	23628.00	4-2	R27	H_2O
23638.0	23637.82	4-2	R26	CH_4
23642.5	23642.46	3-1	R5	CH_4
23648.1	23648.08	4-2	R25	CH_4
23649.0	23649.09	2-0	P8	CH_4
23658.7*	23658.74	4-2	R24	
23661.3*	23661.42	3-1	R4	
23669.9	23669.85	4-2	R23	CH_4
23673.7	23673.73	2-0	P9	H_2O
23680.6	23680.81	3-1	R3	CH_4
23681.6	23681.37	4-2	R22	H_2O, CH_4
23693.4	23693.31	4-2	R21	CH_4
23705.5	23705.68	4-2	R20	CH_4, H_2O
23723.8	23724.33	2-0	P11	CH_4, H_2O
23745.5*	23745.33	4-2	R17	
23750.4*	23750.28	2-0	P12	
23784.1	23784.18	3-1	P1	Fe
23788.8	23788.81	4-2	R14	H_2O
23803.8	23803.54 23804.16	2-0 4-2	P14 R13	H_2O
23806.6	23806.16	3-1	P2	CH_4
23824.4	23824.25 23824.69	5-3 5-3	R47 R52	CH_4
23830.5	23830.84 23830.24	2-0 5-3	P15 R55	
23831.7	23831.76	5-3	R43	H_2O, CH_4
23835.9	23836.14 23836.17	4-2 5-3	R11 R57	H_2O, CH_4
23839.9	23839.80	5-3	R58	CH_4, H_2O

Table 1 - Continued

λ_{obs}	λ_{calc}	Band	Line	Blends
23842.0	23841.97	5-3	R40	CH_4
23844.2	23843.88	5-3	R59	H_2O
23846.3*	23846.24	5-3	R39	
23848.1	23848.41	5-3	R60	CH_4
23851.3	23851.42 / 23850.94	3-1 / 5-3	P4 / R38	H_2O, CH_4
23855.9	23856.08	5-3	R37	H_2O, CH_4
23859.2	23858.81	5-3	R62	Mg, CH_4
23861.4	23861.65	5-3	R36	CH_4
23864.9*	23864.70	5-3	R63	
23867.8	23867.64	5-3	R35	CH_4
23871.4*	23871.03	5-3	R64	
23877.8	23877.83	5-3	R65	H_2O
23880.7*	23880.94	5-3	R33	
23885.3	23885.09	5-3	R66	
23887.1	23886.77 / 23887.35	2-0 / 4-2	P17 / R8	
23888.1	23888.24	5-3	R32	
23893.0	23892.80	5-3	R67	CH_4
23898.3*	23898.44	3-1	P6	
23903.8	23904.13	5-3	R30	CH_4
23905.3*	23905.29	4-2	R7	
23912.4*	23912.72	5-3	R29	
23915.0*	23915.42	2-0	P18	
23921.3	23921.74	5-3	R28	CH_4
23922.4*	23922.62	3-1	P7	
23923.3	23923.66	4-2	R6	CH_4
23931.0*	23931.19	5-3	R27	
23941.1	23941.09	5-3	R26	CH_4
23942.8	23942.46	4-2	R5	CH_4
23947.2	23947.23	3-1	P8	CH_4
23951.5	23951.40	5-3	R25	CH_4
23972.4*	23972.30	3-1	P9	
23972.9*	23973.34	5-3	R23	
23973.5*	23974.08	2-0	P20	
23981.4*	23981.38	4-2	R3	
23984.9	23984.96	5-3	R22	CH_4
24001.3*	24001.50	4-2	R2	
24004.1*	24004.10	2-0	P21	
24009.5*	24009.49	5-3	R20	
24022.3	24022.06 / 24022.42	4-2 / 5-3	R1 / R19	
24023.8*	24023.78	3-1	P11	
24077.1*	24077.06	3-1	P13	
24078.6*	24078.47	5-3	R15	
24104.4*	24104.39	3-1	P14	
24109.5	24109.11	5-3	R13	H_2O, CH_4
24125.0*	24125.10	5-3	R12	
24129.1	24128.82	2-0	P25	H_2O
24139.8	24140.21	6-4	R44	H_2O
24141.1	24141.52 / 24140.86	5-3 / 6-4	R11 / R54	
24142.6	24142.62	6-4	R43	
24143.6	24143.42	6-4	R55	
24146.6	24146.42	6-4	R56	
24148.7	24148.76	6-4	R41	
24160.3	24160.42	3-1	P16	H_2O
24161.0	24161.17 / 24161.31	2-0 / 6-4	P26 / R38	
24163.2	24163.04	6-4	R60	
24166.2	24166.38	6-4	R37	CH_4
24171.7	24171.89	6-4	R36	
24194.0	24194.00	2-0	P27	CH_4
24198.4	24198.38	6-4	R32	
24202.5	24202.55	4-2	P6	CH_4
24206.3	24206.11	6-4	R31	
24211.8	24211.64	5-3	R7	H_2O
24218.3*	24218.29	3-1	P18	
24223.0	24222.90	6-4	R29	
24227.2	24227.30 / 24227.14	2-0 / 4-2	P28 / P7	CH_4
24230.1	24230.27	5-3	R6	CH_4
24241.4	24241.45	6-4	R27	
24247.9*	24247.92	3-1	P19	
24249.2	24249.36	5-3	R5	CH_4
24251.3	24251.40	6-4	R26	CH_4

Table 1 - Continued

λ_{obs}	λ_{calc}	Band	Line	Blends
24261.4	24261.08	2-0	P29	
	24261.79	6-4	R25	
24268.9*	24268.89	5-3	R4	
24272.4	24272.61	6-4	R24	
24277.8	24278.03	3-1	P20	
	24277.68	4-2	P9	
24283.8	24283.89	6-4	R23	CH_4
24288.8*	24288.88	5-3	R3	
24295.6	24295.35	2-0	P30	
	24295.61	6-4	R22	
24303.7*	24303.64	4-2	P10	
24307.9	24307.78	6-4	R21	H_2O
24308.6	24308.60	3-1	P21	H_2O
24320.3	24320.38	6-4	R20	H_2O
24329.7	24330.10	2-0	P31	H_2O
	24330.06	4-2	P11	
	24330.18	5-3	R1	
24333.4	24333.44	6-4	R19	
24365.2	24365.34	2-0	P32	CH_4
24371.0*	24371.18	3-1	P23	
24384.2*	24384.30	4-2	P13	
24400.8*	24401.07	2-0	P33	
24402.9*	24403.18	3-1	P24	
24405.1	24405.41	6-4	R14	
24411.9	24412.12	4-2	P14	H_2O
24435.7*	24435.67	3-1	P25	
24437.4	24437.29	2-0	P34	H_2O
	24437.35	6-4	R12	
24440.5*	24440.40	4-2	P15	
24460.7	24460.86	7-5	R43	
24461.6	24461.28	7-5	R54	
24470.5	24470.39	7-5	R40	
24479.0	24479.02	7-5	R38	
24480.1	24480.08	7-5	R59	
24484.4	24484.03	7-5	R37	
24515.3	24515.85	7-5	R32	
24523.3	24523.58	7-5	R31	
24527.8	24528.10	4-2	P18	H_2O
24535.8	24536.03	3-1	P28	H_2O
24549.0	24548.96	2-0	P37	
	24549.49	7-5	R28	

λ_{obs}	λ_{calc}	Band	Line	Blends
24558.0*	24558.28	4-2	P19	
24570.2	24570.47	3-1	P29	
24579.1	24579.48	7-5	R25	H_2O
24582.6	24583.22	6-4	R4	H_2O
24588.7*	24588.95	4-2	P20	
24601.5	24601.76	7-5	R23	
24605.3	24605.40	3-1	P30	H_2O
24613.7	24613.57	7-5	R22	H_2O
24641.0	24640.83	3-1	P31	H_2O
24643.8*	24643.42	5-3	P11	
24652.0	24651.73	4-2	P22	
	24651.77	7-5	R19	
24665.6	24665.42	7-5	R18	
24677.3*	24676.75	3-1	P32	
24684.2	24683.85	4-2	P23	H_2O
24693.9	24694.09	7-5	R16	
24698.7	24698.64	5-3	P13	H_2O
24705.5	24704.95	2-0	P41	H_2O
24740.8	24740.54	7-5	R13	
24756.1*	24755.77	5-3	P15	
24757.1	24756.94	7-5	R12	
24759.0	24758.55	6-4	P3	
24774.0	24773.81	7-5	R11	H_2O
24783.5*	24783.17	4-2	P26	
24786.5	24786.05	2-0	P43	H_2O
24788.0	24787.57	3-1	P35	H_2O
24814.4	24814.83	5-3	P17	
24816.6	24817.28	4-2	P27	
24852.1*	24851.88	4-2	P28	
24865.6	24865.13	7-5	R6	
24955.1*	24954.60	2-0	P47	
24982.9	24982.56	3-1	P40	H_2O
24995.7	24995.37	4-2	P32	H_2O
24998.7	24998.09	2-0	P48	H_2O
25003.9*	25003.80	5-3	P23	
25032.8	25032.52	4-2	P33	H_2O

tions, respectively, while column 5 denotes blending with telluric lines, usually H_2O or CH_4. Approximate equivalent widths for those lines that appear in the spectrum of the disk center have been published previously.[5]

MOLECULAR CONSTANTS

The general agreement between the solar wave lengths and those calculated from the constants of Plyler, Benedict, and Silverman is very good and is adequate for purposes of identification. However, small systematic differences are present, which are in some cases as large as 0.5 A and which are especially noticeable among lines with very high J values. Consequently, it appeared desirable to attempt an analysis of the solar wave lengths with the aim of deriving another set of constants that might lead to better agreement with the observed wave lengths.

It is well known[9] that the wave numbers, σ, of lines in vibration-rotation bands can be represented by the equation

$$\sigma = \sigma_0 + (B_{v+2} + B_v)\, m + (B_{v+2} - B_v)\, m^2 - 2\,(D_{v+2} + D_v)\, m^3 - (D_{v+2} - D_v)\, m^4 , \quad (1)$$

where σ_0 is the position, in wave numbers, of the band center and m is an integer equal to $J + 1$ in the positive branch and to $-J$ in the negative branch. The quantities B and D are functions of the vibrational quantum number, v, and are related to the rotational molecular constants by the following expressions:

$$B_v = B_e - (v + \tfrac{1}{2})\, \alpha_e + (v + \tfrac{1}{2})^2 \gamma_e + \ldots ; \quad (2)$$

$$D_v = D_e + (v + \tfrac{1}{2})\, \beta_e \ldots . \quad (3)$$

Similarly, the band center σ_0, for a transition $v \rightarrow v + 2$, may be expressed in terms of the vibrational constants as follows:

$$\sigma_0 (v \rightarrow v + 2) = 2\omega_e - (4v + 6)\, \omega_e x_e + (6v^2 + 18v + \tfrac{31}{2})\, \omega_e y_e . \quad (4)$$

The problem is to derive values of the rotational constants B_e, α_e, γ_e, D_e, and β_e and of the vibrational constants ω_e, $\omega_e x_e$, and $\omega_e y_e$ from the observed values of σ in the four bands 2–0, 3–1, 4–2, and 5–3. The lines selected for analysis are indicated by asterisks in Table 1. As far as possible, only unblended lines were chosen, the blended lines being eliminated with the aid of laboratory spectra of CH_4 and H_2O. Blends with other solar lines were also recognized from abnormally high intensities. The wave numbers were calculated from the measured wave lengths with the aid of H. D. Babcock's[10] extrapolation of the infrared index of refraction of air. Within the accuracy of the measured wave lengths, this procedure is equivalent to the use of a constant value of the index, equal to 1.000272, throughout the spectral region 2.3–2.5 μ.

Molecular constants may be evaluated from observed wave numbers either by the method of differences, as was done by Plyler, Benedict, and Silverman,[7] or by the method of least squares. The former method is not feasible for the solar spectrum, however, since the number of differences between consecutive band lines is severely limited by blending. Hence a least-squares procedure was adopted. As a first step in the solution, values of σ_0 and of the coefficients of the various powers of m in equation (1) were obtained for each of the four bands. An attempt was then made to obtain from equations (2), (3), and (4) values of the rotational and vibrational constants that best fitted σ_0 and the coefficients B and D. It was found, however, that the rotational constants could not be determined with high accuracy by this method, largely because the coefficients in equation

[9] G. Herzberg, *Molecular Spectra and Molecular Structure*, Vol. I: *Diatomic Molecules* (New York: D. Van Nostrand Co., Inc., 1950), p. 114.

[10] *Phys. Rev.*, **46**, 382, 1934.

(1) are not entirely independent of one another. The following alternative procedure was then employed.

If the values of B and D given by equations (2) and (3) are substituted in equation (1), a different form of the observational equation is obtained, viz.:

$$\frac{\sigma-\sigma_0}{2m}=B_e-\left[m+\frac{2v+3}{2}\right]\alpha_e+\left[\left(v^2+3v+\tfrac{13}{4}\right)+(2v+3)m\right]\gamma_e \qquad (5)$$
$$-2m^2D_e-\left[m^3+(2v+3)m^2\right]\beta_e .$$

Furthermore, if σ_0 is known in advance for each band, a single least-squares solution of equation (5), including lines from all four bands, gives directly the constants B_e, α_e, γ_e, D_e, and β_e. The values of σ_0 were taken from the least-squares solutions of equation (1), referred to above. The resulting molecular constants are given in Table 2, where they are compared with other determinations by Plyler, Benedict, and Silverman[7] and by Rao.[6] The general agreement is very good, the differences becoming important only for high rotational quantum numbers. It is interesting to note that our values of D_e and β_e are in good agreement with the theoretical values,[11] 6.12×10^{-6} cm^{-1} and -1.1×10^{-9} cm^{-1}, respectively.

TABLE 2

MOLECULAR CONSTANTS, IN KAYSERS, DERIVED FOR CARBON MONOXIDE FROM SOLAR WAVE LENGTHS AND COMPARED WITH EARLIER DETERMINATIONS

	Goldberg and Müller	Plyler, Benedict, and Silverman	K. N. Rao
ω_e	2169.83	2169.81	2170.21
$\omega_e x_e$	13.297	13.284	13.461
$\omega_e y_e$	0.0115	0.010	0.0308
B_e	1.93141	1.93130	1.93139
α_e	0.017520	0.017543	0.017485
γ_e	2.96×10^{-6}	4.5×10^{-6}	
D_e	6.18×10^{-6}	5.95×10^{-6}	6.43×10^{-6}
β_e	-1.76×10^{-9}	0	4×10^{-8}

TABLE 3

CALCULATED COEFFICIENTS OF FIRST-OVERTONE BANDS OF CARBON MONOXIDE

Band	σ_0	$B_{v+2}+B_v$	$B_{v+2}-B_v$	$2(D_{v+2}+D_v)$	$D_{v+2}-D_v$
2–0	4260.05	3.81029	−0.035023	2.471×10^{-5}	-3.5×10^{-9}
3–1	4207.14	3.77527	−.035011	2.470×10^{-5}	-3.5×10^{-9}
4–2	4154.37	3.74027	−.034999	2.469×10^{-5}	-3.5×10^{-9}
5–3	4101.73	3.70527	−.034987	2.468×10^{-5}	-3.5×10^{-9}
6–4	4049.24	3.67029	−.034975	2.468×10^{-5}	-3.5×10^{-9}
7–5	3996.88	3.63532	−0.034964	2.467×10^{-5}	-3.5×10^{-9}

Table 3 contains values of the coefficients of equation (1) calculated from the molecular constants for all first-overtone bands up to and including 7–5. The predicted wave lengths in Table 1 have been calculated from these coefficients. Inasmuch as numerous predicted wave lengths in the 6–4 and 7–5 bands agree closely with the positions of solar lines that strengthen at the limb, it must be concluded that both bands are present in the solar spectrum.

[11] G. Herzberg, *op. cit.*, p. 107.

SOLAR ABUNDANCE AND EXCITATION TEMPERATURE

Carbon monoxide is one of the few molecules of astrophysical interest for which absolute absorption coefficients have been measured in the laboratory with high accuracy. The number of *CO* molecules effective in producing the line spectrum may therefore be determined with some precision by the curve-of-growth method. According to Penner and Weber,[3] the integrated band absorption coefficient per molecule in the lowest vibrational state is 2.89×10^{-7} cm^2 sec^{-1} and 2.00×10^{-9} cm^2 sec^{-1} for the 1–0 and 2–0 bands, respectively. The values given refer to the absorption by the entire band in contrast with the integrated line-absorption coefficient. The integrated absorption coefficient for individual lines of the fundamental band is given by[3]

$$S_{JJ'} = S_{vv'} \frac{\sigma}{\sigma_0} \frac{|m|}{2J+1} FG , \tag{6}$$

where $S_{JJ'}$ is the line-absorption coefficient for the transition $J \rightarrow J'$ per molecule in rotational level J; $S_{vv'}$ is the band-absorption coefficient for the transition $v \rightarrow v'$ per molecule in vibrational level v; and $|m|$ is equal to $J + 1$ for the positive branch and to J for the negative branch. The factor F is different in the positive and negative branches but is unity for small J values in both branches. In the positive branch, F decreases slowly with J and has the value 0.79 at $J = 30$. In the negative branch, however, F increases with J and is equal to 1.22 at $J = 30$. The quantity G takes account of the reduction in the absorption coefficient due to stimulated emissions and is given by

$$G = 1 - e^{-hc\sigma/kT} . \tag{7}$$

It is inserted into equation (6) on the assumption that $S_{vv'}$ has been measured at room temperature with G equal to unity.

Measurement of the absorption coefficient has been accomplished only for the 1–0 and 2–0 bands. Absolute theoretical intensities have, however, been calculated for all vibration-rotation bands of *CO* by Scholz.[12] Since the relative values of the theoretical intensities are likely to be more accurate than the absolute values, the absolute values of the absorption coefficients for the 3–1, 4–2, and 5–3 bands were calculated from the relative values of Scholz and the absolute value for the 2–0 band by Penner and Weber.[3]

Penner[13] has prepared extensive tables of approximate line-absorption coefficients for *CO*, calculated for the vibrational transitions 1–0, 2–1, 3–2, 4–3, 5–4, 6–5, 2–0, and 3–1 and for temperatures between 300° and 5000° K. The values given in Penner's tables are in units of cm^{-1} per atm-cm at the given temperature. They differ dimensionally from the $S_{JJ'}$ in equation (6) by the factor n_J/c, where c is the velocity of light and n_J is the number of molecules in rotational level J in 1 cc of *CO* at 1 atm. pressure and at the given temperature. In preparing the tables, Penner has assumed that the factors F, derived by Oppenheimer[14] for the 1–0 transition only, are also valid in the calculation of the overtone intensities. This assumption may not be justified, and it will be shown below that the solar evidence from the overtone bands may favor F constant.

The weakness of the solar *CO* lines, especially at the center of the disk, has both disadvantages and advantages. The errors in the measured intensities arising from blends with even very weak lines can become quite large percentagewise. On the other hand, the lines are so weak that they fall on the linear portion of the curve of growth, and their equivalent widths are equal to the absorption coefficient integrated over all molecules along the line of sight.

[12] *Zs. f. Phys.*, **78**, 751, 1932.

[13] *Wave Number and Intensity Tables for Carbon Monoxide* (California Institute of Technology Guggenheim Jet Propulsion Center, 1952).

[14] *Proc. Cambridge Phil. Soc.*, **23**, 327, 1926.

For the determination of the solar abundance and excitation temperature, 26 lines were selected on the basis of freedom from blending, and their equivalent widths in the spectrum of the disk center were measured in kaysers.[15] For very weak lines, the equivalent width, A, is given by

$$A = N_J S_{JJ'} , \tag{8}$$

where

$$N_J = \frac{N}{Q_r Q_J} (2J+1)\, e^{-(E_v+E_J)/kT} . \tag{9}$$

In equation (9), N is the total number of *CO* molecules per square centimeter in the line of sight; E_v and E_J are the vibrational and rotational energies, respectively, of the level

TABLE 4

VALUES OF A AND Y FOR *CO* LINES USED IN TEMPERATURE AND ABUNDANCE DETERMINATION

A (Kaysers)	Y	Line	E_v+E_j	A (Kaysers)	Y	Line	E_v+E_j
3.322×10^{-3}	15.586	2–0, P18	644.16	2.087×10^{-3}	15.239	4–2, R3	4282.50
3.738×10^{-3}	15.570	2–0, R19	723.04	6.461×10^{-3}	15.077	3–1, R34	4381.68
4.303×10^{-3}	15.609	2–0, R20	799.05	4.079×10^{-3}	14.870	4–2, R17	4831.73
4.884×10^{-3}	15.587	2–0, R24	1140.86	2.799×10^{-3}	14.718	5–3, P11	6594.85
3.955×10^{-3}	15.446	2–0, R27	1436.78	5.943×10^{-3}	14.728	4–2, R35	6606.82
3.400×10^{-3}	15.321	2–0, R31	1883.91	4.657×10^{-3}	14.762	5–3, R15	6794.67
2.692×10^{-3}	15.347	3–1, R7	2248.98	4.869×10^{-3}	14.606	4–2, R38	7018.34
3.414×10^{-3}	15.398	3–1, R8	2279.18	4.172×10^{-3}	14.554	5–3, R22	7286.23
4.188×10^{-3}	15.158	3–1, R18	2788.31	2.219×10^{-3}	14.350	3–1, R63	9659.36
5.893×10^{-3}	15.249	3–1, P23	3183.69	2.711×10^{-3}	14.194	4–2, R55	9963.22
5.024×10^{-3}	15.145	3–1, P25	3368.02	1.478×10^{-3}	14.161	3–1, R65	10,133.72
5.318×10^{-3}	15.124	3–1, R25	3368.02	1.292×10^{-3}	14.096	3–1, R66	10,376.10
5.482×10^{-3}	15.136	3–1, P28	3672.48	3.070×10^{-3}	14.225	4–2, R58	10,589.53

considered; and Q_v and Q_r are the vibrational and rotational partition functions, respectively. To adequate approximations,[16]

$$Q_v = (1 - e^{-hc\omega_e/kT})^{-1} , \tag{10}$$

where $\omega_e = 2170$ K, and

$$Q_r = \frac{kT}{hcB} , \tag{11}$$

where $B = 1.93$ K.

If we substitute equations (6) and (9) in equation (8), set F equal to unity, and take logarithms, we obtain

$$Y = \log A - \log S_{vv'} \frac{\sigma}{\sigma_0} \mid m \mid G = \log \frac{N}{Q_r Q_J} - 0.4343 \frac{E_v + E_J}{kT} . \tag{12}$$

Values of A and Y are given in Table 4. In the usual fashion, Y is plotted against $E_v + E_J$ (see Fig. 2 *a*), and the slope and intercept of the resulting straight line yield the temperature and abundance, respectively. The resulting excitation temperature is 4300° K, which agrees very well with other determinations from molecular spectra.[17] The value of N is 1.45×10^{19}/per cm^2.

[15] By recent international agreement the unit of wave number, formerly denoted by cm^{-1}, is the *kayser*, abbreviated K.

[16] G. Herzberg, *Infrared and Raman Spectra* (New York: D. Van Nostrand Co., Inc., 1945), p. 503.

[17] Cf. J. Hunaerts, *Trans. I.A.U.*, **7**, 462, 1950.

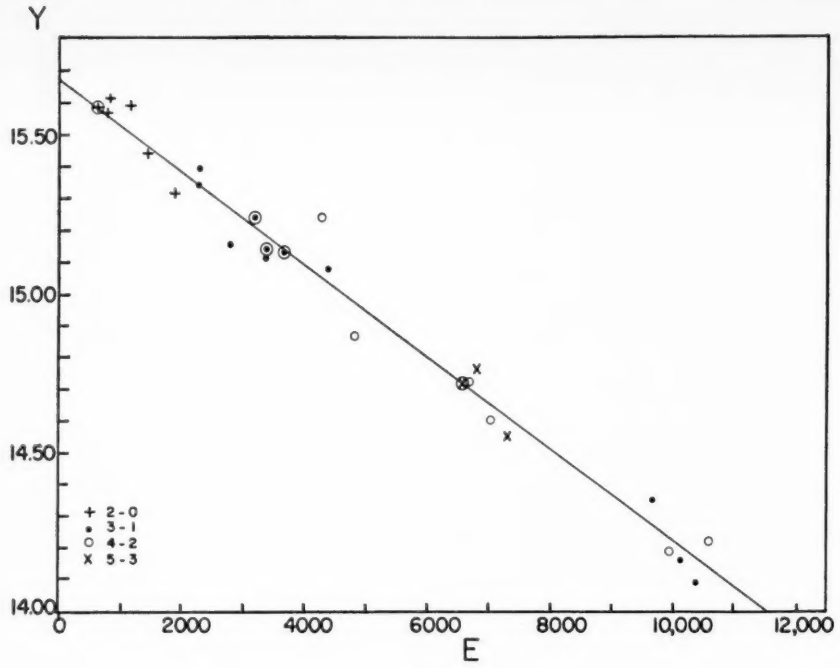

a

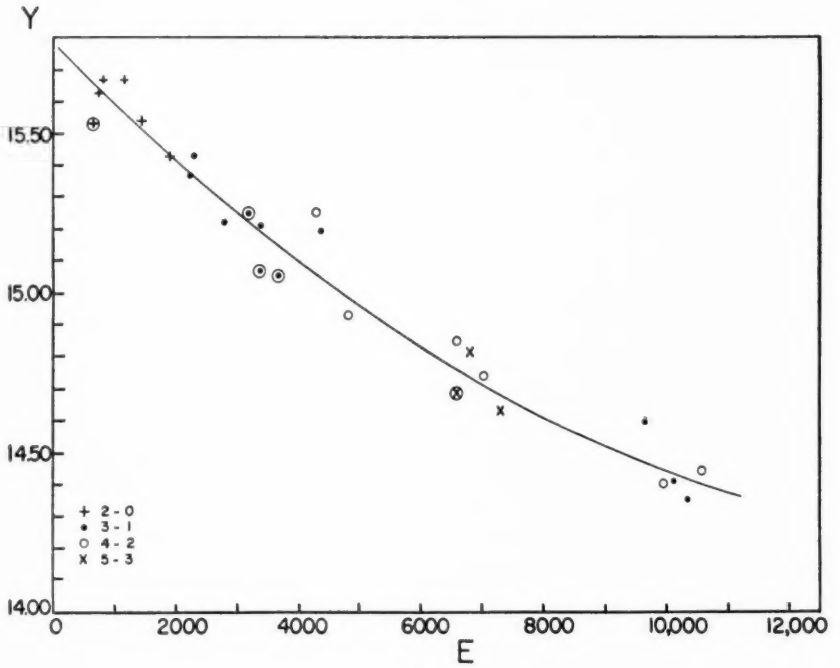

b

FIG. 2.—Temperature determination from *CO* lines: *a*, line strengths with $F = 1$; *b*, line strengths with values of F according to Oppenheimer.

The circled points in Figure 2 *a*, which denote lines in the negative branch, should appear displaced systematically upward from the positive branch lines if it is necessary to include the F factors in equation (6). There is no indication of such a displacement, which should amount to about 0.18 in the logarithm for $J = 30$. On the other hand, a plot similar to that in Figure 2 *a*, but with the F factor included (Fig. 2 *b*), not only appears to make the negative branch ordinates systematically too low but defines a curve rather than a straight line. Thus, although the use of the F factors may be justified for the lines of the 1–0 band, it seems best to omit them in analyses of the overtone bands.

INTENSITIES OF FUNDAMENTAL LINES

The ratio of the integrated absorption coefficients for the 1–0 and 2–0 bands is about 140, but there are three reasons why the actual line-intensity ratio in the sun is very much less.[18] First, the continuous absorption coefficient at 4.6 μ, according to Chandrase-

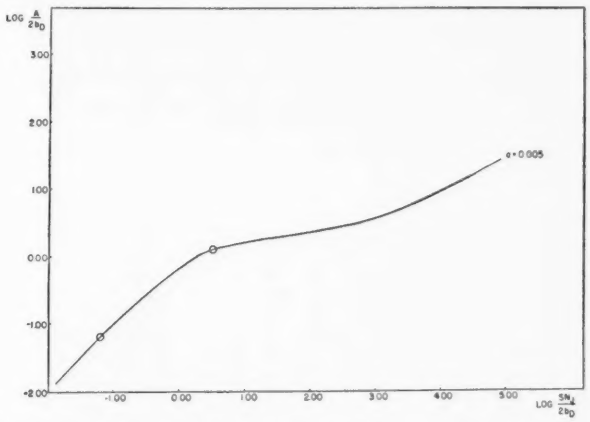

FIG. 3.—Solar curve of growth for *CO* lines with $a = 0.005$ and $b_D = 2.2 \times 10^5\ \sigma$. The circles represent the positions of the R30 fundamental and overtone lines.

khar and Breen,[19] is nearly four times as large as at 2.3 μ. Second, the reduction of the line-absorption coefficient by stimulated emissions is 50 per cent greater at 4.6 μ than at 2.3 μ. Finally, as pointed out also by Locke and Herzberg,[20] the intensities of the fundamental lines are suppressed by the curve-of-growth effect. The intensity of the R30 line in the 1–0 band may be estimated with the aid of the abundance determined above, and a curve of growth calculated for the case of pure absorption, with $a = 0.005$. This value of the parameter a, the ratio of the collisional width at half-intensity, $\gamma/2\pi$, to the Doppler displacement, b_D, corresponding to the most probable molecular velocity, is reasonable for the high layers of the atmosphere. If a turbulent velocity of 1.5 km/sec is assumed, b_D has the value $2.2 \times 10^5\ \sigma$, where σ is the wave number in kaysers. The intensity of the R30 fundamental line turns out to be about 0.040 cm^{-1}, which agrees with the order of magnitude of the observed intensities of lines identified as solar *CO* in the 4.6 μ region.[20] The curve of growth employed in the calculation is shown in Figure 3, the positions of the 2–0 and 1–0 lines being indicated by open circles.

[18] L. Goldberg, paper presented at Ohio State Symposium on Molecular Structure, June, 1952.

[19] *Ap. J.*, **104**, 430, 1946.

[20] *Canadian J. Phys.*, **31**, 504, 1953.

DISCUSSION

Within the error of its determination, the excitation temperature of 4300° K agrees with the boundary temperatures derived from analysis of limb-darkening observations.[21] Additional evidence that the *CO* molecules are concentrated near the top of the photosphere comes from the strengthening of the lines toward the limb and from calculations of dissociative equilibrium in a model solar atmosphere. If $p(C)$ and $p(O)$ are the partial pressures of atomic carbon and oxygen, respectively, then the partial pressure of *CO* is given by

$$p(CO) = \frac{p(C)\, p(O)}{K(CO)}, \qquad (13)$$

where $K(CO)$ depends upon the molecular constants and upon the temperature.[22] In a model atmosphere it is possible to calculate $p(CO)$ from equation (13) as a function of optical depth, provided that the abundances of carbon and oxygen and the dissociation

TABLE 5

VARIATION OF *CO* PARTIAL PRESSURE WITH MEAN OPTICAL DEPTH IN MODEL SOLAR ATMOSPHERE, ASSUMING DISSOCIATION ENERGIES OF 11.1 AND 9.6 E.V.

τ	$p_{(CO)}$ for $D=11.1$ e.v.	$p_{(CO)}$ for $D=9.6$ e.v.	τ	$p_{(CO)}$ for $D=11.1$ e.v.	$p_{(CO)}$ for $D=9.6$ e.v.
0.01	2.1613×10^{-1}	0.4677×10^{-2}	0.08	4.5787×10^{-1}	1.3183×10^{-2}
.02	4.4219×10^{-1}	1.0233×10^{-2}	.09	4.0368×10^{-1}	1.2023×10^{-2}
.03	4.9301×10^{-1}	1.2023×10^{-2}	.10	3.5583×10^{-1}	1.0965×10^{-2}
.04	5.2116×10^{-1}	1.3183×10^{-2}	.20	2.4626×10^{-1}	0.8710×10^{-2}
.05	5.2935×10^{-1}	1.3804×10^{-2}	.30	1.2930×10^{-1}	0.5248×10^{-2}
.06	5.1248×10^{-1}	1.3804×10^{-2}	.40	1.0126×10^{-1}	0.4467×10^{-2}
0.07	4.9582×10^{-1}	1.3804×10^{-2}	0.50	0.7875×10^{-1}	0.3715×10^{-2}

energy of *CO* are known. The atomic abundances may be estimated with reasonable accuracy,[23] but the value of the dissociation energy is still controversial. It is not yet possible to choose between the competing values 9.6 and 11.1 e.v., although recent astrophysical evidence[24] tends to favor the lower value.

In Table 5, $p(CO)$ has been tabulated as a function of the mean optical depth, according to the model atmosphere recently derived by Aller and Pierce,[25] which calls for a boundary temperature of 4500° K. In the calculation of $p(CO)$ from equation (13), it was assumed that the ratios of the partial pressures of *C* and *O* to the total gas pressure ($H + He$) are 1.7×10^{-4} and 4.2×10^{-4}, respectively. Regardless of whether one assumes 9.6 or 11.1 e.v. for the dissociation energy, the maximum concentration of *CO* occurs at about $\tau = 0.05$. The predicted values of the *CO* abundance differ by about a factor of 40, according to the choice of dissociation energy. Hence a comparison between the predicted and observed line intensities may serve to establish the correct value of the dissociation energy. A preliminary calculation by Mr. G. A. Newkirk, Jr., of the inten-

[21] A. K. Pierce and L. H. Aller, *Ap. J.*, **114**, 145, 1951; D. Labs, *Zs. f. Ap.*, **29**, 199, 1951; L. Neven and C. de Jager, *B.A.N.*, **11**, 291, 1951.

[22] L. Rosenfeld, *M.N.*, **93**, 724, 1933.

[23] M. Minnaert, *Trans. I.A.U.*, **7**, 457, 1950.

[24] M. Schwarzschild, L. Spitzer, Jr., and R. Wildt, *Ap. J.*, **114**, 398, 1951.

[25] *Ap. J.*, **116**, 176, 1952.

sity of the R30 line in the 2–0 band by the method of weighting functions[26] suggests that the 11.1 e.v. value is the correct one. However, the result is far from conclusive, since it suffers from uncertainties both in the atomic abundances and especially in the temperature distribution of the sun's outer layers; the greatest contribution to the line intensity appears to come from optical depths (at 2.3 μ) less than 0.02. It is entirely possible, for example, that the lower value of the dissociation energy is the correct one and that the boundary temperature of the sun is appreciably less than the 4500° K value assumed in Newkirk's calculation, as has been suggested by Labs[21] and by Neven and de Jager.[21] The adoption of higher abundances for *O* and *C* would also favor the lower value. A detailed investigation of the problem, involving analysis of center-limb variations in the line intensities, is now being carried out by Newkirk. The results should provide improved values of the carbon and oxygen abundances, as well as information on the dissociation energy of *CO*.

We are very much indebted to our colleagues at the McMath-Hulbert Observatory for securing and making available to us the tracings of the infrared solar spectrum upon which this investigation is based.

[26] M. Minnaert, *Zs. f. Ap.*, **12**, 313, 1936.

SPECTRA AND INTENSITY OF LIGHT FROM SOLAR CRESCENTS NEAR TOTALITY OF ECLIPSE OF FEBRUARY 25, 1952

F. J. HEYDEN, S.J.
Georgetown University Observatory, Washington, D.C.
and
C. A. BECK, D. J. LOVELL, W. B. FUSSELL, J. H. HANCOCK, AND E. O. HULBURT
Naval Research Laboratory, Washington, D.C.
Received March 13, 1953; revised April 7, 1953

ABSTRACT

At Khartoum during the eclipse of February 25, 1952, calibrated spectra were photographed each $\frac{3}{4}$ second of the light from the solar crescents near second and third contacts. From these the spectral intensity distribution was determined from 3800 to 5800 A and was found to be approximately constant over the outer 1.2 per cent of the solar radius, and somewhat redder than at 5 per cent in from the limb. In this spectral region the radial variation of the solar emission was found to decrease rather steadily to a low value near the limb.

Continuous recordings were made with photocells with a broad maximum of sensitivity at 7000–9000 A, and from these the limb darkening was determined over the outer 0.2 per cent of the solar radius.

INTRODUCTION

The eclipse parties of the Naval Research Laboratory and of the Air Force and Georgetown Observatory went to Khartoum, Sudan, to observe the total solar eclipse of February 25, 1952. They set up their equipment in a flat open field of sand at latitude 15°34′ north and longitude 32°34′ east, about 3 km south of Khartoum. The altitude above sea-level was 380 meters (1247 feet). Spectra were photographed, and intensity measurements were made with photocells of the illumination received from the solar crescents near the times of second and third contacts, in order to determine the darkening of the sun as close to the limb of the sun as possible for a number of optical wave lengths. The spectra were made by the NRL party and the photocell records by the Air Force and Georgetown party. The experimental programs of the two parties were in general quite different, but in the matter of the light from the crescents the two sets of observations supplemented each other to such a valuable extent that the results were worked up together and are reported here.

The weather on eclipse day was very good; there were no clouds near the sun throughout the entire eclipse. The vertical photopic transmission of the atmosphere was 0.79, which indicated fairly clear air when it is recalled that the value is about 0.90 for a pure Rayleigh atmosphere. A general description of the Khartoum weather and of the measurements of the spectral transmission of the atmosphere on the morning of eclipse has already been written[1, 2] and need not be repeated here. The times of second and third contacts calculated from the Ephemeris were G.C.T. $9^h9^m11^s.2$ and $9^h12^m20^s.2$, respectively. The duration of totality was 189.2 seconds, and the altitude of the sun was 61°52′ at mid-totality. There were no shadow bands at our site at either second or third contact. The following quantities are used: $r_s = 16'.1883$ is the radius of the solar disk; r_m is the radius of the moon and was $16'.7791$ and $16'.7803$ at second and third contacts, respectively; r is the distance to the center from a point P on the solar disk; A is the area of the exposed crescent of the sun when the edge of the moon is at r and δ is the maximum width of the crescent along a solar radius, $\delta = r_s - r$; J_λ is the total emission from the

[1] E. O. Hulburt, *Sci. Mon.*, **75**, 306–309, 1952.

[2] C. A. Beck, D. J. Lovell, and E. O. Hulburt, *J. Opt. Soc. Amer.*, **43**, 405–406, 1953.

solar crescent, and e_λ is the emission per unit area of the solar disk at P, in the wave-length interval λ to $\lambda + d\lambda$.

From geometry one derives

$$A = r_s^2 \cos^{-1} \frac{x_1}{r_s} - r_m^2 \cos^{-1} \frac{x_2}{r_m} + (x_2 - x_1)(r_s^2 - x_1^2)^{1/2}, \tag{1}$$

where

$$x_1 = \frac{r_s - \delta\,[1 + \delta/2\,(r_m - r_s)]}{1 + \delta/\,(r_m - r_s)}, \tag{2}$$

$$x_2 = \frac{r_m + \delta\,[1 + \delta/2\,(r_m - r_s)]}{1 + \delta/\,(r_m - r_s)}. \tag{3}$$

In the present experiments values of J_λ were observed by means of spectra over the outer 1.2 per cent of r_s for narrow-wave-length regions (less than 30 A) from 3500 to 5500 A; and values of J_λ over the outer 0.2 per cent of r_s were observed by means of photocells for a band of wave lengths extending across the optical spectrum into the near infrared with a broad maximum at 7000–9000 A. From J_λ the values of e_λ were calculated and were found to descend from the value at $r/r_s = 0.995$ to nearly zero, or rather to the intensity of the corona, at the limb where $r/r_s = 1$.

By means of spectroscopic measurements on the uneclipsed sun, values of e_λ have been determined from the center of the solar disk to r/r_s about 0.995 for various wave lengths in the optical spectrum; recent data are those of Minnaert *et al.*[3] and of Krat,[4] a portion of which are plotted in Figure 11. But for r/r_s from about 0.995 to unity, e_λ may not be obtained reliably from the uneclipsed sun because of scattered light and of the boiling at the limb caused by atmospheric scintillation. However, it was suggested by Julius[5] many years ago that e_λ near the limb may be derived from measurements of the illumination from the crescents of the eclipsed sun near totality. Such observations were made at the total eclipses of 1912,[5] 1936,[6] and 1948[7] and at a partial eclipse of 1949.[8] The Dutch data[6] for wave length 4540 A were analyzed by Kopal,[9] and the Göttingen observations[8] for a wave-length band from 6250 to 6600 A were analyzed by Fellget and Schmeidler.[10] Osawa[7] analyzed his own data for wave length 4000 A. The results of the several observers are assembled in Figure 11, together with the results of the present work. The differences between the values of e_λ of the various investigations are quite noticeable and appear to be due to differences in experimental data rather than to methods of analysis.

SPECTROSCOPIC OBSERVATIONS

The arrangement of apparatus is shown in Figure 1. A large heliostat mirror M_1 directed the sunlight onto a concave mirror C, 30 cm in diameter and 150 cm in focal length, which brought the light to a focus 16 cm in front of the slit of the spectrograph. The spectrograph[11] was an $f/6.6$ instrument of unit magnification with achromatized

[3] *B.A.N.*, **11**, 55–61, 1949.

[4] *Pulkovo Pub.*, **17**, 1–38, 1948.

[5] *Ap. J.*, **23**, 312, 1906; **37**, 225, 1913.

[6] J. G. Ferwerda, J. Uitterdijk, and A. J. Wesselink, *B.A.N.*, **9**, 81–100, 1940.

[7] K. Osawa, *Ann. Tokyo Astr. Obs.*, 2d ser., **3**, 53–85, 1951.

[8] P. ten Bruggencate, H. Gollnow, and F. W. Jäger, *Zs. f. Ap.*, **27**, 223–236, 1950.

[9] *Ap. J.*, **105**, 60, 1946.

[10] *M.N.*, **112**, 445–451, 1952.

[11] D. J. Lovell, H. S. Stewart, and S. Rosin, *J. Opt. Soc. Amer.* (in press). This paper describes the design of the spectrograph for operation at high speeds. For the low speed required for the eclipse, the film mechanism was modified considerably.

quartz-fluorite lenses and prisms. The lenses of the spectrograph were at no time filled by the light from the slit, and hence the illumination of the spectrum was at all times proportional to the sunlight intensity. The dispersion was 250, 150, 100, and 60 A mm^{-1} at 6000, 5000, 4000, and 3000 A, respectively; the distance on the negative from 3000 to 6000 A was 20 mm. The width of the slit was 0.4 mm. Therefore, the impurity in the spectrum was about 100, 60, 40, and 24 A at wave lengths 6000, 5000, 4000, and 3000 A, respectively.

Eastman Super XX 70-mm film was used in the spectrograph, each frame being exposed $\frac{3}{4}$ second; and, owing to the multiple-slit mechanism of the spectrograph, the exposure of each frame began about 0.02 second before the preceding frame had been stopped. A four-step neutral filter, of transmissions 1, 0.3, 0.10, and 0.03, was mounted over the slit. Thus in each frame there were four solar spectra of known relative densities. In addition, alongside these in each frame was impressed the spectrum of a tungsten lamp incorporated in the spectrograph. Along the margin of the film time marks were impressed each second by a small light actuated by the chronometer. A number of frames

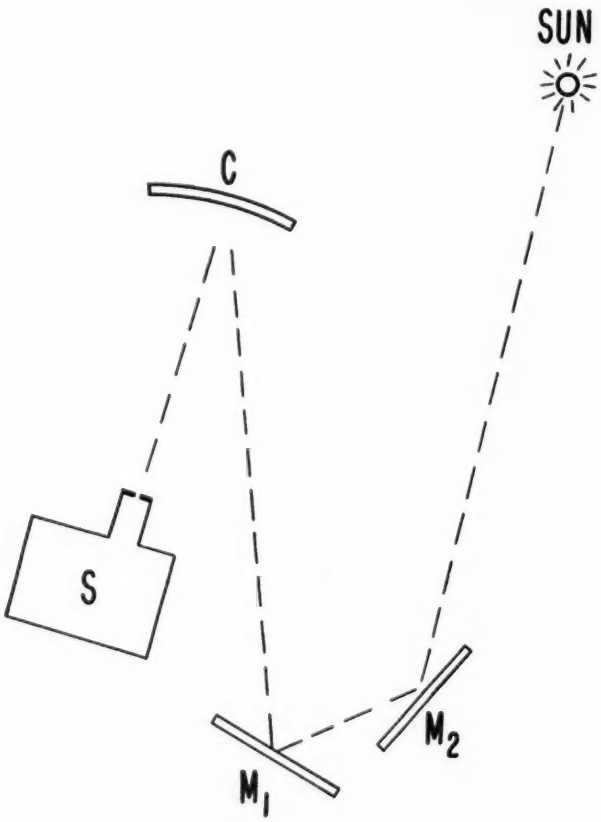

FIG. 1.—Arrangement of spectroscopic apparatus; heliostat mirrors M_1 and M_2; concave mirror, C; spectrograph, S.

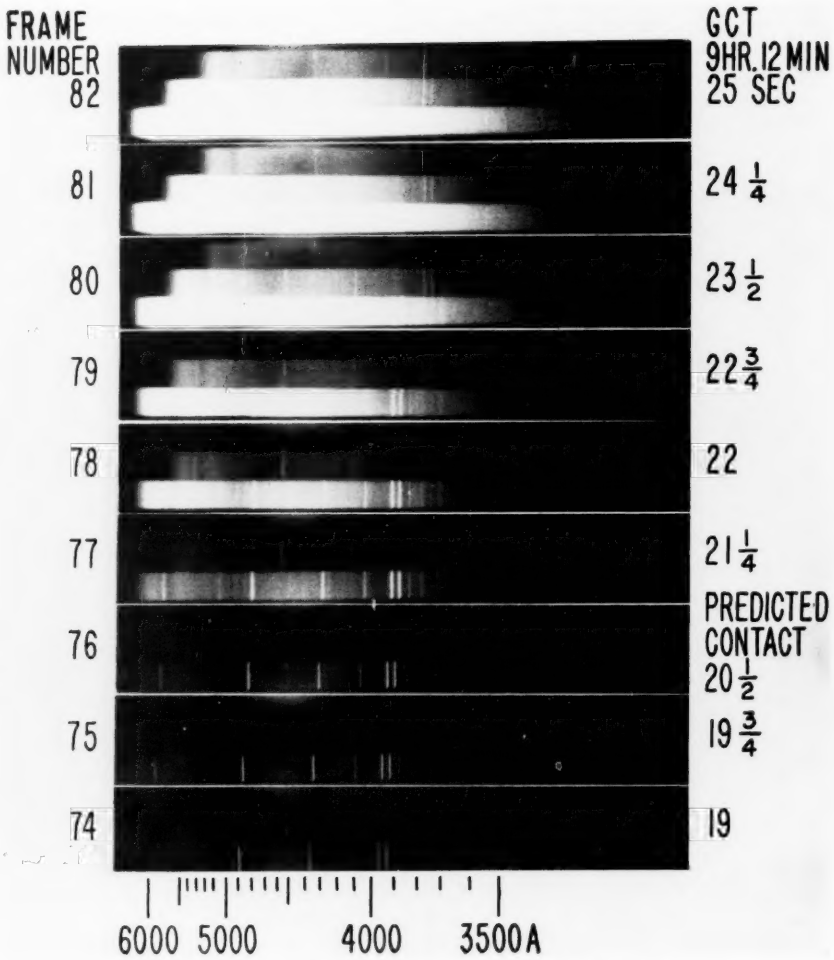

FIG. 2.—Spectra of crescents near third contact at Khartoum

are shown in the prints of Figure 2; each print shows only three solar spectra, because the weakest solar spectrum and the tungsten spectrum, being of little pictorial interest, were cut off from the print to save space. The relative lateral displacement of the several solar spectra of a frame was due to a novel and ingenious film advance device built into the spectrograph. All mechanisms, such as those of the spectrograph and heliostat, were electrically operated.

Since there were four frames per inch, a 100-foot roll of film was sufficient for about a 50-minute run at the rate of $\frac{3}{4}$ second per frame. During the eclipse the spectrograph was put into operation several minutes before second contact and allowed to run continuously throughout totality and several minutes after third contact. Only the spectra for about 30 seconds before second and after third contact were of interest in the present analysis. In order to obtain correct exposures during the changing light-intensity, the exposures were begun with a neutral density filter of 0.011 transmission over the entire slit. At 90 seconds before second contact, this was replaced by one of 0.06 transmission, which was removed at 16 seconds before second contact. At third contact the process was repeated in reverse order; namely, at third contact no filter was used, after 16 seconds the 0.06 filter was inserted, and after 90 seconds it was replaced by the 0.011 filter. At the beginning and end of the run, frames were taken with the same time of exposure as was used for the frames during the eclipse of light from a second tungsten lamp in a quartz envelope, external to the spectrograph, which passed through the identical optical train traversed by the light of the solar crescents. This tungsten lamp had a precision ribbon filament and was carefully standardized by the National Bureau of Standards; the spectral intensity distribution of its light was therefore known to the accuracy that the emissive power of tungsten as a function of temperature is known. Both tungsten lamps were run on constant current. The one inside the spectrograph, whose spectrum was on each frame, was used to determine the relative intensity of each frame with respect to the other frames; and the external tungsten lamp was used to determine the spectral intensity distribution across the solar spectra.

To increase the chance of securing correctly exposed spectra, a second equipment was operated during the eclipse similar to that just described, but with a spectrograph of twice the dispersion and one-sixth the optical speed. This equipment produced spectra during the eclipse which were too weak to be useful in the desired region.

Figure 2 gives a sample of the several hundred spectra which were taken. It shows prints of nine consecutive frames; *74* and *75* are the flash spectrum, *76* is at third contact, and the following frames show the increasing light-intensity as the sun emerged from behind the moon. A similar figure for second contact (not shown here) appeared identical to Figure 2. The times of contact indicated by the spectra with a broadness of $\frac{3}{4}$ second were the same as those calculated from the Ephemeris. A question arises about the time of contact. This may be calculated by using a lunar radius which takes irradiation into account or a lunar radius from occultation data. The first is used in the Ephemeris eclipse computations (also used throughout this paper), but the second, which is 0.0763 per cent larger than the first, might be supposed to be the true physical size of the moon and hence more appropriate in the calculation of crescent areas. If the occultation radius were used instead of the irradiation radius, the contacts at Khartoum would be about 2 seconds farther from mid-totality than those calculated from the Ephemeris. This would mean that, for example, the third contact would have been at about frame *78* instead of frame *76* (Fig. 2). But the spectra *appear* to indicate that contact was at frame *76*, in accordance with the Ephemeris calculation with the irradiation radius, because the continuous spectrum between the stronger lines first appears in frame *76*. Therefore, all computations of this paper are based on the Ephemeris, but we feel quite confused. Perhaps the "time of contact" is not a unique quantity but one which requires definition in any particular case.

Densitometer-curves were made of each solar spectrum and tungsten spectrum of each

frame. The width of the densitometer slit was 0.1 mm and therefore $d\lambda$ was 25, 15, and 10 A at 6000, 5000, and 4000 A, respectively. These values of $d\lambda$ were about one-fourth of the spectral impurity because of the width of the spectrograph slit, and therefore added little to that impurity. Smooth regions, not on obvious absorption lines, were selected for measurement; but in such small spectra the smooth regions were, of course, mainly unresolved blends of fine Fraunhofer absorptions. The details of the densitometer work were routine, extensive, and tedious and need not be described here. From the

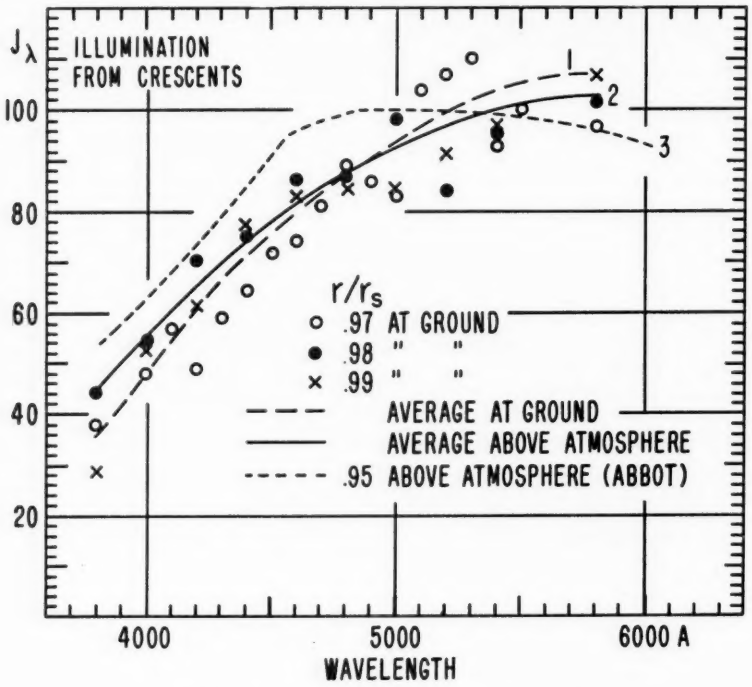

FIG. 3.—Spectral intensity distribution of crescents

densitometer-curves the (1) relative intensities across the spectrum and the (2) relative intensity of each frame with respect to the other frames were determined.

The spectral intensity-distribution results are given in Figure 3, in which J_λ is the intensity of wave length λ of the light of the crescent whose maximum width is $r_s - r$ measured along a solar radius. The circles, dots, and crosses of Figure 3 refer to $r/r_s = 0.97$, 0.98, and 0.99, respectively, i.e., to crescents of maximum width 3, 2, and 1 per cent of the solar radius. Curves through the circles, dots, and crosses were normalized to fall on one another as closely as possible and showed no differences in trend with wave length within experimental error; an average dotted curve *1* was therefore drawn through them. From the spectral transmission coefficients of the Khartoum atmosphere observed[2] on the morning of eclipse day and from the known zenith angle of the sun at totality, the full-line curve *2* was calculated from curve *1;* curve *2* is the spectral intensity distribution above the atmosphere of the light of crescents cut from the outer 1, 2, or 3

per cent of the solar disk. For comparison the similar curve of Abbot[12] for the outer 5 per cent of the solar disk is drawn in curve *3*. Curve *2* appears to be a little redder than curve *3;* neither curve fits well on a black-body-curve.

From the densitometer-curves of the spectra the relative values of J_λ as a function of the time from contact, and hence of the size of the crescent as measured by r/r_s, were determined for five wave lengths for the 30-second interval before second and after third contacts. Samples of the detailed data for the two contacts separately for 12 seconds are plotted in Figures 4 and 5. The curves for the several wave lengths were all adjusted to pass through the same ordinate at 12 seconds, and it is seen that the curves for all the five wave lengths from 3500 to 5500 A had the same trend within experimental error. Extensions of the plots of the data to 30 seconds, not shown here, gave the same result. This showed that the spectral intensity distribution in this wave-length region was the same for all the solar crescents up to 30 seconds, which meant that within the error of experiment the color of the solar disk did not change over the outer 1 per cent of the radius. The result, although approximately true, can certainly not be exactly true. As a matter of fact, the present method of photographing spectra of successive crescents is not a sensitive one to disclose a change in spectral distribution along a solar radius, because each larger crescent is a composite of the smaller crescents.

In Figures 6 and 7 the data of both contacts out to 30 seconds are plotted together; Figure 7 is merely the continuation of Figure 2, with ordinate scale reduced five times. The crosses and circles in these two figures refer to second- and third-contact data, respectively, for 5000 A; thus up to 12 seconds they are the same as the dots in Figures 4 and 5. It would have been too confusing to plot all the data for the other wave lengths in Figures 6 and 7. The abscissa scale at the top of these two figures is the time t from contact. The bottom abscissa scale is r/r_s calculated from the relation

$$\frac{r}{r_s} = 1 - \frac{st}{r_s}, \tag{4}$$

where s is the speed of the moon across the sun in minutes of arc per second of time and t is the time from contacts. It was sufficiently accurate to take $s = 6.255 \times 10^{-3}$, which was the average of the values 6.248 and 6.262×10^{-3} at second and third contacts, respectively.

It is seen that the crosses and circles in Figures 6 and 7 fell approximately on the same curve; therefore, an average dotted curve was drawn through them. This same curve has also been drawn in Figures 4 and 5, merely to orient the data. The fact that the J_λ values of second and third contacts fell approximately along the same curve indicated that the sun and moon were optically symmetrical on the two sides and that the time of central eclipse calculated from the Ephemeris was correct within $\frac{3}{4}$ second. The departures of the crosses and circles from the average curve, which are particularly noticeable in Figure 6 from $r/r_s = 0.9975$ to 0.9955, were confirmed by a repetition of the entire densitometer work on the films in this region. Therefore, the departures were unquestionably on the films, but it seems more probable that they were due to some undetermined experimental circumstance than that they were due to optical asymmetry on the sun. It is true that there was a bright area near the limb near third contact (as seen on spectroheliograms in calcium light) and a bright region in the corona above it, but it is difficult to believe that these could produce the departures.

PHOTOCELL OBSERVATIONS

A gas-type photocell, RCA type 927, S-1, was mounted in a small metal box at the end of a tube, blackened on the inside, which limited the field of view to a circle about 45 minutes of arc in diameter. This was fixed to a small equatorial mounting, which allowed

[12] C. G. Abbot, *Smithsonian Physical Tables* (8th rev. ed., 1933), Table 769.

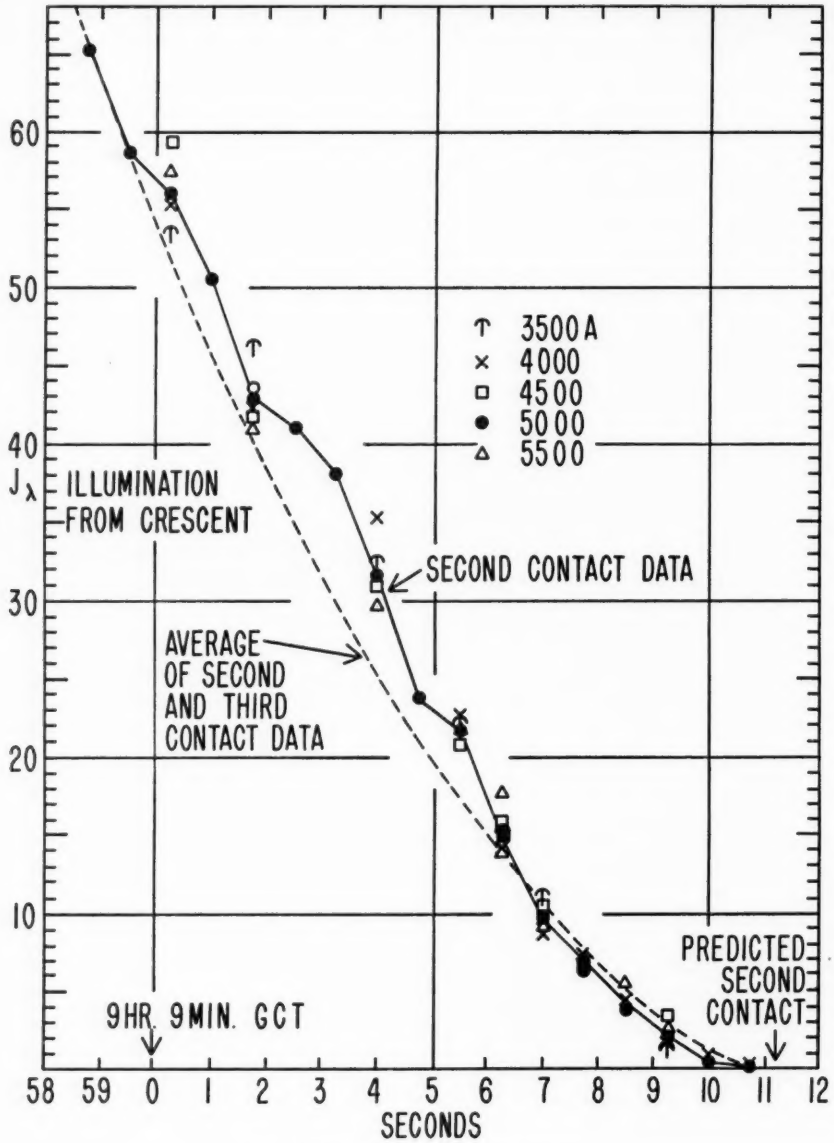

FIG. 4.—Values of J_λ near second contact

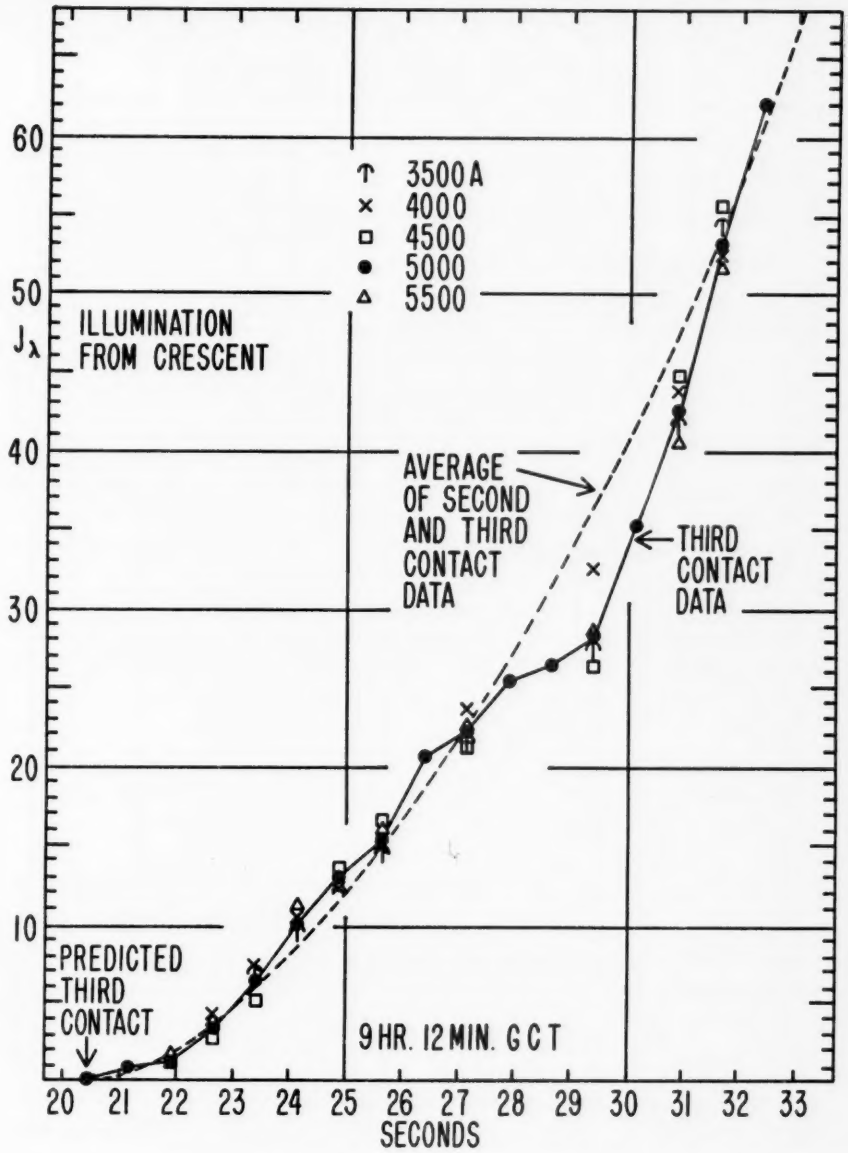

FIG. 5.—Values of J_λ near third contact

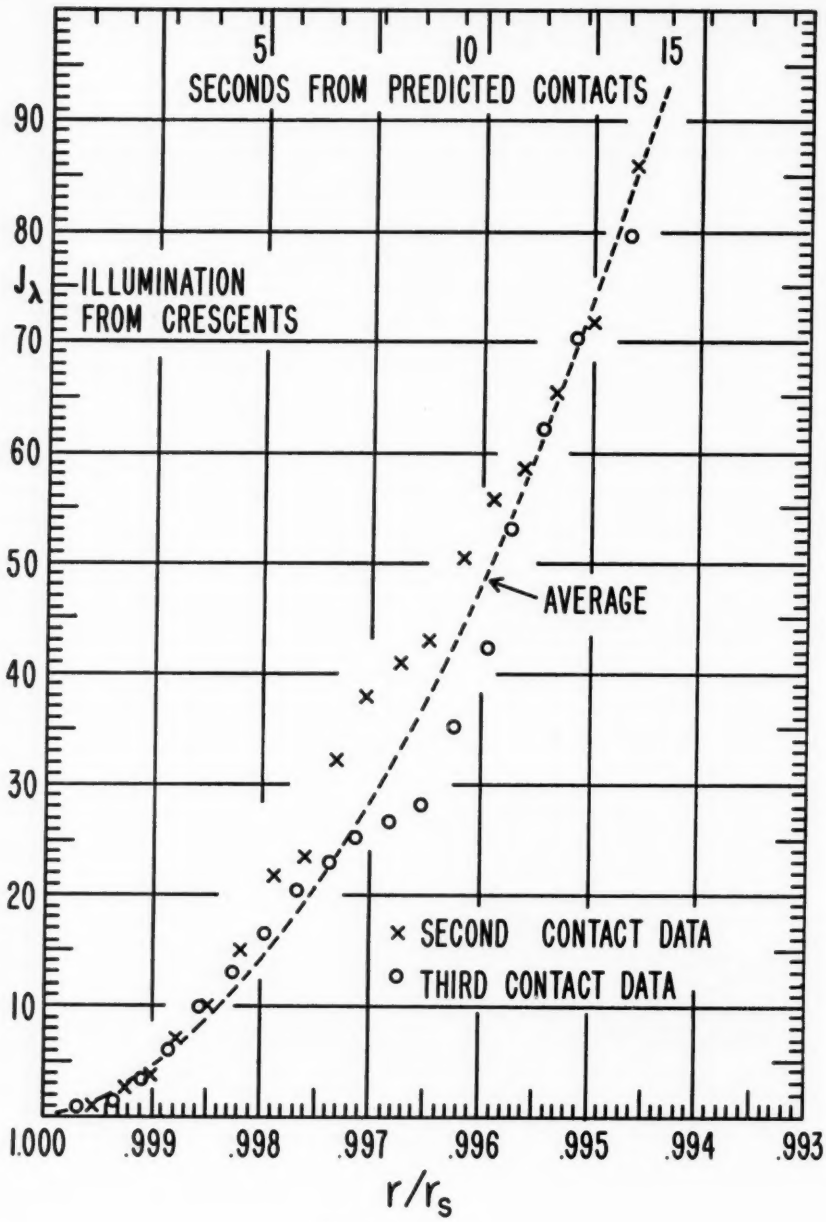

FIG. 6.—Values of J_λ

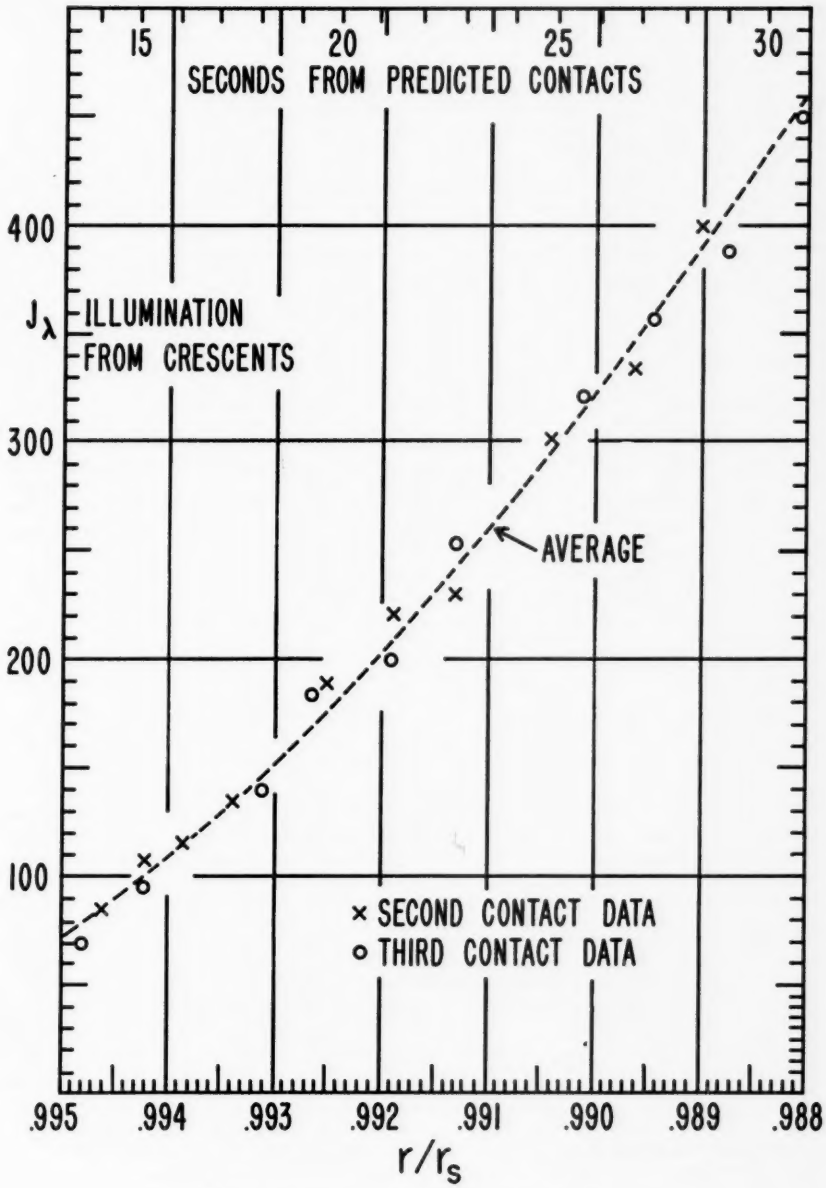

FIG. 7.—Values of J_λ (continuation of Fig. 6)

the observer to guide the instrument on the sun during the eclipse. The photocell was connected through a bridge circuit with a similar balancing cell in the dark to compensate for temperature variations, to a Brush BL-932 amplifier and BL-222 pen recorder. The spectral sensitivity-curve of the photocell,[13] shown in Figure 8, extended across the optical spectrum with a broad maximum at about 8000 A. Similar photocell equipments were at Khartoum, Bangui, and Port Sudan. Since these were designed primarily for observing the times of contact, they were not calibrated in energy units, and hence gave only relative values of J_λ. Also, after about 5 seconds from the time of contact, when J_λ had increased to more than 100 times the corona illumination during totality, the photocell readings departed from linearity. Therefore, only the readings during the first few seconds from contact were useful.

A good photocell record was obtained at Khartoum through totality and third contact. The record near second contact was lost, owing to trouble with the balancing of the bridge circuit. A portion of the record at every 0.1 second is plotted in the dots of Figure 9. It had been hoped that, by using a red-sensitive photocell, there would be a sharp difference in the response between the outer limb of the sun and the inner corona at the beginning and ending of totality. However, this was not the case; for, as shown by the dots of Figure 9, the response increased smoothly through contact without any marked change in slope. Actually, the response was about 1 scale division at mid-totality, and increased to 1.9 at third contact. Therefore, 1.9 was subtracted from the ordinate of each dot of Figure 9; this gave the J_λ-curve in Figure 9. From this curve are plotted the dots of Figure 10 against r/r_s as abscissas. Similar records (not shown here) were obtained for both contacts at Bangui and Port Sudan; when the J_λ-curves for both contacts at the respective stations were superimposed, they fitted closely. The resulting values of J_λ are plotted as circles and crosses in Figure 10, the values for the three stations being normalized at $r/r_s = 0.9988$; the average curve was drawn through them. We remark in passing that the photocell-curves, such as the dots of Figure 9, rose gradually from totality through contact into penumbra and hence were not adequate to determine the time of contact very accurately. However, by superimposing the curves of second and third contacts at a station, the time of mid-totality could be determined to within 0.1 second.

Now at totality the lunar radius r_m was 16′.791, 16′.780, and 16′.759 at Port Sudan, Khartoum, and Bangui, respectively. Therefore, the solar-crescent areas at the other two stations for crescent widths a less than 0′.02 differed from those at Khartoum by about 1 and 2 per cent, respectively. These differences were small enough to disregard, and it was therefore permissible to plot J_λ of all three stations in Figure 10 against the same r/r_s and to draw the average curve through them. The differences in the values of J_λ for the three stations, which were particularly noticeable for r/r_s from 0.999 to 1, were probably due mainly to instrumental variations. However, it is just in this region that irregularities in the lunar profile and coronal distribution may be apparent, and some of the differences may be due to these effects.

CALCULATION OF e_λ FROM J_λ

It is well known that, in general, the calculation of e_λ from J_λ is difficult. Analytical methods have been described,[7, 9, 10] but in the present case the ring method of Julius[5] is used. In this method the sun is divided into a number of concentric rings numbered $1, 2, 3, \ldots, j$ successively inward from the limb, the ring at the limb being 1. The inner edges of the respective rings are numbered $1, 2, 3, \ldots, i$. The subscript λ is dropped temporarily from e_λ and J_λ and is replaced later. The emission per unit area from ring j, e_j, is assumed to be constant over the ring; in general, e_j is different for each ring. The moon is tangent to each ring, in turn, at position i. The exposed area of ring j for the moon in position i is a_{ij}; and $j \leqq i$, because rings for $j > i$ are not exposed. The total

[13] *RCA Tube Handbook* (1946).

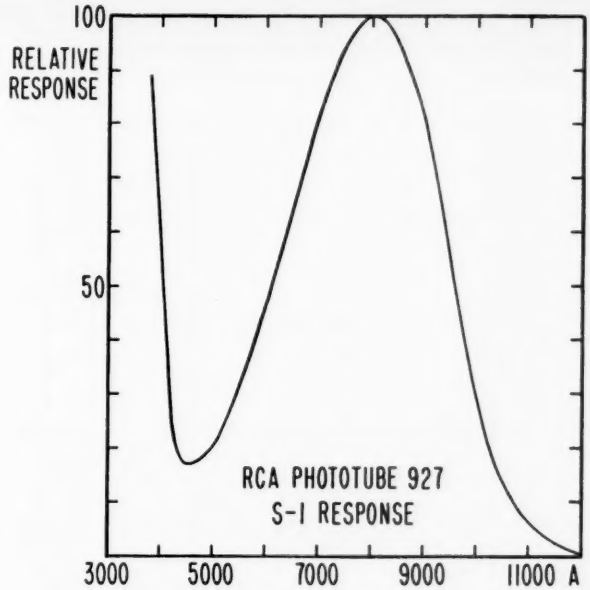

FIG. 8.—Spectral sensitivity-curve of RCA phototube 927 S-1

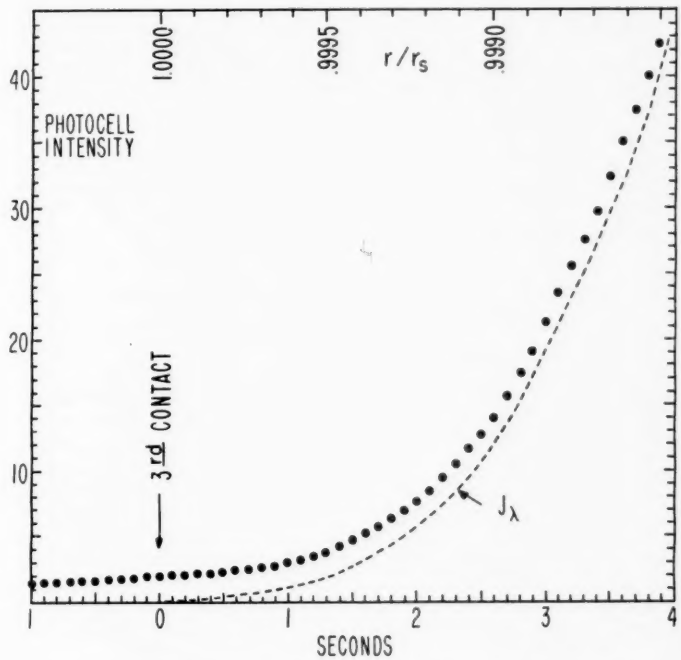

FIG. 9.—Photocell intensities at Khartoum; *dots*, observed; *dotted curve*, J_λ

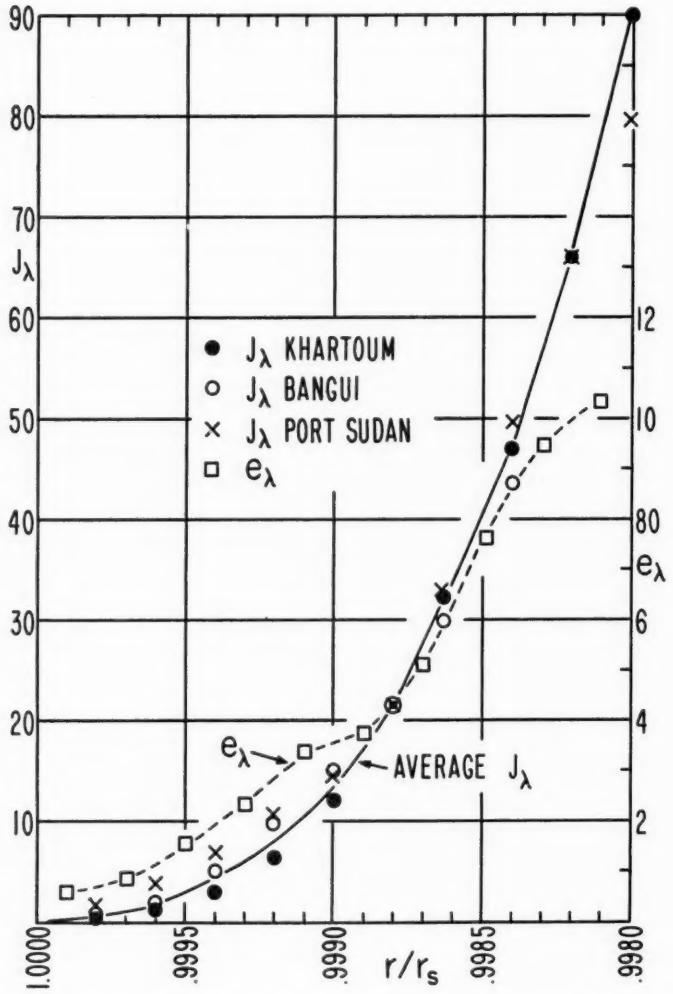

FIG. 10.—Values of J_λ from photocell records at three stations and their average; e_λ calculated from average J_λ.

emission from the crescent formed when the moon is in position i is J_i and is equal to the sum of the emissions from the portions of the rings which make up the crescent. Hence

$$J_i = \sum_{j=1}^{j=i} e_j a_{ij}, \tag{5}$$

which may be written

$$J_i = \sum_{j=1}^{j=i-1} e_j a_{ij} + e_{j=i} a_{ii}. \tag{6}$$

Solving for $e_{j=i}$, we obtain

$$e_{j=i} = \frac{J_i - \sum_{j=1}^{j=i-1} e_j a_{ij}}{a_{ii}}. \tag{7}$$

The calculation of e_j is a step-by-step process. One begins with $i = 1$; then $j = 1$, and the crescent is a piece of ring 1 of area a_{11}. Equation (7) becomes $e_1 = J_1/a_{11}$; J_1 is read from the curve of Figure 6 (for example), and e_1 is calculated. Then with $i = 2$, j has values 1 and 2, and the crescent area is made up of pieces of rings 1 and 2 of areas a_{21} and a_{22}, respectively. Equation (7) becomes $e_2 = (J_2 - e_1 a_{21})/a_{22}$; J_2 is read from the curve, and e_2 is calculated. And so forth.

In order to carry out the ring calculation, Tables 1 and 2 of values of a_{ij} were calculated by means of equation (1) for two sets of rings: Table 1 for 12 rings of width 0.001 r_s from $r/r_s = 1.000$–0.988, and Table 2 for 10 rings of width 0.0002 r_s from $r/r_s = 1.000$–0.9980. (The arithmetic work of Table 1 was correct within 3 per cent, and of Table 2 within 5 per cent.) Values of J_λ from the average curves of Figures 6 and 7 for the rings of Table 1 are given in Table 3, third column. From these and Table 1, e_λ was calculated by means of equation (7) and is given in Table 3, fourth column. Since the values of e_λ were relative and were the same for the wave lengths of Figure 2, the family of curves (with dots) of Figure 11 for the various wave lengths were calculated from these relative values and the spectral intensities of Figure 2. The curve for 5600 A was adjusted to pass through the value $e_\lambda = 0.393$ at $r/r_s = 0.990$, as observed by Minnaert *et al.*[3] For comparison the results of Minnaert[3] and of Krat[4] for the uneclipsed sun and of the other observers for the eclipsed sun are plotted in Figure 11; the curve of Osawa was adjusted to pass through $e_\lambda = 0.22$ at $r/r_s = 0.988$, and of ten Bruggencate to pass through $e_\lambda = 0.44$ at $r/r_s = 0.990$. All the curves of Figure 11 pass through unity at the center of the solar disk.

The use of the average J_λ-curve of Figure 6 instead of the respective J_λ-curves of the second and third contacts to calculate e_λ deserves comment. If the differences of the J_λ-curves of second and third contacts were real and were due to unsymmetrical bright areas near the solar limb, then the essential assumption of radial symmetry in e_λ was not true, the Julius method does not apply, and equation (7) could not be used to calculate e_λ from J_λ. For example, when J_λ from the second- and third-contact data was introduced into equation (7), the resulting values of e_λ oscillated from ring to ring with increasing magnitude and finally became negative, showing, as was obvious, that the use of equation (7) under such conditions was meaningless.

The photocell data are of interest because they covered the region of the sun very close to the limb with greater accuracy than did the spectroscopic data, although in a different wave-length region. The values of J_λ were read from the average photocell curve of Figure 10 for the rings of Table 2 and are given in Table 4, third column. From these and Table 2, e_λ was calculated by means of equation (7); the values are listed in Table 4, fourth column, and are plotted in the curve of Figure 10 on a relative scale. The curve

TABLE 1

$a_{ij} \times 10^6$ FOR 12 RINGS OF WIDTH 0.001 r_s FROM $r/r_s = 1.000$ TO 0.988 AS FRACTIONS OF AREA OF SOLAR DISK

i	j											
	1	2	3	4	5	6	7	8	9	10	11	12
1	100											
2	180	98										
3	231	178	97									
4	271	228	176	96								
5	304	268	225	174	95							
6	333	301	264	223	171	94						
7	359	329	297	261	220	170	92					
8	382	355	325	293	258	217	167	91				
9	403	378	350	321	290	255	215	165	90			
10	422	399	373	347	318	287	252	212	163	89		
11	440	418	394	369	343	314	284	249	210	162	88	
12	457	435	413	388	365	337	311	280	246	208	160	87

TABLE 2

$a_{ij} \times 10^7$ FOR 10 RINGS OF WIDTH 0.0002 r_s FROM $r/r_s = 1.000$ TO 0.998 AS FRACTIONS OF AREA OF SOLAR DISK

i	j									
	1	2	3	4	5	6	7	8	9	10
1	88									
2	161	88								
3	209	161	88							
4	248	209	161	88						
5	282	248	209	161	88					
6	312	281	247	208	160	87				
7	339	311	281	247	208	160	87			
8	365	339	311	280	246	207	160	87		
9	389	364	338	310	280	246	207	160	87	
10	411	388	364	338	310	279	246	207	159	87

TABLE 3

RELATIVE VALUES OF J_λ FROM SPECTROSCOPIC DATA AND OF e_λ FOR RINGS 0.001 r_s IN WIDTH

Ring j	r/r_s	J_λ	e_λ	Ring j	r/r_s	J_λ	e_λ
1	0.999	4.3	0.430	7	0.993	152	1.81
2	.998	14.0	0.639	8	.992	203	1.88
3	.997	28.5	0.742	9	.991	260	1.91
4	.996	47.4	0.846	10	.990	322	1.97
5	.995	72.5	1.146	11	.989	389	2.02
6	0.994	108	1.74	12	0.988	460	2.10

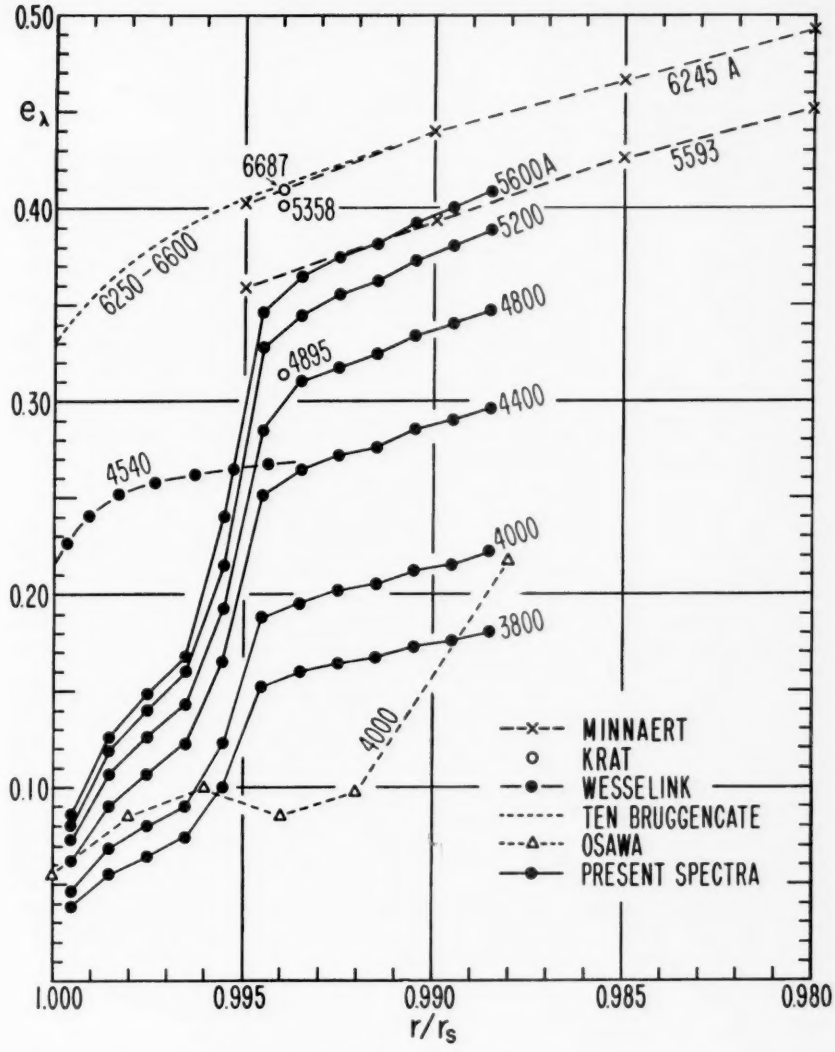

FIG. 11.—Values of e_λ; *crosses and circles*, from observations of uneclipsed sun; other curves from eclipses.

cannot be oriented among the curves of Figure 11 because its wave-length region, extending into the near-infrared, was not included in Figure 2. It is hardly necessary to remark that the inaccuracy of the values of e_λ of Tables 3 and 4 increased rapidly with increasing j because of the iteration of equation (7). Actually, the values of e_λ have been smoothed indirectly, because they were calculated from the values of J_λ read from the smoothed average curves of Figures 6, 7, and 10.

The differences between the values of e_λ of the various observers brought out in Figure 11 are probably due mainly to differences in the observational data rather than in

TABLE 4

RELATIVE VALUES OF J_λ FROM PHOTOCELL DATA AND OF e_λ FOR RINGS 0.0002 r_s IN WIDTH

Ring j	r/r_s	J_λ	e_λ	Ring j	r/r_s	J_λ	e_λ
1	0.9998	0.51	0.580	6	0.9988	21.3	3.62
2	.9996	1.69	0.859	7	.9986	32.0	5.30
3	.9994	3.98	1.57	8	.9984	47.1	7.63
4	.9992	7.70	2.20	9	.9982	67.4	9.46
5	0.9990	13.6	3.42	10	0.9980	92.4	10.3

procedures of analysis.[14] There is no question that the various observations were made with experience and care and that the processes of analysis, although approximate, were adequate. The fundamental difficulty appears to lie in the Julius method of measuring J_λ of the crescents in order to determine e_λ; the method requires great accuracy in J_λ, in order to obtain even moderate accuracy in e_λ. This has been thoroughly discussed by all who have used the method. Improved experimental methods have been thought of, but these pose formidable difficulties in the matter of elaborate and expensive equipment. However, in spite of its shortcomings, the Julius method is effective from the practical experimental standpoint and is worth while being repeated at future eclipses with accurate photocell recordings for several wave lengths.

[14] Dr. T. C. Doyle of this laboratory has pointed out that Osawa (see n. 7) has omitted a factor of 2 in his eq. (16) which is present in his eq. (14). If this is not a misprint, it will have some effect on his final curve in his Fig. 12, which has been plotted here in our Fig. 11.

ISOPHOTAL PHOTOMETRY OF A SOLAR FLARE

DONALD E. BILLINGS AND WALTER ORR ROBERTS
High Altitude Observatory of Harvard University and University of Colorado
Received March 18, 1953; revised July 17, 1953

ABSTRACT

The paper presents isophotal contour maps of the solar flare of April 12, 1950, at various stages of development, and a plot of integrated intensity of the flare as a function of time. Our measurements indicate that at flare maximum the earth received a radiation of solar $H\alpha$ energy/sec which exceeded "quiet"-sun $H\alpha$ radiation by nearly 2×10^{18} ergs/sec. The estimated total energy in $H\alpha$ reaching the earth from the sun between the recognized start of the flare and its end exceeded that from the quiet sun for a corresponding time interval by approximately 9×10^{21} ergs.

INTRODUCTION

For nearly a century, dating from the famous visible light-flare observations of Carrington in 1859,[1] there has been widespread interest in the relationship between solar flares and accompanying terrestrial disturbances. In many respects the sudden rise of intensity of the light emitted from a solar flare resembles, though perhaps superficially, as Richardson has pointed out,[2] a typical light-curve of a nova. The sudden explosive rise, often assignable in time with a precision of better than 1 minute, helps make certain the correspondence of flares to sudden ionospheric disturbances, to crochets in geomagnetic records, to short-wave fadeouts, to sudden phase anomalies, to increases of long-wave atmospherics, and to other phenomena.[3] In recent years the relationship of solar flares and geomagnetic character to meteorological phenomena has come under intensive study, with a clear correlation coming from the work of Craig.[4] This correlation promises, as Willett[5] and others have indicated, results of great theoretical and practical importance in meteorology.

In spite of the importance of the solar flare in solar-terrestrial relationships, the observations of solar flares undertaken generally fall short, even now, of providing sufficient quantitative information for adequate theoretical treatment. A large fraction of all available information published in the *Quarterly Bulletin of Solar Activity*, for example, consists simply of eye-estimates of intensity made at the observing instrument or from photographic records therefrom. Progress in the understanding of flares and their terrestrial influences therefore now demands greater refinement in flare measurement. We report here our first efforts to measure the brightness in $H\alpha$ of all parts of a solar flare photographed at selected times through a birefringent filter centered at $H\alpha$. We used, for this measurement, a new electronic isophotometer[6] that gave us an isophotal contour map of the flare for each photograph. From the maps we derived information on the variation with time of the rate of energy output of the flare in $H\alpha$.

PHOTOMETRY OF EMISSION FROM SOLAR FLARES

Although the published reports are dominated by eye-estimates of the photometric properties of solar flares and although such eye-estimates have been of great value, more

[1] Bartels, *J. Terr. Mag.*, **42**, 235, 1937; Stewart, *Phil. Trans., London*, **151**, 423, 1861.

[2] *Ap. J.*, **114**, 356, 1951.

[3] M. A. Ellison, *Pub. R. Obs. Edinburgh*, **1**, 53, 1950.

[4] *Jour. Meteorol.* **9**, 126, 1952.

[5] Paper presented at the *Symposium on Climatic Change* of the American Academy of Arts and Sciences, May 9–10, 1952, to be published with other Symposium papers by the Academy.

[6] Fowler, Johnson, and Billings: *J. Opt. Soc. Amer.*, **43**, 63, 1953.

precise photometry of solar flares has occupied the attention of many workers.

In 1939, Richardson[7] determined "integrated intensities" as a function of time for eighteen solar flares. He obtained this "integrated intensity" by estimating the brightness of the projected image of flare photographs and then multiplying the estimated brightness by the measured area of the bright region.

Giovanelli,[8] in 1940, made eye-estimates of the intensity of a flare during its progress. He calibrated the arbitrary scale of his eye-estimates by projecting a variable artificial source of known properties alongside the flare and matching the two. In 1947 Mohler,[9] using the K line of *Ca*, and Dodson,[10] in 1949, using *Hα*, determined curves of intensity as a function of time for selected points in flares by measurements on successive standardized spectroheliograms. Barton,[11] Newton,[12] Barton, Laurie, and Rhodes,[13] and Ellison[14] have measured the central intensity in the *Hα* spectrum of flares as a function of time, generally selecting the brightest portion of the flare for such measurements. Mustel and Severny[15] in 1950 made microphotometer tracings of spectra from flares, using various emission lines in hydrogen and ionized calcium and measuring from standardized spectra obtained from a spectrohelioscope. In 1952, Newkirk,[16] using a direct-intensity recording microdensitometer, made isophotal contour maps of five frames in the *Hα* record of the flare of July 22, 1950.

The quantity used most extensively to designate the progress of a flare has not been a photometric one, however, but the measurement of the line width, most often in *Hα*.[17, 18, 19, 20, 21, 22] This procedure is usually quicker than measuring central line intensity, and there appears to be an approximate relationship between the two quantities.

Bracewell and Straker[23] and others have compared curves of the various quantities used for describing the progress of flares with the time-curves of radio-propagation phenomena associated with these flares. These comparisons emphasize the importance of more precise photometric studies of flares.

The following material describes our preliminary application of a breadboard model of an electronic contour densitometer or isophotometer recently constructed with the support of the Office of Naval Research by the staff of the High Altitude Observatory. Its design evolved from suggestions by Oliphant[24] and Babcock.[25] The instrument scans a flare photograph and automatically displays, on an oscilloscope screen, contours of equal density in the original photograph. By measuring the areas within these contours and calibrating the density steps in terms of brightness of the flare, we can obtain information of considerable significance in the study of the energy output of a flare.

METHOD OF ANALYSIS

For the work reported in this paper we selected nine photographs of the solar disk made at Boulder, Colorado, before, during, and well after maximum activity of a brilliant flare. The photographs were taken on 35-mm *Hα* film through a birefringent filter that admitted a band of half-width approximately 0.5 A, centered at *Hα*. We analyzed

[7] *Ap. J.*, **90**, 368, 1939.
[8] *Ap. J.*, **91**, 334, 1940.
[9] *Pub. A.S.P.*, **59**, 266, 1947.
[10] *Ap. J.*, **110**, 382, 1949.
[11] *Observatory*, **68**, 191, 1948.
[12] *Observatory*, **69**, 235, 1949.
[13] *Observatory*, **71**, 170, 1951.
[14] *Pub. R. Obs. Edinburgh*, **1**, 75, 1952.
[15] *Ann. Crimean Ap. Obs.*, **5**, 3, 1950.
[16] *Astr. J.*, **57**, 21, 1952.
[17] Ellison, *M.N.*, **109**, 3, 1949.
[18] *Ibid.*, **106**, 500, 1946.
[19] Conway, *Observatory*, **69**, 68, 1949.
[20] Barocas and Righini, *Observatory*, **69**, 228, 1949.
[21] Link and Maskova, *Bull. Central A. Inst. Czechoslovakia*, **2**, 186, 1951.
[22] Svestka, *Bull. Central A. Inst. Czechoslovakia*, **2**, 81, 1951.
[23] *M.N.*, **109**, 28, 1949.
[24] *Observatory*, **69**, 108, 1949.
[25] *Pub. A.S.P.*, **62**, 18, 1950.

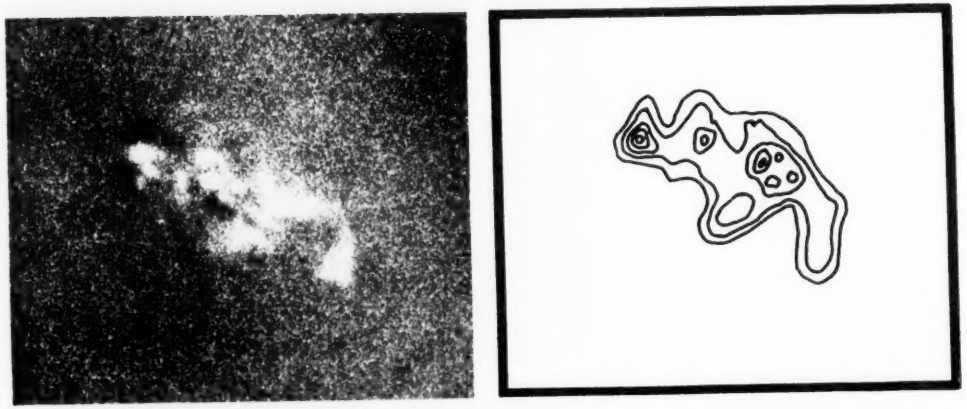

A *B*

FIG. 1.—*Hα* flare photograph of April 12, 1950, at 19:16 U.T., shown at *A*, with a corresponding series of contours at *B*, produced by electronic isophotometer.

positive contact prints of these photographs, although the original negatives would have served the purpose equally well.

We do not give here the details of the photometric procedures used in relating the variations of density of the original films to the corresponding brightness levels of the flare, or of the additional step relating the density of the original film to the density setting of the isophotometer for each contour. Checks of the density of selected portions of a flare photograph by two entirely independent methods indicate that the density values assigned to the contours are satisfactory. The principal sources of errors affecting our intensity calibrations are the following:

a) The original films did not contain direct-intensity standards. Standards were deduced by applying sensitometric calibrations to similar film at a later date and by processing that film in developer made to the same formula for the same time and at the same temperature.

b) Prints were used rather than the original films, and these prints were "masked" to permit us to eliminate shadings that existed in the originals as a result of defects of homogeneity in the calcite of the birefringent filter. A standard mask was produced for the purpose and its photometric properties studied. In addition, sensitometric spots were carried in the printing process to keep account of the photometric properties of the film used in this step.

c) We have no definite knowledge of the amount of scattered light admitted at wave lengths other than the center of $H\alpha$ for the filter then in use. However, on the basis of performance of an exactly similar filter, we have corrected for a total amount of scattered light equal to the amount of light from the quiet solar disk admitted in the band-pass of the filter.

The foregoing errors may, at the most, introduce an uncertainty that would halve or double the absolute energy values assigned to the flare. The relative energy values are obviously more certain. Thus the changes in the pattern of the flare with time, shown by Figure 2, the shape of the brightness-area-curves of Figure 3, and the shape of the power-time-curve of Figure 4 are all determined with higher precision.

With the isophotometer we first produced a series of isophotal contours from the masked prints differing by density steps of 0.1. For each photograph we then determined the brightness level corresponding to each of the contours. The levels were spaced by steps of approximately 0.04 in the logarithms of intensity. Hence the contours are slightly closer than those used by Newkirk.[16]

Figure 1 shows the appearance of a direct print from the original flare film with the corresponding set of isophotal contours for comparison. The apparent differences between *A* and *B* probably result principally from (*a*) the appreciable size of the scanning spot —causing spread of finer details, thus affecting the appearance of the contours, but only secondarily the integrated intensities measured therefrom; (*b*) the tendency of the eye to be sensitive to small gradients of brightness rather than to brightness level.

Figure 2 contains the contours of nine such photographs produced for nine stages of development of the flare. The outermost contour in each case is the largest contour we could distinguish with the isophotometer as a feature rising above the general background of the masked print of the solar disk. In all analysis we have neglected applying any projection corrections, both because the flare was near the center of the solar disk and because we seriously doubt the validity of assuming the flare to lie in a plane parallel to the solar surface. Nor have we applied corrections for limb darkening.

From these contour maps we then obtained integrated flare intensities through application of the following steps:

a) We measured the area inclosed by each contour.

b) We plotted the brightness corresponding to each contour as a function of the area inclosed, taking as a unit of brightness the apparent brightness of the quiet solar disk in $H\alpha$. Figure 3 shows the resulting curves for the nine photographs. As a consequence

of the irregularity of the filter, each curve in Figure 3 is asymptotic to a brightness value greater than unity indicated by the dotted horizontal line. The unit of brightness was derived in a low-transmitting portion of the filter.

c) We obtained the integrated intensities (in excess of quiet solar-disk intensities) of the flare by measuring the shaded areas in Figure 3.

Figure 4 shows the history of the integrated intensity of the flare during the time in-

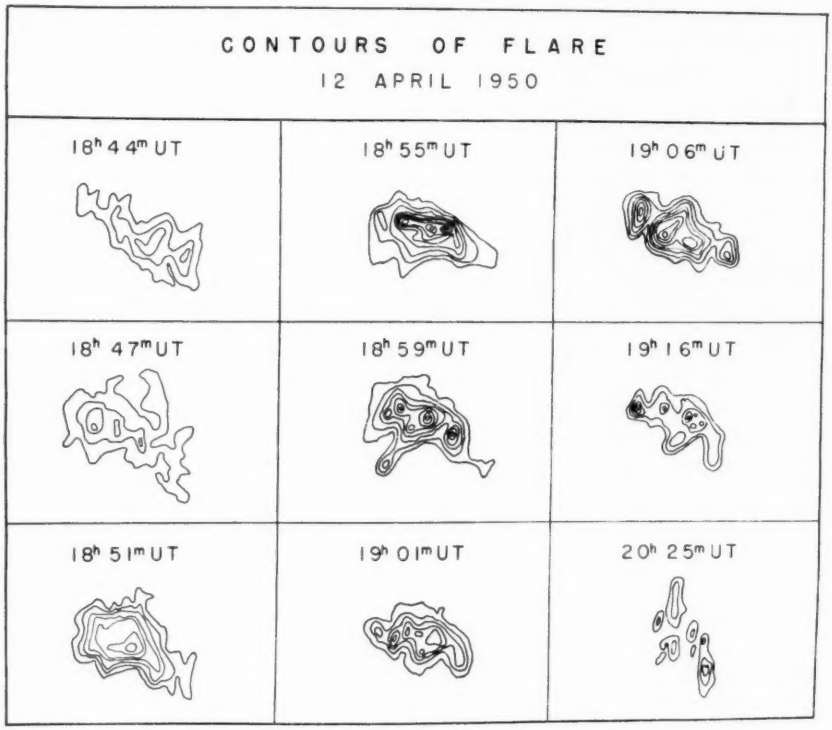

FIG. 2.—Isophotal contours of the flare at various stages of its development. The spacing between contours represents density intervals of 0.1 on the film used in the isophotometer. The outermost contour in every case includes not only the flare but the associated plage region—a total area several times as large as that of the flare proper.

terval covered by the analysis. The area under this curve, thus, gives the total energy (in excess of the energy from a corresponding portion of the quiet disk) radiated by the flare in a wave-length range passed by our filter, during this time interval. Uncertainties are introduced by the limited number of photographs analyzed and, of course, by the experimental errors of the measurement procedure.

RESULTS

The flare chosen for analysis occurred on April 12, 1950, between about 18:42 and 23:00 U.T. The first and brightest phase of the flare, however, was largely dissipated by

20:25 U.T. It was a large, moderately intense flare,[26] rated importance 2 by Mount Wilson Observatory.[27] It occurred in the large complex sunspot group listed as Mount Wilson No. 10303, having magnetic classification γ, for which a maximum magnetic field of 4200 gauss was reported.[28] The active region was also characterized by coronal phenomena

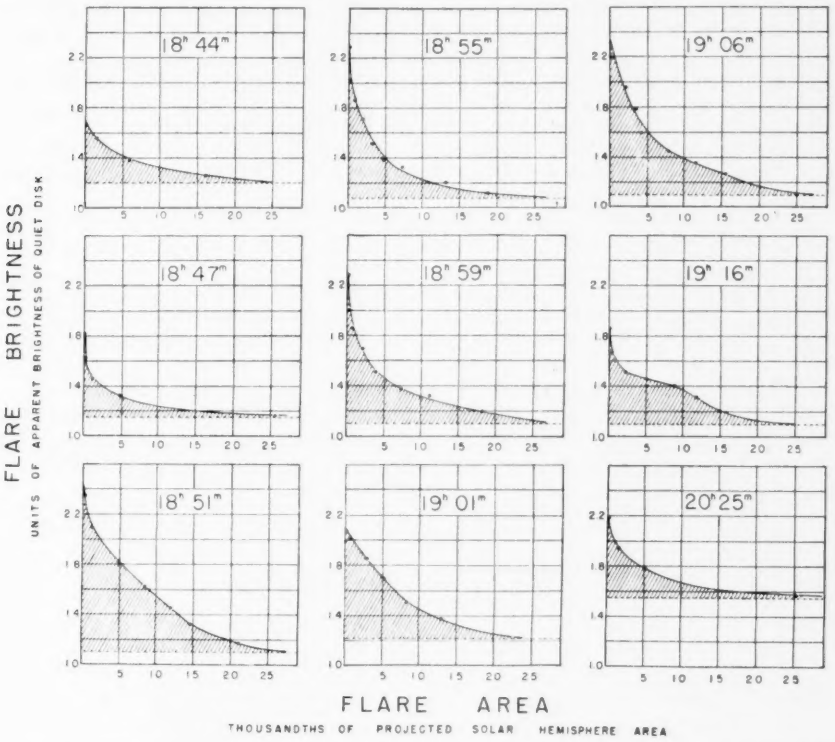

FIG. 3.—Disk brightness corresponding to the isophotal contours of Fig. 2 plotted as a function of the area within the contours. The shaded area under each curve represents the difference between the integrated intensity of the flare region and the integrated intensity of an equal area of the undisturbed solar disk at the same wave length.

typical of the regions that produce the yellow coronal line λ 5694.[29] Coronal spectra from Climax show the occurrence of this rarely seen line on April 20 directly over the position where the flare had occurred on April 12. The prominences in the region also exhibited the high velocities and symmetry over the region typical of the extreme active centers from which the yellow coronal line is radiated. Accompanying the flare was a pronounced sudden ionospheric disturbance that produced a complete fadeout on four circuits received at Washington, D.C., from 18:39 to 21:20 U.T.[30]

[26] *CRPL, National Bureau of Standards Report F-72* (August, 1950), p. 44.

[27] *I.A.U. Quart. Bull.* p. 132, 1949–1950.

[28] *Pub. A.S.P.*, **62**, 123, 1950.

[29] Roberts, *Ap. J.*, **115**, 488, 1952.

[30] CRPL, *National Bureau of Standards Report F-69* (May, 1950), p. 30.

The contour maps of Figure 2 reveal the history of the flare. The region shown at 18:44 U.T. is composed principally of the bright plage from which the flare erupted. By 18:51 the entire region had brightened greatly, and the integrated intensity, as shown by Figure 4, had reached a maximum. The bright points were scattered by 18:59, and by 19:01 several were no longer evident. A new region in the left portion of the 19:01 map rose up and reached the greatest brightness in the flare at 19:06. By 20:25 the flare was in a new phase in which the bright regions were greatly dispersed. It maintained this latter essential pattern until it disappeared at 23:00 U.T.

The curve of integrated intensities versus time (Fig. 4) bears a marked resemblance to *Hα* line width versus time-curves for the more brilliant flares analyzed by Link and Maskova,[21] for a flare discussed by Barocas and Righini,[20] and for the March 24, 1951, flare analyzed by Ellison.[14] The relation of the integrated intensity-curve to the dotted exponential curve in Figure 4 indicates that the decay may have had an exponential

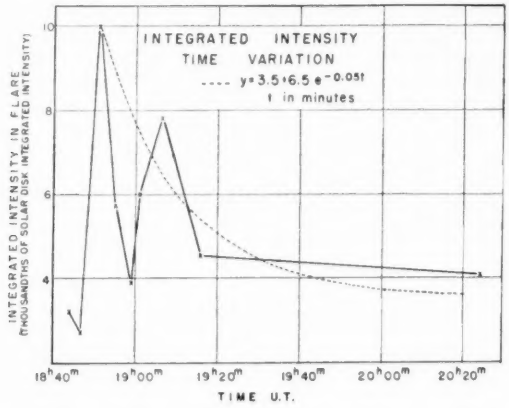

FIG. 4.—Integrated intensity above that of the solar disk for the flare at the various times in its development. The points represent the shaded areas of Fig. 3. The area under this curve, in turn, is a measure of the total energy at *Hα* added to the quiet-disk value by the flare during the time interval designated. The dashed line represents an exponential that decays with time to the value 3.5, approximately equal to the plage intensity.

character, thereby following a decay law suggested by Mohler[9] and Dodson[10] from single-point photometry. The extreme complexity of this flare's history, with first one position brightening, then another, tends in integrated intensity to mask any simple decay law that might be exhibited by single points of the solar surface.

Because the line width of *Hα* during the course of a flare varies by several angstroms, the integrated intensity calculated as we have done it does not accurately reflect the total energy per unit time radiated by the flare. If we had sufficient information about the variation with time of the line width, we could combine this with Figure 4 to compute the rate of radiation from the flare at each stage of its life.

For this particular flare we have no such information. However, Ellison has shown that for flares in general the central intensity and the line width of *Hα* are approximately related.[17] Thus if we know the relative amounts of *Hα* and scattered light transmitted by the filter, we can make estimates of the rate of total *Hα* radiation from the flare. Scattered light transmitted by a similar filter now in use at the High Altitude Observatory is approximately equal to *Hα* light. Hence the maximum brightness of the flare was of

the order of magnitude of the brightness of the continuum adjacent to *Hα*. From information by Ellison[17] we conclude that the effective line width was approximately 2 A.

We assumed the above estimated line width for the life of the flare. As a unit of measurement of *Hα* radiation, we used the radiation of the full solar disk in a 1 A band of the solar continuum adjacent to *Hα*. Our measurements indicate that the earth received at flare maximum a radiation of solar *Hα* energy/sec which exceeded "quiet" sun *Hα* radiation by approximately 0.008 units, or nearly 2×10^{18} ergs/sec. From the area under the integrated intensity versus time-curve we deduce that the total flare energy received in the solid angle subtended by the earth between 18:44 and 20:25 U.T., the period of principal activity of the flare, was approximately 5×10^{21} ergs, while that throughout the entire life of the flare was approximately 9×10^{21} ergs, including what might be regarded by some as the period of slow return to "normal" of the brightening in the plage left by the flare.

Some authors give flare energies in terms of the total radiation from the flare, assuming that the radiation takes place in a hemispherical solid angle. In such terms the maximum rate of radiation and the total energy radiated between 18:44 and 20:25 U.T. given above, become 1×10^{27} ergs/sec and 3×10^{30} ergs respectively. In a comparison of these values with those of other authors, it should be noted that the outer contours detected by the isophotometer lie well outside the area one would generally consider, by visual inspection, to be the area of the flare. Approximately 30 per cent of the maximum rate of radiation is contributed by the outlying plage areas thus included. If we make a 30 per cent downward correction, the maximum rate of radiation from the flare proper in *Hα* becomes approximately 1.7 times the value given by Richardson[2] for radiation from the K line for the flare of February 21, 1950, and lies directly in the range of values published by Ellison.[14]

We acknowledge with appreciation the use of films obtained during a development project supported by the Geophysics Research Directorate, Air Force Cambridge Research Center. We also acknowledge with thanks support of the Office of Naval Research in development of the isophotometer and of Research Corporation in certain other phases of the work reported here. Finally, we express appreciation to Dr. Joseph H. Rush and Dr. John W. Evans for discussions of the progress of this work.

A STUDY OF THE MOTIONS OF SOLAR PROMINENCES

LEWIS LARMORE*
Physics and Astronomy Departments, University of California, Los Angeles, California
Received February 9, 1953; revised June 8, 1953

ABSTRACT

The motions of knots of four prominences were studied from Climax films. Measurements were taken by means of a polar grid superimposed on photographic prints of each frame. The four prominences include active, eruptive, sunspot, and active-eruptive types. There are no cases of sudden velocity increase, as found by Pettit. The good detail shown by the Climax films points to a twofold explanation of the supposed first law of prominence motion. It is attributed to (1) approximations involved in curve-fitting and (2) overtaking or ambiguity of identification of the knots and streamers. A parabola approximates the time-distance diagrams to a high degree of accuracy. On this basis, average accelerations are determined graphically for 85 knots and listed for both radial and angular components. The trajectories follow closely those computed by Evans on the basis of an electromagnetic field. The force fields for knots traveling similar trajectories are found to be nearly constant with time as long as the form of the prominence is constant, but the forces apparently change when the form changes. A theory of an eruptive mechanism for prominences is suggested.

I. INTRODUCTION

For the past few years the High Altitude Observatory has made time-sequence photographs of the solar prominences as a part of the observing program. These photographs are on 35-mm motion-picture film and, when projected at normal motion-picture speeds, produce spectacular results. A detailed analysis of all the films is impractical. However, many of them are of such excellent quality and of sufficient duration that they are worth the time and effort required for an intensive study.

Early work by Pettit[1] on the knots and streamers of prominences revealed that the motions are of a peculiar type. Later work by Pettit and others[2] confirmed these results and led to the two laws of prominence motion. The two laws, particularly the second law, have been open to criticism, especially with regard to the methods of curve-fitting on which the laws are based.[3]

Although many velocities of prominence knots and streamers have been published, values of acceleration are relatively few. The films used for this study are of sufficiently small interval between exposures that, in most cases, acceleration measurements are possible, even though the time of acceleration may be of the order of a very few minutes. Later in this paper the results will be applied to a discussion of the time and space constancy of forces in the prominences.

II. EXPERIMENTAL PROCEDURE

The original time-sequence photographs from which this investigation was made were taken with the coronagraph of the (now) High Altitude Observatory, at Climax, Colorado. This particular instrument has been described elsewhere,[4] and the description will not be repeated here. The photographs were made with the light of the *Hα* line by means of an interference polarization monochromator[5] transmitting a band about 6 A wide. The

* Present address: The Rand Corporation, 1700 Main St., Santa Monica, California.

[1] *Pub. Yerkes Obs.*, **3**, 4, 1925.

[2] E. Pettit, *Ap. J.*, **78**, 9, 1932; *ibid.*, **84**, 319, 1936; R. R. McMath and E. Pettit, *Ap. J.*, **85**, 279, 1937.

[3] E.g., see H. R. Hulme, *M.N.*, **99**, 634, 1939.

[4] W. O. Roberts, *Sky and Telescope*, **4**, 3, 1945; D. H. Menzel, *Our Sun* (New York: Blakiston Co., 1949), pp. 167–77.

[5] J. W. Evans, *J. Opt. Soc. Amer.*, **39**, 229, 1949.

FIG. 1.—*a*, Prominence F-189, January 4, 1945, $18^{h}38^{m}40^{s}$ G.C.T.; *b*, prominence F-202, March 20, 1945, $16^{h}35^{m}00^{s}$ G.C.T.; *c*, prominence F-222, June 28, 1945, $15^{h}08^{m}00^{s}$ G.C.T.; *d*, prominence F-222 A, June 28, 1945, $22^{h}48^{m}30^{s}$ G.C.T.

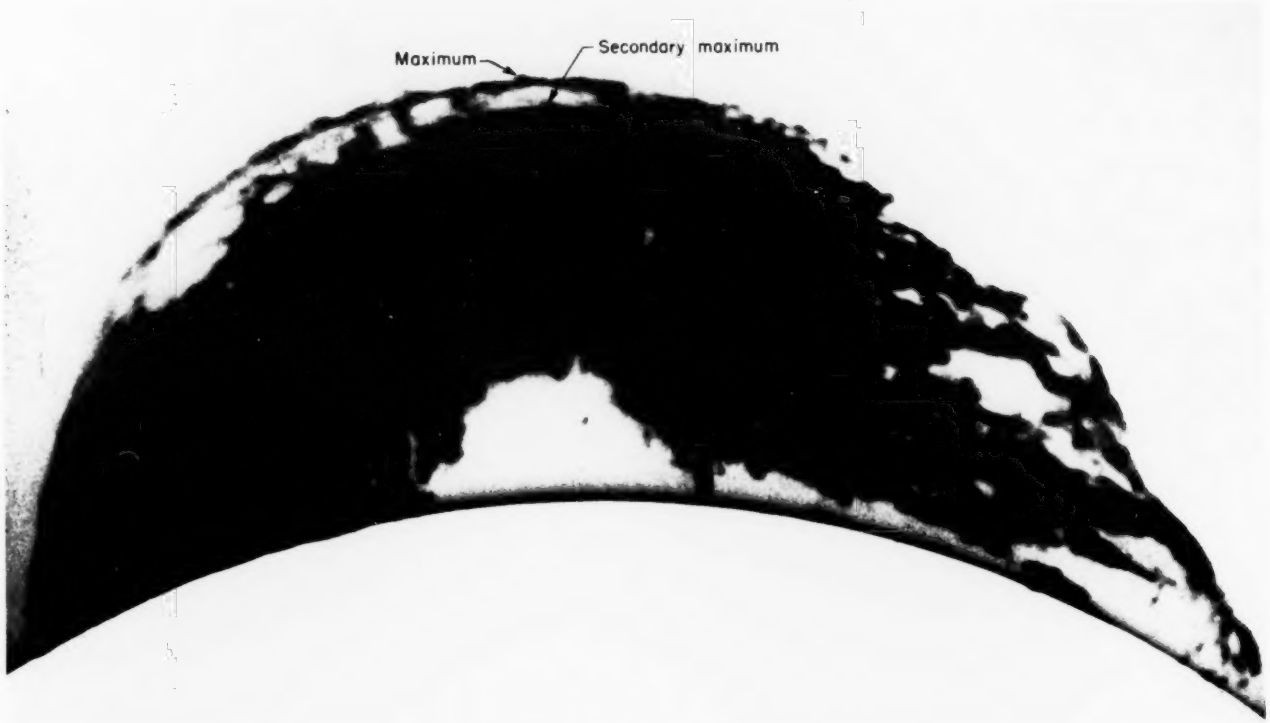

FIG. 2.—Prominence F-327, June 4, 1946, $16^{h}18^{m}00^{s}$ G.C.T.

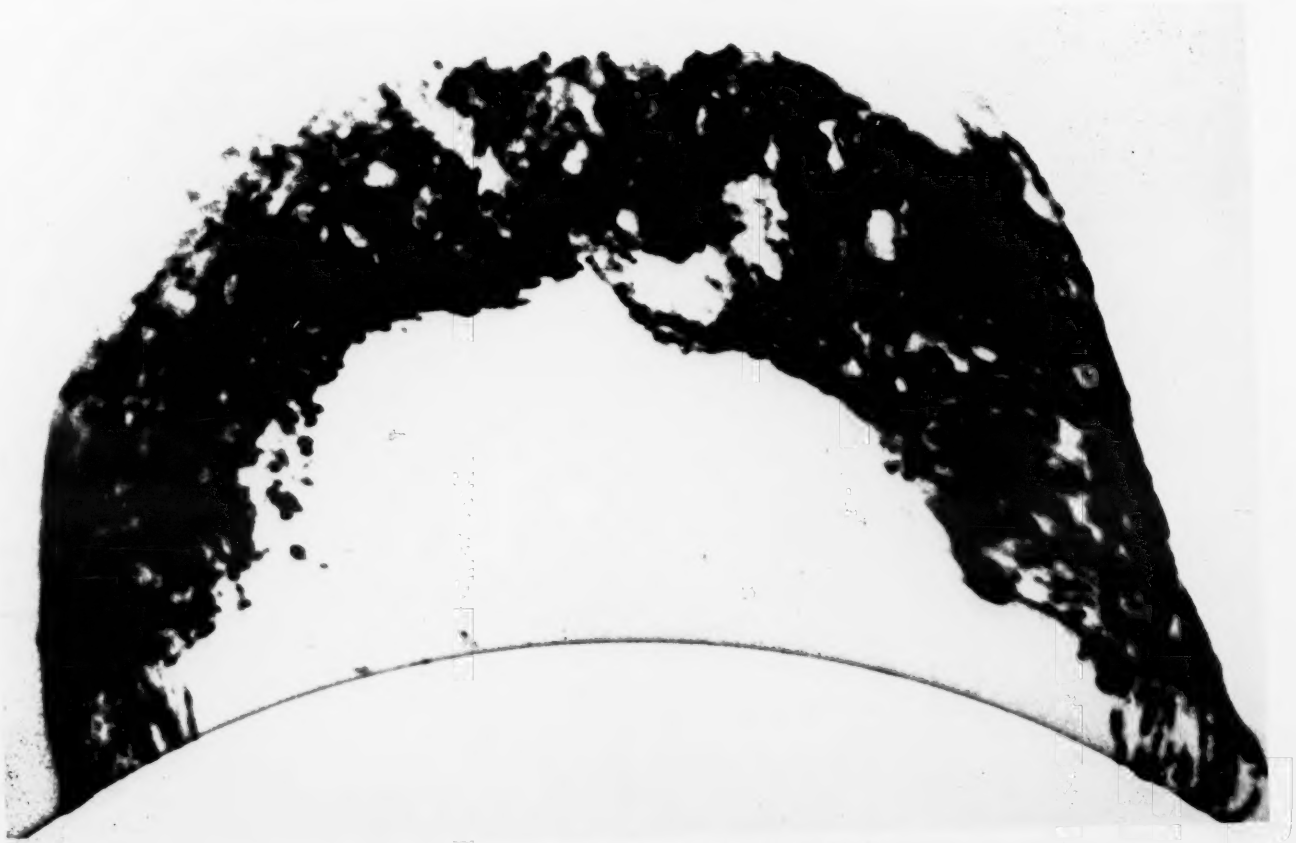

FIG. 3.—Prominence F-327, June 4, 1946, $16^{h}46^{m}00^{s}$ G.C.T.

exposures were 2 seconds long, and the interval between successive exposures could be varied from 10 seconds to 2 minutes. Both the exposure time and the intervals between exposures were controlled automatically by means of synchronous motors. The guiding mechanism for the coronagraph was a photocell electronic arrangement which controlled corrections for both right ascension and declination motions.

Previous studies of prominence motions have been carried out by projecting the negatives on a suitable screen and making measurements on the image. For this investigation, prints were made of each frame with a measuring grid superimposed upon each one. The chief advantage of making prints from each frame is that two or more frames can be viewed simultaneously, and the possibility of ambiguous knot identification is reduced.

From a practical standpoint, the prominence photographs are more easily measured in negative form than in positive. In order to obtain negative prints, positive contact transparencies were made from the negatives of several of the best prominence movies. Four of the best prominence sequences were selected from which prints were made. The four which were used are given in the accompanying tabulation.

Film No.	Date	Time of Start (G.C.T.)	Time of Stop (G.C.T.)	Frames per Min.	Apparent Position Angle
F-189	Jan. 4, 1945	18^h02^m	22^h37^m	3	115°
F-202	Mar. 20, 1945	16 20	17 10	6	90
F-222	June 28, 1945	15 05	17 13	3	225
F-222A	June 28, 1945	22 46	25 08	6	215
F-327	June 4, 1946	16 01	22 06	2	195

Figures 1, 2, and 3 show selected frames from these prominences, in order that the over-all appearance may be seen. The apparent position angle refers to the orientation of the camera on the coronagraph. It is measured from true north eastward through 360°. Thus the orientation of the center of the film was determined and the position relative to the sun computed by making the necessary correction for the inclination of the sun's axis relative to the axis of the earth.

In accordance with Pettit's classification, we note that F-189 is active, F-202 is sunspot, F-222 is active and later erupts, and F-327 is eruptive. Prominence F-327 is the largest eruptive prominence on record and has been measured by Pettit[6] from spectroheliograms made at the Mount Wilson Observatory.

The measurements of the positions of the prominence knots were done by means of polar grids with the pole at the center of the sun's image. The grids were made photographically and placed in contact with the prominence films for enlarging. The alignment of the grid produced the largest errors in the measurements. The probable error of this alignment was about 300 km.

III. THE DATA

From the four prominence films, 85 knots were found which lent themselves to reasonably accurate measurements. The positions of the knots were read directly from the prints and tabulated opposite the corresponding frame number of the film. Thus the solar position angle of the knot was determined from the position angle of the camera and a knowledge of the orientation of the north pole of the sun with respect to the north pole of the earth.

From the tabular data, the radial (R) and angular (θ) positions were plotted against frame number (proportional to time) for the 85 knots. These diagrams will not be reproduced in their entirety here, but Figure 4 shows the results for representative knots from

[6] *Pub. A.S.P.*, **58**, 310, 1946.

prominence F-327. Note that the x's refer to values for R, and the o's show positions of angle.

In order to compare results of this study with those of others, time-distance diagrams were made for motion along the trajectory. Special polar graph paper, similar to the grid but on an expanded scale, was constructed for this purpose. The positions of several knots were replotted and the trajectories determined by visual curve-fitting. Perpendicular lines were drawn from each knot position to the trajectory, and the incremental

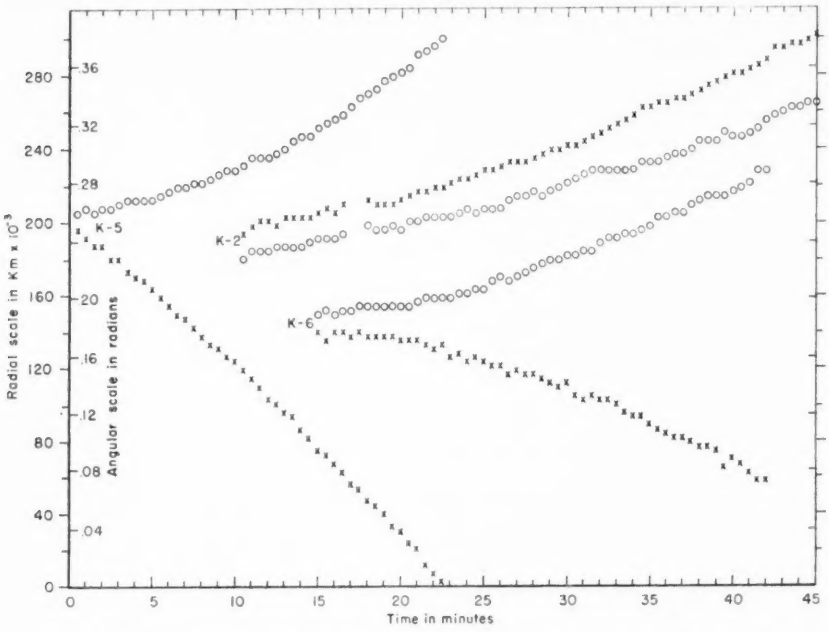

FIG. 4.—Representative R-time and θ-time graphs for F-327. The x's refer to radial positions, and the o's to angular positions. They are displaced in both time and space for convenience in plotting.

changes were measured along the path. Figure 5 shows the results of one such determination for F-327, K-5 (this knot is also shown in Fig. 4).

Besides this method for obtaining the time-distance diagrams, several of the R and θ diagrams occurred in which either R or θ was constant and gave time-distance diagrams along the trajectory directly.

VELOCITIES AND ACCELERATIONS OF THE PROMINENCES

Tables 1, 2, 3, and 4 give information concerning the motions of 85 knots selected from the four prominences. In each table the first column lists the number of the knot. This number has significance only as reference to this particular study. The second column gives the Greenwich Civil Time (G.C.T.) of the beginning of the measurement of the knot. This time generally represents the time at which the knot first became distinct enough to measure. The third column shows the length of time through which the position of the knot was measured. The rest of the columns give positions, velocities, and accelerations in R and θ. The values of the velocities and accelerations shown were deter-

mined on the assumption that the series of time-position points can be fitted to parabolas. The justification for this assumption will be given in Section IV.

The values listed were obtained graphically in the following manner. The R position of a knot at time t is given by

$$R = R_0 + \dot{R}_0 t + \frac{\ddot{R} t^2}{2}, \tag{1}$$

where R_0 is the initial position, $\dot{R}_0$ is the initial velocity in the R-direction, and $\ddot{R}$ is the (average) acceleration. Equation (1) results from the assumption that the co-ordinates are adjusted so that $t = 0$ at the beginning of the knot sequence.

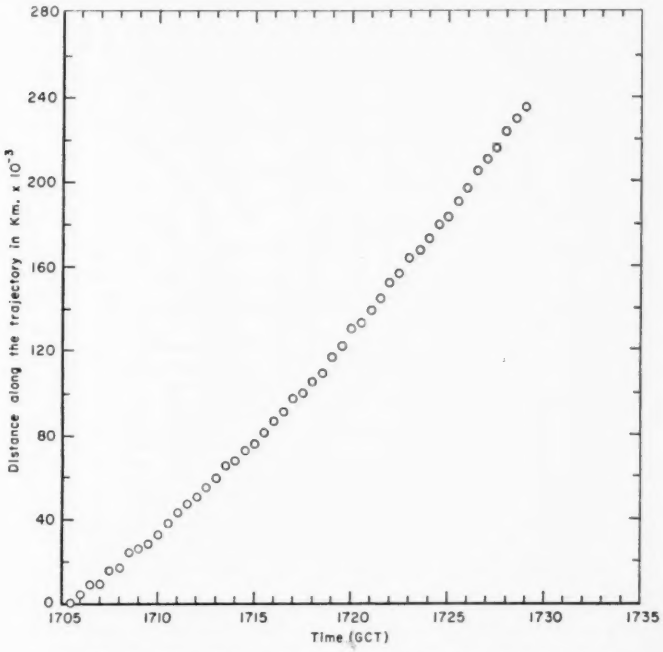

FIG. 5.—Time-distance graph along the trajectory of F-327, K-5

For a segment of a parabolic curve, the curvature is a function of the distance between the curve and a straight line joining its end-points. Let the distance between the parabola and the straight line be measured parallel to the ordinate axis at $t = \Delta t/2$ (see Fig. 6). Then, if this distance is s, the acceleration is

$$\ddot{R} = \frac{8\,s}{(\Delta t)^2}. \tag{2}$$

The initial velocity becomes

$$\dot{R}_0 = \frac{\Delta R - 4\,s}{\Delta t}, \tag{3}$$

and the final velocity is

$$\dot{R}_f = \frac{\Delta R + 4\,s}{\Delta t}, \tag{4}$$

where ΔR is the difference between the initial and final positions. The same type of analysis applies to the θ-time graphs.

The fourth to eleventh columns, inclusive, were derived from these relations and from the actual values of ΔR and s obtained by measurements of the plotted time-position diagrams.

The fourth column gives the initial height above the sun's limb in hundreds of kilometers. To convert this value to the radius vector, R_0, it is necessary to add 696,500 km to the value given. The fifth and sixth columns list the initial and final velocity components, respectively, of the knot in the R-direction in kilometers per second. Positive velocities

TABLE 1

POSITIONS, VELOCITIES, AND ACCELERATIONS OF KNOTS OF F-189

Knot No.	Time (t_0)	Δt	R_0' (Km × 10^{-2})	$\dot{R}_0$ (Km/Sec)	$\dot{R}_f$ (Km/Sec)	$\ddot{R}$ (Km/Sec²)	θ_0 (S.P.A. Degrees)	$\dot{\theta}_0$ (Rad/Sec×10^5)	$\dot{\theta}_f$ (Rad/Sec×10^5)	$\ddot{\theta}$ (Rad/Sec²×10^6)
1	18h02m00s	9m20s	708	0	− 33.1	−0.0591	125.1	−13.87	− 7.14	+11.98
2	18 05 20	18 00	395	+ 1.1	− 41.9	− .0397	108.5	+14.87	+ 9.63	− 4.84
3 A	18 02 00	18 00	685	+ 7.5	+ 7.5	0	120.1	+ 3.32	+ 5.92	+ 2.41
3 B	18 20 00	44 40	766	+ 5.0	− 17.2	− .0083	122.9	+ 1.54	+10.32	+ 3.27
4	18 07 40	12 00	464	+ 14 5	+ 14.5	0	109.3	+10.20	+ 6.94	− 4.54
5	18 20 40	24 40	743	− 0.5	− 23.1	− .0153	127.3	− 4.34	−10.37	− 4.08
6	18 46 00	5 40	464	− 62.8	−155.5	− .2726	122.0	−12.96	− 2.59	+30.50
7	18 02 00	33 20	441	0	0	0	120.4	+ 5.45	+ 7.34	+ 0.94
8	18 06 40	34 40	801	− 1.6	− 14.1	− .0060	119.5	+ 2.40	+ 7.37	+ 2.39
9	18 47 00	8 40	499	− 29.0	−118.3	− .1718	120.6	−10.74	− 3.96	+13.01
10	18 35 40	22 20	842	− 5.5	− 22.2	− .0124	126.9	− 5.91	− 6.62	− 0.52
11	18 52 20	5 00	464	−105.2	−142.3	− .1236	119.7	−11.95	− 5.68	+20.88
12 A	19 24 00	15 20	592	− 28.0	+ 0.2	+ .0307	106.6	+ 6.75	+10.82	+ 4.44
12 B	19 39 20	19 20	464	+ 5.0	− 27.0	− .0276	111.2	+ 6.41	+ 9.05	+ 2.27
13	19 59 00	4 00	267	− 72.5	− 72.5	0	116.6	+ 4.89	+ 4.89	0
14 A	19 35 20	32 20	511	− 2.8	− 10.4	− .0039	100.1	+ 6.21	+17.60	+ 5.87
14 B	20 09 40	8 40	302	− 17.4	− 67.4	− .0963	113.2	+10.18	+12.44	+ 4.34
15	20 03 20	5 40	418	− 18.4	− 2.1	+ .0480	109.9	+13.82	+ 6.92	− 2.04
16	19 32 40	17 00	546	− 8.7	− 5.0	+ .0036	105.0	+ 7.17	+15.02	+ 7.69
17	19 52 00	12 40	430	− 13.7	− 13.7	0	102.3	+12.00	+12.00	0
18	19 59 00	29 00	488	0	0	0	123.7	− 5.92	− 4.04	+ 1.08
19 A	20 01 20	6 00	534	0	0	0	100.7	+ 3.68	+ 3.68	0
19 B	20 07 20	15 00	534	− 4.9	− 23.4	− .0206	101.5	+ 8.80	+ 4.66	− 4.60
20	20 05 00	28 00	488	0	0	0	101.0	+ 5.41	+ 8.77	+ 2.00
21 A	20 19 00	10 40	569	− 18.3	+ 2.0	+ .0158	102.0	+ 6.06	+14.16	+12.64
21 B	20 29 40	10 40					105.8	+13.04	+ 7.16	− 9.19
22	20 43 00	11 40	488	+ 0.3	− 23.6	− .0341	116.7	− 3.15	−13.23	−14.41
23	20 43 00	16 20	441	− 22.5	− 22.5	0	116.0	+ 8.04	+ 0.36	− 7.86
24	20 41 20	27 00	255	0	0	0	94.1	+ 3.71	+ 7.19	+ 2.15
25	20 38 20	26 20	255	0	0	0	96.4	+ 6.13	+ 9.12	+ 1.88
26 A	20 41 20	8 20	418	0	0	0	99.2	+ 2.06	+11.47	+18.82
26 B	20 49 40	24 00	418	− 4.7	− 9.8	− .0036	101.2	+ 1.72	+ 8.90	+ 4.99
27	21 07 40	13 40	511	+ 4.2	− 63.7	− .0828	119.4	− 3.19	−11.51	−10.15
28	21 00 00	12 40	627	0	0	0	100.6	+ 2.44	+ 8.01	+ 7.33
29	21 15 40	14 20	592	− 11.6	− 18.1	− .0075	111.7	+ 4.21	+ 9.13	+ 5.72
30	21 15 00	20 20	488	− 1.5	− 13.7	− .0100	127.7	− 8.68	− 8.68	0
ETOP A	21 50 40	2 00	116	+193.5	+193.5	0	117.1	+ 8.57	+ 8.57	0
ETOP B	21 53 00	7 20	371	+226.3	+354.0	+ .2878	117.2	+ 8.75	+28.00	+43.73
E 1	22 00 00	7 20	1207	+305.7	+221.3	− .1921	120.4	+17.43	+12.63	−10.95
E 2	22 00 40	13 00	836	+178.6	+178.6	0	120.8	+14.92	+ 7.69	− 9.26
E 3	22 08 40	17 00	1648	− 65.6	−134.6	− .0678	122.4	+16.45	+ 9.51	− 6.79
E 4	22 14 20	16 00	1625	− 44.9	−134.0	−0.0926	122.6	+14.58	+ 9.93	− 4.85

are upward (away from the sun). The seventh column gives the acceleration, with positive values upward also.

The eighth column gives the initial solar position angle (S.P.A.) of the knot. This is given in degrees and is the angle measured from the point defined by the intersection of the axis of solar rotation and the northern limb of the sun; the direction of measurement is counterclockwise (through east) to the knot. The ninth and tenth columns give the

TABLE 2

POSITIONS, VELOCITIES, AND ACCELERATIONS OF KNOTS OF F-327

Knot No.	Time (t_0)	Δt	R_0' (Km × 10^{-2})	$\dot{R}_0$ (Km/Sec)	$\dot{R}_f$ (Km/Sec)	$\ddot{R}$ (Km/Sec²)	θ_0 (S.P.A. Degrees)	$\dot{\theta}_0$ (Rad/Sec × 10^5)	$\dot{\theta}_f$ (Rad/Sec × 10^5)	$\ddot{\theta}$ (Rad/Sec² × 10^5)
Max.	16h01m00s	33m30s	2171	+ 31.6	+127.5	+0.0478	208.3	0	0	0
S Max.	16 01 30	42 30	2043	+ 34.6	+119.0	+ .0329	209.2	0	0	0
1	17 02 30	18 30	1788	−143.2	−170.0	− .0241	230.0	+ 4.71	+17.00	+11.08
2	16 01 30	34 30	1939	+ 20.7	+ 84.4	+ .0307	218.3	+ 2.79	+ 7.56	+ 2.30
3	16 10 30	16 00	1857	+ 38.6	+ 38.6	0	194.2	− 4.58	− 4.58	0
4	16 01 30	19 30	1637	+ 28.8	+ 44.6	+ .0135	195.2	− 0.68	− 0.12	+ 0.96
4 A	16 11 15	9 45	.....	.....	.....	.....	200.6	− 0.05	− 0.61	− 0.96
5	17 05 30	23 30	2136	−117.8	−178.2	− .0429	229.4	+ 2.08	+17.10	+10.66
6	17 05 30	27 00	1161	− 13.8	− 89.2	− .0467	179.6	+ 2.39	+ 9.94	+ 4.67
7	17 32 30	22 00	2484	−152.7	−152.7	0	229.5	+ 3.29	+13.62	+ 7.83
8	17 23 30	17 30	2206	−137.0	−137.0	0	229.7	+ 4.81	+11.95	+ 6.83
9	17 39 00	11 30	1637	−188.0	−188.0	0	236.7	+10.49	+ 9.11	− 2.00
10	17 58 00	17 00	2531	−181.6	−255.0	− .0720	232.3	− 2.60	+ 6.64	+ 9.05
11	16 56 30	14 30	1486	+195.0	+156.9	− .0440	187.7	− 5.41	− 5.41	0
12	17 11 00	13 30	1904	−139.6	−169.2	− .0368	234.6	− 0.43	+10.57	+13.63
13	17 49 00	11 30	2090	−184.7	−211.8	− .0390	232.8	0	0	0
14	17 57 30	13 30	2647	−148.7	−217.1	− .0846	234.0	− 0.36	+ 5.44	+ 7.16
15	18 10 00	7 30	1138	−149.1	−231.7	− .1833	232.8	+ 0.39	+ 8.75	+18.60
15 A	18 17 30	2 30	255	−108.2	−108.2	0	234.0	+ 5.88	+ 5.88	0
16	18 30 30	20 00	3065	−190.0	−261.0	− .0593	232.4	− 7.84	− 5.88	+11.45
17 A	18 32 30	19 30	3204	−204.0	−204.0	0	233.0	− 4.05	+ 2.79	+ 5.85
17 B	18 52 00	10 00	813	−135.3	−135.5	0	232.5	+ 2.60	+ 5.73	+ 5.23
18	18 28 30	19 00	2554	−190.5	−216.4	− .0228	235.9	− 2.58	+ 8.78	+ 9.97
19	18 29 30	17 30	2113	−156.5	−156.5	0	237.9	+ 1.73	+ 6.66	+ 4.70
20	19 06 00	11 30	2322	−211.6	−158.0	+ .0779	235.2	+ 0.04	+ 5.50	+ 7.92
21	19 08 00	13 00	2252	−174.2	− 93.3	+ .1037	234.8	+ 1.51	+ 1.51	0
22	16 34 00	11 00	1509	+ 72.3	+117.5	+ .0681	205.5	+ 2.67	+ 2.67	0
23	16 39 00	14 00	697	+ 26.0	+167.3	+0.1684	196.1	− 5.95	− 5.95	0

TABLE 3

POSITIONS, VELOCITIES, AND ACCELERATIONS OF KNOTS OF F-202

Knot No.	Time (t_0)	Δt	R_0' (Km × 10^{-2})	$\dot{R}_0$ (Km/Sec)	$\dot{R}_f$ (Km/Sec)	$\ddot{R}$ (Km/Sec²)	θ_0 (S.P.A. Degrees)	$\dot{\theta}_0$ (Rad/Sec × 10^5)	$\dot{\theta}_f$ (Rad/Sec × 10^5)	$\ddot{\theta}$ (Rad/Sec² × 10^5)
1	16h40m00s	13m20s	232	− 2.9	− 37.7	−0.0435	115.6	−0.26	+7.97	+10.30
2 L	16 20 00	14 00	569	−34.8	− 92.4	− .0685	122.3	−6.54	−1.51	+ 6.00
2 T	16 20 00	15 40	627	− 4.7	− 52.1	− .0504	123.2	−5.23	−0.72	+ 4.80
3	16 34 40	11 20	755	− 5.1	− 32.4	− .0401	118.2	+1.34	+5.15	+ 5.61
4	16 44 00	9 20	197	−21.1	− 7.9	+ .0237	117.3	+1.89	+8.56	+12.00
5	16 40 40	12 40	232	− 5.5	− 25.1	− .0258	104.8	+1.47	+7.04	+ 7.33
6	16 31 00	12 20	720	−20.7	−111.0	−0.1221	120.6	−4.41	+0.04	+ 6.01

TABLE 4

POSITIONS, VELOCITIES, AND ACCELERATIONS OF KNOTS OF F-222 AND F-222A

KNOT NO.	TIME (t_0)	Δt	R_0' (KM × 10^{-2})	$\dot{R}_0$ (KM/SEC)	$\dot{R}_f$ (KM/SEC)	$\ddot{R}$ (KM/SEC^2)	θ_0 (S.P.A. DEGREES)	$\dot{\theta}_0$ (RAD/SEC × 10^5)	$\dot{\theta}_f$ (RAD/SEC × 10^5)	$\ddot{\theta}$ (RAD/SEC^2 × 10^8)
	F-222									
1	15^{h}14^{m}20^s	10^{m}00^s	662	− 8.9	−49.1	−0.0670	229.3	+11.61	+ 8.48	− 5.23
3	15 05 00	21 40	325	0	0	0	222.8	+ 3.79	+ 3.79	0
4	15 05 00	6 40	697	−26.1	−26.1	0	213.8	0	0	0
5	15 05 00	50 00	882	+ 5.9	−27.5	− .0111	223.4	+ 0.65	+ 3.47	+ 0.94
6	15 13 00	22 40	952	−15.4	− 1.7	− .0100	216.1	− 0.69	− 2.76	− 1.53
7	15 05 00	38 40	940	− 4.1	−16.9	− .0055	216.3	− 0.43	− 2.86	− 1.05
8	15 26 20	27 20	534	+ 3.1	−28.5	− .0194	223.4	+ 2.87	+ 4.31	+ 0.88
10	15 05 00	38 40	348	+ 1.8	−15.8	− .0076	240.6	+ 1.98	− 4.52	− 2.80
15	16 04 20	17 20	395	−13.4	−13.4	0	248.0	+ 1.98	+ 1.98	0
17	16 59 00	12 00	673	+ 1.6	−50.3	− .0722	229.3	+ 5.67	+ 8.62	+ 4.08
18	16 58 20	11 20	720	− 2.1	−73.0	− .1044	227.2	+ 4.75	+11.68	+10.17
19	16 57 00	10 40	255	− 2.2	−48.6	−0.0725	226.7	+ 3.40	+12.23	+13.80
20	16 57 40	44 40	929	0	0	0	222.9	+ 0.99	+ 2.74	+ 0.65
	F-222A									
1	22 54 00	10 00	871	−24.3	−80.1	−0.0928	219.7	0	− 3.91	− 6.53
2	22 52 40	9 20	813	−31.5	−84.5	− .0947	219.3	− 0.42	− 5.88	− 9.77
3	22 46 40	22 00	1904	+48.9	+32.0	− .0128	215.0	+ 2.65	+ 3.37	+ 0.54
4	22 46 40	9 20	673	−18.7	−18.7	0	224.2	− 3.05	− 4.31	− 2.25
5	23 14 00	10 00	534	+34.8	+65.8	+ .0520	210.1	+ 0.79	− 0.79	− 2.61
6	23 10 00	13 20	2391	+17.4	+63.8	+ .0580	218.8	+ 6.69	+ 8.76	+ 2.57
7	22 46 40	22 00	1834	+10.3	+17.6	+ .0055	224.0	+ 6.54	+ 9.04	+ 1.90
8	23 10 00	14 00	2008	−18.0	−84.2	− .0789	230.6	+ 9.00	+12.35	+ 4.00
9	22 58 40	18 00	1927	+18.9	+24.1	+0.0048	224.6	+ 4.57	+10.68	+ 5.65

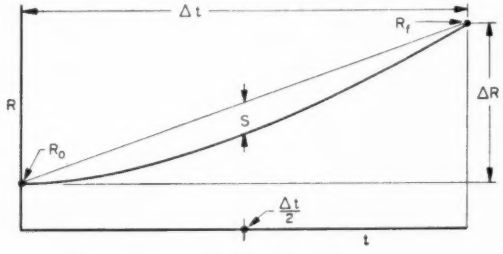

FIG. 6

initial and final angular-velocity components in radians per second. Positive values indicate velocities in increasing (counterclockwise) solar position angle. The eleventh column lists angular acceleration in radians per second squared, directed also with positive values counterclockwise.

To convert the angular velocities and accelerations as given to tangential velocities and accelerations in kilometers per second and kilometers per second squared, it is necessary to multiply the values listed by the instantaneous value of the distance from the center of the sun. This latter value can be determined with the aid of the fourth, fifth, and sixth columns. An order-of-magnitude estimate can be made by taking the number listed (disregarding the power of 10 at the top of the ninth or tenth column) for the angular velocity and multiplying it by 10. For angular acceleration, set the decimal point over two places to the left in the eleventh column. The result will be generally about 25 per cent too high for the proper value of kilometers per second or kilometers per second squared.

From the data in Tables 1, 2, 3, and 4, the velocity along the trajectory, $\dot{S}$, may be found from

$$\dot{S} = \sqrt{\dot{R}^2 + R^2\dot{\theta}^2}\,. \tag{5}$$

The acceleration along the trajectory becomes

$$\ddot{S} = \frac{\dot{R}\ddot{R} + R^2\dot{\theta}\ddot{\theta} + R\dot{R}\dot{\theta}^2}{\sqrt{\dot{R}^2 + R^2\dot{\theta}^2}}\,. \tag{6}$$

RELIABILITY OF TABLES 1, 2, 3, AND 4

Equations (5) and (6) show that the velocity along the trajectory is not a linear function of time and that the acceleration is not constant. This result is not significant, since it reflects only the co-ordinate system chosen and the method of reduction of the observations. There is no more justification for assuming parabolic curves in R and θ than there would be in assuming parabolic curves for the time-distance graphs along the trajectory. Referring to Figure 5, we see that this graph can be represented by a parabola just as well as the R and θ time graphs can. A somewhat easier method of obtaining the acceleration along the trajectory is to find the initial and final velocities from equation (1). The acceleration then is

$$\ddot{S} = \frac{\dot{S}_f - \dot{S}_0}{\Delta t}\,. \tag{7}$$

Good agreement is obtained between the above method of finding velocities and accelerations and the method of replotting the positions to determine the time-distance diagrams along the trajectory. Referring again to F-327, K-5 (see Figs. 5 and 6), we find from equations (5) and (7), with values from Table 2,

$$\dot{S}_0 = 119 \text{ km/sec}, \qquad \dot{S}_f = 215 \text{ km/sec}, \qquad \ddot{S} = 0.068 \text{ km/sec}^2.$$

Measurements on Figure 6 for s and ΔR give

$$\dot{S}_0 = 117 \text{ km/sec}, \qquad \dot{S}_f = 214 \text{ km/sec}, \qquad \ddot{S} = 0.070 \text{ km/sec}^2.$$

On the basis of estimates made by comparing least-squares solutions with the graphical method, the probable errors are as follows:

$$\dot{R} = \pm\frac{2000}{\Delta t} \text{ km/sec}, \qquad \ddot{R} = \pm\frac{4000}{(\Delta t)^2} \text{ km/sec}^2,$$

$$\dot{\theta} = \pm\frac{0.002}{\Delta t} \text{ rad/sec}, \qquad \ddot{\theta} = \pm\frac{0.004}{(\Delta t)^2} \text{ rad/sec}^2.$$

The accuracy of the fourth column, marked R_0', is correct to the nearest 1000 km. The eighth column gives values of θ_0 which are accurate to the nearest 0°.1.

IV. DISCUSSION OF DATA

PETTIT'S LAWS

The results of this study show no basis for the validity of either of Pettit's laws of prominence motion. For example, the maximum height of F-327 ("Max." in Table 2) gives a smooth curve when plotted against time. A comparison between the time-height graph as approximated by a parabola and that approximated by three straight lines is shown in Figure 7. The sum of the squares of the residuals is about 10 per cent smaller for the parabola than for the three straight lines, and the distribution of the residuals is more nearly random for the parabola. F-327 has been measured by Pettit from spectro-

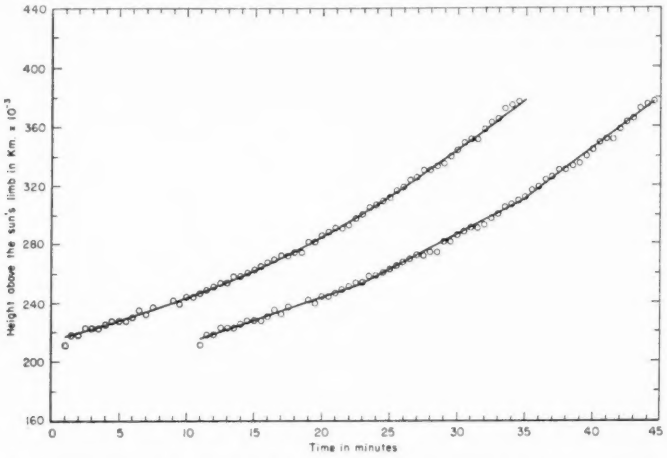

FIG. 7.—Comparison of parabola and three straight lines fitted to the time-height graph of the maximum height of F-327.

heliograms of the Mount Wilson Observatory. He finds uniform velocity with one sudden acceleration. The first uniform velocity covers the entire time period presented in Figure 7. The apparent discrepancy between the two is probably due to lack of a sufficient number of photographs obtained at Mount Wilson for this time interval.

The extensive discussion of solar prominences by Pan Puh[7] shows, principally from a statistical standpoint, the invalidity of Pettit's laws, and it is essentially in agreement with the results of the study presented here.

One effect which gives rise to the type of motion found by Pettit and others results from "grid resonance." For example, the parabola

$$S = 0.05 + 0.025t + 0.0015625t^2, \tag{8}$$

corrected to the nearest grid unit, gives the graph shown in Figure 8. The left-hand graph compares the plotted points with the original parabolic segment, while the right-hand graph compares the points with three straight lines. These three straight lines follow both of Pettit's laws. In this case the sum of the squares of the residuals is also smaller for the parabola.

[7] *Ann. Obs. Paris*, **8**, 4, 1939.

Overtaking of one knot by another leads to the type of sudden velocity increases described by the first law. In F-189 an ejection from the limb of the sun occurred. The measurements of the motion of this ejection are designated with the prefix "E" in Table 1. The leading edge of this ejection is marked "ETOP" and divided into two parts, A and B. The complete time-distance curve of ETOP shows a sudden velocity increase of the type described by Pettit. However, at the time of the sudden increase, one part of the ejection overtook another part, so that the acceleration was not real. No cases of real sudden velocity increases were found in the 85 knots of this study.

APPARENT SUDDEN VELOCITY DECREASES

As examination of Tables 1 and 2 reveals ten knots which have been designated A or A and B. In five of these cases the distinction has been made because the parabolic approximation did not seem tenable throughout the life of the knot. For these five cases there were no sudden changes in velocity, but the inclusion of a t^3 term was indicated.

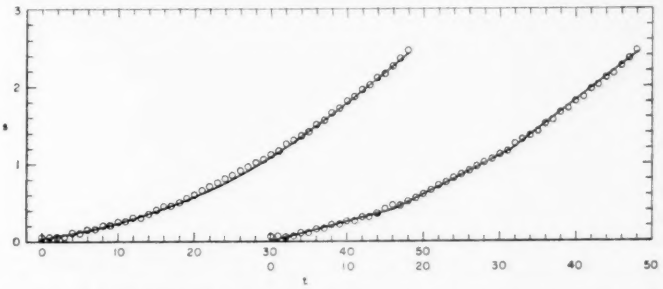

FIG. 8.—*Left curve:* the parabola $S = 0.05 + 0.025t + 0.0015625t^2$ and the points corrected to the nearest measurable unit. *Right curve:* the same points as in the left curve but approximated by three straight lines.

However, the other five showed an apparent sudden velocity change. These five are: F-189; K-3, K-26, and ETOP; F-327; K-17; and K-15. Of these five, only F-189 ETOP (the leading edge of the ejection) showed an increase in velocity. This has already been explained as the overtaking of one part by another. F-189, K-3, and K-26 had an apparent sudden decrease in $\dot{\theta}$, while the R-curve was smooth. F-327, K-15, and K-17 showed apparent suddent decreases in $\dot{R}$, while the θ-curve remained relatively smooth. As yet, no completely satisfactory explanation for these apparent sudden velocity decreases has been found. However, it is significant that no sudden velocity increases were found. As an example, Figure 9 shows the time-distance graph along the trajectory for F-327, K-17. The decrease in velocity occurs at about 18^h53^m G.C.T.

Of these four apparent sudden decreases in velocity, none occurred at the same place or at the same time. A possible explanation for this effect is that it is due to a change in the region of excitation. K-17, for example, changed its form slightly during the period of velocity change.

There is evidence to support the argument that some of the observed phenomena associated with prominence motions are the result of varying regions of excitation. Undoubtedly, there is real motion combined with changes in regions of excitation taking place simultaneously. The following three observational facts bear this out: (1) Doppler displacements, observed from spectra, of the knots and streamers as well as of the main body of prominences indicate actual motion of material. (2) Occasionally the Doppler displacements show violent large-scale turbulent motions of a region, but the time-sequence pictures of the same region show almost no change in form. (3) When knots break

away from a major portion of a prominence, the knots disappear within a short time in the majority of cases. The reverse is true when knots approach the sun's surface or major portion of a prominence.

FORCE-FIELD STUDY

During the later stages of F-327, material appeared from heights as much as 300,000 km above the limb of the sun and streamed down toward the limb between solar position angles 230° and 241°. The paths of thirteen descending knots in this region are shown in Figure 10. There are three cases in which two knots follow very closely the same paths. These pairs are K-1 and K-5, K-7 and K-8, K-17 and K-10. The heights of these pairs plotted against time give the curves shown in Figure 11. In this diagram the pairs of knots have been displaced along the time scale to give the best overlap according to

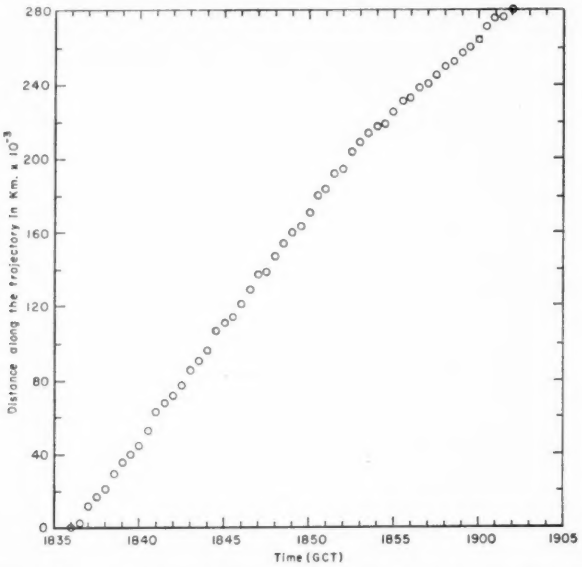

FIG. 9.—Time-distance graph along the trajectory of F-327, K-17. Note sudden decrease of velocity at 18^h54^m G.C.T.

height. The overlap of K-5 and K-1 is extremely good and, even though the acceleration is small, indicates that the components of the force fields in a plane perpendicular to the line of sight were practically identical. The time lag between the two descents was 2.5 minutes. For the pair K-7 and K-8 the superposition is not so well defined as in the previous case, but the acceleration for each knot was small. Here, the time lag was 3.5 minutes. The descent of K-17 and K-10 presents the worst agreement of all, especially during the time when they were near the sun's limb. K-10 descended 40 minutes before K-17.

Table 5 lists the accelerations of these six knots, giving $\ddot{R}$ and $\ddot{\theta}$ directly from Table 2, while $\ddot{S}$ has been computed in the manner previously described. The agreement between the accelerations is good for the pairs which descended with a small time interval between them, but for the pair K-10 and K-17 A the accelerations are significantly different.

A grouping based on the slopes of the various paths (Fig. 10) shows the descending knots resolved into two groups. K-1, K-5, K-7, and K-8 form one group, and the rest

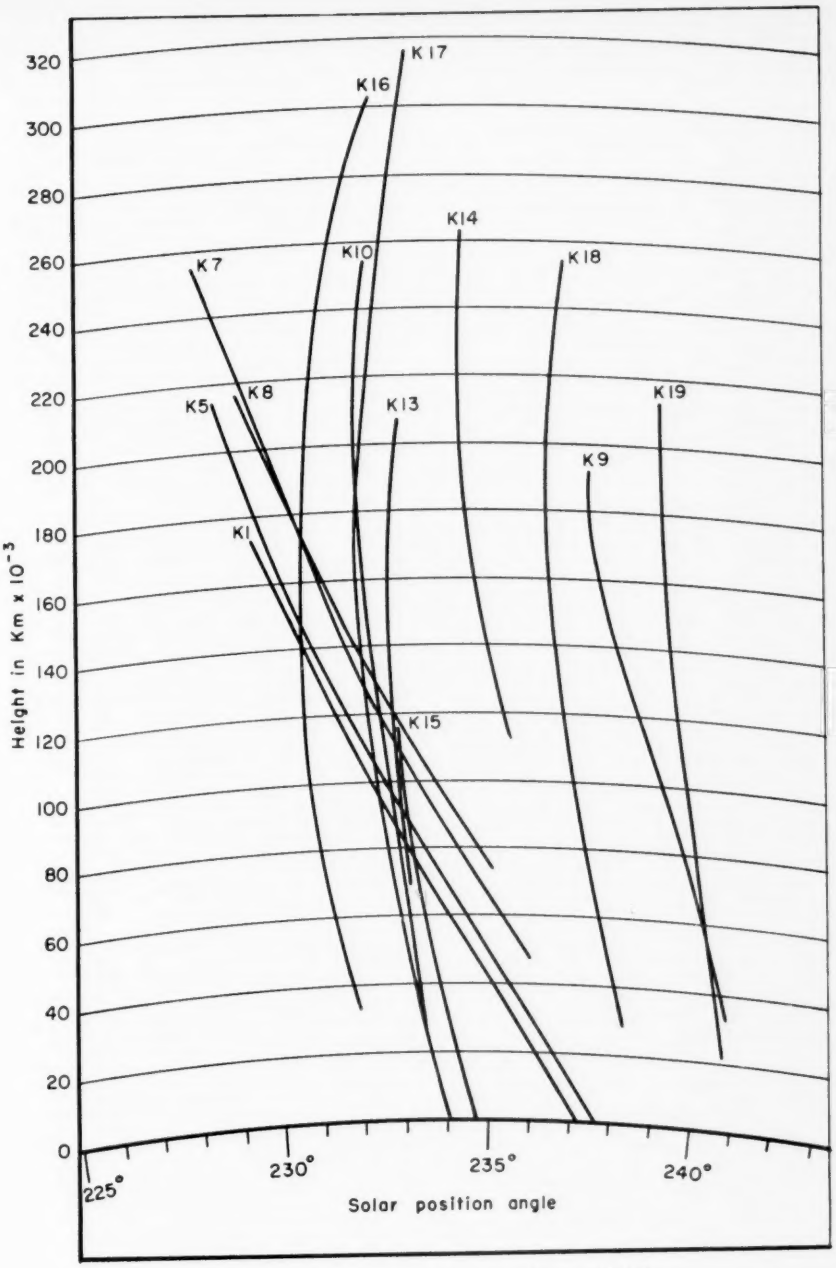

FIG. 10.—Trajectories of descending knots of F-327

form another, with the exception of K-9, which seems to be between the two groups. From a time-of-descent standpoint, the K-1 to K-8 group started descent during the interval 17^h02^m to 17^h32^m G.C.T., while the second group started descent during the interval 17^h49^m to 18^h29^m. The knot K-9 was descending in between the two groups 17^h39^m to 17^h50^m. Thus the trajectories as well as the forces changed during an interval of about 40 minutes.

An analysis of F-189 shows that the forces apparently change with time also, though not nearly so rapidly as for F-329. For example, K-24 and K-25 have a common trajec-

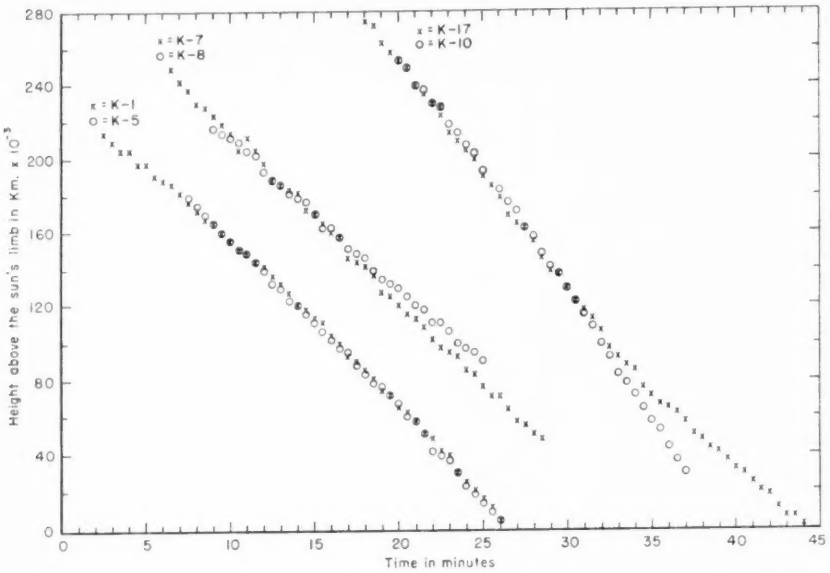

FIG. 11.—Time-height graphs of F-327 for pairs of knots following almost the same trajectories. These are displaced in time to give the best overlap for each pair (cf. Fig. 10).

TABLE 5

ACCELERATIONS FOR THREE PAIRS OF KNOTS WITH ALMOST IDENTICAL TRAJECTORIES OF F-329

Knot No.	$\ddot{R}$ (Km/Sec²)	$\ddot{\theta}$ (Rad/Sec² $\times 10^8$)	$\ddot{S}$ (Km/Sec²)	Time Interval between Descents (Min.)
1.....	−0.024	+11.1	+0.053	2.5
5.....	−0.043	+10.7	+ .068	
7.....	0	+ 7.8	+ .020	3.5
8.....	0	+ 6.8	+ .016	
17 A.....	−0.072	+ 9.1	− .002	40.0
10.....	0	+ 5.8	+0.077	

tory throughout most of the motion. K-24 followed K-25 by about 14 minutes. The $\ddot{R}$-component was zero in both cases, and $\ddot{\theta}$ was -2.15×10^{-8} radians per second squared for K-24 and -1.88×10^{-8} for K-25. No satisfactory example was found of knots following the same trajectory with a very large time interval between them. This is a result of the fact that the whole appearance of the prominence changed over a long period of time and presumably the force field changed with it.

A study by Dodson[8] of an active prominence shows a relationship among nine knots moving with similar trajectories. The knots studied streamed downward from a source about 100,000 km above the sun's limb and occurred during a period of slightly over 2 hours. Dodson was able to show a similarity in velocities and accelerations which indicated a fairly stable force field. On the basis of the two prominences discussed above and the one by Dodson, it appears that the force fields of active prominences change slowly with time but that those of eruptive prominences change appreciably within a period of less than 1 hour.

An idea of the magnitude of the forces involved may be obtained by noting that the gravitational acceleration at the sun's surface is -0.273 km/sec^2. Referring to the maximum height of F-327, for example, the residuals were such that a t^3 term with a small positive coefficient would fit the observations slightly better than the parabola did. This is the same type of correction as that necessary to account for the decreasing gravitational attraction at increasing distance from the sun. At $R_0' = 217{,}500$ km, the height of the prominence at the beginning of the sequence, the gravitational acceleration is -0.159 km/sec^2. At the end of the sequence the maximum height was $R_f' = 378{,}000$ km, and the gravitational acceleration at this point is -0.115 km/sec^2. This decrease in gravitational force is more than enough to account for the slight upward increase in acceleration. Therefore, whatever force was actually pushing the prominence material upward must also have decreased in magnitude with increasing height, but at a slightly slower rate than the gravitational force. The average force upward on the material, excluding gravity, was sufficient to produce an average acceleration of $+0.181$ km/sec^2.

An examination of the radial accelerations in Tables 1, 2, 3, and 4 reveals that there are far more negative than positive values. If the acceleration of gravity is subtracted, all values are positive. In the earth's atmosphere a freely falling object undergoes a negative (downward) acceleration until it reaches its terminal velocity. However, it is generally assumed that the corona is so tenuous that its resistance to motion is negligible. Furthermore, such a resistance does not account for upward accelerations on knots which are moving upward. The action of a magnetic field on charged particles of the prominences could account for many of the observed effects, and it is generally recognized that magnetic fields play an important role in the motions of the prominences.[9]

COMPARISON OF RESULTS WITH THEORY

The forces which we would expect to find acting on the solar prominences are those of radiation pressure, hydrodynamics, electrostatics, gravitation, and electromagnetism. The forces of radiation pressure have been studied by Milne and others. The conclusion is that the radiation pressure is simply not great enough to supply the prominences with sufficient force to compare with the gravitational attraction.

We may obtain an order-of-magnitude estimate of the accelerations caused by hydrodynamic forces by considering a spherical knot which breaks off the main body of a prominence. Such a knot would experience an acceleration of

$$a = \frac{3\Delta P}{4\rho r},$$

[8] *M.N.*, **108**, 390, 1948.

[9] D. S. Evans, *M.N.*, **106**, 300–337, 1946.

where ΔP is the pressure difference between the prominence and the corona, ρ is the density of the knot, and r is the radius of the knot. Putting

$$\Delta P = 1 \text{ dyne/cm}^2, \qquad \rho = 4 \times 10^{-11} \text{ gm/cm}^3, \qquad \text{and} \qquad r = 2.5 \times 10^8 \text{ cm}$$

for an average knot yields an acceleration of 75×10^{-5} km/sec^2. This value is of the order of a hundred times smaller than accelerations observed in Tables 1, 2, 3, and 4. Thus we may conclude that hydrodynamic forces are not the predominating ones. This conclusion is in agreement with that of Evans,[9] who based his work on the velocity of sound in the solar atmosphere.

Electrostatic and electromagnetic forces in the prominences have been studied in detail by Evans.[9] His results show that electrostatic forces will be important in two ways. First, knots and streamers will be repelled from the main body of a prominence even when there is only a very small excess of positive or negative charge within the prominence. This effect gives rise to the same kind of motion as that of a pressure difference previously mentioned. Second, the electrostatic forces are large enough to support the ionized gases against the force of gravity. Such a support is necessary for an explanation of the longevity of many of the prominences. In the first instance we are considering electrostatic forces within the prominence, and in the second we are considering background electrostatic forces.

The principal role of electromagnetic forces has been that of determining the trajectories for the moving material. Charged particles in a magnetic field move with a helical motion, progressing in the direction of the field but with a circular path around the lines of magnetic flux. We make the assumption that the diameter of the circular path is too small to measure, and thus we see only the progressive motion.

Evans has computed trajectories of charged particles for various assumed dipole orientations. Some prominences seem to follow paths which indicate that the dipole axis is tangent to the sun's surface, while others show that the dipole axis is perpendicular. An analysis of the paths from F-327 (Fig. 10) shows that the projection of the dipole axis was nearly perpendicular to the limb of the sun. However, for the first group of knots (K-1, K-5, K-7, and K-8) the upper part of the dipole axis was inclined toward the south pole of the sun, that is, to the left in Figure 10. The second group shows the dipole axis nearly perpendicular to the limb. Thus the dipole apparently "straightened up" during the later stages of the prominence. Mount Wilson spectroheliograms taken of the surface of the sun show that this prominence existed for at least 4 days with little change in form. Then, rather suddenly, it erupted on June 4, 1946. A similar phenomenon occurred for F-222 and has been noticed on many other eruptive prominences.

Consider, now, the magnetic field associated with two dipoles, oriented as shown in Figure 12. If one or both dipoles should straighten up, that is, orient themselves so that they are more nearly perpendicular to the sun's limb, the lines of magnetic flux would apparently expand outward, away from the sun. The effect on a charged particle in this field can be found by considering the equation of motion of a charged particle in a magnetic field:

$$\vec{a} = \frac{Q}{m}(\vec{V} \times \vec{B}), \tag{9}$$

where $\vec{a}$ is the acceleration of the particle, Q its positive charge, m its mass, and $\vec{V}$ its velocity with respect to the magnetic flux density $\vec{B}$. For convenience, we will take $\vec{B}$ to be uniform in the y-direction, and the magnetic field moving in the z-direction (upward) with a velocity of V_B, in the usual set of right-handed Cartesian co-ordinates.

Under a Lorentz transformation for velocities small compared with the velocity of light, equation (9) has the solution[10]

$$x' = \frac{V_B m}{BQ}\left[1 - \cos\left(\frac{BQt}{m}\right)\right], \tag{10}$$

$$z' = V_B t - \frac{V_B m}{BQ}\sin\left(\frac{BQt}{m}\right), \tag{11}$$

where x' and z' are the co-ordinates of the charged particle in reference to the sun. The boundary conditions assumed for this solution were that the charged particle was at rest at the origin when $t = 0$. Equations (10) and (11) are those of a cycloid in the x, z-plane. An initial velocity in the y-direction would give a helical cycloid. Thus we see that a particle charged either positively or negatively would be dragged upward with the magnetic field and, in the absence of other forces, would have the same average velocity as the moving magnetic field.

If the magnetic flux density were 1 gauss (10^{-4} webers per square meter), the period of the cycloid for a proton would be less than a thousandth of a second, and the radius

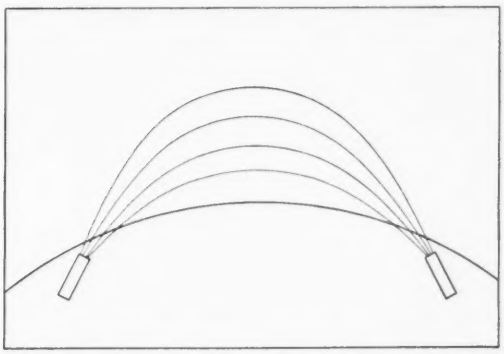

FIG. 12.—Suggested dipole orientation before eruption of F-327

of the "circle of reference" would be about 10 meters. These are obviously far too small to be detected in the measurements of this study. Even for a field of 1 gauss, the electromagnetic forces are still more than a million times greater than the gravitational force.

A study of the literature failed to reveal the above effect mentioned as a possible mechanism for the eruption of prominences. Observational substantiation comes from both the eruptive prominences which were included in this study. F-327 gives evidence because the slopes of the two groups of paths change with time, indicating an apparent change in orientation of the dipole as the prominence material "slid" down the magnetic lines of force. F-222 is an active prominence in which material is flowing from one part to another. As time elapses, the trajectories of the knots gradually progress to higher and higher positions of an arch form. If we assume that the trajectories represent magnetic lines of flux, then there is an expanding magnetic field of the type described.

V. SUMMARY AND CONCLUSIONS

The detailed two-dimensional study of the four prominences used in this investigation has yielded several significant results. There was no substantiation found for the laws of

[10] See, e.g., J. A. Stratton, *Electromagnetic Theory* (New York: McGraw-Hill Book Co., 1941), p. 79.

prominence motion. The observations show an absence of extremely large accelerations, as required by the first law. Accelerations of the knots were essentially uniform in most cases. The results indicated that prominences which do not change form rapidly have a force field essentially constant with time. However, for those prominences which change form rapidly, the forces change with time also.

The different types of prominences have similar R-time and θ-time diagrams. Noticeable differences occurred during periods of eruption or ejection of material, when upward accelerations predominated slightly. During periods of normal activity, downward accelerations far outnumbered the upward ones, but all accelerations were upward after allowance for gravity. Prominences which changed form rapidly were characterized by higher accelerations during the time they were changing form.

The results agree well with those predicted by Evans from a theoretical study of motions of charged particles in a magnetic field. The eruptive mechanism suggested is based on the change of trajectories of the eruptive prominences included in this study, as well as other eruptive arch prominences.

It is a pleasure to acknowledge the co-operation of Dr. W. O. Roberts, of the High Altitude Observatory. Also, I wish to thank Dr. D. M. Popper, of the Department of Astronomy at the University of California, Los Angeles, for many helpful suggestions and discussions during the course of this investigation. I wish to acknowledge my appreciation to members of the Physics Department of the University of California, Los Angeles, for providing facilities and equipment necessary for the reduction of the observations.

THE SPECTRUM OF CHI CYGNI NEAR MINIMUM LIGHT

PAUL W. MERRILL

MOUNT WILSON AND PALOMAR OBSERVATORIES
CARNEGIE INSTITUTION OF WASHINGTON
CALIFORNIA INSTITUTE OF TECHNOLOGY

Received May 18, 1953

ABSTRACT

Long-exposure spectrograms chiefly by I. S. Bowen with the 200-inch telescope show the extraordinary behavior of the rich bright-line spectrum of the long-period variable χ Cygni near minimum light. Of 60 bright lines whose intensities increase markedly during the two months preceding minimum, one-third are forbidden lines of *Fe* II, two-thirds are unidentified. Differences in radial velocity between various groups of lines and between plates at various phases are small. A few suggestions for future observations are included.

The variable star χ Cygni, period 406 days, is famous for its great changes in brightness, the mean range in visual magnitude being from 5.3 to 13.3, with reported extremes of 2.3 and 14.3. Its absorption spectrum combines characteristics of classes M and S. At most phases of the light-cycle, numerous bright lines are conspicuous on the spectrograms; their behavior illustrates the general rule concerning long-period variables, that the greater the amplitude of light-variation, the more intense are the bright lines.

TABLE 1

SPECTROGRAMS OF χ CYGNI

PLATE	OBSERVER	DATE	JD 243	VIS. MAG.	PHASE (DAYS)		EXPOSURE (HOURS)	DISP. (A/MM)
					From Max.	From Min.		
Ce 3505	P. W. M.	1944 July 10–11	1282	11.4	+162	−76	13.2	10
Pc 67	I. S. B.	1951 Mar. 22	3728	11.1	+155	−87	3.7	9
Pd 82	O. C. W.	Apr. 14	3751	12.1	+178	−64	3.7	18
Pd 91	I. S. B.	May 12	3779	13.1	+206	−36	3.4	18
Pd 93	I. S. B.	May 15–17	3783	13.1	+210	−32	19.3	18
Pd 113	I. S. B.	June 23–25	3822	13.0	+249	+ 7	23.1	18
Pe 356	I. S. B.	1952 June 30	4194	13.3	+217	−18	7.0	38

Low-dispersion spectrograms obtained with the 100-inch telescope in October, 1935, just before minimum light showed several individual bright lines and, in addition, a few emission patches of bright lines hopelessly blended.[1] Spectrograms with higher dispersion obtained in 1944 during the postmaximum phase disclosed a rich bright-line spectrum, including some conspicuous lines that could not be identified.[2]

During the spring of 1951, I. S. Bowen and O. C. Wilson obtained with the 200-inch telescope a number of spectrograms near the minimum phase, and in June, 1952, Dr. Bowen obtained an additional plate (see Table 1 and Fig. 1). My best thanks go to these observers for placing their long-exposure photographs at my disposal. The photometric data were kindly supplied by Mrs. Margaret Mayall, of the Harvard Observatory.

[1] P. W. Merrill, *Mt. W. Contr.*, No. 539; *Ap. J.*, **83**, 272, 1936.

[2] P. W. Merrill, *Mt. W. Contr.*, No. 735; *Ap. J.*, **106**, 274, 1947.

Because the medium-dispersion Pd plates were taken before the adjustments of the coudé spectrograph were completed, the definition is imperfect, being decidedly inferior to that attained later. The strongly exposed low-dispersion plate Pe 356 is sharp from λ 3760 to λ 4400.

Data derived from the 100-inch plate Ce 3505 have already been published.[2] The new spectrograms, besides showing the general behavior nearer minimum light, provide more accurate wave lengths for many of the bright lines in the previous list and yield 24 additional lines, about half of them unidentified.

The chief bright lines measured in the spectrum toward the phase of minimum light are listed in Table 2. The wave lengths are mean values from several plates, including Ce 3505. For each plate the measured wave lengths were corrected for the radial velocity derived from the lines of [*Fe* II]; if the mean velocity from all bright lines had been used, the resulting wave lengths would have been algebraically higher by about 0.02 A. For the identified lines, the mean residuals from laboratory wave lengths, regardless of sign,

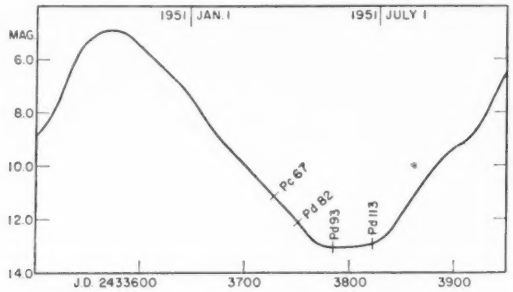

FIG. 1.—Light-curve of χ Cygni showing dates of spectrograms in 1951

are 0.05 and 0.04 A for neutral and ionized lines, respectively. These residuals include, in addition to errors of measurement, displacements intrinsic in the stellar spectrum caused by blending, adjacent absorption lines, etc. For additional lines measured during the postmaximum phase see Table 13 in *Mount Wilson Contributions*, No. 735.[2]

Cursory descriptions of the behavior of various lines with respect to phase in the light-cycle are given by the symbols in the third column of Table 2 and by a few remarks at the end of the table. A portion of plate Pd 93 is shown in Figure 2. The following notes concern certain interesting changes between plates Pd 93 and Pd 113 taken, respectively, near the beginning and near the end of the flat portion of the light-curve at minimum (Fig. 1):

Lines of [*Fe* II] and numerous unidentified lines remain of the same intensity or are somewhat strengthened on the later plate. Nearly all lines of *Fe* I are weakened by a factor of about 2; certain ones more greatly weakened are λλ 3852, 3950, 3977, 4206. The displaced emission portions of the *Ca* II lines λ 3933 and λ 3968 and of the *Al* I lines λ 3944 and λ 3961 are greatly weakened. Perhaps most notable of all is the marked weakening of the *Mn* I lines λλ 4030, 4033, and 4034, and of the *Ga* I line λ 4172. This simultaneous weakening tends to confirm my previous suggestion[2] that the gallium line is fluorescent, the exciting line being one of the manganese lines. A special study of the behavior of these lines in the spectra of several long-period variables has just been published.[3]

An extremely interesting group of lines in Table 2 comprises those described in the third column by "m!" whose intensities increased markedly during the two months preceding minimum light. Of the 60 lines thus listed, one-third are forbidden lines of *Fe* II;

[3] Paul W. Merrill and Louise Lowen, *Pub. A.S.P.*, **65**, 221, 1953.

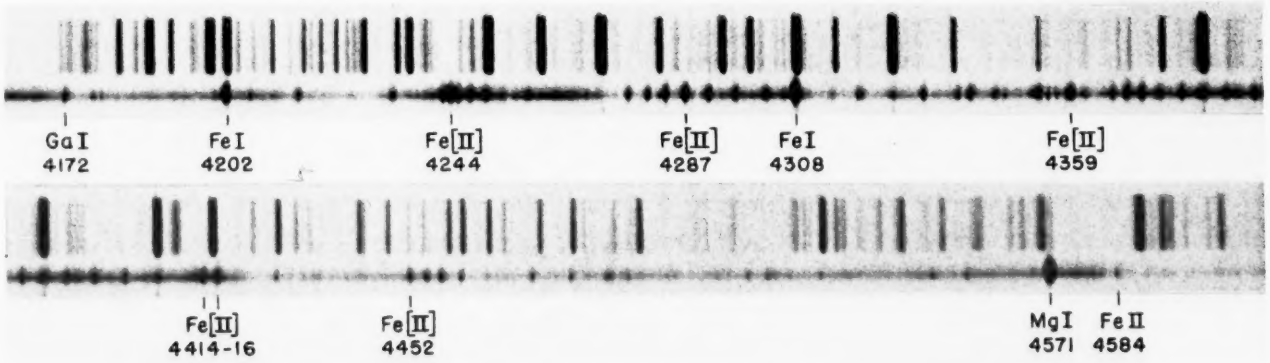

FIG. 2.—The spectrum of χ Cygni, 32 days before minimum light. Plate Pd 93, taken by I. S. Bowen, June 23–25, 1951

TABLE 2

BRIGHT LINES IN THE SPECTRUM OF χ CYGNI NEAR MINIMUM LIGHT

I.A.	Max. Int.	Change with Phase*	Ident.
3277.34	8	p, r1	.35 *Fe* II (1)
3521.27	8	p	.26 *Fe* I (24)
35.18	4	p	.16 *Zr* I (59)
65.39	16	p	.38 *Fe* I (24)
3608.86	5	p	.86 *Fe* I (23)
3735.35	20	m!	.....
49.45	4	p	.49 *Fe* I (21)
57.98	1	p	.24 *Fe* I (21)
59.26	2	p	.29 *Ti* II (13)
61.34	2	p	.32 *Ti* II (13)
63.78	3	p	.79 *Fe* I (21)
67.18	1	p	.19 *Fe* I (21)
70.5	...	d	.63 *H* 11
87.89	1	p	.88 *Fe* I (21)
98.0	...	d	.90 *H* 10
98.52	2	p	.51 *Fe* I (21)
3812.99	1	p	.96 *Fe* I (22)
15.88	1	p	.84 *Fe* I (45)
20.38	2	p	.43 *Fe* I (20)
25.79	2	p	.88 *Fe* I (20)
27.85	2	p	.82 *Fe* I (45)
29.36	4	p	.35 *Mg* I (3)
32.30	6	p	.30 *Mg* I (3)
34.13	1	p	.22 *Fe* I (20)
35.42	...	d	.39 *Hη*
38.28	8	p	.29 *Mg* I (3)
41.12	2	p	.05 *Fe* I (45)
45.51	1	p	.47 *Co* I (34)
52.63	12	d	.57 *Fe* I (73)
58.26	1	p	.30 *Ni* I (32)
87.10	2	p	.05 *Fe* I (20)
88.99	...	d	.05 *Hζ*
3905.53	8	p	.53 *Si* I (3)
32.9	4	r2	.66 *Ca* II (1)
35.97	1	p	.96 *Co* I (32)
38.31	3	p	.29 *Fe* II (3)
43.8	2	r3	.01 *Al* I (1)
50.01	4	p	.95 *Fe* I (72)
61.4	2	r3	.52 *Al* I (1)
67.9	8	r2	.47 *Ca* II (1)
70.00	...	d	.07 *Hε*
77.81	3	p	.74 *Fe* I (72)
92.99	2	m	.....
95.34	2	d	.31 *Co* I (31)
4020.94	1	d	.90 *Co* I (16)
30.68	9	d	.76 *Mn* I (2)
33.03	5	d	.07 *Mn* I (2)
34.43	5	d	.49 *Mn* I (2)
45.73	2	d	.80 *Fe* I (43)
63.57	1	d	.60 *Fe* I (43)
66.52	2	m	.....
68.72	4	m	.62 *S* II (1F)
71.27	2	m!	.....
73.77	2	m!	.....
77.62	2	p	.71 *Sr* II (1)
78.93	2	m!	.....
80.5	1	m!	.....
4081.47	4	m!	.....
84.46	3	m!	.....
86.28	1	p	.30 *Co* I (58)
87.98	3	m!	.....
92.04	3	m!	.....
93.56	1	m!	.....
95.52	2	d	.....
96.83	2	m!	.....
98.19	2	m!	.....
4101.74	...	d	.74 *Hδ*
03.08	2	p	.93 *Si* I (2)
08.84	5	m!	.....
14.70	2	m!	.48 *Fe* II (23F)?
18.80	2	d	.77 *Co* I (28)
29.02	1	m!	.....
66.58	2	d	.51 *Zr* I (–)
72.07	8	d!	.05 *Ga* I (1)
77.32	3	m!	.21 *Fe* II (21F)
78.84	2	p	.86 *Fe* II (28)
4202.06	30	p	.03 *Fe* I (42)
06.61	3	p	.70 *Fe* I (3)
15.51	6	p	.52 *Sr* II (1)
16.05	2	p	.18 *Fe* I (3)
25.3	(2)	m, r4	.73 *Ca* I (2)
33.12	5	p	.17 *Fe* II (27)
40.42	2	d	.44 *Zr* I (–)
42.52	8	m!	.61 *Zr* I (–), —
43.80	14	m!, r5	.98 *Fe* II (21F)
45.26	8	m!	.....
47.42	7	m!	.....
50.30	5	m!	.....
50.72	1	d	.79 *Fe* I (42)
58.28	3	d	.32 *Fe* I (3)
71.74	1	d	.76 *Fe* I (42)
76.84	10	m!	.83 *Fe* II (21F)
80.48	8	m!	.....
82.64	2	d	.41 *Fe* I (71)?
83.77	10	m!	.....
87.42	30	m!	.40 *Fe* II (7F)
91.83	11	m!	.....
96.70	7	m!	.....
4300.10	1	d	.05 *Ti* II (41)
02.11	2	d	.93 *Ti* II (41)
03.0	1	d	.17 *Fe* II (27)
05.81	2	m!	.90 *Fe* II (21F)
07.90	40	p	.91 *Fe* I (42)
15.02	1	d	.98 *Ti* II (41)
19.62	6	m!	.62 *Fe* II (21F)
20.52	6	m!	.....
25.8	3	m, r6	.76 *Fe* I (42), —
31.77	10	m!	.....
38.18	6	m!	.....
40.43	...	d	.47 *Hγ*
45.26	6	m!	.....
46.84	2	m!	.85 *Fe* II (21F)
51.80	2	p	.76 *Fe* II (27)
52.78	2	m!	.78 *Fe* II (21F)

TABLE 2—*Continued*

I.A.	Max. Int.	Change with Phase*	Ident.	I.A.	Max. Int	Change with Phase*	Ident.
4353.26	9	m!		4457.94	8	m!	.95 *Fe* II (6F)
54.98	5	m!		61.59	6	m	.65 *Fe* I (2)
56.59	3	m!		66.59	1	m	.57 *Fe* I (2)
58.44	4	m!	.37 *Fe* II (21F)	74.88	5	m!	.91 *Fe* II (7F)
59.36	10	m!	.34 *Fe* II (7F)	82.13	3	m	.17 *Fe* I (2)
61.81	4	m!		88.8	2	m!	.75 *Fe* II (6F)
67.07	10	m!		89.7	2	m	.74 *Fe* I (2)
69.59	10	m!, r7		4509.6	1	m!	.61 *Fe* II (6F)
72.46	15	p	.38 *Ti* I (277)?	11.32	2	d	.31 *In* I (1)
75.84	3	p	.93 *Fe* I (2)	15.0	2	m, r8	.90 *Fe* II (6F)
79.82	4	m!		18.74	3	m!	
83.42	2	p	.54 *Fe* I (41)	20.16	1	d	.22 *Fe* II (37)
84.40	3	m!		22.64	1	d	.63 *Fe* II (38)
88.10	3	m!		28.53	2	d	.61 *Fe* I (68)
89.75	1	m!		49.46	2	d	.47 *Fe* II (38)
91.0	1	m!		55.93	1	d	.89 *Fe* II (37)
93.34	8	m!		71.10	40	p	.10 *Mg* I (1)
99.03	4	m!		83.77	2	p	.83 *Fe* II (38)
4400.61	1	d		4629.31	3	m	.34 *Fe* II (37)
04.8	1	d	.75 *Fe* I (41)	39.9	5	m!	.68 *Fe* II (4F)
05.32	2	m!		4728.00	3	m!	.07 *Fe* II (4F)
13.80	6	m	.78 *Fe* II (7F)	4814.54	5	m!	.55 *Fe* II (20F)
16.30	5	m!	.27 *Fe* II (6F)	61.23		p	.33 *Hβ*
27.26	4	p	.31 *Fe* I (2)	89.59	2	m!	.63 *Fe* II (4F)
52.13	8	m!	.11 *Fe* II (7F)	4923.90	2	p	.92 *Fe* II (42)
55.34	8	m		5018.41	?	p	.43 *Fe* II (42)

*The letters in this column have the following meanings: p = persistent throughout much of the time of declining light; d = intensity decreases toward minimum light; m = intensity increases toward minimum light; r = remark.

REMARKS

1. λ 3277.34. Measured in the fourth order on several Palomar plates. Previous observations have shown the bright *Fe* II lines of multiplet (1) to be surprisingly strong; these lines merit extensive observation in the spectra of χ Cygni and other long-period variables.

2. Displaced *Ca* II emission; the effective wave length increases toward minimum light.

3. Displaced *Al* I emission; the effective wave length increases slightly toward minimum light.

4. λ 4225.3. Displaced *Ca* I emission; grows stronger toward minimum light but is never outstanding.

5. λ 4243.80. On the higher-dispersion plates the line is seen to have components at λ 4243.67 and λ 4243.99. The second line probably corresponds to [*Fe* II] (21F) λ 4243.98; the other line has not been identified.

6. λ 4325.8. The intensity and wave length increase toward minimum light as if a line of wave length about λ 4326.1 were blending with λ 4325.76 *Fe* I (42).

7. λ 4369.59. The intensity increases rapidly toward minimum light. On the Palomar plates this line is blended with the fourth-order image of λ 3277.35.

8. λ 4515.0. The intensity increases and the wave length decreases toward minimum light. Probably a blend of λ 4515.34 *Fe* II (37) and λ 4514.90 *Fe* II (6F).

the remaining two-thirds are as yet unidentified. A number of the strongest lines have been observed in the spectra of other long-period variables toward minimum light; hence it seems probable that they are characteristic of these variables and that their emission in such great intensity depends, in some way as yet unexplained, on physical processes involved in the large changes in total light.

It is surprising that such a large group of lines, many of them of great intensity compared to the adjacent continuous spectrum, should defy identification. The chief possibilities would appear to be the following:

1. Lines of rare or unstable elements, especially those of high atomic number (e.g.,

rare earths), not yet included in comprehensive spectroscopic lists. This seems improbable; but the appearance of absorption lines of *Tc* I in the spectra of χ Cygni and of other long-period variables also seemed improbable.

2. Weak lines of certain elements, or possibly individual band lines of certain compounds, tremendously intensified by fluorescence. Circumstantial evidence is unfavorable. Many strong lines, including several ascribed to fluorescent effects, are decreasing in intensity at the same time that the unidentified lines are increasing.

3. Forbidden lines not observable in the laboratory. Because the general behavior of the unidentified lines somewhat parallels that of numerous lines of [*Fe* II], this is perhaps

TABLE 3

RADIAL VELOCITIES FROM EMISSION LINES (KM/SEC)

PLATE	PHASE FROM MIN. (DAYS)	*H*		*Fe* I		*Mg* I		*Fe* II		[*Fe* II]		χ CYG*		MEAN VEL.
		Vel.	No.	Vel.	No.	Vel.	No.	Vel.	No.	Vel.	No.	Vel.	No.	
Pc 67	−87	−16.0	5	−15.1	29	−15.9	4	−13.9	12	−12.5	15	−14.5	24	−14.4
Ce 3505	−76	−13.6	7	−15.2	76	−18.2	4	−14.6	18	−13.5	14	.....	.....	−14.9
Pd 82	−64	−18.6	5	−14.0	29	−19.5	4	−14.1	16	−11.7	13	−16.8	30	−15.0
Pd 93	−32	−15.2	5	−11.2	30	− 9.5	4	−11.0	11	−10.3	13	−12.7	33	−11.7
Pc 356	−18	−14.2	4	−10.0	18	−10.2	3	−13.6	3	−13.3	5	−10.8	21	−11.1
Pd 113	+ 7	− 4.9	4	− 7.4	15	− 0.8	4	− 5.3	2	− 8.5	13	− 7.5	30	− 7.1

* Unidentified lines from Table 13, *Mt. W. Contr.*, No. 735; *Ap. J.*, **106**, 274, 1947.

TABLE 4

MEAN VELOCITIES FROM EMISSION LINES (KM/SEC)

Plates	Phase from Min. (Days)	*H*	*Fe* I	*Mg* I	*Fe* II	[*Fe* II]	χ Cyg	All
Contr. No. 735	−138	−14.4	−16.9	−17.1	−14.6	−14.0	.....	−15.4
Pc 67, Ce 3505, Pd 82	− 71	−15.5	−15.0	−17.5	−14.3	−12.7	(−15.4)	−14.7
Pd 93, Pe 356	− 27	−14.9	−10.9	− 9.7	−11.6	−11.1	−12.2	−11.6
Pd 113	+ 7	− 5.	− 7.	− 1.	− 5.	− 8.	− 8.	− 7.1
All except Pd 113	− 79	−15.6	−13.7	−15.2	−13.5	−12.1	−14.2	−13.8
All	− 57	−13.9	−12.7	−12.4	−12.7	−11.6	−12.5	−12.6

the best guess. But I have not detected any significant correspondence with the most likely lines computed for abundant elements.[4]

Radial velocities from emission lines.—Data concerning radial velocities derived from various groups of lines are recorded in Table 3. Mean values appear in Table 4. Differences between results from various plates and between those from various elements on the same plate are small. In other long-period variables the bright lines of *Fe* II have a well-marked positive displacement with respect to lines of neutral atoms, but this effect is not noticeable in χ Cygni. As minimum is approached, there appears a slight general tendency of all bright lines toward algebraically higher values. The especially high value from Pd 113, seven days after minimum, needs confirmation because the definition on this plate was not good. Because of the extremely large magnitude range exhibited by χ Cygni, I am

[4] Charlotte E. Moore, *A Multiplet Table of Astrophysical Interest* (*Contr. Princeton U. Obs.*, No. 20, 1945).

surprised that the differences in velocity are not larger; but in such matters it is better to ask the stars than to tell them.

Absorption lines.—The absorption lines will be discussed very briefly because they are not shown satisfactorily on the new spectrograms. The great intensity of the *K* 1 lines λ 4044 and λ 4047 is noteworthy. Because of the low ionization potential of potassium, these lines are extremely sensitive indicators of temperature in the reversing layers of long-period variables. Asymmetrical emission within the broad absorption *Ca* 1 line λ 4227 is seen on the three or four plates nearest minimum. Similar behavior was previously observed in the spectrum of R Leonis.[5]

The meager data on radial velocities yielded by the absorption lines are summarized in Table 5. The velocities do not differ appreciably from those obtained in other years

TABLE 5

RADIAL VELOCITIES FROM ABSORPTION LINES

Plate	Phase from Min. (Days)	Vel. (Km/Sec)	No.	Plate	Phase from Min. (Days)	Vel. (Km/Sec)	No.
Ce 3505	−76	−6	21	Pe 356	−18	(0)	5
Pd 93	−32	−5	10	Pd 113	+ 7	0	14

nearer maximum light.[2, 6] Hence there is little evidence of change of velocity with phase. If volume pulsations exist in this star, it would seem that the changes in diameter of the reversing layer do not exceed a very few per cent.

Suggestions for future observations.—The present investigation has raised challenging problems concerning the spectra of long-period variables near minimum light. Because certain rapid changes occur, a series of plates of χ Cygni taken at intervals of two weeks right through the minimum phase would be desirable. Even with the fairly low dispersion of 38 A/mm, an all-night exposure with a very large telescope would be required; with 18 A/mm three nights would be needed for a strong exposure. After 1953, conjunction with the sun will interfere with observations near minimum for seven or eight years. Other variables that might be considered for intensive spectroscopic observation near minimum are R Leo, R Hya, R Cas, T Cep, as well as the S-type stars R And and R Cyg.

A few exploratory observations in the spectral region between *Hβ* and *Hα* might be in order. Here the band absorption is very strong, but, since the effective level of emission seems to rise as the phase advances, perhaps toward minimum some bright lines (coronal or other forbidden lines?) might put in an appearance and yield hints that would help to dispel the deep mystery that now surrounds these variables.

[5] P. W. Merrill, *Mt. W. and P. Repr.*, No. 72; *Ap. J.*, **116**, 337, 1952.

[6] P. W. Merrill, *Mt. W. Contr.*, No. 649; *Ap. J.*, **94**, 171, 1941.

LINE INTENSITIES IN THE SPECTRA OF COOL CARBON STARS. I. R STARS IN THE VIOLET

WILLIAM BUSCOMBE*
MOUNT WILSON AND PALOMAR OBSERVATORIES
CARNEGIE INSTITUTION OF WASHINGTON
CALIFORNIA INSTITUTE OF TECHNOLOGY
Received April 5, 1953; revised June 3, 1953

ABSTRACT

The equivalent widths of about 150 absorption lines in the region λλ 3900–4600 have been measured on spectrograms, dispersion 10 A/mm, of three R-type stars, HD 182040, R0; HD 156074, R1; HD 16115, R3. The atomic lines are about equally intense in all three stars. In HD 182040, the weaker *CH* lines indicate only one-tenth as many absorbing *CH* molecules as in the other stars. The measurements are compared with Pannekoek's data for three G-type stars. The relative opacity of the stellar atmospheres in various spectral regions is discussed.

Although the spectra of the stars of spectral types R and N are dominated by absorption bands due to carbon molecular compounds, a study of the intensities of atomic absorption lines has been attempted in some of the windows between these bands. These limited regions offer somewhat better resolution of the severely blended atomic lines. However, it is not possible to measure with confidence any equivalent widths less than 0.1 A which could be used to delineate the curve of growth for the atomic lines. Hence this technique for determining statistically the physical parameters of these stellar atmospheres cannot be applied.

From R. F. Sanford's photographic "Atlas of Spectra of Six Stars of Classes R and N,"[1] it is clear that the most extensive windows, nearly free of absorption by molecular bands, occur in the blue-violet region of the spectra of the early R-type stars. In the later types the *CN* and C_2 bands increase in strength very greatly, in a manner analogous to the *TiO* bands in K and M stars. The detailed comparisons reported here cover the region from λ 3900 to λ 4600, in the spectra of the three bright R-type stars,[2] HD 182040 (R0, $C1_2$), HD 156074 (R1, $C1_2$), and HD 16115 (R3, $C2_3$), photographed at the coudé focus of the 100-inch telescope with a dispersion of 10 A/mm. Tracings were made with the direct-intensity microphotometer designed by H. W. Babcock.

The identifications were made principally by reference to the *Revision of Rowland's Preliminary Table of Solar Spectrum Wave-Lengths*[3] and *A Multiplet Table of Astrophysical Interest (Revised Edition)*,[4] with interpolations from the rotational analyses of the *CH* bands by L. Gerö[5] and E. Fagerholm.[6] For the majority of lines in these complex spectra, only the central depth in percentage absorption can be measured. The entire profile of about one line in five can be sketched with some confidence. The equivalent widths of these lines were used to calibrate the results from the central depths of the other

* Carnegie Institution Fellow, 1950–1952. Present address: Commonwealth Observatory, Canberra, Australia. The writer is indebted to Dr. Sanford for permission to include in this study several plates taken by him.

[1] *Ap. J.*, **111**, 262, 1950.

[2] Spectral types from C. D. Shane, *Lick Obs. Bull.*, **13**, 123, 1928; and Keenan and Morgan, *Ap. J.*, **94**, 501, 1941.

[3] C. E. St. John *et al.*, *Carnegie Inst. Washington Pub.*, No. 396, 1928.

[4] Charlotte E. Moore, *Contr. Princeton U. Obs.*, No. 20, 1945.

[5] *Physica*, **7**, 155, 1940; *Zs. f. Phys.*, **118**, 27, 1941.

[6] *Ark. f. mat., astr. och fys.*, *A*, Vol. **27**, No. 19, 1941.

lines. About 150 lines in the spectral range appeared sufficiently resolved to permit reasonable measurement of the total absorption, although in many cases this depends on an estimate of the proportion of the dominant contributor to a blend. A review of this list, when L. Gratton's identifications in the spectra of K giants[7] came to hand, showed that 138 of these lines had also been considered by him as the dominant contributors to cor-

TABLE 1

MEAN EQUIVALENT WIDTHS IN ANGSTROMS

ELEMENT	E.P. (VOLTS)	$\bar{\lambda}$	NO. OF LINES	STAR AND TYPE					
				182040 (R0, $C1_2$)	156074 (R1, $C1_2$)	16115 (R3, $C2_3$)	Sun (G2 V)	ξ Boo A (G8 V)	η Dra (G8 III)
Mg I	0.0	4571	1	0.28	0.31	.....	0.11	0.18	0.26
Ca I	0.0	4226	1	1.0	1.3	.....	1.2	1.2	3.1
Ca I	1.9	4400	4	0.26	0.29	0.22	0.17	0.36	0.37
Ca II	0.0	3950	2	20	14	.....	13	.....	.....
Sc I	0.0	4000	4	0.18	0.19	.....	0.03:	.....	.....
Sc II	0.3	4246	1	0.26	0.26	.23	0.16	0.20	0.29
Ti I	0.0	4008	1	0.25	0.24	.....	0.08	.....	.....
Ti I	0.8	4500	5	0.23	0.24	.....	0.08	0.16	0.19
Ti I	1.0	4070	3	0.27	0.23	.....	0.05	.....	0.17
Ti I	1.7	4600	2	0.22	0.14	.....	0.06	0.10	0.15
Ti I	2.1	4503	1	0.10	0.08	.....	0.01	0.02	0.06
Ti I	2.6	4278	1	0.18	0.16	.....	0.06	0.13	0.16
Ti II	1.2	4500	7	0.29	0.26	.18	0.11	0.18	0.24
V I	0.3	4400	12	0.18	0.25	.20	0.06	0.11	0.18
Cr I	0.0	4270	2	0.28	0.38	.28	0.31	0.62	0.68
Cr I	0.9	4500	4	0.21	0.24	.....	0.08	0.19	0.23
Cr I	3.0	4400	5	0.17	0.20	.19	0.04	0.11	0.19
Mn I	2.2	4000	5	0.33	0.30	.....	0.15	.....	0.26
Fe I	0.1	4400	4	0.19	0.28	.26	0.10	0.22	0.30
Fe I	1.5	4600	3	0.19	0.24	.....	0.10	0.22	0.26
Fe I	1.5	4400	3	0.38	0.50	.44	0.44	0.90	0.96
Fe I	1.5	4300	3	0.44	0.46	.31	0.59	0.91	1.07
Fe I	1.5	4000	4	0.52	0.71	.....	0.80	.....	1.02
Fe I	2.2	4400	4	0.27	0.29	.16	0.14	0.27	0.36
Fe I	2.3	4600	3	0.17	0.22	.....	0.05	0.11	0.17
Fe I	2.4	4200	4	0.32	0.34	.25	0.35	0.63	0.58
Fe I	2.7	4000	3	0.25	0.20	.....	0.12	.....	.....
Fe I	2.8	4400	3	0.28	0.29	.....	0.14	0.26	0.28
Fe I	3.3	4100	7	0.22	0.21	.....	0.09	.....	0.18
Fe II	2.8	4500	5	0.29	0.21	.....	0.07	0.13	0.21
Co I	0.5	4000	6	0.19	0.24	.....	0.05	.....	.....
Co I	1.0	4000	2	0.24	0.29	.....	0.10	.....	.....
Sr II	0.0	4077	1	0.79	0.67	.....	0.34	.....	0.50
Ba II	0.0	4554	1	0.32	0.32	.....	0.17	0.38	0.47
CH (R)	0.0	4250	7	0.12	0.21	.22	0.18	0.19	0.21
CH (P)	0.0	4350	11	0.17	0.20	0.24	0.14	0.10	0.11

responding blends in the spectrum of α Ser (K2 III–IV) and α UMa (G8 II–III) and that about 10 additional entries might be considered.

The average equivalent widths in angstrom units for small groups of lines, each arising from the same lower energy state of the same atom, are listed in Table 1, in order of increasing atomic number and excitation potential. This procedure was developed by W. Buscombe and P. W. Merrill[8] in a study of the spectra of long-period variables. Included

[7] *Ap. J.*, **115**, 346, 1952.

[8] *Ap. J.*, **116**, 525, 1952.

for comparison are A. Pannekoek's corresponding measures[9] from the spectra of the sun (G2 V), ξ Boo A (G8 V), and η Dra (G8 III), i.e., the coolest stars for which equivalent widths have been published in this spectral region. According to P. C. Keenan and W. W. Morgan's classification scheme,[10, 11] stars of spectral type G8 are equivalent, except for molecular absorption features, to the carbon stars under consideration.

The complexity of these spectra is well shown in Sanford's Atlas,[1] which includes a reproduction of one of the spectrograms of HD 156074 used in the present study. For each of the six lines listed in Sanford's Table 6, which occurs in the spectral region now under discussion, the measured equivalent width agrees very closely with Sanford's visual estimate based on standards measured from his own tracings.

The fiducial continuum was empirically drawn as a smooth curve, always concave downward, through the apparently very narrow windows between absorption lines at λλ 4000, 4229, 4402, 4615, and 4750 on all the tracings, with a few other peaks on individual tracings. Some confidence in the adopted curve was gained, since the broad wings of the *Ca* II H and K lines showed profiles approximating to an $I_\lambda \sim (\Delta\lambda)^{-2}$ relation. Also the integrated intensities attributed to several vibrational bands in the C_2 Swan system were very similar to those obtained in the spectra of two of these same stars by A. McKellar and W. Buscombe[12] on tracings made at Victoria from prismatic plates of somewhat lower dispersion. The fractional uncertainty in the equivalent width of a single line is of the order of 30 per cent, mainly owing to blending and to difficulty in locating the continuous background. Accordingly, a difference between two stars of more than 20 per cent in the average intensity for a particular group of lines seems rather significant.

It appears from Table 1 that the general average equivalent width for all lines measured is almost the same for each of the three R-type stars. That is to say, the fiducial continuum has been drawn on each of the tracings independently, as though the continuous opacity in this spectral region were the same for each of these stars. On the other hand, the mean equivalent width is greater for each of the R-type stars than for the sun, but intermediate between the values for ξ Boo A and for η Dra. Besides, certain trends may be noted; for example, the ultimate lines of the neutral atoms and of the *CH* molecule become stronger in the later spectral classes, while the lines due to ionized elements and the subordinate neutral lines, especially of *Fe* I, weaken. This quantitatively suggests a temperature sequence consistent with the visual estimates from spectrograms of lower dispersion, on which the classification systems are based.

Although it is not known precisely how blending and damping in the stellar atmospheres affect the total absorption by adjacent groups of rotational lines in the G band of *CH*, it appears reasonable that at least ten times fewer *CH* molecules are absorbing in the atmosphere of HD 182040 than in the other R stars studied. This is in line with a suggestion of K. Wurm[13] that this star may actually be deficient in hydrogen. Earlier measures[12] also showed the integrated absorption of the *CH* band weaker in HD 182040 than in other early R-type stars, although the C_2 and *CN* bands do not show this anomaly.[14] The lines $H\alpha$ and $H\beta$ are also weaker in HD 182040, but no Balmer series member in the present spectral region is sufficiently resolved to be measured.

In view of the very great uncertainty, from a theoretical point of view, as to the source of continuous absorption in the atmospheres of these red giant stars, it may be of

[9] *Pub. Dom. Ap. Obs. Victoria*, **8**, 141, 1950.

[10] *Astrophysics*, ed. J. A. Hynek (New York: McGraw-Hill Book Co., 1951), chap. i.

[11] *Ap. J.*, **94**, 501, 1941.

[12] *Pub. Dom. Ap. Obs. Victoria*, **7**, 361, 1948.

[13] *Naturwiss.*, **29**, 686, 1941.

[14] W. P. Bidelman, *Ap. J.*, **117**, 25, 1953, has also illustrated the weakness of the *CH* band in this star's spectrum, but gave no intensity measurements.

some interest to infer their opacity ratios in different parts of the spectrum. This may be done very roughly from the integrated band intensities, as measured by McKellar and Buscombe,[12] for the (1, 0) and (0, 1) vibrational band sequences in the Swan system of C_2. The most consistent temperature dependence was obtained by using the transition probabilities (J^2) determined in the laboratory by R. B. King.[15] In addition to the stars HD 182040 and HD 156074, we may consider the case of HD 76396 (R4, C1p_2), a high-velocity *CH* star.[16] For the average of the bands in the λ 5600 region, the relative values of the ratio $W/\lambda J^2$ for these stars are 9, 3, and 8, respectively, while in the λ 4700 region the corresponding value is 3 for each. If the band absorptions are not reduced by saturation or damping, one may conclude that the relative opacity increases at least threefold between λ 5600 and λ 4700 in the atmospheres of HD 76396 and HD 182040, but remains almost constant in HD 156074. Since McKellar and Buscombe's assumption that the integrated band intensities vary linearly with the number of absorbing molecules led to rather high excitation temperatures, it is quite plausible that at least the stronger bands would lie on the transitional part of the curve of growth. In this case the relative opacity increase would be even greater and the temperatures lower. It is evident from the well-known depression of the violet in the spectra of N stars that their opacity varies even more rapidly with wave length.

[15] *Ap. J.*, **108**, 429, 1948.

[16] P. C. Keenan, *Ap. J.*, **96**, 101, 1942.

A STUDY OF LINE PROFILES: THE SPECTRUM OF RHO LEONIS*

SU-SHU HUANG AND OTTO STRUVE
Berkeley Astronomical Department, University of California
Received May 14, 1953

ABSTRACT

The broad absorption lines of the B0 I supergiant ρ Leonis have been compared with several theoretical line profiles computed for different kinds of mass motion. The observed profiles agree with the rotational profiles (or perhaps with profiles broadened by vertical convection with an assumed distribution of velocities according to a step function).

A simple method of determining the velocity of mass motion has been developed. When this method is applied to the medium and weak lines in ρ Leonis, a mean rotational velocity of 61.8 km/sec, with a probable error of 5.8 km/sec, is obtained. If the broadening of lines in ρ Leonis is due to convection instead of rotation, the value thus determined can be interpreted as the maximum velocity (in the step-function distribution) of the convection motion. Because of the observational uncertainties as well as the theoretical complications, we cannot be certain which of the two possibilities is the correct one.

The original lines, before being broadened by 61.8 km/sec of rotation (or of convection), have large widths and shallow depths, suggesting the presence of other kinds of large-scale motion. We have estimated from the curve of line-width correlation that such a large-scale motion has a velocity of about 18 km/sec, while the small-scale turbulent motion and the thermal motion combined have a velocity of 10 km/sec. The stronger lines do not show appreciable rotation (or convection). They are perhaps broadened by other kinds of mass motion, possibly by large-scale turbulence.

I. DEFINITIONS AND PLANS

For convenience, we shall designate as Doppler broadening of the first kind that produced by motion of material which does not change the shape of the effective mean atomic-line absorption coefficient. This motion includes rotation, expansion, contraction, mass convection, large-scale turbulence, etc. In a similar way we shall designate as Doppler broadening of the second kind that produced by motion of material which redistributes the effective mean atomic-line absorption. This includes thermal motion, small-scale turbulent motion, etc. By utilizing these definitions,[1] it is possible to discuss velocities of both kinds of Doppler motion without necessarily giving a physical interpretation of the observed effects. A line profile will depend upon Doppler motion of both kinds, but in the present paper only the first kind will be discussed. As in a previous paper[2] we define a fictitious line, without Doppler broadening of the first kind, as the line that would be recorded on the photographic plate, were the star concerned to stop its Doppler motion of the first kind but otherwise to remain the same. The form of the final line, $A'(x)$, will depend upon the form of the fictitious line, $A(x)$, and the broadening function, $B(x)$, which can be derived from the velocity distribution of the Doppler motion of the first kind. If $B(x)$ is normalized, we have

$$A'(x) = \int_{-\infty}^{\infty} B(x-y)\, A(y)\, dy\,. \tag{1}$$

It is evident that $A'(x)$ will become $A(x)$ when the ratio of the width of $B(x)$ to that of $A(x)$ approaches zero, and $A'(x)$ will assume the form of $B(x)$ when the same ratio approaches infinity. This behavior considerably simplifies the problem, because a simple profile may be used for the fictitious line in computing the broadened profile, if the

* The coudé spectrogram used in this investigation was obtained by Mr. Struve as a guest investigator at the Mount Wilson Observatory. This work was supported by the Office of Ordnance Research.

[1] S. S. Huang and O. Struve, *Ap. J.*, **116**, 410, 1952.

[2] S. S. Huang, *Ap. J.*, **118**, 285, 1953.

Doppler broadening of the first kind greatly exceeds that of the second kind (Sec. III). The extent of the Doppler broadening of the first kind over that of the second may be seen from the degree of shallowness of the lines.

An investigation has been made of the various kinds of possible mass motion (including rotation) in stellar atmospheres which might cause Doppler broadening of the first kind. From the nature of the motion a broadening function $B(x)$ for each case can be derived (Sec. II), and a theoretical line profile can therefore be computed from equation (1) for each kind of mass motion (Sec. III).

In Section IV a convenient method of determining the rotational velocity is developed. It determines also the width and the central depth of the fictitious line without rotational broadening.[2] Doppler velocities in the atmosphere of ρ Leonis are determined by this method in Sections V and VI.

II. THE BROADENING FUNCTION FOR VARIOUS KINDS OF MASS MOTION

We shall now consider different kinds of mass motion and derive the corresponding broadening functions. The broadening function for rotation is well known:[3]

$$B(x) = \frac{3}{3+2\beta}\left[\frac{2}{\pi}(1-x^2)^{1/2} + \frac{\beta}{2}(1-x^2)\right] \qquad (|x| \leqslant 1), \quad (2)$$

where β is the limb-darkening constant and will be set equal to 1.5 throughout this paper. The unit of x is the rotational width, defined as

$$(\Delta\lambda)_R = \frac{\lambda v \sin i}{c}. \quad (3)$$

Regarding the broadening function due to Doppler motion other than rotation, we must examine each case separately. First, let us consider random motions of large eddies. If the velocities have a Maxwellian distribution, the broadening function will be[4]

$$B(x) = \frac{1}{\sqrt{\pi}}\, e^{-x^2} \qquad (|x| \leqslant \infty), \quad (4)$$

where x is in units of the Gaussian width, defined as

$$(\Delta\lambda)_G = \frac{v^*\lambda}{c}, \quad (5)$$

and v^* is the most probable velocity in the Maxwellian distribution.

Next we investigate the random motions of large masses parallel to the surface of the star (such as the horizontal motion of clouds in our atmosphere). If all horizontal motions had the same speed, what would be the velocity distribution along the line of sight? Because of the spherical shape of the surface, the direction of the space velocity can be regarded as oriented in a random manner. Hence the distribution of the component of velocity, along the line of sight, v, is given by a step function.[5] (Here we have neglected the effect of limb darkening.) Let v_0 be the absolute value of the space velocity; the required distribution is

$$f(v, v_0)\, dv = \frac{dv}{2v_0} \qquad (|v| \leqslant v_0) \quad (6)$$
$$= 0 \qquad (|v| > v_0).$$

[3] E.g., A. Unsöld, *Physik der Sternatmosphären* (Berlin: J. Springer, 1938), p. 318.

[4] A. Unsöld and O. Struve, *Ap. J.*, **110**, 455, 1949.

[5] S. S. Huang, *Ap. J.*, **112**, 399, 1950.

Since we assume random motions of the masses, all values of v_0 should be possible. Assume, first, that the distribution $P(v_0)dv_0$ of v_0 is governed by a Gaussian error law,

$$P(v_0)\,d\,v_0 = \frac{2\gamma}{\sqrt{\pi}}\, e^{-\gamma^2 v_0^2} d\,v_0 \qquad (0 \leqslant v_0 \leqslant \infty). \quad (7)$$

The final distribution of the velocity component along the line of sight is

$$f(v)\,d\,v = d\,v \int_v^\infty P(v_0)\, f(v, v_0)\, d\,v_0 = \frac{\gamma}{2\sqrt{\pi}} E_1(\gamma^2 v^2)\, d\,v\,, \quad (8)$$

where $E_1(x)$ is the exponential integral. If we use the Gaussian width defined in equation (5) (here $v^* = 1/\gamma$) as the unit for measuring the wave length, the broadening function becomes

$$B(x) = \frac{1}{2\sqrt{\pi}} E_1(x^2) \qquad (|x| < \infty). \quad (9)$$

If in the previous case v_0 is not distributed according to the error law but is uniformly distributed over a range such that

$$P(v_0)\,d\,v_0 = \frac{d\,v_0}{v_m} \qquad (0 \leqslant v_0 \leqslant v_m), \quad (10)$$

then the broadening function will be[6]

$$B(x) = -\tfrac{1}{2} \ln(|x|) \qquad (|x| \leqslant 1), \quad (11)$$

provided that the maximum width,

$$(\Delta\lambda)_M = \frac{v_m \lambda}{c}\,, \quad (12)$$

is taken as the unit of x. We should note that although the broadening functions given in equations (9) and (11) diverge at $x = 0$, the integrals, $\int_0^x B(x)dx$, always remain finite.

Finally, we consider the random motions of large masses in the radial direction (such as vertical convection and prominences[7]). In order to derive the corresponding broadening function, we assume, first, that all masses move either upward or downward with the same speed. This reduces the problem to one of radial expansion and contraction. The distribution of the velocity component in the line of sight, v, for the latter problem is well known.[8] If v_0 is the speed of all masses (moving either upward or downward with equal probability), the distribution function is

$$f(v, v_0)\,d\,v = \frac{3}{3+2\beta}\left[\left|\frac{v}{v_0}\right| + \beta\left(\frac{v}{v_0}\right)^2\right]\frac{d\,v}{v_0} \qquad (|v| \leqslant v_0). \quad (13)$$

If v_0 is not a constant but is distributed according to the error law given in equation (7), the distribution of the velocity component along the line of sight becomes

$$f(v)\,d\,v = \frac{3}{3+2\beta}\,\frac{2\gamma}{\sqrt{\pi}}\,d\,v \int_v^\infty e^{-\gamma^2 v_0^2}\left[\left|\frac{v}{v_0}\right| + \beta\left(\frac{v}{v_0}\right)^2\right]\frac{d\,v_0}{v_0}. \quad (14)$$

The integration involved in equation (14) can be easily effected, and after some simple

[6] We shall use ln x to denote the natural logarithm of x and log x to denote the common logarithm of x.

[7] O. Struve, *Pub. A.S.P.*, **63**, 138, 1951; *A.J.*, **56**, 115, 1951; A. McKeller, G. J. Odgers, L. H. Aller, and D. B. McLaughlin, *Nature*, **169**, 990, 1952.

[8] H. Shapley and S. B. Nicholson, *Proc. Nat. Acad. Sci.*, **5**, 417, 1919; A. van Hoof and R. Deurinck, *Ap. J.*, **115**, 166, 1952.

calculations we obtain the broadening function,

$$B(x) = \frac{6}{(3+2\beta)\sqrt{\pi}}\{(1+\tfrac{1}{2}\beta)\, e^{-x^2} - \sqrt{\pi}\,|x|\,[1-H(|x|)] - \tfrac{1}{2}\beta x^2 E_1(x^2)\}, \quad (15)$$

where $H(x)$ is the probability integral. The unit of x is the Gaussian width defined by equation (5) (here $v^* = 1/\gamma$).

Similarly, if the distribution function of v_0 has a rectangular form like equation (10), the corresponding broadening function will be

$$B(x) = \frac{3}{3+2\beta}\left[(1-|x|) + \frac{\beta}{2}(1-x^2)\right] \qquad (|x| \leqslant 1), \quad (16)$$

the unit of x being the maximum width defined in equation (12).

When the upward and downward motions are not equally probable or the distribution of the amplitude v_0 for the upward motion is different from that for the downward motion, an asymmetrical function for $B(x)$ will be obtained, and the observed lines will show asymmetry accordingly.

III. LINE PROFILES BROADENED BY MASS MOTION

When the Doppler motion of the first kind is large, the form of $A(x)$ will not be important, and we may choose a rectangular form for $A(x)$ in order to simplify the calculation. Let

$$\begin{aligned} A(x) &= 1 \qquad (|x| \leqslant k) \\ &= 0 \qquad (|x| > k). \end{aligned} \quad (17)$$

Equation (1) now becomes

$$A'(x) = \int_{x-k}^{x+k} B(y)\, dy. \quad (18)$$

Using equation (18) together with formulae (2), (4), (9), (11), (15), and (16) obtained in Section II, we can compute different $A'(x)$'s, respectively, for different cases of mass motion. Thus from equations (2) and (18) we have, for rotation,

$$\begin{aligned} A'(x) = {} & \frac{1}{\pi}(\theta_2 + \tfrac{1}{2}\sin 2\theta_2 - \theta_1 - \tfrac{1}{2}\sin 2\theta_1) \\ & + \frac{\beta}{6}[\sin\theta_2(2+\cos^2\theta_2) - \sin\theta_1(2+\cos^2\theta_1)], \end{aligned} \quad (19)$$

where θ_1 and θ_2 are suitable limits which depend on whether $k \leqslant 1$, $k \geqslant 1$, $0 \leqslant x \leqslant |k-1|$, and $|1-k| \leqslant x \leqslant 1+k$.

While we have normalized on the x-scale all the broadening functions given in Section II, no attempt has been made to normalize any $A'(x)$ in this section, because the constant factor should be determined by the equivalent width or the central depth of the observed line.

From equations (4) and (18) we can derive the profile broadened by mass motion having a Maxwellian distribution of velocities; hence

$$A'(x) = H(x+k) - H(x-k). \quad (20)$$

A profile broadened by random motion (parallel to the surface) having a Gaussian distribution of the absolute values of the space velocity can be obtained from equations (9) and (18),

$$\begin{aligned} A'(x) = {} & (x+k)E_1([x+k]^2) - (x-k)E_1([x-k]^2) \\ & + \sqrt{\pi}\,[H(x+k) - H(x-k)]. \end{aligned} \quad (21)$$

In case the distribution of the absolute values of the space velocity is rectangular, the broadened profile should be obtained by combining equations (11) and (18); thus

$$A'(x) = (x-k)\,[\ln(|x-k|) - 1] - (x+k)[\ln(x+k) - 1] \quad (0 \leqslant x \leqslant 1-k);$$
$$A'(x) = 1 + (x-k)[\ln(|x-k|) - 1] \qquad (1-k \leqslant x \leqslant 1+k). \tag{22}$$

Two similar equations for random motion in the radial direction are given below; one broadened by $B(x)$ as given in equation (15):

$$A'(x) = \phi(x) - \sqrt{\pi}\,(x-k)^2 \qquad (0 \leqslant x \leqslant k);$$
$$A'(x) = \phi(x) \qquad (k \leqslant x \leqslant \infty), \tag{23}$$

where

$$\phi(x) = \frac{\sqrt{\pi}}{2}\{[1 - H(x-k)][\tfrac{1}{2} + \tfrac{1}{3}\beta + (x-k)^2] - [1 - H(x+k)]$$
$$\times [\tfrac{1}{2} + \tfrac{1}{3}\beta + (x+k)^2]\} - (\tfrac{1}{2} + \tfrac{1}{6}\beta)[(x-k)\,e^{-(x-k)^2} - (x+k)\,e^{-(x+k)^2}] \tag{24}$$
$$-\frac{\beta}{6}[(x+k)^3 E_1([x+k]^2) - (x-k)^3 E_1([x-k]^2)],$$

and another by $B(x)$ as given in equation (16):

$$A'(x) = (2+\beta)\,k - \frac{(x^2+k^2)}{2kx} - \beta k\,(x^2 + \tfrac{1}{3}k^2) \quad (x-k \leqslant 0),$$

and (25)

$$A'(x) = \tfrac{1}{2} + \tfrac{1}{3}\beta - \left(1 + \frac{\beta}{2}\right)(x-k) \mp \tfrac{1}{2}(x-k)^2 + \frac{\beta}{6}(x-k)^3 \quad (x-k \leqslant 0),$$

for $0 \leqslant x \leqslant 1-k$ and for $1-k \leqslant x \leqslant 1+k$, respectively.

The units in all formulae for $A'(x)$ are the same as those used in their respective broadening functions. These profiles can be used as a standard for quantitative comparison with observed profiles, provided only that the latter are very broad and shallow. In Figure 1 we have plotted such profiles according to equations (19)–(23) and (25), together with their corresponding broadening functions (2), (4), (9), (11), (15), and (16). They give us a general idea of the shapes of line profiles broadened by different kinds of mass motion. When the line profiles observed in ρ Leonis were compared with these calculated curves, we found that most lines show the character of rotational broadening (see Secs. V and VI). Hence in the next section we shall consider the rotational profile more in detail.

We should further mention that formulae (22) and (25), like (19), should have different forms according as $k \leqslant 1$ or $k \geqslant 1$. We have given the result only for $k \leqslant 1$, because this is the only important case here.

IV. COMPUTATION OF ROTATIONAL PROFILES AND DETERMINATION OF ROTATIONAL VELOCITIES

The rotational profile given in Figure 1, *a*, is valid only when the rotational width is much larger than the line width of the fictitious line without rotation. Here we shall consider the rotational profile without this restriction. Except for the *H* and *He* lines, the profiles of the spectral lines observed in any normal supergiant star without appreciable rotation can be well represented by a Gaussian error-curve. Therefore, we should compute the broadened profile by using

$$A(x) = e^{-\gamma^2 x^2}, \tag{26}$$

where x is expressed in the rotational unit. Hence the half-width of the Gaussian profile

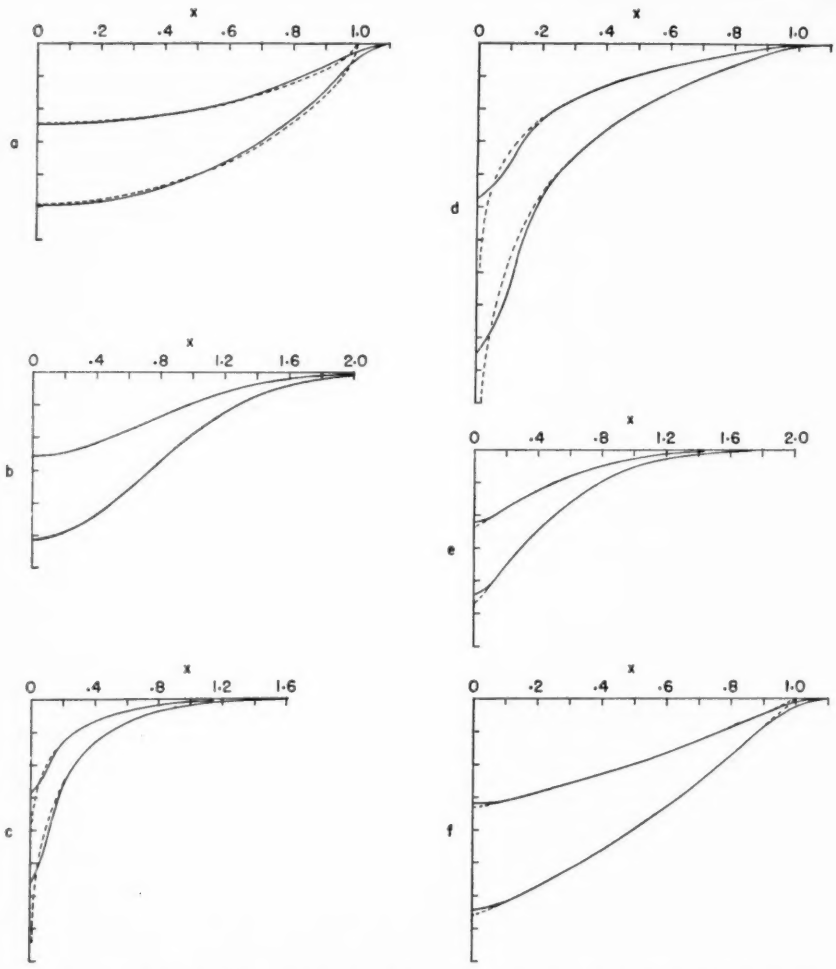

FIG. 1.—Broadening functions and broadened line profiles corresponding to different kinds of mass motion: (*a*) rotation; (*b*) Maxwellian distribution; (*c*) horizontal random motion with a Gaussian distribution of velocities; (*d*) horizontal random motion with a step-function distribution of velocities; (*e*) vertical random motion with a Gaussian distribution of velocities; (*f*) vertical random motion with a step-function distribution of velocities. The broken line represents the broadening function; the solid line represents the broadened profiles (in all cases $k = 0.1$). In case *b* we cannot distinguish the broadening function from the broadened profile in the figure. The units of x are different for different cases and are given in the text. Two curves, corresponding to two different central depths, are drawn for each case. The scale of the ordinate is indeterminate by a constant factor.

is $2(\ln 2)^{1/2}/\gamma$ that of the rotational width. Substituting equations (2) and (26) in equation (1), we can derive the required result. Unfortunately, one of the resulting integrals cannot be put in terms of tabulated functions, and a graphical or numerical integration is necessary. The final results are given in Figure 2 for different values of γ. In the same figure we have also drawn the rotational profiles computed from equation (17) as well as from a triangular profile given by

$$A(x) = 1 - \frac{x}{k} \qquad (0 \leqslant x \leqslant k); \tag{27}$$

$$A(x) = 1 + \frac{x}{k} \qquad (-k \leqslant x \leqslant 0).$$

In each case of comparison the central depth (equal to 1 in eqs. [26], [17], and [27]) and the equivalent width are taken to be the same; hence k in both equations (17) and (27)

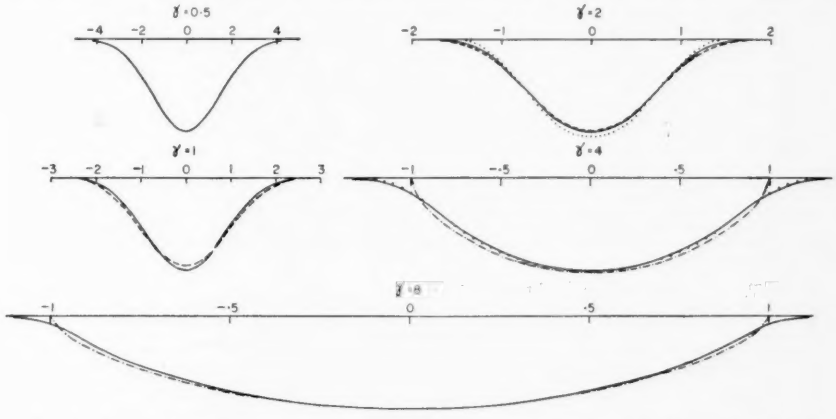

FIG. 2.—Rotational profiles. All curves in the figure represent profiles broadened by rotation, but the original lines are different: they may be Gaussian (*solid line*), triangular (*broken line*), rectangular (*dotted line*), or infinitely narrow (*broken line with dots*). The purpose of the figure is to show that the profiles broadened from a Gaussian curve by rotation can be approximated by those broadened from a simpler curve. The unit of the abscissa is the rotational width, and γ is a parameter proportional to the ratio of the rotational width to the natural width of the line.

can be determined in terms of γ. We can see from the figure that, for $\gamma \geqslant 2$, equation (27) yields a profile nearly the same as one computed from equation (26), and, for $\gamma \geqslant 4$, equation (17) already gives a good rotational profile. The rotational profile derived from equation (17) has already been given in equation (19) and that derived from equation (27) can be written in a similar manner. We will not give the explicit formula here, because it is quite long. Hence if $\gamma \geqslant 2$ (or 4), it would save some labor to use equation (19) (or a corresponding equation for the triangular $A[x]$) instead of integrating numerically equations (1), (2), and (28). Finally, we should note that γ depends upon the ratio of the rotational width to the width of the original line and can therefore be different from line to line, even for the same star.

No general formula can be obtained for computing the rotational profile of *He* I lines, although they are very important. We have taken the profile of *He* I 4471 from γ Peg,[9] a star without appreciable rotation, as $A(x)$ and have numerically integrated the final profile for different rotational velocities. The results, given in Figure 3, agree in general

[9] A. B. Underhill, *Ap. J.*, **107**, 349, 1948.

with those previously obtained.[10] Even at 100 km/sec, the blend is washed out, leaving a slightly asymmetrical profile. It is interesting to see that the center of the line shifts toward the side where the blend is located, but the apparent shift becomes unnoticeable when the rotational velocity is very large.

The line *Mg* II 4481 is also important for studying stellar rotation. Since this line can be well represented by a Gaussian curve, we can use the previous result.

Regarding the determination of rotational velocities, O. Struve and C. T. Elvey[11]

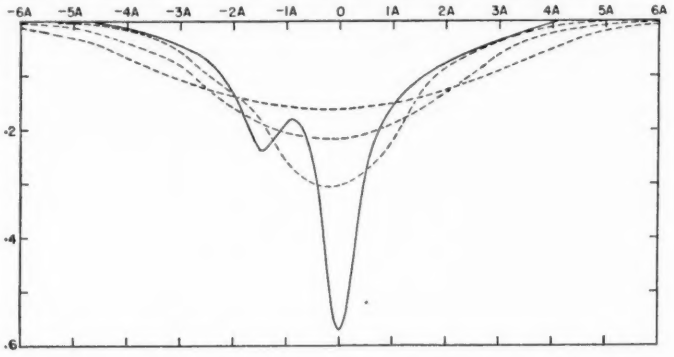

FIG. 3.—Rotational profiles of *He* I 4471. The solid curve is the observed profile of *He* I 4471 in γ Peg. The broken curves represent the same line hypothetically broadened by rotations of 100, 200, and 300 km/sec, respectively.

established a method which has been followed by many investigators.[12] In the following paragraph we shall present a different method.

Let us consider a spectrum known to be broadened by rotation. An actual line profile observed in the spectrum depends on several parameters: the central depth and the width of the original line and the rotational velocity, the first two varying from line to line, even in the same spectrum. Moreover, we do not know any of these three parameters beforehand. Hence a direct comparison of line profiles demands a series of theoretical line profiles, each representing a particular set of values of these three parameters. This is, of course, impracticable. But if we plot the line profile in logarithmic scales (both the wave length and the depth), the form of the curve will depend only on the ratio of the original width to the rotational width (or the constant γ, which is related to the ratio). The logarithmic rotational profiles derived from equations (1) and (26) are plotted in Figure 4 for a set of values of γ. We now slide the observed profile (plotted on the same scales) vertically and horizontally over the theoretical curves until the best fit is found. The shift in the abscissa determines the rotational velocity, because

$$\log x = \log(\Delta\lambda) + \log\left(\frac{c}{v\lambda}\right), \tag{28}$$

and the shift in the ordinate determines the central depth, R_0, of the original line, because the ordinate of the theoretical curve is $\log(e^{-\gamma^2 x^2})$, while that of the observed one is $\log(R_0 e^{-\gamma^2 x^2})$.

[10] O. Struve, *Ap. J.*, **72**, 1, 1930.

[11] *Ap. J.*, **72**, 267, 1930; *M.N.*, **91**, 663, 1931; O. Struve, *Ap. J.*, **72**, 1, 1930; **74**, 225, 1931; G. Shajn and O. Struve, *M.N.*, **89**, 222, 1929; C. T. Elvey, *Ap. J.*, **70**, 141, 1929; **71**, 221,1930.

[12] E. van Dien, *J.R.A.S. Canada*, **42**, 249, 1948; A. Slettebak, *Ap. J.*, **110**, 498, 1949.

V. DETERMINATION OF DOPPLER VELOCITIES IN SPECTRUM OF ρ LEONIS BY INDIVIDUAL LINE PROFILES

The intensities of lines in ρ Leonis have been studied by A. B. Underhill.[9] Its rotational velocity is 70–100 km/sec estimated directly on Lick Observatory plates[2] and is 80 km/sec on Yerkes Observatory plates.[13]

The present analysis is based on a coudé spectrogram[14] taken on April 16, 1952, at the Mount Wilson Observatory, with a dispersion of 3 A/mm. The identification of the lines in the spectrum was made by using several wave-length tables.[15] Profiles of some

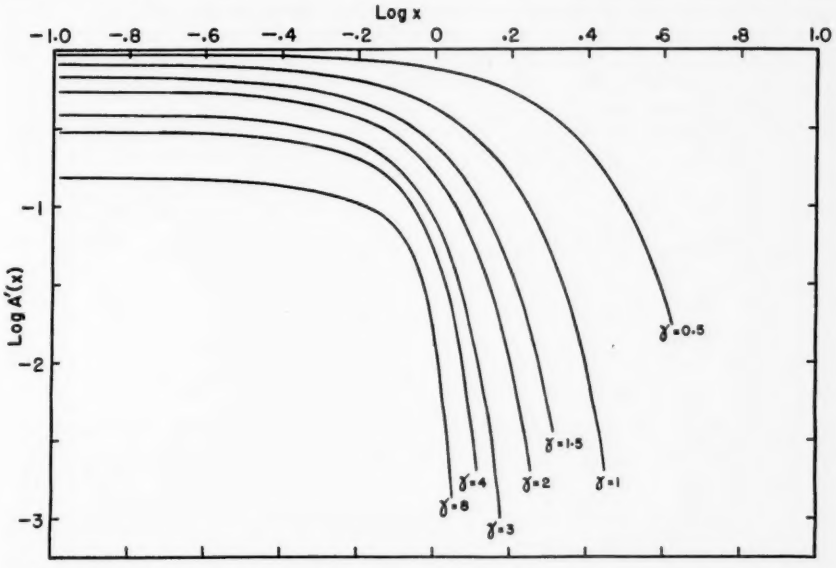

FIG. 4.—Rotational profiles in the logarithmic scale. Scale factors such as wave length, equivalent width, etc., are removed from these curves. They show, therefore, the intrinsic difference between profiles broadened by different amounts of rotation.

lines have been checked with those obtained at the Dominion Astrophysical Observatory, Victoria, B.C.[16] The agreement is good. In Figure 5 we have drawn two profiles of the same line, λ 4366.91: one from the Mount Wilson Observatory plate and another from the Dominion Astrophysical Observatory plate.

Comparing the observed profiles with those given in Figure 1, we can see that the broadening can be due either to rotation (the curve *a* superimposed on the curve *b*) or to vertical convection with a step-function distribution of the velocities (the curve *f* superimposed on the curve *b*), for the two kinds of mass motion broaden the spectral line in quite similar ways. Hence the value determined according to the method developed in

[13] C. Westgate, *Ap. J.*, **77**, 141, 1933.

[14] An ultraviolet spectrum of the same star taken at the McDonald Observatory has been published by O. Struve in *Ap. J.*, **90**, 699, 1939.

[15] O. Struve, *ibid.*, **74**, 225, 1931; **90**, 699, 1939; O. Struve and T. Dunham, Jr., *Ap. J.*, **77**, 321, 1933; C. E. Moore, *Contr. Princeton U. Obs.*, No. 20, 1945.

[16] A. B. Underhill, private communication.

Section IV can be either the rotational velocity, the maximum velocity of convective motion, or any combination of the two. Strictly speaking, we should compute a set of curves similar to Figure 4 for the convective motion, but the observational accuracy does not justify such tedious computation.

Thus we plot the observed profile on a logarithmic scale and fit it to one of the theoretical curves given in Figure 4. While weak and medium lines fit the theoretical curves well, medium-strong lines do not fit any of the computed rotational profiles. The reason for this will be discussed in Section VI. According to the method described in Section IV, we determine the rotational velocity, etc., from those lines which fit the computed curves. The results of the determination from 34 lines are given in Table 1.

The equivalent width (in angstrom units) of the line can be measured directly from the observed profile. This is given in the last column of the table. At the same time we can compute the equivalent width when γ, R_0, and $(\Delta\lambda)_R$ have been determined. The area under the curve $R_0 e^{-\gamma^2 z^2}$ is $R_0\sqrt{\pi}/\gamma$ in rotational units, or $R_0(\Delta\lambda)_R\sqrt{\pi}/\gamma$ after conversion into angstrom units. Equivalent widths thus determined are given in the sixth column of the table. We can see how good the agreement is between the values of the

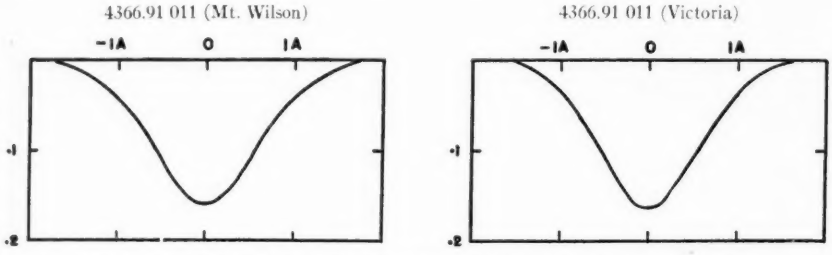

FIG. 5.—Comparison of line profiles traced from plates taken at two observatories

equivalent width measured directly and those determined indirectly. While the agreement shows the intrinsic consistency of the present method, it does not imply that the value of the rotational velocity thus determined is as accurate as that of the equivalent widths. Looking at the values of the rotational velocities determined from different lines, we see that the scatter is not so small as would be inferred from the agreement of the equivalent widths. The agreement of the computed equivalent widths with the measured values is due to the fact that the computed equivalent width does not change appreciably when we make an error in the determination of γ. On the other hand, the rotational velocity is sensitive to the value of γ, and we can easily make an error in the determination of γ because the difference in shape between profiles for different γ is not large. From Table 1 we find that the average of rotational velocities determined from all 34 lines is 62.5 km/sec, with a probable error of 7.3 km/sec.

The half-half-widths of the original lines can be computed from the expression $(\ln 2)^{1/2}(\Delta\lambda)_R/\gamma$ (in angstrom units). They are given in the fifth column of Table 1. The average value of the original half-half-width is 0.451 A. The average equivalent width (measured) is 1.840 A. The average value of the central depths, R_0, of the original lines is 0.197. Hence we can imagine an average line having a half-width of 0.902 A, an equivalent width of 1.840 A, and a central depth of 19.7 per cent situated at about λ 4300. This average original line is still rather broad and shallow, or, in other words, Doppler motion of the first kind other than rotation (which may be motion of large eddies, etc.) is operative in broadening the spectral lines. We can estimate the velocity of the motion (whatever type is present) by using the curve of line-width correlation.[1] At first, it seems im-

possible to determine the velocities by means of one single point on the curve of line-width correlation (corresponding to the average line) because we could make this single point fall on any part of the theoretical curve of line-width correlation. But we have two vitally important facts to guide us. First, the turbulent velocity of small eddies (including thermal motion), i.e., ξ_1, according to the notation used in the previous paper,[1] has a lower limit due to the thermal motion of the absorbing atoms. Second, the value ξ_1 should always be smaller than ξ_2, which is the velocity that should be derived from the line

TABLE 1

ROTATIONAL VELOCITIES, ETC., DETERMINED FROM DIFFERENT LINES

Wave Length	γ	R_0	Rot. Vel. (Km/Sec)	Half-half-width (A)	Equiv. Width (A)	Equiv. Width (A)
3791.41 *Si* III	3	0.200	79.1	0.278	0.118	0.119
3882.20 *O* II	2	.184	77.2	.416	.163	.160
3911.96 *O* II	1.25	.126	61.0	.530	.142	.142
3924.44 *Si* III	2	.145	60.6	.331	.102	.097
4035.09 *N* II	1	.091	44.9	.501	.097	.090
4043.54 *N* II	1.5	.112	64.4	.481	.115	.106
4072.16 *O* II	1	.178	43.4	.490	.186	.182
4075.87 *O* II	1.5	.263	56.5	.418	.240	.223
4089.29 *O* II	1.5	.242	61.1	.463	.238	.232
4119.22 *O* II	2	.195	56.2	.322	.134	.123
4164.96 *S* III	1.5	.080	45.5	.351	.060	.063
4176.16 *N* II	2	.127	64.5	.375	.101	.104
4179.67 *N* II	2	.094	52.6	.305	.060	.058
4185.46 *O* II	2	.195	64.0	.372	.154	.150
4241.79 *N* II	2	.212	66.7	.394	.177	.175
4253.98 *O* II	2	.266	63.6	.375	.212	.208
4319.63 *O* II	1.5	.221	65.5	.525	.247	.233
4336.86 *O* II	3	.368	85.9	.344	.270	.267
4345.56 *O* II	2	.288	68.4	.412	.253	.249
4366.90 *O* II	1	.180	51.5	.625	.239	.237
4395.95 *O* II	1	.094	46.7	.570	.114	.108
4414.91 *O* II	1.5	.302	57.1	.468	.301	.300
4447.03 *N* II	2	.224	71.4	.440	.210	.216
4452.38 *O* II	1.5	.123	73.5	.605	.158	.155
4574.78 *Si* III	1	.204	55.2	.701	.304	.314
4590.97 *O* II	1.5	.219	53.7	.456	.212	.212
4607.15 *N* II	3	.316	81.6	.349	.235	.228
4613.87 *N* II	2	.151	65.0	.416	.131	.126
4621.39 *N* II	1.5	.141	54.5	.465	.139	.132
4630.54 *N* II	0.9	.269	54.5	.780	.445	.432
4634.16 *N* III	2	.153	76.0	.489	.159	.149
4638.85 *O* II	2	.251	67.0	.431	.230	.234
4661.64 *O* II	2	.257	79.0	.512	.280	.270
4676.23 *O* II	2	0.224	56.5	0.366	0.171	0.167

profile and is therefore a superposition of velocities of large eddies, small eddies, thermal motion, etc. Moreover, because of the shallowness of the average line, we can see that ξ_1 must be much smaller than ξ_2. We estimate from the curve of line-width correlation that the value of ξ_2 is between 17 and 27 km/sec and $R_c\xi_1$ between 4 and 8 km/sec. Or, roughly, we can set ξ_2 equal to 22 km/sec and $R_c\xi_1$ to 6 km/sec. If we take the limiting central depth, R_c, for B stars to be 0.6, we get $\xi_1 = 10$ km/sec, and the Doppler velocity of the first kind other than rotation (or convection) is[1]

$$(\xi_2^2 - \xi_1^2)^{1/2} = 18 \text{ km/sec}.$$

The instrumental broadening of the high-dispersion coudé spectrograph at the Mount Wilson Observatory from which we obtained our spectrogram is very small and can be neglected.

VI. STUDY OF AVERAGE LINE PROFILES AND MODELS OF DOPPLER MOTION IN ATMOSPHERES OF SUPERGIANT STARS

Because of accidental errors involved in obtaining an individual line profile, the latter might not give a good representation of the true profile. Hence we have grouped the lines in Table 1 and computed average profiles for each group. The actual procedure is as

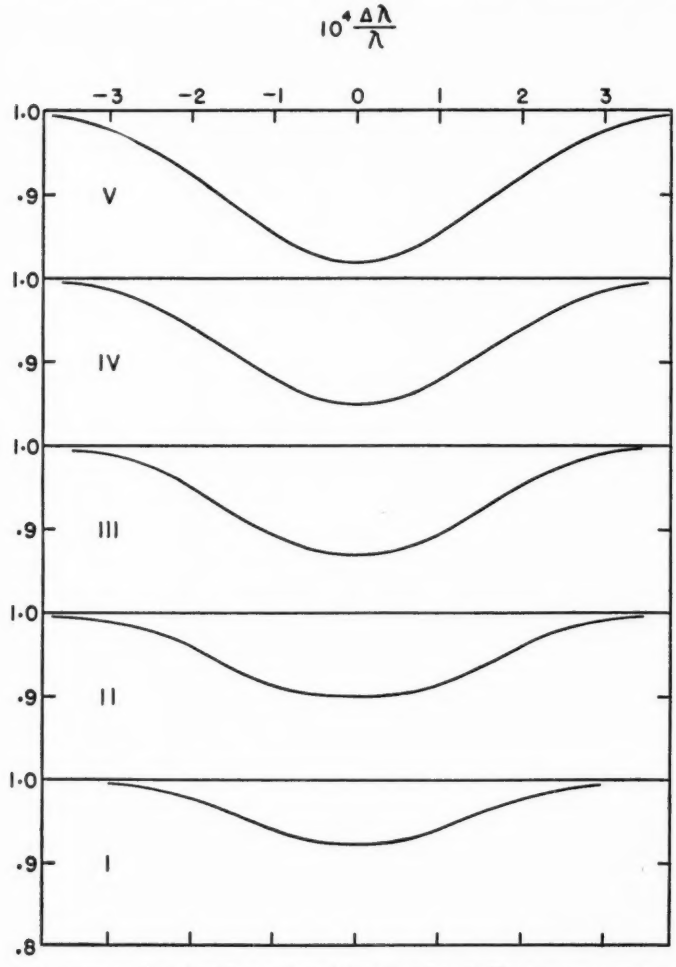

FIG. 6.—Average profiles of medium and weak lines in ρ Leonis. The average represents lines over a wide spectral region; it is therefore necessary to use the dimensionless scale ($\Delta\lambda/\lambda$) instead of angstrom units ($\Delta\lambda$). These average lines show clearly the character of rotational profiles (cf. Fig. 2).

follows: First, we divide the measured equivalent width by the corresponding wave length (i.e., W_λ/λ). Then we classify the lines in Table 1 into five groups according to the values of W_λ/λ. Next, we take the average value of the central depths of all lines in each group and normalize the central depths of these lines in each group to the average value. We plot these normalized line profiles on the scale of $\Delta\lambda/\lambda$ and derive an average profile from them. The results are given in Figure 6. From these average profiles we can determine the rotational velocity by the method given in Section IV. The fit of these curves to the theoretical rotational profiles (Fig. 4) is excellent. The results are given in Table 2, in which the weight represents the number of individual lines in each group. The last column represents the half-half-width of the original line unbroadened by rotation. We have expressed it in units of kilometers per second, because here we discuss the lines without referring to their locations in the spectrum. The weighted average of the rotational velocity is 61.0 km/sec, with a probable error of 3.0 km/sec. Hence the present determination is consistent with the value (62.5 ± 7.3 km/sec) determined in Section V from the individual lines. The dispersion here is much smaller, because we are concerned with average lines instead of with individual lines. The weighted mean value of the half-half-width is 33.6 km/sec (corresponding to a most probable velocity of 40.4 km/sec) as compared with the 31.6 km/sec (corresponding to a most probable velocity of 38.0 km/sec) determined in the previous section.

TABLE 2

ROTATIONAL VELOCITIES, ETC., DETERMINED FROM AVERAGE PROFILES

Group	$10^5(W_\lambda/\lambda)$	Weight	γ	Rot. Vel. (Km/Sec)	Half-half-width (Km/Sec)
I.....	2–3	8	1.5	59.0	33.0
II.....	3–4	6	2	69.0	28.8
III.....	4–5	7	1.5	60.0	33.4
IV.....	5–6	7	1.5	61.0	34.0
V.....	6–7	3	1	52.4	43.8
VI.....	8–11	4	<0.5	<25	≈45

We have also computed an average profile from four relatively strong[17] lines ($8 \times 10^{-5} < W_\lambda/\lambda < 11 \times 10^{-5}$). Three of them (λλ 3995.00 *N* II, 4552.65 *Si* III, and 4567.87 *Si* III) are not included in Table 1 because they do not fit any of the rotational profiles in Figure 4. The fourth line is λ 4630.54 *N* II, which, though included in Table 1, does not fit the theoretical profile ($\gamma = 0.9$) very well. The average profile of these medium-strong lines, like the individual ones, shows small rotational broadening. In fact, it resembles a Gaussian error-curve. We have illustrated this in Figure 7, in which the average profile is drawn as a solid line, while the Gaussian error-curve is drawn as a broken line. The half-half-width is measured to be 46.5 km/sec (corresponding to a most probable velocity of 55.8 km/sec). Assuming the original profile of these medium-strong lines to have a Gaussian form also, we find that γ must be less than 0.5. In other words, the rotational velocity would then be less than 25 km/sec. These values are given in the last row of Table 2.

Table 2 shows a tendency for the strong lines to give small rotational (or convective) velocities but large half-widths of the original lines, while the weak and medium lines indicate large rotational (or convective) velocities but small half-widths of the original

[17] They are weak compared to the *H* and *He* lines, which have not been considered. For example, λ 4471 *He* I is twice as strong as these lines.

lines. As the velocity difference is quite large, this cannot be due to accidental errors. Unless the assumption of a Gaussian profile for the original line should in some way lead to a spurious effect in the values of the three parameters for these moderately strong lines (a possibility that cannot now be definitely tested), this result should reveal some important physical fact concerning the atmosphere. Since the weak and medium lines are produced in the lower part of the atmosphere, this empirical result can be explained by assuming that regular mass motion (rotation or convection) prevails in the lower layers of the atmosphere. But in the outer parts of the atmosphere, the regular motion gradually breaks up into irregular mass motion (i.e., large-scale turbulence). Hence the velocity distribution of the mass motion in the upper atmosphere would be completely random. In other words, the broadened profile should follow the Gaussian error-curve as observed in the strong lines. Therefore, we suggest here two models for ρ Leonis, derived directly from the observed results. The first model requires that the star (being a super-

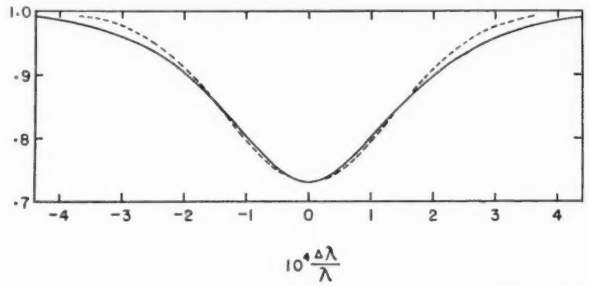

FIG. 7.—The average profile of strong lines. The solid line represents the average profile in ρ Leonis; the broken line, a Gaussian profile which has the same half-width as the average profile. The figure illustrates the fact that these strong lines are probably not broadened by rotation but rather by another kind of mass motion, such as large-scale turbulence. The latter might be created by differential rotation in the upper layers of the atmosphere.

giant) rotate, but rotation is not shared by the outermost layers of the atmosphere. Instead, turbulent motion is created in the upper part of the atmosphere. If this model were correct, it might be generally true for all supergiant stars which rotate. Also it explains the fact that rotation of supergiant stars is not frequently observed,[18] for the thick but rarefied layers of the atmosphere could veil the rotation of the star completely. Hence all supergiant stars in which large turbulet velocities are observed might rotate under the veil of the shell.

Another model involves a convective zone or, more probably, a field of prominences[7] in the atmosphere, the convective currents or prominences creating large-scale turbulence in the highest layers of the atmosphere.

In any case, the present investigation supports the idea that turbulence in stellar atmospheres is created either by convection or by differential rotation. Also it suggests that very low density favors the creation of turbulence. This is consistent with the recent theory that the turbulent velocity is higher in the upper atmosphere than in the lower atmosphere.[1, 4, 19]

We are grateful to Miss A. B. Underhill for sending us some reduced line profiles of ρ Leonis traced from a spectrogram taken at the Dominion Astrophysical Observatory, Victoria, B.C.

[18] O. Struve, *Stellar Evolution* (Princeton: Princeton University Press, 1950), p. 128.

[19] E.g., S. S. Huang, *Ap. J.*, **114**, 287, 1951.

THE SPECTROSCOPIC BINARY 12 COMAE BERENICES*

GEORGE H. HERBIG AND BEVERLY A. TURNER†
Lick Observatory, University of California
Received May 10, 1953

ABSTRACT

An examination of photoelectric and spectroscopic data for the spectroscopic binary 12 Comae Berenices has resulted in an interpretation of the system that is consistent with all the available evidence. The primary star has a spectral type near G0 III–IV, while the companion is of type A3. The mass ratio is near 2.

The spectrum of 12 Comae Berenices[1] was classified as composite by R. K. Young and W. E. Harper,[2] who assigned spectral types of dF and A to the components. R. J. Trumpler[3] classified the spectrum as gF4 + A. The radial velocity of the primary (the star of later type) was discovered to be variable by P. W. Merrill in 1910, and orbital elements were determined by Miss J. M. Vinter Hansen;[4] the period was found to be 396 days. Although she could detect no lines of the early-type star, Miss Vinter Hansen noted that the lines of the primary in the λ 4500 region were veiled, presumably by the continuous spectrum of the companion.

C. U. Cesco and J. Sahade[5] examined four McDonald Observatory spectrograms, taken in 1943, that covered the region λλ 3400–5500. They found no evidence of the spectrum of the secondary: the metallic absorption lines in the ultraviolet measured by them gave the velocity of the star of later type, as did a few hydrogen lines. Only the K line gave a discrepant velocity of −22 km/sec as compared to +11 km/sec from the other lines.

The photoelectric magnitude and color obtained for 12 Comae by O. J. Eggen[6] cannot be reconciled with the composite spectral type assigned by Trumpler, for, while the observed absolute magnitude (obtained from the apparent magnitude and the known distance modulus of the Coma cluster) is brighter than that of an F4 giant, as is to be expected, the observed color is redder than is normal for such a star. The presence of an early-type companion would make the combined color bluer than that of the primary alone.

H. F. Weaver[7] observed the veiling of the F-type features, but he could see no lines of the companion. He assigned a type of F8:p to the spectrum by making an allowance for the effect of the veiling upon the spectral-type assignment. On the other hand, the lines of an early-type star were observed at $H\delta$ and at the K line by W. P. Bidelman[8] and independently by Miss Nancy G. Roman.[9]

* *Contributions from the Lick Observatory*, Ser. II, No. 48.

† Lick Observatory Fellow, 1953–1954.

[1] $\alpha_{1900} = 12^h17^m.5$, $\delta_{1900} = +26°24'$; = Boss 3224 = HD 107700 (F5).

[2] *Pub. Dom. Ap. Obs. Victoria*, **3**, 3, 1924.

[3] *Lick Obs. Bull.*, **18** (No. 494), 167, 1938.

[4] *Lick Obs. Bull.*, **19** (No. 504), 101, 1940.

[5] *Ap. J.*, **99**, 317, 1944. We are indebted to the Yerkes and McDonald Observatories for the opportunity to examine the original spectrograms.

[6] *Ap. J.*, **111**, 414, 1950; *Contr. Lick Obs.*, Ser. II, No. 27.

[7] *Ap. J.*, **116**, 635, 1952; *Contr. Lick Obs.*, Ser. II, No. 44.

[8] Unpublished paper read at a meeting at the Yerkes Observatory in April, 1949. We wish to thank Dr. Bidelman for furnishing us with a copy of this paper.

[9] Private communication.

These conflicts between the interpretation of the spectrum of 12 Comae by different workers led the present writers to take up the study of this system on the basis of new material, in an attempt to clarify the situation. On January 26, 1950, a plate of 12 Comae was obtained with the coudé spectrograph of the 100-inch telescope at Mount Wilson. This spectrogram covered the region λλ 3500–5000 with a dispersion of 10 A/mm. The plate immediately demonstrated the presence of an early-type star: broad absorption wings on the hydrogen lines are fairly conspicuous at $H\delta$ and become outstanding in the higher Balmer lines. Their strength is entirely too great for an F-type star. Furthermore, the K line appears as a rather narrow core superimposed upon a wide, shallow absorption line. The veiling of the absorption lines of the primary star is very conspicuous on this spectrogram; but, since the exposure was made with the Wood grating, which has been reported to introduce considerable scattered light in the ultraviolet,[10] no quantitative measurements of the amount of veiling were attempted. More suitable for this purpose, as will be described later, are a number of additional spectrograms of 12 Comae that were obtained in the λλ 4000–5000 region with a dispersion of 19 A/mm at $H\gamma$, produced by a three-prism spectrograph and 16-inch camera on the 36-inch Lick refractor. These plates show the marked veiling of the lines of the star of later type at shorter wave lengths, as well as the wings on the $H\delta$ line of the primary. The λλ 3850–4000 region was necessarily observed with lower dispersion (26 and 53 A/mm at λ 3950) because of the low transmission of the 36-inch objective at those wave lengths. The McDonald spectrograms studied by Cesco and Sahade were compared also with spectra of standard stars taken with their instrument. On these plates the spectrum of 12 Comae in the near ultraviolet looks, superficially, much like that of β Cassiopeiae (F2 IV),[11] but the match is discrepant in several important details. The spectrum of 12 Comae can be satisfactorily explained only as the combination of an early A-type with a late F- or early G-type star; in the near ultraviolet, the two stars are approximately equal in brightness.

From an examination of the plates of 19 A/mm dispersion, we conclude that the spectral type of the primary star is very near G0. This classification is based on lines in the λλ 4400–4700 region that we believe are not affected by lines of the early-type star. In addition, the presence of the G band in moderate strength shows that the primary is not much earlier than G0 and cannot be later than G2. The considerable strength of the *CN* band head at λ 3883, when matched against standard spectra of stars of similar luminosity, indicates that the primary star must be later than F8. The earlier spectral types assigned by others probably arose from the effect of the weak K line and the strong hydrogen lines upon the type assignment. Both these features give spurious results because of the contribution of the companion.

The luminosity class of the primary of 12 Comae is not so certain because of the veiling of its absorption features. The G0 component seems definitely to be less luminous than both 31 Comae, of type G0 III (although the lines in 31 Comae are quite wide and precise comparison with 12 Comae is difficult with 19 A/mm dispersion), and ϕ Virginis (G2 III). On the other hand, it seems to be of somewhat higher luminosity than η Bootis (G0 IV) and μ Cancri (G2 IV). We therefore adopt a classification of G0 III–IV for the primary component of 12 Comae.

The magnitude of the Balmer jump in 12 Comae and the suppression of the continuum to the longward of the Balmer limit by the merging wings of the hydrogen lines show that the companion must be a late B- or early A-type star. Below λ 3650, the lines of the primary are still well seen, which must be due to the depression of the early-type con-

[10] See, e.g., L. H. Aller, *Ap. J.*, **104**, 345, 1946; and J. W. Chamberlain and L. H. Aller, *Ap. J.*, **114**, 54, 1951.

[11] The spectral types and luminosity classes used in this paper are on the *Revised Atlas System* of W. W. Morgan and P. C. Keenan (*Ap. J.*, **117**, 313, 1953). We are grateful to Dr. Morgan for allowing us to see a copy of a paper describing the *Revised System* in advance of publication.

tinuum by continuous Balmer absorption, as was suggested by Cesco and Sahade. Presumably the early-type star would become predominant at very short wave lengths. A comparison of the width and strength of the core of the K line in 12 Comae with standard A-type stars observed with the 53 A/mm dispersion yields a type of about A3 for the secondary.

The difference in magnitude between the two stars can be determined from the equivalent widths (or profiles, if spectrograms of sufficient resolving power are available) of lines in the composite spectrum, if their widths in single stars of the same type and luminosity are known. This technique has been used successfully by W. Petrie[12] in the study of spectroscopic binaries. Some difficulty was encountered in finding for the primary of 12 Comae a comparison star whose spectral type, luminosity, and line width were nearly enough the same. The comparison star finally chosen, ι Virginis (type F6 IV) is somewhat earlier than desirable, but it was the most satisfactory one that could be found. Only a minority of the giant stars in the interval F5–G2 have lines as sharp as those of 12 Comae when observed with a dispersion of 10–20 A/mm. Some otherwise satisfactory objects (such as ϵ Hydrae) could not be used because of the presence of companion stars.

Values of the equivalent widths determined in representative early A-type stars by other workers[13] were used in allowing for the effect of superposition of the early-type line spectrum upon that of the primary. The process of reduction was essentially that used by Petrie. The measurements were made at the K line and for lines in the vicinity of λ 4060 and λ 4450. The result is that

$$m_{\lambda\ 4200}(\text{A3 star}) - m_{\lambda\ 4200}(\text{G star}) = -0.1 \pm 0.3\ (\text{p.e.})\ \text{mag.},$$

where the probable error is entirely an internal one, derived from the interagreement of the different lines. This result that, photographically, the two stars are essentially equal in brightness has the following consequences. Since the combined photographic absolute magnitude[6] is +0.66, then

$$M_{pg}(\text{A3}) = M_{pg}\,(\text{G}) = +1.41\,.$$

The color index of the early-type star should be about +0.02 mag.; in order to reproduce the combined $M_{vis} = +0.27$, the star of later type must have $M_{vis} = +0.75$, so that its color index is +0.66 mag. For a star of type G0 III–IV, however, we should expect a color index in the neighborhood of +0.55 mag. from the run of color with spectral type in stars of luminosity classes III and IV. This discrepancy in the color of the G-type star may be due either to an error in the assumption of precise photographic equality of the two components or to the fact that the spectral class of the primary is G2 rather than G0, or both. We do not believe that our data are sufficiently precise to rule out either possibility.

The general correctness of this interpretation of 12 Comae is supported by two additional pieces of evidence: (1) It will be noted that the value of $M_{pg} = +1.4$ for the early-type component of 12 Comae, which was obtained spectrophotometrically, is that to be expected[14] for a main-sequence star of spectral type between A2 and A3, in agreement with the type estimated from the appearance of the K line. (2) A plausible value of the mass ratio is obtained from measurements of the displacement of the K line throughout the cycle. The radial-velocity results available to us are summarized in Table 1.

The phases and predicted velocities in Table 1 were computed from Miss Vinter Hansen's elements. The measured velocities of the G-type star for the three Lick spectro-

[12] *J.R.A.S. Canada*, **37**, 277, 1943.

[13] γ Gem (type A1): L. H. Aller, *Ap. J.*, **96**, 321, 1942; W. Buscombe, *Ap. J.*, **114**, 73, 1951. 95 Leo (type A4): Chamberlain and Aller, *Ap. J.*, **114**, 52, 1951.

[14] P. C. Keenan and W. W. Morgan, *Astrophysics* (New York: McGraw-Hill Book Co., Inc., 1951), p. 23.

grams depend upon laboratory wave lengths of eight relatively unblended lines of *Fe* I in the region λλ 3900–4071. The main difficulty in measuring the radial velocity of the primary component of 12 Comae in this wave-length region is the uncertainty in setting upon the heavily veiled lines. Tests on other stars have indicated that the systematic correction required to reduce velocities obtained with this spectrograph to the system of *Lick Publications*, Volume **16,** is quite small. Therefore, we may correlate the K-line

TABLE 1

RADIAL VELOCITIES OF 12 COMAE

PLATE	JD 2430000+	PHASE (DAYS)	PREDICTED VELOCITY (KM/SEC)	OBSERVED VELOCITY (KM/SEC)	
				G Star	K Line
McDonald*. . .	0912.8	26.0	+13.5	+11	−22
Mt. Wilson†. .	3307.91	42.2	+15.7	+16	−31
35464‡.	4236.69	178.0	−24.2	−30	+39
36361‡.	4428.98	370.2	+ 6.8	+12	−13
36430‡.	4439.92	381.2	+ 8.2	+ 9	−28

* Dispersion 40 A/mm at K; mean of 4 plates.

† Dispersion 10 A/mm.

‡ Lick spectrograms; dispersion 26 A/mm at λ 3950.

velocities with the predicted G-star velocities for the same phase, both measured from the γ-velocity determined by Miss Vinter Hansen, in order to determine the mass ratio. A value of

$$\frac{m\,(\text{G star})}{m\,(\text{A3 star})} \cong 2$$

is found, which should be regarded as only a very rough determination of the mass ratio, to be superseded once a suitable series of spectrograms covering the whole cycle becomes available. The velocity results are presented here only to demonstrate that the displacement of the core of the K line, both in amount and with phase, is consistent with its identification as part of the spectrum of an A-type component.

It is concluded that all the available observational evidence is in acceptable agreement with the interpretation of 12 Comae as a binary, composed of a primary star of spectral type near G0 and luminosity perhaps somewhat below that of a normal giant, and a main-sequence star of spectral type about A3.

THE LIGHT-VARIATIONS OF HD 217050

MERLE F. WALKER*

Berkeley Astronomical Department, University of California

Received April 7, 1953; revised May 27, 1953

ABSTRACT

Photometric observations of HD 217050 in 1950, 1951, and 1952 reveal the occurrence of light-minima having depths ranging up to 0.20 mag. The duration of the minima is about 0.4 day, and the period of repetition is about 0.8 day. Changes occur in both the length of the period and the phase of minimum light. The light-variations are not accompanied by any large alterations in the spectrum or velocity of the shell. It is suggested that the observations might be explained by temporary dark disturbances on the surface of the star which are carried across its disk by the stellar rotation.

Two-color photometric observations of the shell star HD 217050[1] were made at the Lick Observatory, concurrently with observations of the β Canis Majoris star 16 Lacertae, in 1950,[2] 1951, and 1952. With the exception of August 13, 1951, when the Crossley reflector was used, all the observations were made with the 12-inch Lick refractor. The photometric equipment, together with the methods of observation and reduction, have already been described.[2, 3, 4]

As in the case of 16 Lacertae, the comparison star used was 14 Lacertae. Observations of HD 217227 were made on several nights to check the constancy of 14 Lacertae, since the latter appears to be variable from night to night by a few hundredths of a magnitude.[3] The nightly mean blue-magnitude differences, HD 217227 *minus* 14 Lacertae, are given in Table 1.

TABLE 1

BLUE-MAGNITUDE DIFFERENCE, HD 217227 *minus* 14 LACERTAE

Date U.T.	Δ Mag.	Date U.T.	Δ Mag.
1951:		*1952—Continued:*	
Aug. 25	+1.124	Aug. 12	+1.112
Sept. 8	+1.078	13	+1.124
21	+1.123	14	+1.098
28	+1.084	15	+1.095
Oct. 6	+1.128	16	+1.096
1952:		17	+1.096
Aug. 10	+1.114	18	+1.096
11	+1.096		

The light- and color-curves are shown in Figures 1–5. The dots represent blue-magnitude differences, and the circles, color differences, HD 217050 *minus* 14 Lacertae, reduced to no atmosphere. The most striking feature of the observations is that the star is normally bright and experiences occasional decreases in light which appear to have about the same duration but different amplitudes. The largest observed decrease in

* Since October, 1952, Carnegie Fellow at the Mount Wilson and Palomar Observatories.

[1] HR 8731 = MWC 394 = BD+47°3985; R.A. = 22^h52^m7; Decl. = +48°09′, 1900; vis. mag. = 5.20; Sp. = B5ne.

[2] M. F. Walker, *Pub. A.S.P.*, **63**, 35, 1951.

[3] M. F. Walker, *Ap. J.*, **116**, 106, 1952.

[4] M. F. Walker, *Pub. A.S.P.*, **65**, 39, 1953.

brightness is about 0.20 mag. There is also a suggestion that the star becomes slightly redder while it is passing through a light-minimum. The amount of this color variation seems to be about 0.01 mag. for every 0.10 mag. change in light. In addition, even making allowance for the variability of 14 Lacertae, the level of maximum light of HD 217050 appears to change by several hundredths of a magnitude from night to night.

Table 2 lists the observed times of minimum light. Some of the times of minimum are uncertain by several hundredths of a day, owing to the shortness of the runs. On several nights the amplitude was so small that it is difficult to decide whether or not the variation was real.

Since the duration of the minima, estimated from the shapes of the curves, is around 0.4 day, the period of the variation, if a period exists, could hardly be less than about 0.8 day. Thus the minima observed on successive nights, such as August 14 and 15, 1951, August 12 and 13, 1952, and August 17 and 18, 1952, must represent the actual interval

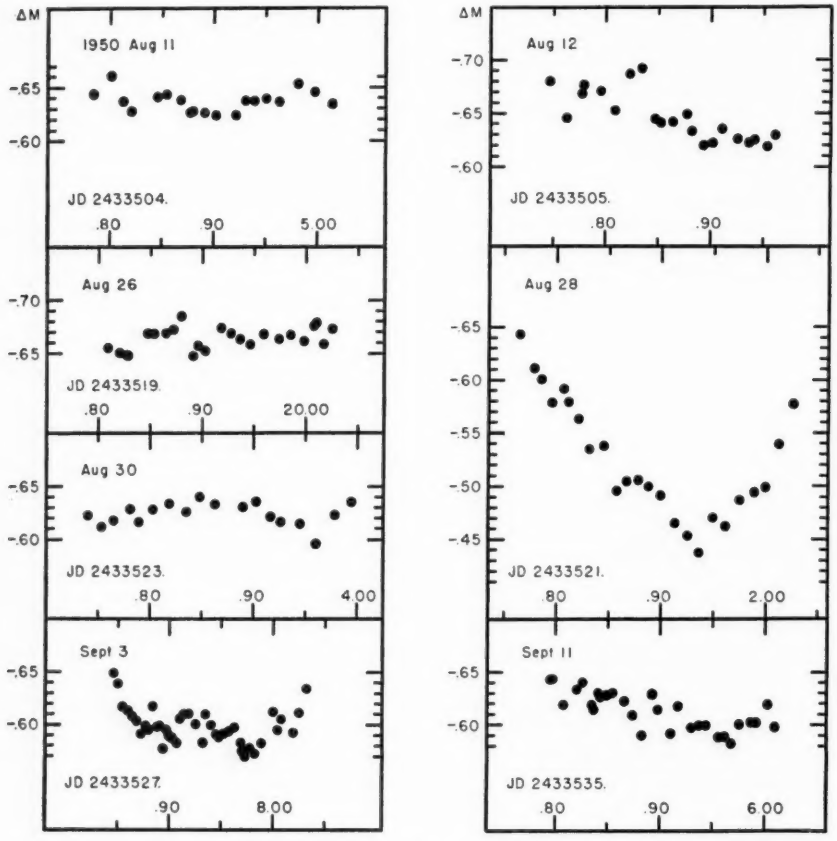

FIG. 1.—Photometric observations of HD 217050 in 1950. The ordinate is the blue-magnitude difference, HD 217050 *minus* 14 Lacertae, reduced to no atmosphere.

of repetition of the phenomenon. Yet, if we attempt to find a period close to 0.8 day which will represent the observed minima, we obtain rather curious results.

All the minima observed in 1951 can be represented by a period of 0.7364 day, as is shown by the residuals between the observed and predicted minima in Table 2. At the same time, this period predicts minima on several nights when the brightness of the star was observed to be constant. These dates are JD 2433884.05, 889.94, 904.66, 917.92, and 926.00. Thus, if this period is correct, the amplitude of the light-variation decreased to

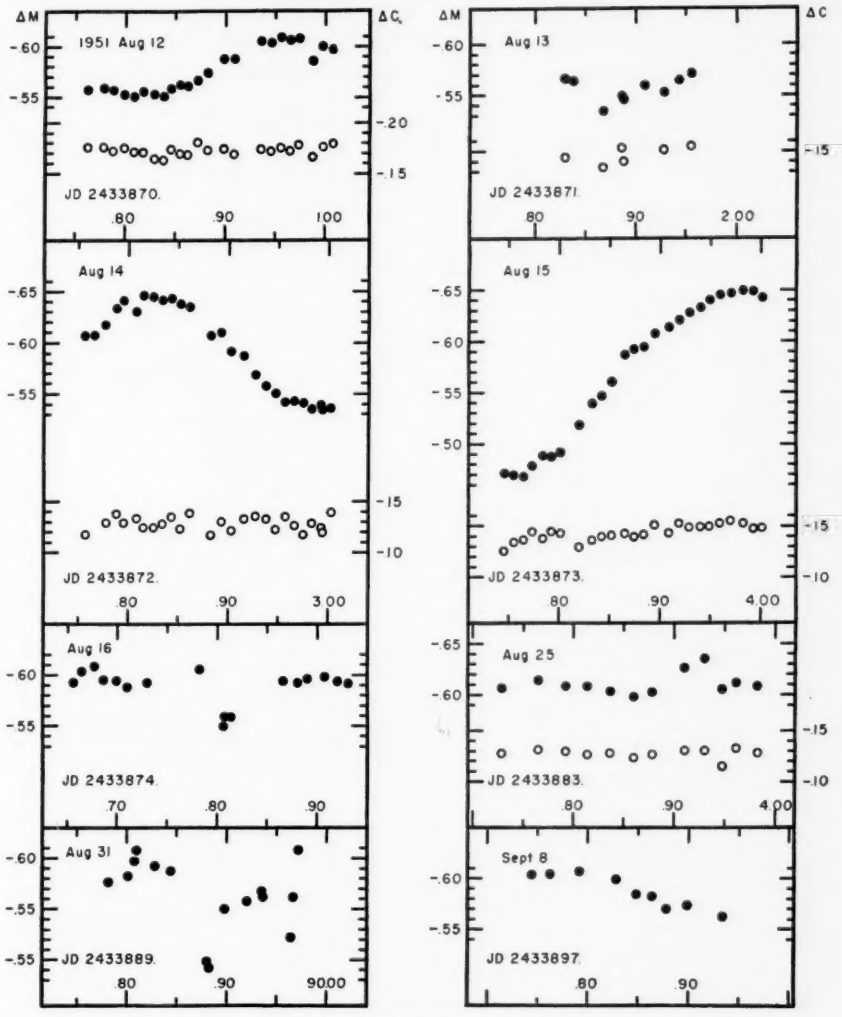

FIG. 2.—Photometric observations of HD 217050 in 1951. The dots represent blue-magnitude differences, and the circles color differences, HD 217050 *minus* 14 Lacertae, reduced to no atmosphere.

zero, increased again, and then once more died away. There are not enough observations to make certain the unique determination of the period; yet it must be nearly correct, from the spacing of the two well-determined minima on August 14 and 15.

The 1952 observations cannot be fitted with the 0.7364-day period. The minima of August 12, 13, and 16 can be represented by a period of 0.800 day. However, this period will not represent the other observed minima, nor has any other period been found which will represent all of them. It is possible that the correct period has not been found or that the phenomenon is not strictly periodic. On the other hand, it seems more likely, from the available material, that changes occur in the phase of the light-variation: The period of 0.800 day represented the observations on August 12–16. Yet on the following two

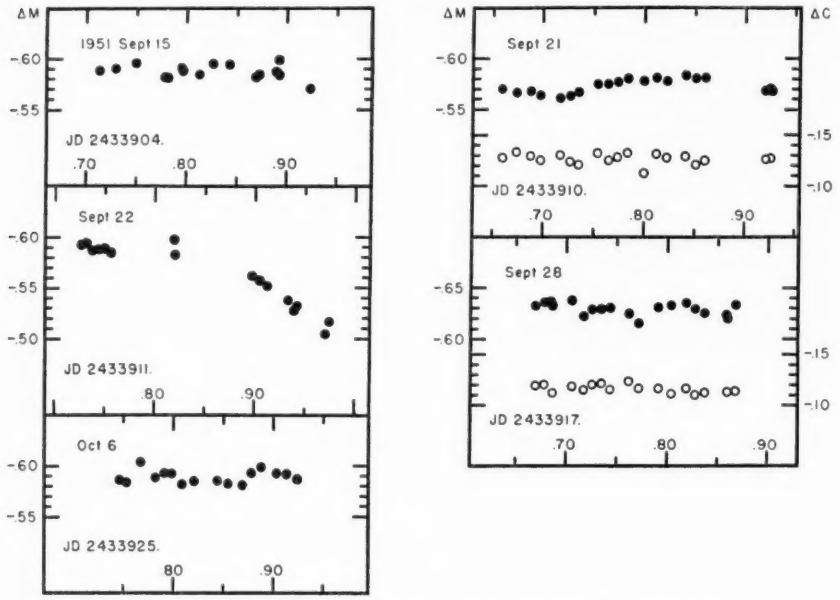

FIG. 3.—Photometric observations of HD 217050 in 1951. Ordinates and symbols as in Fig. 2

nights a pair of minima occurred, separated by about 0.8 day, but 0.2 day later than the predicted times.

Owing to these difficulties, no attempt has been made to combine the observations from the different years. The residuals in Table 2 between the observed minima and those predicted by the two periods discussed above refer to epochs chosen in each season. The few 1950 observations are too scattered to make worth while an attempt to fit a period to them.

In an effort to ascertain whether the changes in light are paralleled by variations in the spectrum or radial velocity of the star, several spectrograms were obtained during, or on the same nights as, the photometric observations. In 1951, one Mills spectrogram was obtained on each of five nights when photometric observations were made. In August, 1952, H. Abt secured another spectrogram for me with the two-prism spectrograph of the 36-inch Lick refractor and a 12-inch camera. The dispersion of the Mills plates is 11 A/mm at 4500 A, while the dispersion of the two-prism, 12-inch plate is

37 A/mm at $H\gamma$. The dates of the spectrograms and the velocities derived from them are shown in Table 3.

In order to eliminate the effects of misidentification or blending of lines within this group of observations, only seven shell lines of *Fe* II and *Ti* II, which were measured on all the plates, were used in deriving the velocities. The probable error of a single Mills

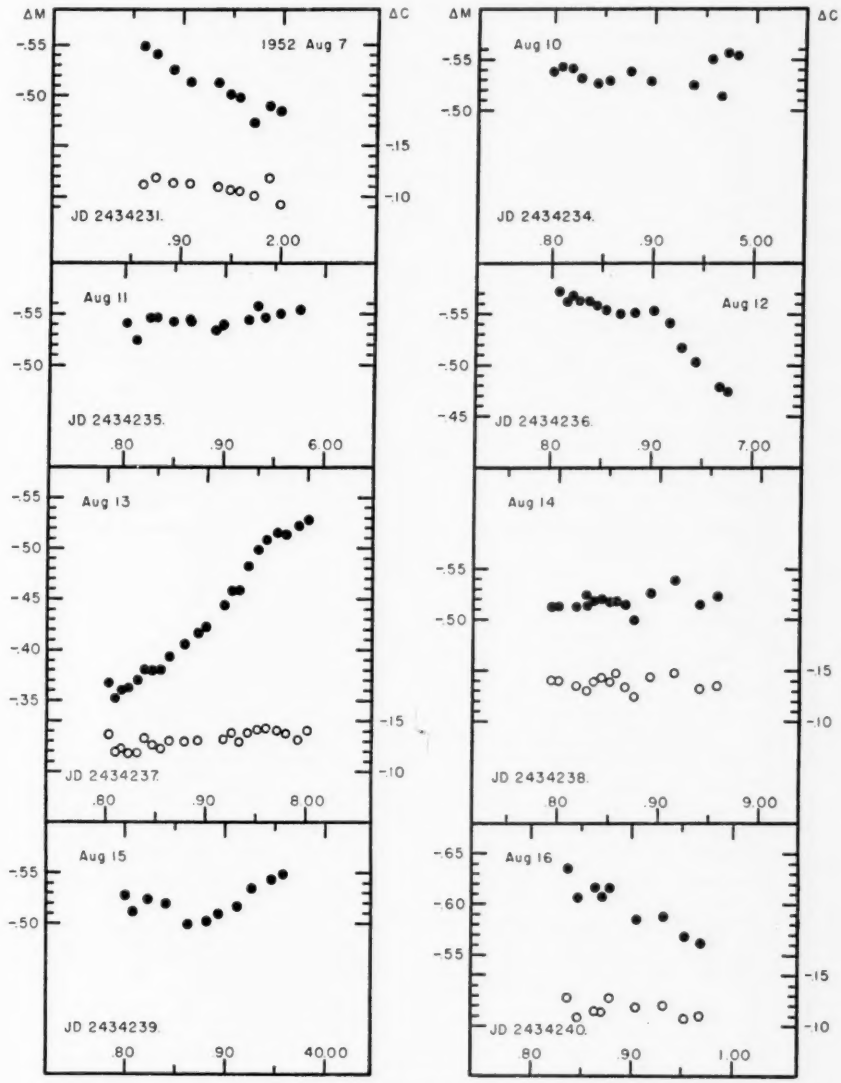

FIG. 4.—Photometric observations of HD 217050 in 1952. Ordinates and symbols as in Fig. 2.

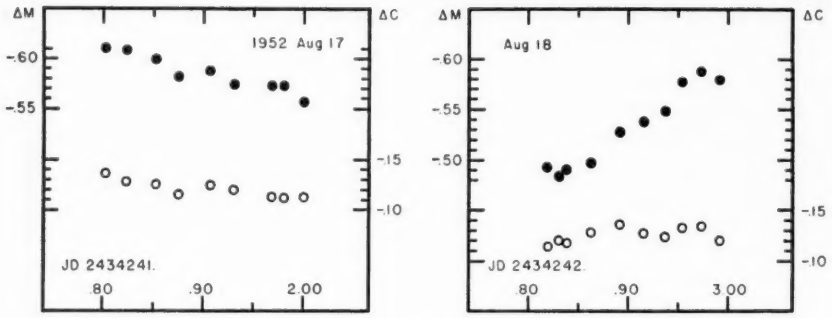

FIG. 5.—Photometric observations of HD 217050 in 1952. Ordinates and symbols as in Fig. 2

TABLE 2

OBSERVED MINIMA OF HD 217050

JD	O−C (DAY)		JD	O−C (DAY)	
	$P=0.7364$	$P=0.800$		$P=0.7364$	$P=0.800$
2433			2434		
506.00			232.06*	0.00	−0.14
521.94			237.01*	− .20	+ .01
535.96			237.80	− .15	.00
870.79	0.00	0.00	241.00*	+ .10	.00
873.01	+ .01	− .18	242.00*	− .37	+ .20
873.75	+ .01	− .24	242.80*	−0.31	+0.20
898.00*	− .04	+ .01			
912.03*	0.00	−0.36			

* Uncertain by several hundredths of a day.

TABLE 3

RADIAL VELOCITIES OF HD 217050

JD	Radial Velocity (Km/Sec)	JD	Radial Velocity (Km/Sec)	JD	Radial Velocity (Km/Sec)
2433		2434		2434	
897.968	−21.8	326.631	−20.0	327.624	−16.3
910.892	−20.4	.642	−16.3	.636	−14.8
911.858	−23.3	.653	−17.4	.649	−15.3
917.896	−20.4	.665	−17.4	.660	−16.5
925.967	−18.3	.676	−17.5	.672	−12.6
2434		.688	−14.9	.685	−19.6
237.883	−21.7	.699	−14.3	.697	−13.8
326.608	−14.4	327.600	−19.0		
.619	−14.1	.612	−15.7		

plate is ± 2.0 km/sec, and for the two-prism, 12-inch plate it is ± 4.7 km/sec. The velocities from all the plates agree quite well, and their mean agrees closely with the means of other published velocities.[5, 6] The 1952 observation with the two-prism, 12-inch spectrograph was the only plate obtained during a light-minimum. Since it yields a velocity which is comparable to the Mills velocities, it appears that no large change in velocity occurred during the light-minimum.

It is certain, from tracings of the spectra, that no large changes took place in the appearance of the spectrum. Owing to the lower dispersion of the two-prism, 12-inch spectrograph and the fact that only a single plate is available, it is not possible to determine whether very small changes occurred during the light-minimum. O. Struve[5] suspected that changes in the intensities of the α Cygni lines take place within a few days. If such variations are present in the series of Mills plates, they are just at the limit of detection. On a few of the plates some of the lines appear slightly stronger, but the variations are so small that one would require spectra of higher dispersion, as well as several plates on each night, in order to be certain of their reality. The general appearance of the spectrum is still very similar to the description of the 1940 spectrum given by R. B. Baldwin.[7]

Two series of spectra were obtained by O. Struve on two successive nights in November, 1952, to investigate possible short-period variations in the spectrum or velocity. The spectra were obtained with the Cassegrain spectrograph of the 60-inch Mount Wilson reflector and an 18-inch camera. The dispersion is 38 A/mm at $H\gamma$. The resulting velocities, measured by S. M. Kung, are listed in Table 3, together with those discussed previously. The average probable error of a single velocity is ± 3.8 km/sec. The velocities show no short-period fluctuations significantly larger than the probable errors of the observations. However, the difference of -5 km/sec between the mean of these velocities and the mean of the Mills plates may be real. Struve suspects that changes in the spectrum may have occurred during each of the runs. However, the effects are again just at the limit of detection.

The nature of the light-variations, together with the shortness of the period and the fact that the observations cannot all be represented by one period, makes it difficult to interpret the observed phenomena in terms either of binary motion or of pulsation. A possible explanation is that the light-variations are caused by temporary disturbances which form on or near the surface of the star and are carried across its disk by the stellar rotation. The passage of a dark, cooler region across the visible hemisphere of the star could account for the light-variation and possible color variations, as well as for the change in the amplitudes of the minima, as the disturbance grew and diminished in size and intensity. One objection to this explanation is the large size required for the disturbances. Even assuming that the star has a limb-darkening coefficient of 0.5 and that the disturbed region is completely opaque, the radius of the disturbance would have to be about 0.4 that of the star in order to produce the observed decrease in light of 0.20 mag.

If this interpretation is correct, then the period of light-variation should be equal to the rotational period of the star. Hence this value, together with the observed rotational velocity of the star, ought to give a radius which is consistent with the dimensions to be expected in a star of this spectral class. A. Slettebak,[8] from an analysis of the width of the photospheric *He* I 4026 line, has derived a rotational velocity for the star of $v \sin i = 380$ km/sec, with an uncertainty of from 40 to 70 km/sec. Since HD 217050 is a shell star, we may assume that i is near 90°. Using 0.7364 day for the rotational period, the radius of the star is then 4.0×10^6 km, $\pm 0.7 \times 10^6$ km, owing to the uncertainty in v

[5] O. Struve, *Ap. J.*, **99**, 205, 1944.

[6] E. M. and G. R. Burbidge, *Ap. J.*, **113**, 703, 1951.

[7] *Ap. J.*, **97**, 388, 1943.

[8] *Ap. J.*, **110**, 498, 1949.

sin i. According to Kopal and Treuenfels,[9] the average radius of a main-sequence B5 star, as determined from studies of eclipsing binaries, is 3.1×10^6 km, with a spread of about $\pm 1.1 \times 10^6$ km. Thus the radius obtained for HD 217050 does agree quite well with the value we would expect for a star of its spectral type.

If this star possesses an equatorial acceleration like the sun, the observed differences in the period of the light-minima might result from our observing disturbances located at different latitudes on the surface of the star. If the percentage variation in the value of the rotational period with latitude is the same as in the sun, a difference in latitude of 36° would be required to explain the two periods of 0.7364 and 0.800 day found in 1951 and 1952, respectively. This difference seems rather large, but there is no assurance that the variation with latitude would be the same in both stars. Alternatively, we might suppose that the disturbances drift with differing velocities over the surface of the star.

Also, on this hypothesis, the variation in phase of the observed minima might be explained by the development of disturbances at different longitudes on the surface of the star. In addition, we might expect the observed fact that little or no change takes place in the spectrum or velocity of the shell during the light-minima. However, changes in the rotational profiles of the photospheric lines might be expected during the minima; simultaneous spectroscopic and photometric observations will be required to ascertain whether or not this occurs.

Although the concept of disturbances on the surface of the star accounts fairly well for the observations, it must be remembered that the observational material is not sufficient to permit a definite conclusion to be reached as to the cause of the phenomena. The interpretation proposed here can be regarded only as a working hypothesis. Whether or not this hypothesis is correct, the present observations do indicate the desirability of investigating the problem of short-period variations in the Be stars.

It is a pleasure to thank Dr. C. D. Shane for the use of the Lick telescopes, Dr. H. Abt for obtaining a spectrogram for me, and Dr. P. W. Merrill for several stimulating discussions of this problem.

[9] *Harvard Circ.*, No. 457, 1951.

LIGHT-VARIATIONS OF PECULIAR A STARS

SANFORD S. PROVIN
Yerkes Observatory
Received June 19, 1953

ABSTRACT

Light-curves have been established for three peculiar A stars: ϵ Ursae Majoris, χ Serpentis, and HD 224801. A new light-curve for α^2 Canum Venaticorum is presented. Results on thirteen other stars are given in tabular form. A period of the line-intensity variation of 21 Comae has been determined (Appendix 1). In Appendix 2, colors of twenty peculiar A stars are given.

I. INTRODUCTION

The peculiar A stars have recently come into prominence in astronomy as stars which frequently show large magnetic fields. The study of peculiar A stars began in 1906, when Sir Norman Lockyer and F. E. Baxandall[1] found that some absorption lines in the stars α Andromedae and ϵ Ursae Majoris undergo changes in intensity. In the same year Ludendorff[2] announced the variability of lines in α^2 Canum Venaticorum. In the years since 1906 the number of known peculiar A stars has grown steadily, and it is now clear that at least 10 per cent of all A stars are peculiar, in that lines of one or more groups of elements are strong in the spectrum. The peculiar A stars fall into two groups: (1) those with absorption lines some of which are abnormal but constant in intensity and (2) those with absorption lines some of which vary periodically (the spectrum variables). The study of brightness changes of peculiar A stars was initiated by Guthnick and Prager[3] in 1914, when α^2 Canum Venaticorum was observed. This star has been observed several times since 1914.[4] Two other stars have been observed previously for variation in total light, viz., ϵ Ursae Majoris[5] and HD 125248.[6]

The present investigation was undertaken with a view to extending our knowledge of the light-variations of peculiar A stars. The work was divided into two parts: (1) intensive observation of those stars, accessible at Yerkes Observatory, known to be spectrum variables and/or to have magnetic fields and (2) observation of a selected number of peculiar A stars that show no known line-intensity changes or magnetic fields.

II. EQUIPMENT AND PROCEDURE

The observations were made with two telescopes: the 12-inch refractor of the Yerkes Observatory and the 13-inch reflector of the McDonald Observatory. The measures were made at two effective wave lengths at Yerkes and at three effective wave lengths at McDonald. The yellow ($\lambda_{eff} \sim 5500$) and blue ($\lambda_{eff} \sim 4400$) were isolated by a Corning 3384 filter and by a cemented Corning 5030 plus Schott GG-13 filter, respectively. The ultraviolet ($\lambda_{eff} \sim 3550$) was isolated by a Corning 9863 filter for the third effective wave length at McDonald.

In this investigation two comparison stars were used when suitable near-by stars were available. The choice of comparison stars was made on the basis of color and no known

[1] *Proc. R. Soc.*, *A*, London, **77**, 550, 1906.

[2] *A.N.*, **173**, 4, 1906.

[3] *Veröff. Sternw. Berlin-Babelsberg*, **1**, 44, 1914.

[4] M. Gussow, *A.N.*, **229**, 199, 1926–1927; P. Guthnick, *A.N.*, **205**, 100, 1917–1918; W. S. Tai, *M.N.*, **100**, 94, 1939; Nikonov and Brodskaya, *Bull. Abastumani Ap. Obs.*, **11**, 7, 1950.

[5] P. Guthnick, *Sitz. Preuss. Akad. Berlin*, No. 29, p. 657, 1931.

[6] Stibbs, *M.N.*, **110**, 395, 1950.

evidence of variability. In the reductions of the observations, mean extinction coefficients, for stars of about class A0, were used.[7]

III. THE OBSERVATIONS

Of the seventeen stars investigated, four show well-defined light-variation. These stars will be considered in detail, and the results on the thirteen other stars will be presented in tabular form. Light-curves of three peculiar A stars have been published previously by the writer.[8]

ϵ URSAE MAJORIS

ϵ Ursae Majoris is classified as A0p in the *Henry Draper Catalogue*. Several lines in the spectrum show abnormal intensities. Because of its brightness (1.69 mag.), it has been the subject of a number of investigations, notably by P. Guthnick,[9] Swensson,[10] and Struve and Hiltner.[11]

Guthnick found that the period of this spectrum variable is 5.0887 days. Observations by Struve and Hiltner and again by Swensson indicated that the minima of *Ca* II K were occurring later than the times predicted by Guthnick's period and epoch, by about 0.25 day. This would indicate a period slightly longer than 5.0887 days. Spectra taken on eleven nights during April–May, 1952, indicate that a minimum occurred about JD 2434130.9. The minimum predicted by Guthnick's elements occurs on JD 2434131.124, or about 0.2 day later than that found by the present series of plates. In view of the foregoing, it is concluded that Guthnick's elements predict the minima of *Ca* II K correctly.

Observations of the star's brightness were also carried out by Guthnick.[9] He found evidence of variation. In the present investigation, observations were made on seventeen nights in 1952. The star δ Ursae Majoris (A3; 3^m27) was used for comparison. The observations are compiled in Table 1 and are plotted against phase in Figure 1. The observations show that ϵ Ursae Majoris varies in both yellow and blue light with amplitudes near 0.025 mag. There is little or no color change. Maximum light occurs near *Ca* II minimum intensity. The light-curve has two maxima separated by about $\frac{1}{2}$ period. It is noted that the two minima correspond to the phases when Struve and Hiltner[11] found that a number of lines in the spectrum of the star are double. If one compares the light-variation with Guthnick's velocity-curve (range 4 km/sec), it is found that maximum light occurs at the mean velocity when there is a change from approach to recession.

α^2 CANUM VENATICORUM

This star is designated as A0p in the *Henry Draper Catalogue*. Since it is also a bright star (2.90 mag.), it has been the subject of many investigations. In fact, α^2 Canum Venaticorum is the most extensively studied peculiar A star. Most of the investigations have been concerned with its spectrum; but the constancy of light was subject to investigation as early as 1914 by Guthnick and Prager.[3] They found that there was a range in brightness of 0.051 mag. M. Gussow[4] also observed the light of the star in 1925–1926 and found an amplitude of 0.034 mag. W. S. Tai[4] found an amplitude of 0.035 mag., and Nikonov and Brodskaya[4] found a change in color amounting to 0.06 mag.

In the present investigation the star was observed on nine nights. As comparison stars

[7] In the reductions of those observations made at McDonald Observatory it was necessary to take into account the dependence of the extinction coefficients on color if the stars were observed over large ranges of sec z.

[8] 73 Dra and ϵ Cas: *Ap. J.*, **117**, 21, 1953; and 56 Ari: *ibid.* (in press).

[9] *Sitz. Preuss. Akad. Berlin*, No. 27, 1931; No. 30, 1934.

[10] *Ap. J.*, **99**, 258, 1944.

[11] *Ap. J.*, **98**, 225, 1943.

14 C Vn (B9; 5^m15), HR 4875 (A2; 5^m86), and 15 C Vn (B9; 6^m22) have been used. The first, 14 C Vn, was suspected by Baker[12] of being a variable with rapid fluctuations and a range of 0.2 mag. Gussow[4] checked the constancy of the star during her investigation of α^2 C Vn and found no large fluctuations. In the present series of observations the comparisons of 15 C Vn with 14 C Vn (the mean of only two observations a night) show no deviations greater than 0.008 mag. from the mean. However, the star HR 4875 does show large residuals (0.02 mag.) when compared with both 14 and 15 C Vn. From these results it is concluded that 14 C Vn and 15 C Vn are constant in light and that HR 4875 is not. The observations are compiled in Table 2 and plotted against phase in Figure 2. Zero phase corresponds to *Eu* II maximum, according to the elements given by Miss G.

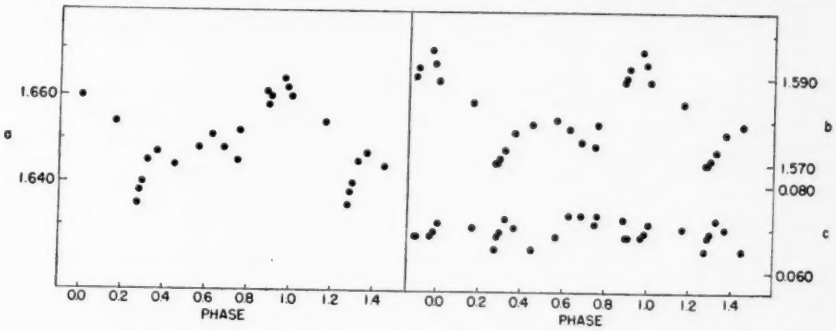

FIG. 1.—δ U Ma − ϵ U Ma: *a*, $\lambda_{eff} \sim 4400$; *b*, $\lambda_{eff} \sim 5500$; *c*, color

TABLE 1

PHOTOMETRIC OBSERVATIONS OF ϵ URSAE MAJORIS

DATE, 1952 U.T.	PHASE $P = 5.0887$	δ UMa − ϵ UMa		
		V	*B*	*C*
Jan. 24.360	0.279	1.570	1.635	0.065
27.448	.886	1.589	1.661	.072
29.467	.283	1.570	1.638	.068
Feb. 10.408	.629	1.578	1.651	.073
17.313	.986	1.593	1.662	.069
22.313	.969	1.596	1.664	.068
Mar. 17.313	.685	1.575	1.648	.073
Apr. 8.292	.004	1.589	1.660	.071
15.230	.368	1.577	1.647	.070
16.230	.564	1.580	1.648	.068
17.180	.751	1.574	1.645	.071
25.170	.321	1.573	1.645	.072
28.085	.894	1.590	1.658	.068
28.156	.908	1.592	1.660	.068
30.145	.299	1.571	1.640	.069
May 11.097	.451	1.579	1.644	.065
June 4.105	.169	1.584	1.654	.070
7.113	0.760	1.579	1.652	0.073

[12] *Pop. Astr.*, **34**, 148, 1926.

Farnsworth.[13] The observations have been corrected for the light of the companion, α^1 C Vn (F0; 5^m39).

The observations confirm the variation found by others. The amplitudes are 0.050 mag. in the yellow and 0.030 in the blue, with a color change of 0.02. The star is bluest at minimum light. The different ranges in the two colors will account for the diverse results obtained by the early observers. Miss Gussow's work was done with a potassium cell,

TABLE 2

PHOTOMETRIC OBSERVATIONS OF α^2 C Vn

DATE, 1952 U.T.	PHASE $P = 5.46939$	14 C Vn − α^2 C Vn			HR 4875 *minus* 14 C Vn	15 C Vn *minus* 14 C Vn	15 C Vn *minus* HR 4875
		Y	*B*	*C*	*Y*	*Y*	*Y*
Feb. 22.348	0.376	2.379	2.393	+0.014	0.725	.....	.....
Mar. 17.308	.757	2.401	2.398	− .003	.730	.....	.....
Apr. 8.320	.781	2.402	2.403	+ .001	.716	.....	.....
15.344	.065	2.426	2.418	− .008	.746	1.040	0.294
16.302	.241	2.398	2.402	+ .004	.731	1.045	.314
17.240	.412	2.374	2.383	+ .009	.720	1.035	.315
28.125	.402	2.376	2.390	+ .014	.706	1.043	.337
30.210	.784	2.404	2.400	− .004	0.721	1.036	0.315
May 12.210	0.795	2.394	2.394	0.000	.....	1.050	.....

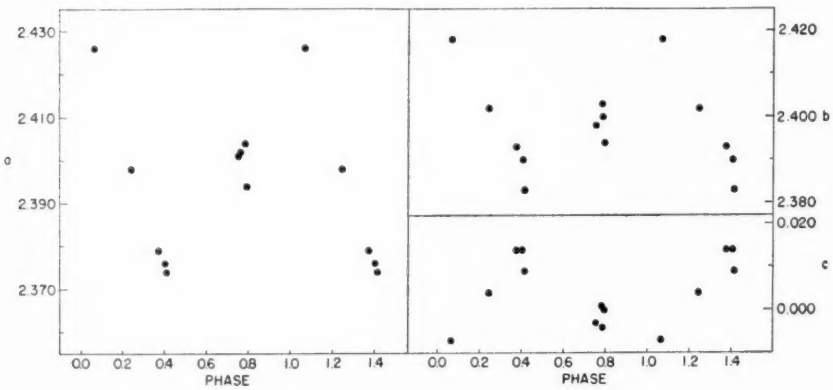

FIG. 2.—14 C Vn − α^2 C Vn: *a*, $\lambda_{eff} \sim 5500$; *b*, $\lambda_{eff} \sim 4400$; *c*, color

which has its maximum sensitivity near λ 4000, and the observations were made without a filter. Guthnick and Prager's observations were made with a sodium cell with maximum sensitivity at λ 5500, and they used no filter.

The star has been subject to study by Babcock and his associates.[14] There is a large magnetic field, and maximum negative field occurs at *Eu* II maximum intensity. This is the phase of maximum light, while minimum li ht occurs at the time of maximum positive magnetic field.

[13] *Ap. J.*, **75**, 364, 1932.

[14] H. W. Babcock and Sylvia Burd, *Ap. J.*, **116**, 7, 1952.

A comparison of the light-variation with the radial velocity, measured by the above observers and also by Struve and Swings,[15] shows that maximum light coincides with times of mean velocity, as *Eu* II changes from approach to recession and as *Cr* II changes from recession to approach. Minimum light occurs at times when the radial velocity of *Eu* II changes from recession to approach, while *Cr* II is at one of its two maxima of recession.

χ SERPENTIS

In the *Henry Draper Catalogue* χ Ser (HD 140160) is designated as A0p. Its magnitude is 5.26 The feature which marked this star as peculiar was the strength of the *Sr* II line at λ 4078. In a spectroscopic investigation of peculiar A stars, Deutsch[16] found that the lines of *Sr* II vary in intensity. He determined the period of variation to be 2.675

TABLE 3

PHOTOMETRIC OBSERVATIONS OF χ SER

DATE, 1952 U.T.	PHASE $P = 1.59584$	HD 141400 − χ SER			HD 141400 *minus* HR 5870
		V	*B*	*C*	*V*
Jan. 27.500	0.433	1.445	1.441	−0.003	.....
Apr. 8.367	.467	1.443	1.428	− .015	.....
15.363	.863	1.461	1.451	− .010	1.062
16.346	.467	1.450	1.428	− .022	1.064
May 11.230	.060	1.464	1.459	− .005	1.056
July 2.168	.606	1.463	1.450	− .013	1.054
4.130	.835	1.461	1.453	− .008	1.059
5.167	.485	1.441	1.436	− .005	1.056
6.130	.088	1.458	1.453	− .005	1.060
9.125	0.965	1.466	1.453	−0.013	1.065

days. More recent observations by the same investigator[17] indicated that the period 2.675 days is not the actual period of variation but that the related period, 1.59584 days, is the true period. His elements are:

$$Sr \text{ II max.} = \text{JD } 2434134.06 + 1.59584\,E\,.$$

Photoelectric observations were made at Yerkes Observatory on ten nights. HD 141400 (A0; 6^m8) was used as primary star for comparison with χ Ser; and HR 5870 (A0; 5^m72) was observed as a check on HD 141400. The observations are given in Table 3 and are plotted in Figure 3 in accordance with the new elements given by Deutsch. The observations show that χ Ser varies in both the blue and the yellow with an amplitude of 0.02 mag. Maximum light corresponds to strontium maximum intensity.

HD 224801 (=HR 9080).

The star HD 224801 is designated as A0p in the *Henry Draper Catalogue*. Its magnitude is 6.25. Lines at λλ 4128–4131 are strong, and the radial velocity is variable.[18] The star has a magnetic field (see Table 6, n. †). It was first observed photoelectrically in the late months of 1951. As comparison stars, HR 1 (A0; 6^m51) and HR 9070 (B5; 6^m49) were used. The observations gave strong indications of variability at that time.

[15] *Ap. J.*, **98**, 361, 1943.
[16] *Ap. J.*, **105**, 293, 1947.
[17] *Pub. A.S.P.*, **64**, 315, 1952.
[18] *Pub. David Dunlap Obs.*, **1**, 123, 1939.

TABLE 4

It was again observed, beginning in July, 1952. Twenty-eight observational points on twenty-three nights were obtained at Yerkes Observatory, and an additional twenty-three observational points were obtained at McDonald Observatory on fifteen nights. The period of light-variation, which is 3.7422 days, has been found from the observations made at both observatories. The elements are:

$$\text{Light-max.} = \text{JD } 2434222.77 + 3.7422\,E\,.$$

In the series of observations made at Yerkes Observatory, HD 224801, HR 1, and HR 9070 received equal weight with respect to number of observations. It became evi-

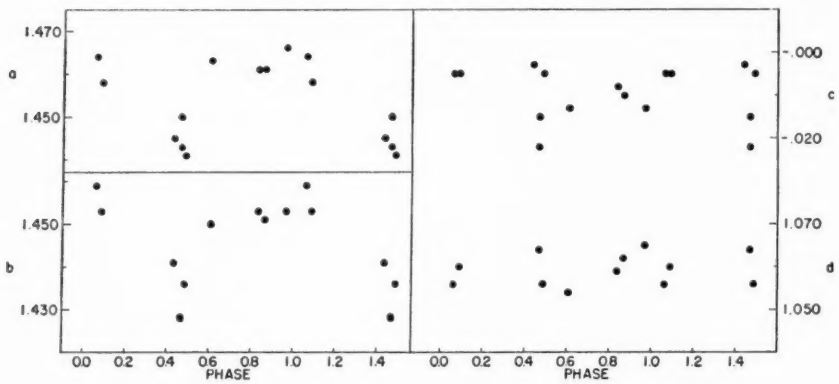

FIG. 3.—HD 141400 = χ Ser: *a*, $\lambda_{eff} \sim 5500$; *b*, $\lambda_{eff} \sim 4400$; *c*, color; *d*, comparison of HD 141400 with HR 5870 at $\lambda_{eff} \sim 5500$.

dent from the comparisons of HR 1 with HR 9070 that one of the stars was not constant in light. On consulting the Yerkes plate files, it was found that a slit spectrogram had been obtained for the star HR 9070 in the course of the B-star program. The star had been classified as B3nne. To make certain which comparison star was variable, HR 9086 (B9; 6^m13) was observed after September 16, 1952. HR 9070 was dropped after two nights. For the six observational points obtained while HR 9086 was observed, the comparisons of HR 1 with HR 9086 are in quite satisfactory agreement. During this interval, September 16, 1952—October 3, 1952, HD 224801 was observed at maximum light on two nights. The observations are compiled in Table 4, and the comparisons of HD 224801 with HR 1 are shown in Figure 4. The 1951 observations are indicated by open circles in this figure.

The yellow and blue light-curves from the McDonald observations are essentially the same as those shown by the Yerkes observations (Fig. 4). However, an ultraviolet light-curve was also obtained at McDonald. These observations are given in Table 5 and plotted in Figure 5. The comparisons of color, $U - B$, are also shown, as well as the comparisons of HR 1 with HR 9086 (all single comparisons).

The observations indicate that HD 224801 varies in the yellow with an amplitude of 0.04 mag. The amplitude in the blue is slightly smaller. There is a color change, $B - V$, of 0.015, with the star bluest at minimum light. The ultraviolet amplitude is about 0.06 mag. The color change, $U - B$, is about 0.04 mag., with the star most ultraviolet at maximum light. Two maxima are shown by the blue observations, and there is evidence of two maxima in the yellow.

TABLE 4

PHOTOMETRIC OBSERVATIONS OF HD 224801*

DATE, 1951–1952 U.T.	PHASE $P = 3.7422$	HR 1 − HD 224801			HR 1 *minus* HR 9070	HR 1 *minus* HR 9086
		Y	*B*	*C*	*Y*	*Y*
Sept. 14.304	0.764	0.332	0.424	0.092	0.181	.....
15.295	.029	.378	.450	.072	.177	.....
16.267	.289	.329	.409	.080	.182	.....
Oct. 10.338	.721	.343	.418	.075	.169	.....
25.205	.694	.330	.426	.096	.179	.....
Jan. 13.005	.019	.371	.437	.066	.....	.....
July 24.333	.680	.329	.420	.091	.182	.....
29.333	.016	.364	.440	.076	.193	.....
31.366	.559	.342	.430	.088	.177	.....
Aug. 1.330	.817	.353	.442	.089	.172	.....
7.327	.420	.336	.432	.096	.212	.....
12.321	.756	.324	.422	.098	.170	.....
13.323	.022	.368	.446	.078	.175	.....
19.230	.600	.331	.428	.097	.203	.....
22.227	.402	.329	.418	.089	.186	.....
22.323	.427	.335	.427	.092	.177	.....
23.204	.662	.331	.425	.094	.201	.....
24.200	.928	.363	.445	.082	.191	.....
Sept. 5.150	.122	.349	.427	.078	.202	.....
5.190	.134	.343	.426	.083	.195	.....
5.250	.148	.342	.425	.083	.188	.....
16.142	.059	.363	.440	.077	.174	0.448
17.155	.330	.325	.414	.089	0.187	.442
23.198	.944	.365	.442	.077	.....	.437
28.121	.260	.331	.414	.083	.....	.444
28.312	.311	.315	.406	.091	.....	.438
28.364	.317	.331	.422	.091	.....	.446
Oct. 3.102	0.591	0.334	0.426	0.092	.....	0.451

* Yerkes observations.

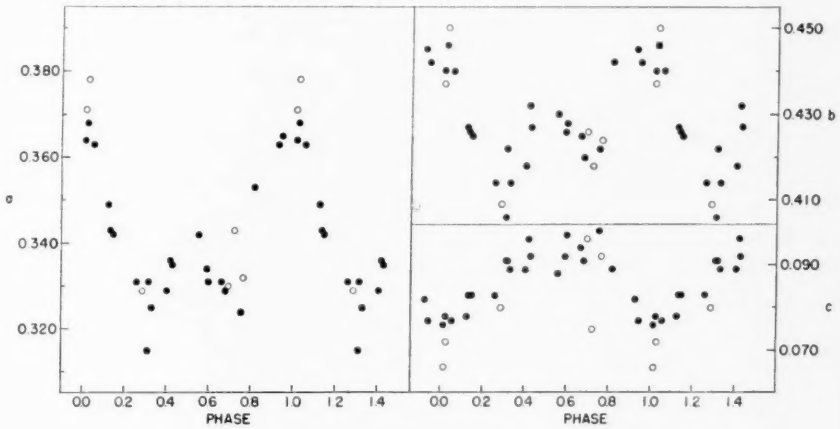

FIG. 4.—HR 1 − HD 224801: *a*, $\lambda_{eff} \sim 5500$; *b*, $\lambda_{eff} \sim 4400$; *c*, color

TABLE 5

PHOTOMETRIC OBSERVATIONS OF HD 224801*

DATE, 1952 U.T.	PHASE $P = 3.7422$	HR 1 − HD 224801		HR 1 *minus* HR 9086
		U	$U-B$	U
Nov. 6.173	0.696	0.884	0.439	0.972
11.046	.998	.926	.468	.....
11.143	.024	.936	.483	.....
12.181	.301	.888	.464	.972
14.162	.831	.916	.455	.965
15.137	.091	.915	.474	.953
19.119	.155	.890	.465	.958
20.147	.430	.883	.447	.976
Dec. 1.111	.360	.873	.446	.968
1.308	.413	.857	.429	.....
2.090	.622	.865	.435	.965
2.314	.681	.860	.420	.....
4.050	.145	.896	.460	.976
4.177	.179	.884	.450	.972
8.052	.214	.886	.460	.963
11.083	.025	.931	.475	.976
11.188	.053	.918	.471	.967
11.260	.072	.911	.453	.967
15.071	.090	.915	.469	.....
15.160	.114	.899	.462	.964
15.266	.143	.874	.449	.....
16.046	.351	.873	.443	.969
29.131	0.848	0.922	0.462	0.965

* McDonald observations.

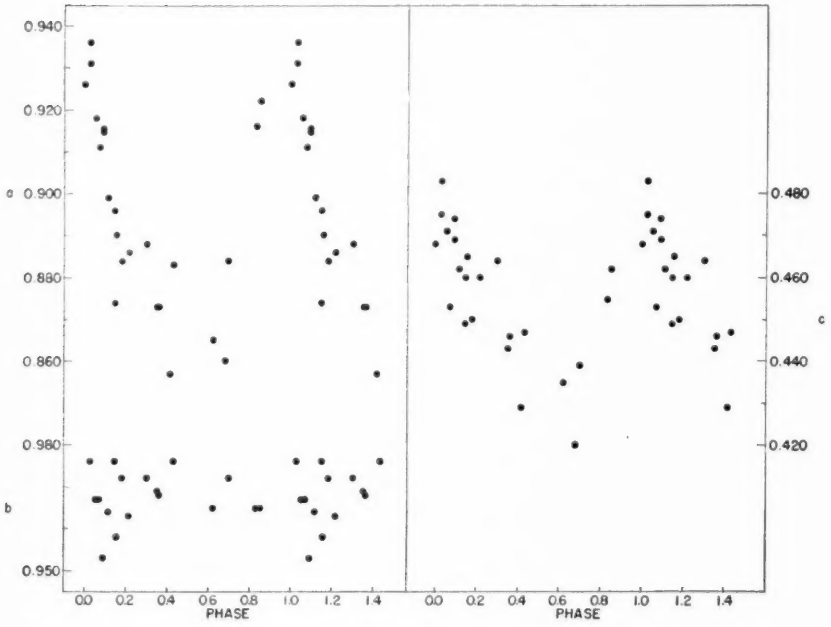

FIG. 5.—HR 1 − HD 224801: *a*, $\lambda_{eff} \sim 3550$; *b*, HR 1 − HR 9086 at $\lambda_{eff} \sim 3550$; *c*, $U - B$

73 DRACONIS

Observations of 73 Draconis, made in 1951, have been published previously.[8] Observations were made on fifteen nights in 1952. The new series confirms the variation in the yellow found in 1951, but with slightly smaller amplitude. The second maximum in the yellow is also confirmed. The minimum shown by the blue observations of 1951 is not present in the observations made in 1952. The results on the thirteen other stars are given in Table 6.

IV. DISCUSSION

Of the four stars discussed here and the three that were published previously,[8] six are known spectrum variables. On the other hand, two stars in Table 6, HR 1732 and 21 Comae, which do not show well-defined light-variation, are also spectrum variables. Another spectrum variable, 45 Leonis, gives no indication of variability in light. It appears that spectrum variables may or may not show decided light-variation.

The variable magnetic fields of two stars in Table 6, HD 133029 and HD 153882,

TABLE 6

HD Number	Other Desig.	α_{1900}	δ_{1900}	m	HD Type	Peculiarity	No. of Nights	Remarks
34452	HR 1732	$5^h12^m.4$	33° 39′	5.39	A0p	λ 4128–4131	15	Light-variation indicated but evidence inconclusive (sp. var.)
38104	27 *o* Aur*	5 38.2	49 47	5.52	A0	λ 4171	4	No indication of variability
42616	.....	6 6.6	41 44	6.95	A0p	λ 4128–4131	11	No indication in yellow and blue; some variation indicated in UV (mag. fld.)†
71866	.....	8 24.6	40 33	6.66	A0p	λ 4128–4131	6	Variation of small amplitude possible (mag. fld.)
4101	45 Leo‡	10 22.4	10 16	5.87	A0	λ 4078, λ 4171	7	No indication of variability (sp. var.) (mag. fld.)
108945	21 Com	12 26.0	25 7	5.39	A3p	λ 4078	16	Light-variation indicated; but not well defined (sp. var.)
133029	.....	14 57.2	47 40	6.16	A0p	λ 4128–4131	10	No indication of variability (mag. fld.)
153882	.....	16 57.0	15 5	6.16	A0p	λ 4128–4131	18	Definite indication of variability in blue; curve not well defined (mag. fld.)
179761	21 Aql§	19 8.7	2 7	5.10	B8	.....	4	No indication of variability (mag. fld.)
204411	HR 8216‖	21 23.3	48 24	5.31	A3	λ 4128–4131 λ 4171	8	Some indication of variability
205087	HR 8240#	21 27.9	22 57	6.44	B9	λ 4078, λ 4171	4	No indication of variability
219749	HR 8861	23 13.2	44 57	6.32	B9p	λ 4128–4131	5	Some indication of variability
220825	κ Psc	23 21.8	0 42	4.94	A2p	λ 4078	6	Some in lication of variability

* Nancy G. Roman, *Ap. J.* **110,** 232, 1949.
† Those stars which are known to have magnetic fields are listed by T. G. Cowling and H. W. Babcock (*M.N.*, in press).
‡ Nancy G. Roman, *ibid.*, **113,** 705, 1951.
§ W. W. Morgan, *Ap. J.*, **76,** 275, 1932.
‖ Unpublished.
Unpublished.

have been discussed;[19] they do not show noticeable spectral variations. There is no indication of light-variation for the first star from the ten nights it was measured, while light-variation is indicated for HD 153882, but a curve is not well defined. On the other hand, α^2 Canum Venaticorum has a magnetic field with about the same range as that of HD 153882, and in this case light-variation as well as spectrum variation is large and well defined. From this investigation there is no apparent relation between light-variation and magnetic variation.

Four of the seven stars with well-defined light-variation show two maxima (or

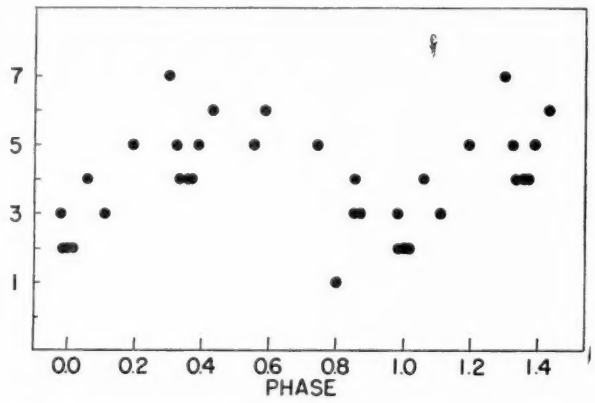

FIG. 6.—Intensity variation of λ 4215 in the spectrum of 21 Comae

minima). They are: 73 Draconis, ϵ Ursae Majoris, 56 Arietis, and HD 224801. An exception, α^2 Canum Venaticorum, did show definite evidence of a hump on the rising portion of some of the light-curves determined by Guthnick[4] and Miss Gussow.[20] It seems that the occurrence of double waves in the light-curves of peculiar A stars is not uncommon.

APPENDIX 1

In the course of the program, spectra were obtained of 21 Comae on twenty-one nights, in an effort to determine the period of spectrum variation in the same interval that observations were made photoelectrically. The variable line, *Sr* II λ 4215, was compared with a feature at λ 4170. Independent eye-estimates of the ratio on a scale 1–7 were made on three occasions separated by two-month intervals. The means of the estimates, rounded off to the nearest integer, are given in Table 7.

The present series of plates at once suggests a long period, as do plates taken twenty years ago; however, in the present series, spectra obtained on five nights during one observing week indicate rapid changes. It has been found that the period 7.75 days[21] agrees best with the current series. The intensity estimates are plotted in Figure 6, where zero phase is taken as

$$Sr\ \text{II min.} = \text{JD}2434101.73\,.$$

[19] H. W. Babcock and Sylvia Burd, *Pub. A.S.P.*, **63**, 81, 1951; Guro Gjellestad and H. W. Babcock, *Ap. J.*, **117**, 12, 1953.

[20] *A.N.*, **237**, 334, 1929–1930.

[21] These observations do not eliminate the related periods near 1 day.

TABLE 7

INTENSITY ESTIMATES OF λ 4215

Plate X	Date, 1952 U.T.	λ 4215	Phase*
1976	Feb. 9.275	5	0.554
1984	23.278	4	.360
1986	Mar. 2.265	5	.391
1990	16.239	5	.195
1992	17.260	5	.326
1995	29.248	3	.873
1997	30.228	2	.999
2002	Apr. 15.178	4	.058
2006	17.072	7	.302
2009	18.084	6	.433
2010	19.072	6	.584
2013	28.250	5	.744
2015	29.107	4	.855
2018	30.107	2	.984
2021	May 1.107	3	.112
2025	3.094	4	.369
2027	14.203	1	.803
2031	26.094	4	.337
2037	30.094	3	.853
2038	31.094	3	.982
2040	June 8.108	2	0.016

* Phase = 0 at JD 2434101.73 + 7.75*E*.

TABLE 8

COLORS OF STANDARD STARS

Star	*B*−*V*	*U*−*B*	Star	*B*−*V*	*U*−*B*
α Ari	1.149 (1.153)	1.10 (1.12)	β Cnc	1.483 (1.478)	1.77 (1.77)
HR 875	0.068 (0.085)	0.08 (0.05)	η Hya	−0.178 (−0.196)	−0.75 (−0.74)

TABLE 9

COLORS OF PECULIAR A STARS

Star	*B*−*V*	*U*−*B*	Star	*B*−*V*	*U*−*B*
ι Cas	+0.13	+0.04	α C Vn (A+B)	−0.09	−0.33
56 Ari	− .11	− .45	78 Vir	+ .02	.00
HR 1732	− .21	− .63	β C Br	+ .27	+ .14
27 Aur	+ .02	+ .05	73 Dra	+ .07	+ .13
HD 42616	+ .08	+ .03	γ Equ	+ .25	+ .13
53 Cam	+ .16	.00	HR 8216	+ .06	+ .17
HD 71866	+ .07	.00	HR 8240	− .09	− .27
45 Leo	− .06	− .09	HR 8861	− .06	− .25
21 Com	+ .04	+ .12	κ Psc	+ .01	− .03
ε U Ma	−0.03	+0.02	HD 224801	−0.09	−0.36

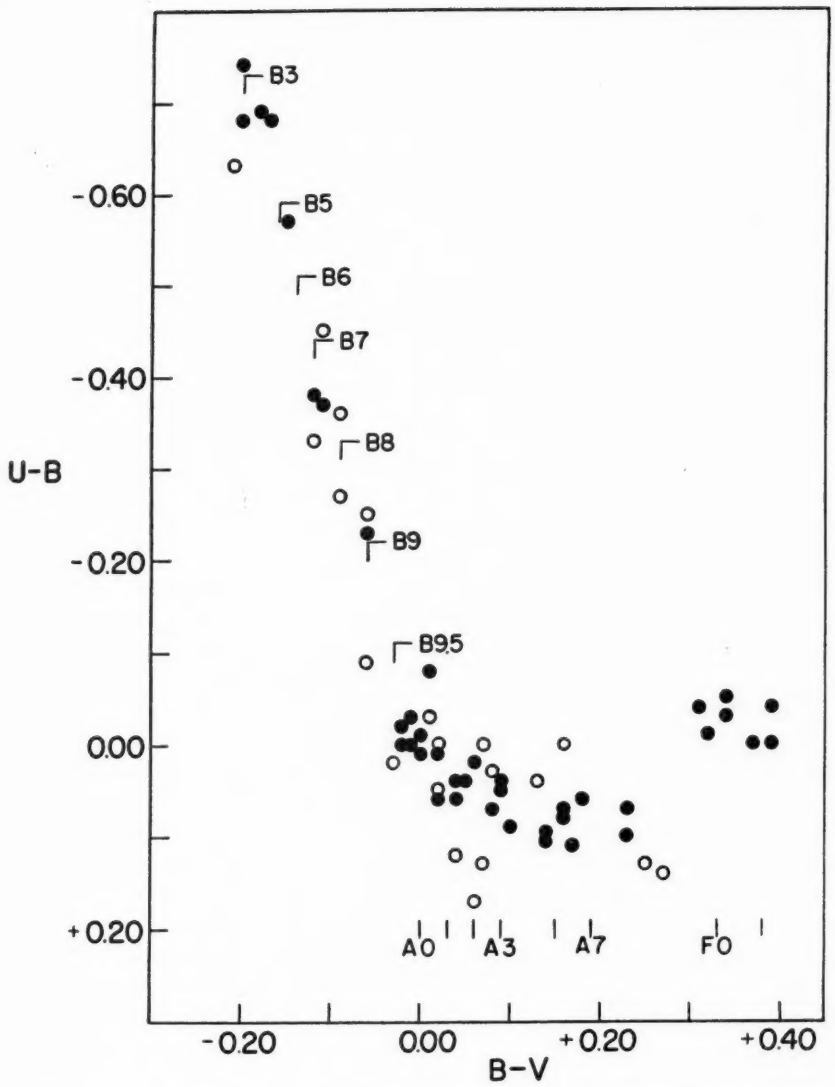

FIG. 7.—$U - B$ versus $B - V$ for the peculiar A stars and normal dwarf stars. The peculiar stars are indicated by the open circles.

APPENDIX 2

Observations for color have been made of eighteen peculiar A stars at McDonald Observatory. These colors have been referred to Johnson and Morgan's $B - V$ and $U - B$ system.[22] The extinction observations were reduced in a manner similar to that described by Johnson and Morgan[23] and by Sharpless.[24] The transformation to the above system depends on observations of four standard stars. These standards and the values of the indices, $B - V$ and $U - B$, from the present set of observations are listed in Table 8. Johnson and Morgan's[23] values are given in parentheses.

The peculiar stars with the observed values of $B - V$ and $U - B$ are given in Table 9. The author is indebted to Dr. D. L. Harris for the values for 78 Virginis and β C Br.[25]

It is of interest to compare $B-V$ and $U-B$ for the peculiar stars with the intrinsic colors of normal stars. This is done in Figure 7, where the pecuilar stars are shown by open circles and the normal main-sequence stars by the filled circles. The intrinsic colors of the normal stars have been provided by Drs. W. W. Morgan, D. L. Harris, and H. L. Johnson (in press). It is concluded from this diagram that the peculiar A stars follow the same run of $B - V$ versus $U - B$ as do the normal dwarfs.

In conclusion I wish to thank Dr. W. A. Hiltner for supervising this work.

[22] *Ap. J.* (in press).

[23] *Ap. J.*, **114**, 522, 1951.

[24] *Ap. J.*, **116**, 251, 1953.

[25] The agreement between the author's values of $B - V$ and $U - B$ for ϵ Ursae Majoris and α Canum Venaticorum (A + B) and those of Harris for the same stars (unpublished) is quite satisfactory.

RED AND INFRARED MAGNITUDES FOR 138 STARS OBSERVED AS PHOTOMETRIC STANDARDS*

GERALD E. KRON AND HOWARD S. WHITE
Lick Observatory, University of California
AND
S. C. B. GASCOIGNE
Commonwealth Observatory, Canberra, Australia
Received June 2, 1953

ABSTRACT

Red and infrared magnitudes were determined photoelectrically for 138 stars, some groups in a uniformly distributed series of Harvard Standard C and D regions and others at random in declination approximately $-15°$ to $+15°$. The C and D region stars may be used for magnitude zero-point standards and for limited-range color standards. The randomly distributed individual stars were picked to represent an extremely wide color range, for use in color standardization on photometric programs requiring wide, stable color ranges. All the stars are situated in the sky so that they can be observed with precision from a large percentage of all the observatories in both hemispheres. Every effort was made to reduce the systematic and random errors to as small a size as practicable.

I. INTRODUCTION

This paper is a report on an extension of photometric work, already published,[1] on photoelectric red and infrared magnitudes. Late in 1950 the senior author decided to extend to the entire sky a Lick Observatory program for the measurement of red and infrared magnitudes of near-by stars. This decision required a journey to the Southern Hemisphere and the establishment of standards of magnitude in two colors suitable for stabilization of a two-color magnitude system to be used over the whole sky with maximum feasible precision. It was decided that the magnitude zero-point standards should be stars in uniformly distributed small areas zigzagging across the equatorial region of the sky and that the color standards should be individual stars selected for color characteristics and randomly distributed in the declination belt included by the zero-point standard areas.

II. THE PHOTOMETER

The photometer used was the same one described elsewhere,[1, 2] with cell CE25 A/Be. The grid resistor, however, was changed from one of 2.5×10^{13} ohms to one of 5.0×10^{13} ohms, and the unnecessary increase in the signal resulting from this change was reduced by decreasing the gas-multiplying factor of the photocell from 24 to 6 during 1951, and to 10 in 1952–1953; the last value was found to give about optimum signal-to-noise ratio. The reduction in the gas-multiplying factor increased the magnitude range for which the photometer was useful. The range was further increased by adding 1 mag. to the range of the attenuation control of the power amplifier. This change resulted in signals as high as 25 volts appearing across the grid resistor for bright stars. Although the manufacturer states that the resistor will have no voltage coefficient up to 50 volts, the rather high signal voltage we sometimes used, plus the change in the grid resistor itself, made necessary a new linearity check for bright stars. This check was accomplished by measuring the extinction factor of the three neutral screens used for magnitude-scale extension throughout the program. There was no evidence that the screen extinction factors, as

* *Contr. Lick Obs.*, Ser. II, No. 49.

[1] G. E. Kron and J. L. Smith, *Ap. J.*, **113**, 324, 1951; *Contr. Lick Obs.*, Ser. II, No. 34.

[2] G. E. Kron, *Ap. J.*, **115**, 1, 1952; *Contr. Lick Obs.*, Ser. II, No. 38.

measured with the photometer, depended upon star brightness. We take this result as convincing indication that the photometer response is linear for bright stars, and it is justifiable to assume that the response will be linear for faint stars on the basis of previous experience. The sensitivity steps built into the electronic equipment were checked, at reasonable intervals, for constancy to 0.2 per cent of their ratios. In general, the same standards of precision of the photometer described in the previous paper[1] have been maintained throughout the work.

III. COLOR SYSTEMS

The infrared magnitudes were obtained with the same Wratten 88A gelatin filter cemented between glass. The red magnitudes, however, unlike the previous work, were obtained with a new filter, which rejected the blue with a piece of Schott OG-1 filter glass and which excluded the infrared with a 13-film interference filter. This filter was made by J. Lynn Smith,[3] who has described its construction and determined its transmission-curve, which shows sharp cutoffs at both ends of the passband and high maximum transmission. It is designated OG1-74 in this work. The new photoelectric color system was reduced to the ***R, I*** system of red and infrared magnitudes by observing 59 stars in common with the old system. The system used in the Southern Hemisphere in 1951 and that in the Northern Hemisphere in 1952–1953 were brought into agreement by observation of 68 stars common to both.

IV. OBSERVING TECHNIQUE

The results for 1951 were obtained with the 29-inch Reynolds reflecting telescope at the Commonwealth Observatory, Mount Stromlo, Australia, and the 1952–1953 observations were made with the 36-inch refractor of the Lick Observatory. The Reynolds was used at its Newtonian focus with a focal-plane aperture 35 seconds of arc in diameter. The 36-inch refractor was used with a 30-second aperture, and a focus 20 mm inside the focus determined visually through the red filter (placed inside the focus) with a knife-edge test. The observing pattern of deflections was the same as described previously.[1]

The range of sensitivity under electrical control was too small to permit working on the full brightness range of all stars on our program without some additional means of sensitivity control. Following Seares and Stebbins, we adopted screens for reduction of the bright stars to increase the magnitude range. An objective screen of extinction 1.94 mag. was used with the Reynolds in 1951, and the Crossley reflector objective screen of extinction 2.43 mag. was used with the 36-inch in 1952. The use of an objective screen with a large refractor is inconvenient, so on January 22, 1953, we changed to a double thickness of a nickel screen of 1000 meshes per inch, diameter $1\frac{1}{2}$ inches, placed 10 inches inside the focus.[4] This remarkable screen material, when doubled, gave an extinction of 3.99 mag. and was neutral. All visible light diffracted away from the optic axis appeared well clear of the focal-plane aperture, even at the short distance of 10 inches. The rather fragile screen material was supported by clamping it between two pieces of UV transparent glass, each 2 mm thick. This screen unit makes a permanent, very stable, practical method of extending a magnitude range without resort to additional electrical control, with its attendant possibility of overillumination of the photocell.

As usual, the sensitivity of the photometer was monitored by means of an artificial source made from a luminescent radioactive mixture.[1, 5] The luminescent mixture was tested for temperature coefficient and showed no significant effect.

[3] *Pub. A.S.P.*, **63**, 91, 1951.

[4] We are indebted to W. A. Hiltner for calling our attention to the existence of such screen material and for furnishing us with the material.

[5] Joel Stebbins and J. Lynn Smith, *Pub. A.S.P.*, **63**, 203, 1951.

The Harvard Standard Regions, the color standards, and the near-by stars were all observed on the same program. The zero point of the Standard Regions was twice carried completely around the sky from one region to the next in the order of right ascension, once in 1951 in the Southern Hemisphere and once in 1952 in the Northern Hemisphere.

V. REDUCTIONS

As before, we used the general method of reduction employed by Eggen, except that we employed mean extinction coefficients. During the first 12 nights of observing at Mount Stromo we determined extinction coefficients for this site by following a C region to large zenith distances. The mean values for extinction coefficients so obtained, however, were 0.12 and 0.07 mag. in the red and infrared, respectively, which are the same as those used before and after 1951 at Mount Hamilton. Throughout this work we had no trouble with extinction for normal skies either at Mount Hamilton or at Mount Stromlo. Although Mount Stromlo has an elevation of only 2600 feet, it has nearly the same extinction in the red and infrared as Mount Hamilton, elevation 4200 feet. It is of interest to note that if all observations of the present program were made at zenith

TABLE 1

OBSERVING SCHEDULE

REYNOLDS REFLECTOR		36-INCH REFRACTOR	
Date	Program*	Date	Program
May 9, 1951	C6, D6, C8, extinction	Mar. 20, 1952	C4, D6, color
May 10	C6, D6, C8, extinction	Mar. 26	C4, D6, color
May 11	C6, D6, extinction	Apr. 2	C4, D6, color
May 12	C6, D6, extinction	Apr. 15	C4, D6, C6, C8
May 16	C6, D6, extinction	May 10	D6, C6, C8, color
May 17	D6, C8, extinction	May 14	D6, C6, color
May 30	D6, C8, extinction	May 21	C6, C8, color
May 31	D6, C8, extinction	May 26	C6, C8, color
June 1	D6, extinction	June 18	C6, C8, D10, color
June 2	D6, extinction	July 15	C8, D10, color
June 29	C8, D10, extinction	Aug. 14	C8, D10, color
July 1	C8, D10, extinction	Aug. 23	D10, C12, color
July 10	D10, C12	Aug. 24	D10, C12, color
July 28	C8, D10, C12	Aug. 25	D10, C12 color
July 29	C8, D10	Sept. 20	C12, D2, color
Aug. 27	D10, C12, D2	Sept. 21	C12, color
Oct. 4	C12, D2, color	Oct. 24	C12, D2, C4, color
Oct. 9	C12, D2, color	Oct. 25	C12, D2, C4, color
Oct. 15	C12, D2, color	Nov. 18	C12, D2, color
Nov. 17	D2, C4, color	Nov. 25	C12, color
Nov. 20	D2, C4, color	Jan. 29, 1953	C4, color
Dec. 6	D2, color	Feb. 16	C4, color
Dec. 12	C4, C6, color	Mar. 3	C6, color
		Mar. 5	C4, color
		Mar. 15	C4, color
		Apr. 1	C6, color
		Apr. 14	C4, color

* The word "color" appearing in this column means that color standards were observed on the indicated night.

TABLE 2

MAGNITUDES OF THE ZERO-POINT STANDARDS

STAR	R	A.D.	$(R-I)$	A.D.	No. of Nights 1950, 1951, 1952
	Area D2 (3^h04^m, $-14°$)				
A	5^m70	2	$+0^m42$	1	0, 7, 3
B	6.73	2	+ .22	2	0, 7, 3
G	7.34	3	+ .36	2	0, 7, 3
C	7.54	2	+ .14	2	0, 7, 3
H	7.75	2	+ .31	2	0, 7, 3
E	8.39	3	− .03	2	0, 6, 3
K	9.01	3	+0.13	3	0, 7, 3
	Area C4 (7^h02^m, $+15°$)				
D	6.59	2	+0.33	1	4, 3, 5
F	6.92	2	+ .38	1	3, 3, 6
A	7.23	2	− .15	1	5, 3, 6
B	7.50	2	− .02	1	5, 3, 6
E	7.58	2	+ .19	1	2, 2, 6
K	8.01	1	+ .38	1	5, 2, 3
G	8.99	3	− .08	3	1, 2, 3
L	9.21	3	+0.20	2	2, 2, 3
	Area C6 (11^h00^m, $+15°$)				
K	6.40	1	+0.80	1	6, 4, 7
A	7.00	2	− .10	2	6, 5, 7
D	7.11	2	+ .18	1	6, 5, 7
G	7.24	1	+ .34	1	6, 5, 7
M	7.70	1	+ .45	2	6, 5, 5
F	7.85	1	+0.14	1	6, 5, 6
	Area D6 (11^h05^m, $-16°$)				
Q	7.45	2	+0.58	1	0, 10, 6
G	7.59	1	+ .19	1	0, 11, 6
F	7.81	2	+ .13	1	0, 11, 6
M	8.01	2	+ .34	2	0, 9, 6
I	8.14	1	+ .17	2	0, 9, 6
K	8.85	2	+ .04	2	0, 6, 3
S	8.97	1	+ .39	1	0, 5, 0
N	9.26	2	+0.17	2	0, 4, 6
	Area C8 (15^h00^m, $+15°$)				
D	6^m14	2	$+0^m46$	1	0, 9, 9
C	6.49	2	+ .33	1	0, 9, 9
F	6.67	1	+ .40	2	0, 9, 9
A	6.78	2	+ .20	1	0, 9, 9
B	7.27	3	− .01	1	0, 7, 7
E	8.07	2	+ .06	3	0, 3, 6
N	8.36	1	+0.42	2	0, 4, 4
	Area D10 (19^h10^m, $-15°$)				
M	*	.....	+1.42	2	0, 6, 6
H	6.26	1	+ .56	1	0, 6, 6
O	6.70	1	+ .82	1	0, 6, 6
E	7.47	1	+ .17	2	0, 6, 6
C	7.88	1	− .05	2	0, 6, 6
Q	8.16	1	+ .52	2	0, 6, 5
F	8.38	1	−0.08	2	0, 6, 6
	Area C12 (23^h00^m, $+15°$)				
D	5.99	1	+0.45	1	7, 10, 7
E	6.66	1	+ .37	1	4, 10, 7
A	6.94	3	− .10	1	7, 10, 7
C	7.44	2	− .02	1	3, 10, 7
I	7.47	2	+ .45	1	3, 10, 7
+15°4733	7.58	1	+ .88	1	7, 6, 7
M	7.86	1	+ .53	2	3, 5, 7
F	8.19	1	+0.08	2	6, 5, 7

*Variable; mean 5^m75; amplitude 0^m24.

distances of such size that air mass 1.5 was never exceeded and if all results were reduced to the mean air mass 1.25, instead of to air mass zero, then the largest error, even if extinction corrections were completely neglected, would be only 0.03 mag. for the red and less than 0.02 mag. for the infrared. Throughout most of this work an effort was made to observe with an air mass less than 1.5, which was done in all but a small percentage of the observations. It is probable that some of the systematic errors made in extinction corrections applied to stars observed in the Standard Regions will cancel or partly cancel in the combination of the data from the two hemispheres.

No appreciable color-closure error was found in the closed circuits around the sky in either the 1951 or the 1952 series of data, a result indicating that the ability of the photometer to carry the color was good. Closure errors in magnitude were found for both years, in the sense that the end-season results indicated fainter magnitudes than those found at the beginning. The closure errors were 0.030 mag. for 1951 and 0.006 mag. for 1952. For both years these errors were assumed to be uniformly distributed throughout

TABLE 3

SYSTEMATIC MEAN SEASONAL DIFFERENCES FOR COLOR AND MAGNITUDE

REGION	(O−C) (UNIT = 0m01)					
	1950		1951		1952	
	Mag.	Color	Mag.	Color	Mag.	Color
D2	.....	.....	+1.4	−0.2	−3.7	+0.2
C4	−0.8	−0.1	+1.8	+0.5	−0.2	−1.1
C6	+ .3	− .1	−0.8	−0.3	+0.1	+0.7
D6	.....	.....	−0.5	+1.0	+0.4	−1.0
C8	.....	.....	−1.3	−0.9	+1.0	+0.6
D10	.....	.....	+0.2	+0.4	−0.2	−0.9
C12	+0.1	+0.8	+0.2	−0.5	−0.2	−0.9
Mean	−0.1	+0.2	+0.2	±0.0	−0.4	−0.3

seven transfers made in the closed circuit, and corrections were made accordingly. A comparison between the 1951 magnitudes and the independently determined 1952 values, after both sets had been corrected for closure errors, indicated such close agreement that no further work to investigate these errors seemed necessary.

VI. THE OBSERVATIONS

The schedule of observing is given in Table 1, and Table 2 contains the magnitudes and colors for the seven Harvard Standard Regions. The headings of the columns are self-explanatory. Three Standard Regions—C4, C6, and C12—are common with the earlier work, and the results therefore represent improvements based on additional observing. The tabulated values for R and $(R - I)$ are means for all nights on each star after reduction of each season independently to the R, I system. The average deviations, formed from these means, thus contain the effects of any season-to-season systematic differences present in the data, and for this reason they are in some cases larger than average deviations given for the same stars in the relatively lower-weight results previously published.[1] Mean values for each star for each season were also formed from the night-to-night data, and we have computed, from these seasonal means, the systematic mean seasonal differences for color and magnitude given in Table 3. These mean seasonal differences were obtained by subtracting the magnitudes and colors for each star for

TABLE 4

COLOR STANDARDS

Star	1900 Position		Spectral Type	R	A.D.	$(R-I)$	A.D.	n
	R.A.	Dec.						
γ Peg	00h08m1	+14° 38′	B2 IV	3m06	1	−0m22	1	4
η Psc	1 26.1	+14 50	G8 III	3.23	3	+0.32	1	5
τ Cet	1 39.4	−16 28	G8 V	3.16	2	+0.26	1	5
−18°359	2 00.1	−18 06	.....	9.00	1	+1.02	2	4
+2°348	2 07.4	+03 10	.....	9.02	3	+0.86	1	4
ξ^2 Cet	2 22.8	+08 01	B9 III	4.45	3	−0.13	1	3
HR 753B	2 30.6	+06 25	.....	10.26	3	+1.28	2	6
HR 875	2 51.6	−04 07	A1 V	5.26	2	−0.04	1	3
κ Cet	3 14.1	+03 00	G5 V	4.57	4	+0.22	1	8
o Tau	3 19.4	+08 41	G8 III	3.28	1	+0.32	1	4
ϵ Eri	3 28.2	−09 48	K2 V	3.33	2	+0.30	1	4
o^2 Eri A	4 10.7	−07 49	.....	4.07	3	+0.31	2	3
γ Tau	4 14.1	+15 23	K0 III	3.30	1	+0.34	1	4
δ Tau	4 17.2	+17 18	K0 III	3.41	1	+0.34	1	4
π^3 Ori	4 44.4	+06 47	F6 V	3.05	2	+0.16	2	5
π^4 Ori	4 45.9	+05 26	B2 III	3.86	3	−0.19	1	4
β Eri	5 02.9	−05 13	A3 III	2.82	3	−0.01	2	5
HD 35299	5 18.6	−00 15	B2 V	5.91	2	−0.23	1	4
γ Ori	5 19.8	+06 16	B2 III	1.84	3	−0.25	1	4
−3°1123	5 26.4	−03 42	.....	6.87	2	+0.84	1	5
υ Ori	5 27.1	−07 23	B0 V	4.84	3	−0.25	1	5
HD 36591	5 27.6	−01 40	B1 V	5.53	2	−0.20	2	4
ι Ori	5 30.5	−05 59	O9 III	2.95	3	−0.24	1	4
ϵ Ori	5 31.1	−01 16	B0 Ia	1.88	2	−0.20	1	4
ζ Lep	5 42.4	−14 52	A3 V	3.61	2	−0.05	1	4
134 Tau	5 43.9	+12 37	B9 IV	5.04	1	−0.14	1	4
Ross 614AB	6 24.3	−02 44	.....	9.42	2	+1.38	2	5
+17°1320	6 31.5	+17 38	.....	8.64	2	+0.74	1	4
γ Gem	6 31.9	+16 29	A1 IV	2.02	2	−0.09	1	4
γ CMa	6 59.2	−15 29	B8 II	4.24	1	−0.16	1	3
λ Gem	7 12.3	+16 43	A3 V	3.64	3	−0.05	2	5
Luyten's Star	7 22.0	+05 31	.....	8.40	3	+1.19	1	6
Ross 882	7 39.4	+03 48	.....	9.76	4	+1.40	3	6
β Cnc	8 11.1	+09 30	K4 III	2.77	1	+0.52	1	4
C Hya	8 20.7	−03 35	A0 V	4.03	2	−0.14	1	4
η Hya	8 38.0	+03 45	B3 V	4.47	1	−0.21	2	4
θ Hya	9 09.2	+02 44	A0p	4.01	1	−0.15	1	6
−12°2918	9 26.4	−13 03	.....	8.84	1	+1.04	1	3
α Leo A	10 03.3	+12 27	B7 V	1.48	3	−0.17	1	3
ρ Leo	10 27.5	+09 49	B1 I	4.01	2	−0.19	1	7
Wolf 359	10 51.6	+07 37	.....	11.28	1	+1.85	1	3
Ross 128	11 42.6	+01 23	.....	9.55	1	+1.30	1	5
β Leo	11 44.0	+15 08	A3 V	2.18	2	−0.06	1	4
β Vir	11 45.5	+02 20	F8 V	3.39	1	+0.16	1	8
γ Crv	12 10.7	−16 59	B8 III	2.72	2	−0.16	2	3

TABLE 4—*Continued*

Star	1900 Position		Spectral Type	R	A.D.	$(R-I)$	A.D.	n
	R.A.	Dec.						
Wolf 424 AB	12^{h}28^{m}4	+09°34′	.....	10^{m}50	1	+1^{m}62	3	4
+0°2989	12 45.6	−00 13	M0.5 V	7.58	2	+0.66	2	5
α Vir	13 19.9	−10 38	B1 V	1.19	1	−0.26	1	6
70 Vir	13 23.5	+14 19	G5 IV–V	4.68	1	+0.24	2	7
η Boo	13 49.9	+18 54	G0 IV	2.45	2	+0.20	1	4
109 Vir	14 41.2	+02 19	A0 V	3.86	1	−0.10	2	6
α^2 Lib	14 45.3	−15 38	A3 V	2.82	1	−0.03	2	3
β Lib	15 11.6	−09 01	B8 V	2.72	3	−0.14	2	3
−7°4003	15 14.2	−07 21	.....	9.26	2	+1.10	1	4
α Ser A	15 39.3	+06 44	K2 III	2.10	1	+0.37	2	4
β Ser A	15 41.6	+15 44	A2 IV	3.74	2	−0.06	2	6
λ Ser	15 41.6	+07 40	G0 V	4.20	1	+0.20	1	6
γ Ser	15 51.8	+15 59	F6 IV	3.67	1	+0.14	3	5
−12°4523	16 24.7	−12 25	.....	8.71	3	+1.20	1	4
ζ Oph	16 31.7	−10 22	O9.5 V	2.64	2	−0.07	1	5
−4°4226	17 00.0	−04 55	M3.5: V	8.99	2	+0.91	2	4
+2°3312	17 20.8	+02 14	K7 V	6.67	3	+0.60	2	3
α Oph	17 30.3	+12 38	A5 III	2.10	1	0.00	2	4
β Oph	17 38.5	+04 37	K2 III	2.24	1	+0.39	1	4
γ Oph	17 42.9	+02 43	A0 V	3.84	1	−0.09	1	5
Barnard's Star	17 52.9	+04 25	M5 V	8.09	1	+1.23	2	4
−3°4233	17 59.8	−03 02	.....	8.34	2	+0.88	1	4
ζ Aql	19 00.8	+13 43	B9.5 V	3.10	1	−0.07	2	5
Wolf 1055 A	19 12.1	+05 03	M3.5 V	7.90	1	+1.00	2	5
+3°4065	19 28.6	+03 34	.....	6.99	1	−0.06	2	5
κ Aql	19 31.5	−07 15	.....	5.02	1	−0.09	2	4
α Aql	19 45.9	+08 36	A7 IV, V	0.76	1	+0.02	1	4
β Aql	19 50.4	+06 09	G8 IV	3.35	2	+0.31	1	3
α Del	20 35.0	+15 34	B9 V	3.91	1	−0.11	2	5
ε Aqr	20 42.3	−09 52	A1 V	3.86	1	−0.11	2	5
Wolf 922	21 25.8	−10 14	.....	10.43	2	+1.36	2	5
LPM 837	22 33.0	−15 52	.....	10.26	2	+1.66	2	5
−15°6290	22 47.9	−14 47	.....	8.76	4	+1.22	2	4
74 Aqr	22 48.2	−12 09	.....	5.95	2	−0.14	1	5
α Peg	22 59.8	+14 40	B9 V	2.63	2	−0.08	1	3
ι Psc	23 34.8	+05 05	F7 V	3.94	1	+0.19	1	4
+1°4774	23 44.0	+01 52	M2 V	7.95	2	+0.87	1	5

each season from the mean values of all seasons and then forming mean values for each Standard Region for each season.

The color standards are listed in Table 4, in which the first eight columns are self-explanatory and the last column gives the number of nights on which the star was observed. The spectral types are on the Morgan, Keenan, and Kellman system, or on the Morgan and Keenan system, compiled from various sources.

Figure 1 is a plot of the $(B-V)$ colors of Johnson and Morgan[6] against our $(R-I)$

[6] In press. We are indebted to H. L. Johnson and W. W. Morgan for permitting us to use their data in advance of publication.

colors for 48 stars in common among the color standards. The effects of luminosity are clearly apparent among giants, but less apparent among the dwarf red stars. Except for BD $-4°4226$ and Barnard's star,[7] a smooth curve could be drawn through all the points from $(R - I) = +0.6$ to $+1.3$ mag. Barnard's Star is well known as a high-velocity star and as a subdwarf, whereas the BD star, also a high-velocity object, has been classified by Eggen[8] as a subdwarf. The apparent scatter at $(R - I) = +0.18$ mag. is caused by an inherent bifurcation of the color diagram that will be discussed on the basis of definitive data in a forthcoming paper. The correlation of the two sets of data plotted in Figure 1 is very high, even though there may be some unaccountable effects of space reddening, and we conclude that the precision of both sets of data is high. We do not make a quantitative analysis of the residuals in Figure 1 (or in Fig. 2), because we

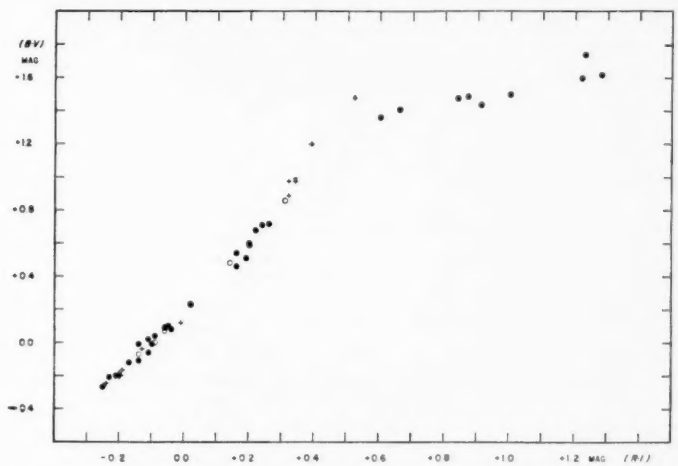

FIG. 1.—Relationship between the $(B - V)$ colors of Johnson and Morgan, and the $(R - I)$ colors for stars in common. Crosses are for stars of luminosity class III, open circles for class IV, and the filled circles for class V.

think the source of these residuals may lie as much in the intrinsic properties of the stars themselves, or in the interstellar medium, as in the properties of the observations. The best quantitative appraisal of the accuracy of the present observations probably can be gained from a study of the average deviations of a single observation given in Tables 2 and 4 and from the systematic mean seasonal differences of the standard regions given in Table 3. The mean average deviation for a single observation of R among the color standards is 0.018 ± 0.0056 (p.e.) mag. and the analogous value for $(R - I)$ is 0.014 ± 0.0038 mag. The average number of nights on which each color standard was observed is 4.5.

Figure 2 is a plot of $(V - R)$ versus $(R - I)$ for the same stars as in Figure 1. In effect, this diagram shows the correlation between the V magnitudes of Johnson and Morgan and our R magnitudes, and it may be seen that this correlation is again very high. The separation of the luminosity classes is weak, if present at all, probably partly

[7] Barnard's Star, $(B - V) = +1.74$ mag., $(R - I) = +1.23$ mag.; BD $-4°4226$, $(B - V) = +1.44$ mag., $(R - I) = +0.91$ mag.

[8] *Ap. J.*, **112**, 160, 1950; *Contr. Lick Obs.*, Ser. II, No. 30, 1950.

from the exclusion from this diagram of any magnitudes made in the blue spectral region and partly from the effect of the relatively small color bases.

Three variable stars were found among those on the program—C12 A, D10 M, and, surprisingly, κ Cet. C12 A is an A-type star that is slowly getting brighter at the rate of 0.03 mag. per year. D10 M probably is an M-type giant, and from the work of Stebbins and Huffer[9] one would expect it to vary. The amplitude is so large that D10 M is useless as a zero-point standard, but we retain it as useful for its color, which apparently remains practically constant. The star κ Cet is a G-type main-sequence star with known parallax

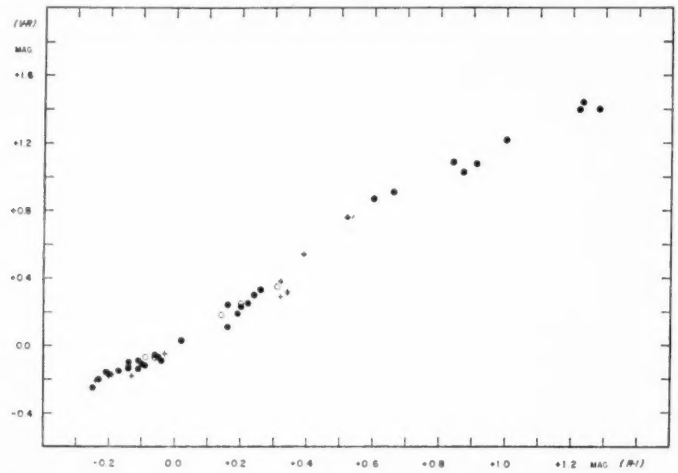

FIG. 2.—Relationship between $(V - R)$ and $(R - I)$. Coding of the plotted points is the same as for Fig. 1.

and no known or suspected peculiarities. The amplitude of variation is approximately 0.10 mag., as determined from two nights in 1950, four in 1951, and two in 1952. The color remains constant. The variation of this star makes it an interesting object, and it may be profitable to follow it.

We are indebted to J. Lynn Smith for help with the observations and to Joel Stebbins, Olin Eggen, and Harold Johnson for valuable discussion. A grant from the American Philosophical Society and funds from the University of California, which made possible the trip to the Southern Hemisphere,[10] are gratefully acknowledged.

[9] *Pub. Washington Obs.*, **15**, 139, 1930.

[10] Katherine Gordon Kron, *Pub. A.S.P.*, **64**, 165, 1952.

RED AND INFRARED MAGNITUDES FOR 27 SOUTHERN HEMISPHERE STARS OF EARLY SPECTRAL TYPE*

GERALD E. KRON
Lick Observatory, University of California
AND
S. C. B. GASCOIGNE
Commonwealth Observatory, Mount Stromlo, A.C.T., Australia
Received June 2, 1953

ABSTRACT

A tabulation is given of photoelectrically determined red and infrared magnitudes of 27 bright stars of the Southern Hemisphere, all of early spectral type. Among these stars are to be found the bluest we have measured.

DISCUSSION

This paper presents red and infrared magnitudes of some stars included in a photoelectric program that has been undertaken at the Lick Observatory. Most of the stars were observed during a recent visit to the Commonwealth Observatory in Australia and are objects of early spectral type in a list of relative gradients of 166 stars.[1] The magnitudes of the stars here published, added to those in our color standard list[2] common to Gascoigne's list, give us a total of 54 stars in common.

The equipment and methods have been described elsewhere.[2, 3] Observing was done along with the program described in the preceding paper, and the same standards of accuracy were maintained. The observations are given in Table 1. The spectral types[1] are on the Morgan, Keenan, and Kellman *Atlas* system. The final column gives the number of nights on which the star was observed. Magnitudes are on the red-infrared system described by Kron and Smith.[3]

All observations were made in 1951 at the Commonwealth Observatory with the Reynolds reflector, except for a few of the miscellaneous stars noted in Table 1. The present list contains some of the bluest stars we have ever measured, β Cen at $(R-I) = -0.28$ mag. and α Cru at -0.27 mag. These stars are bluer than any of the blue stars in the Orion region that have been measured on our program for color standards. The stars σ Sco and ζ Oph (among the color standards) are unusually red for their spectral types, and, though bright stars, they may be space-reddened. Features noted about the colors of these stars are well correlated with the relative gradients.

We are indebted to Howard S. White for aid in preparing this paper and to the American Philosophical Society and the University of California for financial aid.

* *Contributions from the Lick Observatory*, Ser. II, No. 50.

[1] S. C. B. Gascoigne, *M.N.*, **110**, 21, 1950.

[2] *Ap. J.*, **118**, 502, 1953.

[3] G. E. Kron, *Ap. J.*, **115**, 1, 1952; *Contr. Lick Obs.*, Ser. II, No. 38, 1952; G. E. Kron and J. Lynn Smith, *Ap. J.*, **113**, 324, 1951; *Contr. Lick Obs.*, Ser. II, No. 34, 1951.

TABLE 1

RED AND INFRARED MAGNITUDE OF EARLY-TYPE SOUTHERN HEMISPHERE STARS

STAR	1900 POSITION		SPECTRUM	R	a.d.	$(R-I)$	a.d.	n
	R.A.	Dec.						
55 Psc*	00^h34^m7	$+20°53'$	.....	5^m02	1	$+0^m29$	1	3
α Eri	1 33.9	−57 45	B5 IV	0.65	1	−0.15	1	3
β Ori	5 09.7	−08 19	B8 Ia	0.30	3	−0.08	1	4
δ Ori	5 26.9	−00 22	O9.5 III	2.44	2	−0.24	0	4
β CMa	6 18.3	−17 54	B1 II–III	2.24	1	−0.24	1	3
ϵ CMa	6 54.7	−28 50	B1 II	1.67	3	−0.24	1	3
−44°3045 AB*	6 54.9	−44 09	.....	9.53	1	+1.13	3	3
29 CMa	7 14.5	−24 23	.....	5.16	15	−0.17	1	3
τ CMa	7 14.5	−24 47	O9 III	4.54	2	−0.19	1	4
υ^1 Pup	7 14.8	−36 33	.....	4.90	2	−0.15	1	2
υ^2 Pup	7 15.1	−36 34	.....	5.30	2	−0.18	0	2
ζ Pup	8 00.1	−39 43	O5	2.45	2	−0.24	1	4
γ^1 Vel	8 06.4	−47 03	.....	4.47	2	−0.25	2	3
γ^2 Vel	8 06.5	−47 03	WC 7	1.94	1	−0.23	2	3
o Vel	8 37.4	−52 34	B3 V	3.79	2	−0.21	1	3
κ Vel	9 19.0	−54 35	B2 IV	2.66	1	−0.22	1	2
46 Leo*	10 26.9	+14 39	.....	4.36	2	+0.83	2	3
θ Car	10 39.4	−63 52	B0 Vp	2.98	2	−0.24	1	2
δ Cru	12 09.8	−58 12	B2 IV	3.04	1	−0.26	1	2
α Cru AB	12 21.0	−62 33	B1 IV	0.98	3	−0.27	1	3
γ Cen	12 36.0	−48 25	A0 III	2.29	3	−0.11	1	2
β Cru	12 41.9	−59 09	B0 III	1.49	1	−0.25	1	3
β Cen	13 56.8	−59 53	B1 II	0.79	3	−0.28	2	4
ρ Sco	15 50.7	−28 55	B2 V	4.10	2	−0.23	1	3
σ Sco†	16 15.1	−25 21	B1 III	2.87	1	+0.03	1	4
HD 155849*	17 09.0	−26 25	.....	6.95	2	+0.52	1	4
υ Sco	17 24.0	−37 13	B2 IV	2.92	2	−0.24	2	4
λ Sco	17 26.8	−37 02	B2 IV	1.83	3	−0.25	1	3
κ Sco	17 35.6	−38 59	B2 IV	2.61	2	−0.24	1	4
ϵ Sgr	18 17.5	−34 26	B9 IV	1.91	2	−0.08	0	3
17 Lyr AB*	19 03.6	+32 21	.....	5.10	2	+0.11	2	3
α Pav	20 17.7	−57 03	B3 IV	2.15	1	−0.20	1	3

* Miscellaneous stars of later type included for convenience of publication.

† Found by A. R. Hogg (*M.N.*, **111,** 339, 1951) to be a variable star with an amplitude of 0.08 mag.

ON THE FRAGMENTATION OF GAS CLOUDS INTO GALAXIES AND STARS

F. HOYLE*
Princeton University Observatory
Received June 1, 1953

ABSTRACT

The present paper seeks to trace the steps whereby an extensive cloud of density 10^{-27} gm/cm^3 evolves, first into galaxies and then into stars. The indication is that galaxies are likely to form, not as single objects, but in clusters. Stars apparently form at an early stage in the history of a galaxy. There would seem to be reason why the average mass of such stars should lie somewhat below the solar mass.

I. INTRODUCTION

The arguments of the present paper, it should be stated at the outset, are of a mainly tentative character: the theory is still too qualitative and its comparison with observation not sufficiently strict to justify a stronger statement. Yet, in spite of these shortcomings, there seem to be rather many points where the idea of fragmentation—of gravitational turbulence, as it might be called—holds out hope of explaining important observational data that it seems worth while to describe the process at some length.

As examples of the problems that come within the scope of the present paper the following may be mentioned. Why do galaxies tend to occur in clusters?[1] Why are the masses of the galaxies mainly confined in the range $3 \times 10^9 \odot$ to $3 \times 10^{11} \odot$, with possibly a tendency to fall into two groups at the ends of this range?[2] Why is the typical mass of a type II star of order $\odot$? Why do type II stars apparently form almost simultaneously with the origin of a galaxy?

II. DENSITY AND TEMPERATURE IN AN EXTRAGALACTIC HYDROGEN CLOUD

No attempt is made in the present paper to explain the origin of the extragalactic cloud under consideration. This is a matter that must be treated, not in the present Newtonian theory, but in a theory of the expanding universe.

Reference to the expanding universe allows us, however, to make use of a result that appears in all theories of the expanding universe, namely, that it is necessary that the density of our cloud shall appreciably[3] exceed 10^{-28} gm/cm^3, for otherwise the effects of expansion cannot be neglected; the problem becomes Newtonian only when this condition is satisfied.

Now the density of the cloud may reasonably be bracketed between this lower limit of 10^{-28} gm/cm^3 and the upper limit suggested by Sinclair Smith's determination[4] of the mean density within the great nebular clusters. Again, with Baade's new distance scale, this upper limit turns out to be somewhat greater than 10^{-26} gm/cm^3. In the following work we shall use an intermediate value of 10^{-27} gm/cm^3 for the initial density ρ_0 of our cloud.

To estimate the temperature, it is assumed that, in whatever process originally led to the formation of the cloud, mass motions developed within the gas. It is reasonable to

* Normally at Cambridge University.

[1] J. Neyman, E. L. Scott, and C. D. Shane, *Ap. J.*, **117**, 92, 1953.

[2] T. Page, *Ap. J.*, **116**, 63, 1952.

[3] Using Baade's redetermination of the distance scale.

[4] *Ap. J.*, **83**, 23, 1936.

suppose that the velocities so developed were in excess of 10 km/sec, and perhaps, in the case of very large clouds, in excess of 100 km/sec. Now ordinary turbulence must eventually convert mass motions into heat. Thus it is being assumed, in effect, that in the formation of the cloud a supply of energy, ultimately converted into heat, of certainly more than 10^{12} ergs/gm, and perhaps more than 10^{14} ergs/gm is made available. Assuming, then, an initial supply of energy, the next step is to estimate the temperature to which hydrogen gas will be raised. To make such an estimate it is necessary to collect together the following thermal properties of hydrogen:

a) The thermal energy of atomic hydrogen is $\frac{3}{2}\Re T$/gm, where $\Re$ is the gas constant and T is the temperature in ° K. From this it follows that the energy required to increase the temperature of atomic hydrogen from absolute zero up to 10,000° K is somewhat in excess of 10^{12} ergs/gm.

b) Hydrogen becomes collisionally ionized at temperatures higher than 10,000° K. Thus, even in the absence of radiation, hydrogen changes[5] from being largely un-ionized at 10,000° K to being almost wholly ionized at 25,000° K.

c) The energy required to ionize hydrogen is somewhat greater than 10^{13} ergs/gm.

d) The time of formation of our cloud may be taken as of the same order as Hubble's constant, this being about 10^{17} seconds, with Baade's new distance scale. In this length of time, ionized hydrogen radiates an amount of energy that is much greater than the energies arrived at in *a* and *c*. Excluding line emission, the hydrogen radiation amounts to[6]

$$1.45 \times 10^{-27} T^{1/2} \left(1 + \frac{3.85 \times 10^5}{T}\right) N^2 \text{ ergs/cm}^3\text{/sec}, \tag{1}$$

where N is the number of hydrogen atoms per cubic centimeter, and the kinetic temperature T is in ° K. The first term within parentheses gives the contribution of free-free transitions, and the second term takes account of free-bound transitions. It is particularly to be noticed that equation (1) includes the radiation emitted in the Lyman continuum. This radiation escapes from the cloud only when the hydrogen is effectively wholly ionized, as it is at 25,000° K but not at lower temperatures—say at 15,000° K. Thus the escape of radiation from the cloud at 15,000° K must be calculated, excluding the Lyman continuum. In this case the factor $3.85 \times 10^5/T$ in equation (1) must be replaced by $6.5 \times 10^4/T$.

Compare the two temperatures 15,000° and 25,000° K; in the former case the emission of escaping radiation amounts to 3×10^{13} ergs/gm of ionized hydrogen in 10^{17} seconds, and in the latter case to 1.3×10^{14} ergs/gm in 10^{17} seconds. Both these estimates refer to a hydrogen density of 10^{-27} gm/cm.^{3}

e) As the temperature of hydrogen increases above 25,000° K, the rate of radiation decreases until temperatures above 3.85×10^5 ° K are reached. The rate of radiation then slowly increases. At very high temperatures, however, the main energy requirement comes not from the necessity to make good the loss due to radiation but simply from the energy required to heat the hydrogen. Thus the energy required to heat ionized hydrogen to temperature T is $3\Re T$ per unit mass, which amounts to 2×10^{14} ergs/gm at 10^6 ° K; for comparison, the radiation emitted in 10^{17} seconds by ionized hydrogen at 10^6 ° K is only 7×10^{13} ergs/gm.

If one considers, then, the temperature obtained in the cloud as a function of the energy supply (taken to occupy a time of 10^{17} seconds), one may distinguish the following

[5] Cf., e.g, F. Hoyle, *Some Recent Researches in Solar Physics* (Cambridge: At the University Press, 1949), p. 25.

[6] R. Minkowski, *Ap. J.*, **96**, 206, 1942. The formula given by Minkowski is sufficiently accurate for the present purpose. In a more thoroughgoing treatment it would be necessary to include the process of two-quantum emission from the 2s state of the hydrogen atom, discussed by Spitzer and Greenstein in *Ap. J.*, **114**, 407, 1951.

stages. During the early stages (A–B, say), during which atomic hydrogen becomes collisionally ionized, energy is absorbed only in raising the temperature of atomic hydrogen. If all the hydrogen were ionized at 15,000° K (stage C), the energy required for ionization would be 10^{13} ergs/gm, and the energy required to make good the loss through escape of radiation would be 3×10^{13} ergs/gm. But at 15,000° K only about two-thirds of the hydrogen is collisionally ionized. This circumstance reduces the energy required for ionization to $\frac{2}{3} \times 10^{13}$ ergs/gm, and the average radiation rate to $\frac{1}{3} \times 10^{13}$ ergs/gm, thereby giving a total of 2×10^{13} ergs/gm. When the temperature has risen to 25,000° K (stage D), the hydrogen is effectively wholly ionized, and the energy supply must include 10^{13} ergs/gm for ionization, and 1.3×10^{14} ergs/gm for the escape of radiation, giving a total of 1.4×10^{14} ergs/gm. Since radiation then decreases with increasing temperature, the extra energy required to take the hydrogen to 10^{5}° K (stage E) is only a little more than the energy required to reach stage D. The energy at stage C will differ from that at stage B by essentially the difference of thermal energy between 10^{5}° K and 25,000° K. The plot of temperature against energy supply must therefore be very flat between these two stages; it would not steepen again until temperatures exceeding 3×10^{5}° K were reached. This latter steepening arises from the energy required to heat the hydrogen, which becomes the major requirement at temperatures greater than 10^{6}° K. At very high temperatures, the rate of rise of the temperature with energy supply must approach the same slope as during the early stages A–B.

The sequence of events we have described is important in showing that a dichotomy of temperature is to be expected. Excluding temperatures less than 10^{4}° K as corresponding to an improbably small energy supply (mass motions less than 10 km/sec developing during the formation of the cloud), *either the temperature lies in the range 10,000°–25,000° K, or the temperature as a general rule must be high, of the order of* 3×10^{5}° *K or more.*

Intermediate temperatures are not rigorously forbidden, but, owing to the flatness of the temperature rise during stages D–E, it is most unlikely that the energy supply will happen to fall into the narrow range that corresponds to intermediate temperatures.

In concluding the present section, it should be emphasized that although the sequence of effects described would not be affected, its precise form would be altered by changes in the value chosen for the time scale and for the density ρ_0. In this connection it may be noted, however, that the time scale for the formation of the cloud may be expected to be of the order of $(\rho_0 G)^{-1/2}$: for a density of 10^{-27} gm/cm^3 this is precisely of the order of 10^{17} seconds. A reduction of the time scale by a factor y hence implies an increase in density by y^2, and this produces a change in the importance of radiation by y. For $y > 1$ the importance of radiation would be enhanced, and this would have the effect of enhancing to an even greater degree the flatness of the temperature rise between stages D and E. Accordingly, the conclusion of the previous paragraph would be threatened only if $y < 1$, thereby reducing the importance of radiation. But $y < 1$ would imply a time scale $> 10^{17}$ seconds, which seems excluded by data on the expanding universe. Any revision of the values for the time scale and density must, it seems, confirm a fortiori our previous conclusion.

Having now seen physical reasons why a segregation into two temperature classes is to be expected, the further development of a cloud in the low-temperature class will next be investigated in the following three sections; only when we come to Section VII will high-temperature clouds receive further consideration.

It will turn out that, for the low-temperature clouds, radiation by the hydrogen prevents the temperature from ever rising above 25,000° K, while recombination into neutral atoms prevents the temperature from falling much below 10,000° K. Thus fluctuations of temperature are confined to a fairly narrow range. It will be convenient in the following section to ignore any such fluctuations, taking a constant value of 15,000° K as a suitable compromise.

III. THE CONDITION FOR CONTRACTION

It can be rigorously established that when a gas cloud of uniform composition is in hydrostatic equilibrium, with gravitational forces balanced by gas-pressure gradients—radiation pressure being negligible—the total gravitational potential energy Ω (>0) must be equal to twice the total thermal energy of the gas. A spherical cloud contracts if Ω is greater than this and expands if Ω is less than this. As giving an order-of-magnitude estimate, we may adopt a similar criterion for a nonspherical cloud of volume V, the cloud contracting if Ω is greater than twice the total thermal energy. For the total thermal energy we shall write $2.5\,\mathfrak{R}MT$, this being the thermal energy that the cloud would have if all the material were two-thirds ionized at temperature T (hydrogen is two-thirds ionized at $T = 15{,}000°$ K, which is the numerical value used below for T). For Ω we write $GM^2/V^{1/3}$, so that the contraction condition becomes

$$\frac{GM}{V^{1/3}} > 5\,\mathfrak{R}T\,. \tag{2}$$

Combining equation (1) with the condition $M = \rho_0 V$, $\rho_0 = 10^{-27}$ gm/cm^3, and $T = 1.5 \times 10^4\,°$ K gives

$$M > 1.4 \times 10^{10}\odot\,.$$

No cloud with mass appreciably less than this can contract to form a galaxy (this being subject to the value chosen for T, since it is considered improbable that T would initially be much less than 15,000° K).

IV. FRAGMENTATION OF CLOUD OF VERY LARGE MASS INTO CLUSTER OF GALAXIES

Consider a cloud with mass appreciably larger than the lower limit set for condensation. The time required for contraction to reduce the dimensions to, say, half of the initial size of the cloud is of the order of $(\rho_0 G)^{-1/2}$; that is, of the order of 10^{17} seconds. Now we have seen that in this time interval ionized hydrogen at $T = 15{,}000°$ K emits about 3×10^{13} ergs/gm. This may be compared with the thermal energy made available during contraction, which is only of the order of $2\mathfrak{R}T$/gm in a contraction in which the dimensions of the cloud are halved, which amounts to less than 3×10^{12} ergs/gm at $T = 15{,}000°$ K. Thus the early phases of contraction provide quite insufficient energy to raise the temperature of the hydrogen. Indeed, the hydrogen, if initially largely ionized, will tend toward appreciable recombination.

If we next imagine a further phase of contraction in which the size of the condensation is again halved, the energy made available through the work done by the gas pressure is again only of the order of 10^{12} ergs/gm. The time required for collapse is now reduced, however, since the density ρ was increased in the previous contraction. But, although the time of contraction is thus reduced by $\rho^{-1/2}$, the rise of density has increased the radiation per gram per unit time by ρ, and this more than offsets the reduction in the time scale. Hence the hydrogen tends still more toward recombination. The same argument could be repeated for further steps of contraction.

The upshot of the argument is that insufficient energy is made available to keep the hydrogen mainly ionized. On the other hand, there is an inverse condition that must be satisfied. This condition requires that the degree of ionization cannot become too low. Thus radiation would effectively cease if the hydrogen were entirely un-ionized. Free electrons would be supplied only by the very small proportion of metal atoms present in the material, and the rate of radiation would then fall to a value lower than the rate of supply of energy by the contraction process (this argument applies not only to radiation by the hydrogen but also to radiation emitted in the forbidden oxygen lines, for ex-

ample). Hence a balance must be reached in which a proportion—say, a few per cent—of the hydrogen remains ionized. This balance requires the temperature to be maintained near 10,000° K. It follows, therefore, that contraction must be a nearly isothermal process.

Let a uniform isothermal contraction at temperature $T = 10^{4}$° K change the volume of the cloud from V to V'. Then the thermal energy released is given by[7]

$$M\mathfrak{R}T \log_e \frac{V}{V'}. \tag{3}$$

This energy maintains a low degree of ionization in the hydrogen, which adjusts itself so that radiation proceeds at such a rate that the energy leaking away from the system comes eventually into balance with the energy made available by the contraction.

The energy (3), thus lost from the system, may be compared with the gravitational energy released by the compression, which is of the order of

$$\frac{GM^2}{V^{1/3}}\left[\left(\frac{V}{V'}\right)^{1/3} - 1\right]. \tag{4}$$

Now when M is such that $GM^2/V^{1/3}$ is very large compared with $3\,M\mathfrak{R}T$ ($GM^2/V^{1/3} = 3\,M\mathfrak{R}T$ giving the *minimum* mass for contraction when the hydrogen is largely *neutral*), the value of expression (4) is much greater than expression (3), whatever V' may be. Accordingly, the gravitational energy released is not thermally dissipated but must go into mass motions within the condensation, *and these mass motions must be adequate to re-expand the cloud to nearly its original volume.*

It is, of course, possible that before the cloud becomes entirely re-expanded, some of the energy of mass motion so developed will be converted into heat by turbulence and shock waves. This indeed would probably be the ultimate main agency of dissipation if a further process of dissipation were not available. This second process is capable of acting even before substantial mass motions develop, which turbulence and shock waves cannot do. Hence it seems likely that the main dissipation will go through this second process, or, at any rate, that a major proportion of the dissipation so occurs.

The second process arises from the circumstance that since the main cloud mass is, by hypothesis, much larger than the minimum mass that is capable of condensing, the cloud is unstable against the formation of subcondensations. Moreover, since the time of condensation depends only on the inverse square root of the density, it follows that a subregion can condense equally as fast as the main cloud, faster, indeed, if the density in the subregion happens to be higher than the mean density within the cloud.

Next we note that if the contraction condition[8]

$$\frac{GM}{V^{1/3}} > 3\,\mathfrak{R}T \tag{5}$$

is only just satisfied, then formula (4), *applied now with reference to the subregion*, is not much greater than formula (3), provided that V' is not too small compared with V. It will be useful to consider numerical estimates. For $T = 10^{4}$° K, inequality (5) gives a minimum mass of about $3.6 \times 10^{9}\odot$, it being assumed in making this estimate that T falls to about 10^{4}° K before the density rises appreciably above 10^{-27} gm/cm^3. Consider

[7] Let v be the specific volume. The thermal energy released by an isothermal contraction dv is $-p\,dv$ per unit mass. Since $p = \mathfrak{R}\rho T$ for mainly neutral hydrogen, and $\rho = 1/v$, the energy released is $-\mathfrak{R}T\,dv/v$, which, on integrating from v to v', gives $\mathfrak{R}T \log (v/v')$ for the energy released per unit mass. Now for uniform contraction, $v/v' = V/V'$, and hence the energy released is $\mathfrak{R}T \log (V/V')$ per unit mass, and $M\mathfrak{R}T \log_e (V/V')$ for the whole cloud.

[8] This differs slightly from the condition arrived at in Sec. III, the coefficient 3 replacing the previous coefficient 5. The difference is that the temperature has now fallen to about 10,000° K, with the hydrogen mainly neutral, whereas, before, two-thirds of the hydrogen was ionized.

a subunit with approximately this mass. Then for $V' = 10^{-1} V$, expression (3) is comparable with expression (4); for $V' = 10^{-3} V$, expression (3) is still about 30 per cent of (4); but, for $V' = 10^{-6} V$, expression (3) is only about 5 per cent of (4). This means that, for a decrease of linear dimensions by a factor of 2 or 3, there is an almost complete dissipation of the energy of contraction, and hence that a stable bound configuration of about one-third the original dimensions could certainly be formed. It may be that a stable configuration slightly smaller than this could be formed, but in the following discussion we shall accept a permanent shrinkage by a factor of 3. A shrinkage of much more than this would only induce the condition already noted in reference to the main cloud, namely, that the gravitational energy of contraction would go into mass motions that could re-expand the condensation.

Returning, now, to the original cloud of large mass, we have seen that, whereas there is negligible dissipation for a uniform contraction of the whole cloud, the dissipation can be both rapid and considerable if the cloud breaks up into subregions, each subregion possessing a mass that is not greatly in excess of the minimum mass of $3.6 \times 10^9 \odot$, as set by the contraction condition for hydrogen of density 10^{-27} gm/cm^3 that is mainly neutral at a temperature of 10,000° K. We may describe this process by saying that the main cloud fragments into galaxies with masses of the order of $3.6 \times 10^9 \odot$. That the fragments may indeed be described as galaxies is shown by a consideration of their dimensions. Initially, at a density of 10^{-27} gm/cm^3, a sphere of radius 1.2×10^{23} cm contains a mass of $3.6 \times 10^9 \odot$. Permanent contraction by a factor of 3 reduces the radius to about 13,000 parsecs.

Although this is certainly of galactic dimensions, the radius is still considerably greater than the radius of a typical galaxy of mass $3.6 \times 10^9 \odot$. Thus it might appear at first sight as if the degree of permanent contraction were seriously underestimated in the above discussion. It is, however, doubted whether this is so, because there are indications that a considerable further reduction of dimensions is likely to occur at a later phase when stars have formed in these galaxies. This dynamic process is discussed in Section VIII. It may be said that the present calculated radius of 13,000 parsecs should be thought of as a measure of the dimensions of the diffuse extensive halos that surround the galaxies, rather than as an estimate of the final dimensions of the main nucleus.

The results of the present and previous sections might be construed into the conclusion that galaxies never condense singly, that a cluster of galaxies is always formed. Thus if we accept the conclusion of the previous section that no cloud of mass less than $1.4 \times 10^{10} \odot$ can condense in the first place and if we combine this with the galactic mass of $3.6 \times 10^9 \odot$, as deduced above, we see that the smallest condensing cloud should still fragment into about 4 galaxies. The difference between the minimum mass of $1.4 \times 10^{10} \odot$ of Section III and the galactic mass of $3.6 \times 10^9 \odot$, as calculated above, arises from the cooling of the main cloud as it tends to contract. Thus, in Section III an initial temperature of 15,000° K was used, whereas radiative cooling soon reduces this temperature to about 10,000° K. The present argument should not be taken too seriously, however, as it is probably an overstraining of the theory. Even if correct, it does not imply that single galaxies should never be observed; for even if all galaxies do condense into clusters, dynamical encounters must lead to a proportion escaping from their parent-clusters, especially from small clusters.

V. THE HIERARCHY STRUCTURE

The argument presented in the previous section shows that, even when the mass of a galactic condensation is close to the minimum mass set by the contraction condition, effective dissipation of the gravitational energy of contraction is limited to decrease in dimensions by a factor of about 3. Additional contraction simply leads to the development of dynamical motions, with the tendency to re-expand the condensation. Evolution can

proceed alternatively, however, through the formation of a hierarchy structure. *Thus an exactly similar development can be applied to subunits developing within the galaxy itself.* Consider the following step-by-step model, in which the approximation of a constant temperature of 10^4 ° K will be used throughout. This simplification omits any slight cooling that may occur in the earliest phases of contraction.

MODEL FOR THE HIERARCHY STRUCTURE

Step 1.—A spherical galactic condensaton, of mass $3.6 \times 10^9 \odot = M_0$ say, temperature 10^4 ° K, initial density $\rho_0 = 10^{-27}$ gm/cm^3, initial radius $R_0 = 1.2 \times 10^{23}$ cm, contracts by a factor $k^{2/3}$ and then divides into k equal masses, each of radius R_0/k, density $\rho_0 k^2$, and temperature 10^4 ° K.

It will be noticed that the obvious requirements are satisfied by these assumptions. Thus each of the subunits satisfies the contraction condition. Moreover, with their assumed radii the subunits can be fitted into the contracted volume of the galaxy itself. Remembering that in the first shrinkage the galaxy decreases in dimensions by a factor of about 3, it follows that we must put $k^{2/3} \fallingdotseq 3$, which gives $k \fallingdotseq 5$.

Step 2.—The subunits of step 1 themselves contract by a factor of $k^{2/3}$ and then divide into k equal fragments, each of radius R_0/k^2, density $\rho_0 k^4$, and temperature 10,000° K. Once again these smaller fragments satisfy the contraction condition.

Step 3.—The subunits of step 2 themselves contract by a factor of $k^{2/3}$ and then divide into k equal still smaller fragments, each of radius R_0/k^2, density $\rho_0 k^6$, and temperature 10,000° K. Once again these still smaller fragments satisfy the contraction condition.

And so on for further steps.—Now, since the time scale for condensation at each step may be expected to follow the inverse square root of the density, it follows that the ratio of the time required for an infinity of such steps to the time required for just the first step is given by

$$1 + \frac{1}{k} + \frac{1}{k^2} + \frac{1}{k^3} + \ldots = \frac{k}{k-1},$$

which for $k = 5$ gives a ratio close to unity. Thus we see that the main expenditure of time lies in the first step and that further steps require comparatively little time. It is indeed this rapid convergence of the steps that provides the strongest reason for the opinion that dissipation arises from the development of the sort of hierarchy structure postulated above. An alternative scheme of dissipation would lie in the development of dynamical motions in a more or less uniform contraction of the main mass and of the turbulent dissipation of these motions. This may occur in some degree but is considered less likely in view of the time-scale estimates for fragmentation.

Of course, the hierarchy picture suggested above has many analogies with the phenomenon of turbulence. It may be thought of as turbulence in a gravitational field rather than in a pressure field. From the turbulence point of view the present suggestions would seem plausible, since the fact that the gravitational field becomes stronger than the pressure field supplies the very basis of the fragmentation process.

Although it may be useful to think of fragmentation in a hierarchy structure as representing a sort of gravitational turbulence, it is important to realize that a crucial difference exists between the formation of eddies in a pressure field and in the present process. The rise of pressure due to compression in ordinary turbulence tends to disrupt the denser elements of material. It is for this reason that the density of a particular sample of material fluctuates in ordinary turbulence, sometimes being denser than the general average and sometimes being less dense. The formation of a denser element in gravitational turbulence, on the other hand, only increases the ability of the element to hold itself together. Thus there is a rooted difference between the two cases: denser elements are evanescent in ordinary turbulence, denser elements tend to become permanent condensations in gravitational turbulence.

The description of the hierarchy model is still incomplete, in that an explanation of why the temperature is maintained constant at 10,000° K must still be given. It can readily be shown that the dissipation of energy is the same in each step of the hierarchy structure, the dissipation per step being of the order of

$$\frac{GM_0^2}{R_0}(k^{2/3} - 1). \tag{6}$$

Now, since the time scale for each successive step decreases as $1/k$, it follows that the rate at which thermal energy is made available per unit mass increases by a factor k at each step. On the other hand, the rate of radiation per unit mass increases as ρ, which increases by k^2 at each step. Accordingly, radiation is favored by the changes that take place as fragmentation proceeds. There is, therefore, a tendency for the temperature to fall, *but the temperature cannot fall much below 10,000° K, since otherwise the hydrogen would become insufficiently ionized for effective radiation to occur*. This conclusion is subject to the implicit assumption that the fragments remain optically thin to radiation. The entire nature of the condensation process is altered if the fragments become optically thick to the whole of the radiation spectrum of the hydrogen. A discussion of this issue forms the main topic of the following section.

It is desirable to add that the model laid down above is an obvious idealization. We may expect deviations from the model to occur in a number of respects: The formation of subunits would be continuous, not a succession of discrete steps. Even with discrete steps, however, one step need not be exactly like another. Also we have assumed that at each step all the material condenses into subunits. The possible consequences of this assumption's not being strictly satisfied are discussed in the last section of the paper.

VI. FRAGMENTATION OF A GALAXY INTO TYPE II STARS

It is now necessary to investigate whether step-by-step fragmentation continues indefinitely or whether there is some reason why it should end after a finite number of steps. Looking back over the previous argument, it will be seen that fragmentation owes its origin to the maintenance of a near-isothermal condition, that a near-isothermal condition is maintained throughout the condensation on account of radiation by the hydrogen. It is this that leads to the development of dynamical motions, which forms the basis of fragmentation.

If, in contrast, an adiabatic condition was maintained, then the work done by the gas pressure in a uniform change of volume from V to V' releases thermal energy[9]

$$1.5M\mathfrak{R}T_0\left[\left(\frac{V}{V'}\right)^{2/3} - 1\right], \tag{6a}$$

where M is the total mass and T_0 is the temperature at volume V. Comparison with expression (4) shows that the dependence on V/V' is now stronger in expression (6a). Hence under adiabatic conditions a condensation does not necessarily tend toward dynamical motions as it shrinks. Indeed, a mass of gas that is just unstable against contraction shinks only a little before the thermal energy becomes adequate to maintain the gas in hydrostatic equilibrium. It is true that a cloud with a mass that is very large compared with the minimum mass for contraction can shrink appreciably and that during the shrinkage dynamical motions that produce fragmentation can develop; but such fragments cannot themselves contract significantly, since they tend to possess masses that are only slightly above the minimum for contraction.

[9] Let v again be the specific volume. The work done in a small change dv is again $-pdv$ per unit mass. Also $-pdv = -\mathfrak{R}T\,dv/v$ as before, but T now varies as $v^{-2/3}$, so that the work done for a change from v to v' is $1.5\mathfrak{R}T_0\,[(v/v')^{2/3} - 1]$ per unit mass. Thus for uniform contraction with $v/v' = V/V'$, the total energy released for mass M is $1.5M\mathfrak{R}T_0\,[(V/V')^{2/3} - 1]$.

We can readily see why fragmentation should ultimately result in an approximation to the adiabatic condition. Thus after n steps in the hierarchy model the density is $\rho_0 k^{2n}$, and the radius of a fragment is R_0/k^n. Accordingly, the total opacity across the fragments increases with n according to k^n, so that for sufficiently large n the fragments must become highly opaque. This causes a transition to the adiabatic condition. It is now proposed to investigate the nature of this transition.

Opacity may be thought of as arising partly from scattering and partly from absorption. In the present problem the scattering, arising from free electrons, can be shown to be unimportant compared with absorption. Now absorption can become important in impeding the escape of radiation from a fragment only when the absorption by the gas of energy from the radiation field becomes comparable with the energy radiated by the gas. But this is just the condition that the radiation field, in the frequencies under consideration, shall approximate to the black-body distribution. It follows, therefore, that a transition to the adiabatic condition implies that the black-body distribution (over the part of the spectrum that is of interest) has been built up inside the fragment under consideration. The properties of the fragment then become similar to those of a star; and, just as with a star, the fragment radiates at a rate L that can be estimated in terms of temperature, density, opacity, and radius.

For a transition to the adiabatic condition, we require L to become less than the rate at which gravitational energy is being released in our problem. The gravitational energy released per fragment in the nth step of the hierarchy process is of the order of

$$\frac{GM_0^2}{R_0 k^n}(k^{2/3} - 1),$$

the release occupying a time of order $k^{-n}(G\rho_0)^{-1/2}$. In this time the energy radiated is $Lk^{-n}(G\rho_0)^{-1/2}$. Hence a transition from the isothermal to the adiabatic condition begins to occur at the stage where

$$L = \frac{G^{3/2} M_0^2 \rho_0^{1/2}}{R_0}. \tag{7}$$

Now the outward flux at distance r from the center of the fragment is given by

$$\frac{16\pi a c r^2 T^3}{3\kappa\rho}\frac{dT}{dr}, \tag{8}$$

where a is Stefan's constant, c the velocity of light, and κ the coefficient of opacity.

If the fragment were composed of entirely pure hydrogen, κ would become extremely small for temperatures below about 5000° K, since even in the presence of black-body radiation the hydrogen would then be effectively un-ionized (having regard to the important densities turning out to be of the order of 10^{-9} gm/cm^3). Hence expression (8) would become increasingly large as T fell below 5000° K, until ultimately a value equaling $4\pi acR^2T^4$ would be attained. This would imply that the surface temperature of the fragment had been reached, the value so reached being in the neighborhood of 4000° K. At such a surface temperature the fragment would radiate at a much greater rate than the luminosity that obtains when only a very small proportion of the mass consists of nonhydrogenic materials. It is therefore of importance to take account of the presence of a small admixture of elements other than hydrogen.

Metals have the important effect of increasing the opacity for values of T in the range 3000°–5000° K. Free electrons are supplied by the metals, approximately one electron per metal atom. The attachment of free electrons to the neutral hydrogen atoms then causes negative hydrogen ions to be produced, and it is these ions (as was pointed out by Wildt) that produce the opacity in the temperature range in question. At temperatures

below 3000° K molecules begin to be formed, with the probable consequence of a steep rise in the opacity. Indeed, so great is the absorptive power of the molecules likely to be that the smallest value of κ would seem to lie in the range 3000°–5000° K. According to the tables of Chandrasekhar and Münch,[10] the smallest value of κ is likely to occur toward the upper end of this range, where its value is close to $10^{-1}\,P_e$, the electron pressure being denoted by P_e. For the purpose of obtaining a numerical estimate, we shall use $T = 4500°$ K, which is safely below the temperature at which the ionization of hydrogen would have to be taken into account. Such a temperature is sufficiently small compared with the central temperature of 10,000° K for the radius R of the fragment to be used as a suitable approximation for the radial co-ordinate r in expression (8). Next we note that the temperature gradient dT/dr will tend to be least for those values of T where κ is least. But the least value of dT/dr must be of the order of T/R in the present problem.[11] Hence expression (8) must be of the order of

$$\frac{160\,a\,cRT^4}{3\,\rho P_e}. \tag{9}$$

Although expression (9) has not been obtained from a consideration of the extreme outer layers, it must represent the luminosity of the fragment, since, if the surface radiates less energy than is received from below, the surface simply heats up, whereas if the surface radiates more, the surface temperature declines accordingly. Where the opacity is higher toward the center, the same flux must be maintained by a marked steepening of the temperature gradient.

The electron pressure is given by

$$P_e = x\mathfrak{R}\,\rho T\,,$$

where x is the number ratio of metals to hydrogen. Inserting this value for P_e in expression (9) shows that the luminosity is proportional to T^3/ρ^2, which may be taken as not very different from the central value $T_0^3/\rho_0^2 k^{4n}$ (the central density after n fragmentations being $\rho_0 k^{2n}$, ρ_0 being the original density of the cloud). With this further approximation and putting $R = R_0 k^{-n}$, the luminosity becomes

$$\frac{160\pi\,a\,cR_0T_0^3}{3\,x\mathfrak{R}\,\rho_0^2}\,k^{-5n}. \tag{10}$$

We are now in a position to return to our original objective. The luminosity of the fragment is given by expression (10) when the adiabatic condition is satisfied, since it is only then that the black-body distribution is set up. The transition to the adiabatic condition occurs at the stage of the hierarchy system where equation (7) is satisfied. If we insert expression (10) for L in equation (7), we obtain (writing $GM_0/V^{1/3} = 3\mathfrak{R}T_0$)

$$k^{5n} = \frac{160\pi\,a\,cG^{1/2}}{27\,x\mathfrak{R}^3}\,\frac{T_0}{\rho_0^{5/2}}. \tag{11}$$

This procedure constitutes an approximation in the sense that the substitution of expression (10) in equation (7) means that we are using formula (10) at the onset of the

[10] *Ap. J.*, **104**, 446, 1946.

[11] The temperature T falls from 5000° to 3000° K in a distance of the order of, but less than, R. Hence the mean temperature gradient for this range is of the order of T/R, $T = 4500°$ K. Now the mean temperature gradient gives an adequate approximation for dT/dr, since κ does not vary much between 5000° and 3000° K; if there were marked variations from the mean temperature gradient, there would be corresponding variations in the outward flux, and such variations would eventually be damped out. The present argument is, of course, dependent on the surface temperature being lower than 3000° K, a condition that at a later stage will be shown to be satisfied.

transition to the adiabatic condition, whereas, properly, formula (10) should be used only *after* the adiabatic condition is satisfied. Accordingly, we cannot be sure that the numerical value of n given by equation (11) represents the complete end of the fragmentation process. Fragmentation might well go one step further than this. Nevertheless equation (11) is important in giving the end of fragmentation within an uncertainty of about one step. That the uncertainty is not worse than this is shown by the strong dependence of expression (10) on n: an increase of n by 1 decreases formula (10) by a factor of about 5^5.

Now, since $T_0 = 10{,}000°$ K and $\rho_0 = 10^{-27}$ gm/cm^3, the right-hand side of equation (11) is known numerically as soon as a value of x is specified. In stars of type I the value of x is about 5×10^{-5}. This value is now believed, however, to be considerably higher than the value of x occurring in the early history of a galaxy: a value of 5×10^{-6} would perhaps be a more suitable value. Using this for x gives

$$k^n = 2.3 \times 10^9 . \tag{12}$$

Thus for $k = 5$, as indicated in the definition of our model, this gives a value of n of about 13.

The feature of greatest interest, however, is not the number of steps in the hierarchy structure but the mass of the final fragments; this is M_0/k^n. Remembering that M_0 is $3.6 \times 10^9 \odot$, we obtain with equation (12) a fragment mass of about $1.5\odot$. There is an uncertainty, however, in n, as was indicated in the previous paragraph. Thus equation (12) gives k^n only at the onset of the transition to the adiabatic condition, so that one further fragmentation might well occur, which for $k = 5$ would give a final fragment mass of about $0.3\odot$.

The present uncertainty over the precise end of the fragmentation process is, of course, a result of a serious imperfection in the model employed; for it is the assumed discrete nature of the steps that lies at the root of this uncertainty. In a proper theory the whole process would have to be described in continuous terms, and the uncertainty of the discrete model would be replaced by a continuous dispersion of the final masses. It is not possible to say whether or not this dispersion would give a variation between the same values as those indicated above, namely, between $0.3\odot$ and $1.5\odot$. One is encouraged in the belief that it would by the circumstance that the final fragment masses arrived at in the present treatment are entirely independent of the parameter k. In this connection it may be noted that the approximations involved in deriving expression (10) are of a less serious nature than the discrete character of the model, since the approximations affect only the masses of the final fragments in the fifth root.

The radius of the stellar fragment at the onset of the transition to the adiabatic condition is given by $R_0 k^{-n}$, where $R_0 = 1.2 \times 10^{23}$ cm and k^n is given by equation (12): a radius of about 5×10^{13} cm. The luminosity at this stage can be calculated from expression (10) or more simply from the consideration that the dissipation in each step of the hierarchy model is given by expression (6). Thus with $M_0 = 3.6 \times 10^9 \odot$, $R_0 = 1.2 \times 10^{23}$ cm, and $k = 5$, expression (6) amounts to 2.8×10^{55} ergs. This represents the total energy available for the formation of about 5×10^9 fragments, giving about 5.6×10^{45} ergs/fragment. To obtain the luminosity per fragment, this value of 4.6×10^{45} ergs must be divided by the time sacle of the final fragmentation, this being less than the time scale—10^{17} seconds—for the first fragmentation by just the factor k^n. Accordingly, the luminosity during the final fragmentation is about 1.5×10^{38} ergs/sec, corresponding to a bolometric luminosity of about -6.5. The effective surface temperature for a radius of 5×10^{13} cm must be close to 2000° K.

It should now be emphasized that because the first step in the hierarchy system takes longer than all the other steps together, the formation of the stars must be spread over the whole time scale of 10^{17} seconds. This amounts to an average rate of star formation of

about one per year. There will, of course, be variations from this average rate, as, for instance, when any stellar fragment is formed, there must be three or four other stellar fragments produced at the same time. The total bolometric luminosity of such a group would be some five times greater than that of a single fragment, that is, about -8, although the visual magnitude would be substantially less than this, owing to the red color that must accompany the low surface temperatures of the fragments. It might also be added that such an emission would last only for a few years and that fragmentation would induce variability.

After the adiabatic condition becomes satisfied, the star at first shrinks quickly. As the shrinkage proceeds, it slows down, and the luminosity declines. Eventually, in the last stages of the shrinkage, occupying a time of 10^7 years or more, the usual mass-luminosity relation for hydrogen stars comes into force. Shrinkage ceases when the central temperature has risen high enough for the luminosity to be balanced by energy production in the interior.

VII. THE FORMATION OF GALAXIES OF VERY LARGE MASSES

Throughout the last four sections it has been assumed that the initial heating was insufficient to lift the temperature to very high values. In Section II we saw that two temperature classes are to be expected, one in the range 10,000°–25,000° K and the other at temperatures in excess of 10^5 ° K. In the present section we shall consider the latter case.

Once again, if the mass of a cloud is much larger than the minimum mass defined by (now for wholly ionized hydrogen)

$$\frac{GM_0}{V^{1/3}} = 6\Re T_0 , \tag{13}$$

division into a large number of fragments with masses approximately satisfying equation (13) is to be expected.

On the other hand, there is an important difference when T_0 rises above 3×10^5 °K, because radiation then becomes inadequate to dispose of the thermal energy of the hydrogen. Thus at 3×10^5 ° K, hydrogen of density 10^{-27} gm/cm^3 radiates 8×10^{13} ergs/gm in 10^{17} seconds, as compared with the thermal energy content of slightly more than 7×10^{13} ergs/gm. At $T_0 = 10^6$ ° K, the radiation rate is 7×10^{13} ergs/gm in 10^{17} seconds, while the thermal energy is 2×10^{14}/gm.

Now when radiation is unable to dispose of the thermal energy of the hydrogen,we have an approximation to the adiabatic condition, and there is no substantial contraction of clouds with masses slightly in excess of equation (13). Accordingly, it would seem that the formation of galaxies is precluded when T_0 is above 3×10^5 ° K.

But T_0 is not likely to be much below 3×10^5 ° K on account of the flatness of the theoretical relation from 25,000 to 10^5 ° K; so that galaxies of the high-temperature class would seem to fall mainly into the fairly narrow range for T_0 of 10^5 ° to 3×10^5 ° K. Consider the intermediate case $T_0 = 1.5 \times 10^5$ ° K. Then the mass defined by equation (13)—using $M_0 = V\rho_0$ and $\rho_0 = 10^{-27}$ gm/cm^3—is $5 \times 10^{11}\odot$. Galaxies forming in high-temperature clouds should have masses of this order.

At this stage the general line of the argument will be interrupted. It would be natural to go on now to discuss further properties of these specially massive galaxies. This will not be done, however, because this section of the present investigation is so frankly speculative that it has been thought better to include first a more definitive section on the dynamical development of the less massive type of galaxy.

VIII. THE FINAL RADIUS OF A GALAXY OF MASS $3.6 \times 10^9\odot$

At first sight it might seem as if the theory presented above is seriously deficient, in that it predicts far too large sizes—13,000 parsecs (for galaxies of mass 3.6×10^9.)

instead of radii of 1000 or 2000 parsecs. This objection would seem to be entirely overcome, however, by the argument of the present section, which indicates that subsequent dynamical developments greatly reduce the initial radius.

For simplicity, suppose that the angular momentum of the system can be neglected. Then the various groups of condensed stars fall toward the center, where frequent dynamical encounters take place. Now dynamical encounters must introduce a tendency toward an equipartition of energy, in which the small members of the hierarchy structure receive the same energy as the large members. But when a particular member of the hierarchy receives a sufficiently large supply of energy, it is thereby enabled to break loose from the larger member of which it was originally a part. Accordingly, equipartition breaks up the hierarchy structure.

Let us examine the extreme case in which dynamical encounters are adequate to break up the entire detailed structure of the system, so that the stars come to belong to a general amorphous mass. Energy is required for this process. Thus we saw at the end of Section V that the radiative dissipation is the same in all steps of the hierarchy. This dissipation shows itself initially in the binding of the various members of the hierarchy sequence. To disrupt this binding, so that an amorphous group of stars is formed, requires about thirteen times (there are about thirteen steps in the hierarchy) the energy that was released by gravitation in just the first step. This energy has to be supplied by a shrinkage of the main mass, which must accordingly contract down to about one-thirteenth of the main radius at the end of the first step: *that is, the galaxy must shrink to a radius of about 1000 parsecs.*

It may be useful to mention the mechanism by which this shrinkage takes place. The largest members of the hierarchy acquire dynamical energy through falling toward the center of the system. The dynamical energy so acquired is then transferred in encounters to smaller members, thereby rendering the large members unable to expand out to their original distances from the center. It may also be remarked that the process is probably cumulative—the more the system shrinks, the more frequently do dynamical encounters take place.

The estimate of 1000 parsecs is indeed an upper limit to the final radius (the angular momentum still supposed zero); for the above considerations assume that none of the smaller members of the system acquire velocities large enough for them to escape entirely from the galaxy. If any appreciable fraction of the mass does manage to escape, the shrinkage will be greater than that just estimated.

Now a radius of 1000 parsecs is somewhat larger than, but comparable with, the observed radii of galaxies of type E_0 (allowing for Baade's new distance scale). Accordingly, the theory seems in satisfactory agreement with observation in the case where the system possesses negligible angular momentum. When the angular momentum is appreciable, the situation is somewhat altered. Then the final amorphous distribution of stars will possess an ellipticity that depends on the angular momentum. The estimate of 1000 parsecs can then be applied only to the polar radius of the distribution. It must indeed be an upper limit to the polar radius, for the reason that rotation restricts contraction toward the axis of rotation, so that the gravitational energy required to break up the hierarchy structure must be supplied by an extra contraction toward the plane of symmetry of the distribution.

IX. SPECULATIONS ON THE DEVELOPMENT OF A GALAXY OF MASS $5 \times 10^{11} \odot$

We have seen that the temperature is likely to be closely determined in this case. The trend of the theoretical relation above 25,000° K requires the temperature in general to be high, but the necessity for the hydrogen radiation to be capable of radiating the thermal energy places an upper limit to the temperature of about 3×10^5° K.

Now, assuming that radiation is adequate for the initial contraction to be nearly iso-

thermal, the energy supplied per gram of material varies with the density according to log ρ. Thus, since the time scale for contraction varies as $\rho^{-1/2}$, the rate of release of thermal energy per gram varies as $\rho^{1/2} \log \rho$. In contrast, the rate of radiation per gram varies as ρ. Accordingly, radiation slowly becomes dominant as contraction proceeds. This causes a departure from the isothermal condition, and the temperature must fall. But as the temperature falls, radiation becomes even more dominant, since the rate of radiation increases as $T^{-1/2}$, as T falls below 3×10^5 ° K. It seems probable that a temperature instability must develop in this way. A temperature instability implies that the temperature falls low—to about 10,000° K—in a time that is too short for any effective contraction to occur.

The importance of a temperature instability is that the contracting cloud becomes unstable against the formation of subunits of very much smaller mass than that of the galaxy itself. Consider the following model of a large galaxy. A galaxy of mass $M_0 = 5 \times 10^{11} \odot$, initial density $\rho_0 = 10^{-27}$ gm/cm^3, temperature $T_0 = 1.5 \times 10^5$ K, ° and initial radius $R_0 = 5 \times 10^{23}$ cm condenses to radius 10^{23} cm, maintaining a high temperature throughout this contraction. A temperature instability then develops that swiftly reduces the temperature down to 10,000° K. Some fragmentation may occur during the high-temperature phase, but the main fragmentation occurs after the steep fall of temperature. The gas, then having a density of about 10^{-25} gm/cm^3, is unstable against the formation of masses of the order of $3 \times 10^8 \odot$. Each of these masses then fragments along a hierarchy structure of the pattern already discussed in previous sections. Thus it would seem that the characteristic first stage in the evolution of a massive galaxy is not a closely knit series of steps but a widespread breakup into about a thousand or so dwarf galaxies, the whole distribution possessing a radius of some 30,000 parsecs.

Subsequent dynamical evolution is then likely to follow somewhat different lines from those described in the previous section, where the main effect was simply the breakup of the general hierarchy system. In the present case dynamical encounters among the multitude of more or less separate dwarf sytsems must lead to some of the systems acquiring sufficient energy to escape altogether from the galaxy. This causes a general compacting of the whole structure. In the case where such systems acquire only the limiting velocity of escape, the radius of the galaxy varies as the square of the remaining mass: thus if loss of material were to reduce the mass to $2.5 \times 10^{11} \odot$, the radius would shrink from 30,000 to 7500 parsecs. In the case where the escaping material acquires more than the limiting velocity, the shrinkage of the galaxy would be even greater than this.

Accompanying such a shrinkage there would also be a general disintegration of the multitude of dwarf systems, which would again produce an evolution into a general amorphous mass of stars. It can readily be shown that the energy required for such a disintegration does not appreciably add to the shrinkage of the galaxy, in marked contrast with the case discussed in Section VIII. Once most of the dwarf subsystems become disrupted, the effects of dynamical evolution are likely to be much reduced, and the galaxy reaches a more or less stable state.

It is, of course, possible that a subsystem might itself become compacted as a result of the escape of certain of its components caused by internal dynamical encounters. If such were to occur in a sufficient degree, it would be possible for a stable subsystem to arise, capable of resisting the disruptive effects of external dynamical encounters. It is tempting to identify the globular clusters with such cases.

A further tentative identification may be put forward. In recent years it has become increasingly clear that the average space density of faint dwarf galaxies must be rather high. These systems may owe their origin to escape from larger galaxies.

X. SPECULATIONS ON THE FORMATION OF TYPE I STARS

The stars so far discussed are all of type II: stars that form during the actual condensation of the galaxies themselves. Now the above discussion has proceeded on the basis that all the initial gas passes through the hierarchy system. This is probably valid

as a zero-order approximation, but not in higher approximation. Thus at any stage of the condensation process, contraction occurs only where the gas density is higher than average. Where the density is lower than average, condensation is not likely to occur, if only because the self-gravitation of an element of abnormally low density is unable to withstand the tidal shearing of the main field. In step 1 of the hierarchy system the main field should be understood as arising from the whole galaxy; in step 2 as arising from the first set of fragments; and so on.

For this reason it is to be expected that a residuum of gas will remain uncondensed into stars, constituting perhaps 20 or 30 per cent of the original mass. This gas cloud will shrink with the galaxy. Even after the star distribution attains an effective equilibrium size, the gas cloud will continue to shrink; in systems without angular momentum the cloud will shrink toward the center of the system, while in systems with appreciable angular momentum the cloud will shrink to a disk. In either case the density within the cloud eventually rises to such a value that a second phase of condensation can occur: that is, the self-gravitation of an element of material is eventually able to overcome the tidal shearing of the main field.

Two cases may then be distinguished. If the radiative properties of the gas are of the type discussed above, the gas cloud will fragment into stars in essentially the manner already discussed. Such stars would be of type II in the sense of the present paper. In the case where such a condensation occurs in a gaseous disk, we may speak of disk-type II stars or of late-type II stars. A second and radically different case arises, however, if dust has been produced (in some way outside the scope of this paper) in the condensing gas. Dust allows molecules to be formed, and molecules are able to radiate at low temperatures, in contrast to hydrogen, which cannot radiate, once the electrons and protons recombine to form atomic hydrogen. In the dust case, on the other hand, the temperature may well fall to 50° K, as compared to the value of 10,000° K in the type II case.

The whole problem of star formation requires a rediscussion for the low-temperature case, the opacity question being particularly troublesome on account of the effects of molecular absorption. Stars formed at low temperatures may be tentatively defined as the type I stars.

It is of interest to note that the condition for contraction, applied to the case $T_0 = 50°$ K and $\rho_0 = 10^{-23}$ gm/cm^3 (a likely value of the density after contraction), gives a minimum mass of about $10^4\odot$, comparable with the masses of the larger interstellar clouds in the galaxy. The fragmentation time for such a cloud would be less than 4×10^7 years, using the arguments of previous sections. On this basis we should at first sight expect the residuum of gas to become entirely condensed into stars in only 4×10^7 years, reckoned from the time that its density rises high enough for tidal shearing to be unimportant. But such an exhaustion of the remaining gas certainly has not occurred in the galaxy or in the other spirals. The question is: Why? Three tentative suggestions may be made:

a) That in the type I case the fragments become opaque to infrared radiation through absorption by molecules at an early stage of the hierarchy development. If the opacity were sufficiently great, a good approximation to the adiabatic condition could arise, in which case fragmentation would cease. Not only this but contraction could (under suitable conditions) be slowed up almost indefinitely. The dark globules observed in certain interstellar clouds might possibly be identified with fragments in this state.

b) Fragmentation into stars may occur, but into stars that eventually gain (either by direct condensation or by subsequent accretion in the low-temperature gas) masses considerably greater than the masses of the type II stars. If very luminous stars of high temperature are so formed—and there is, of course, observational evidence that this is so—a considerable heating must occur in the gas.[12] This arises from the absorption of

[12] For the details of this process the reader is referred to a forthcoming paper by Oort and Spitzer. The writer is much indebted to Dr. Spitzer for a private communication on this matter and also for general discussions on the whole of the present paper.

ultraviolet light from the stars. It is readily possible for a few highly luminous O stars to heat a gas cloud of mass $10^4\odot$ to such a degree that the cloud is forced to expand under the action of gas-pressure forces—not of radiation pressure. Thus the following situation may well arise: When there are no luminous high-temperature stars, condensation occurs, and O stars are formed. But as soon as O stars are formed, the clouds are expanded and condensation ceases. After the bright stars become exhausted, the clouds then re-form and more stars condense. On this picture a sort of cyclic process is set up—clouds condense; stars form, including O stars; clouds blow up, and star formation ceases; O stars die; clouds re-form; more stars condense, including O stars; etc. The interstellar clouds of small mass would represent bits of clouds left over from the blowing-up process.

c) It has in recent years been thought that the galaxy may possess a substantial magnetic field. It has been suggested that the magnetic field owes its origin to the general motions of ionized interstellar clouds. But this suggestion has the disadvantage, from the point of view of explaining the polarization properties of the interstellar medium, that the magnetic vector cannot apparently maintain its direction over sufficiently great distances. This difficulty is much alleviated if it be supposed that the magnetic field is built up, not in the motions of the interstellar clouds, but by the motions of the original gas cloud out of which the galaxy originally formed. In this case the magnetic vector would also alter in direction from point to point, but alignment might be expected over far greater distances than on the earlier view. Moreover, the concentration of the residuum of gas to a disklike shape would tend to align such a magnetic field parallel to the galactic plane, in accordance with the requirement of Davis and Greenstein in their theory of the polarization properties of the medium.[13]

Now it may occur,[14] after a sufficient fraction of the gas in the disk has become condensed into stars, that the self-gravitation of the remaining gas is insufficient to overcome the magnetic pressure, in which case there is no tendency for large-scale condensation into stars. In exceptional regions, self-gravitation may indeed overcome the magnetic pressure—for example, in the Orion nebula—and extensive condensation may occur there. In this way, it might be possible to explain why a gaseous disk has in the main managed to survive in the galaxy and in other spirals for several billion years.

It remains to mention a final point concerning the residuum of gas. It has been remarked that this might amount to 20 per cent of the original mass of the galaxy. In the case of a galaxy of mass $5 \times 10^{11}\odot$ this would give $10^{11}\odot$ in the form of gas. Now, although the residuum of gas thus amounts to no more than 20 per cent originally, if the mass condensed into a type II hierarchy is reduced by the dynamical escape of various subunits, the type II mass comes nearer to equality with the gaseous residuum. Thus for a loss of half the type II mass, the gas would have mass $10^{11}\odot$, and the mass condensed into the type II hierarchy would be $2 \times 10^{11}\odot$, giving a total mass of $3 \times 10^{11}\odot$.

[13] L. Davis and J. L. Greenstein, *Ap. J.*, **114**, 206, 1951.

[14] I am indebted to Dr. S. Chandrasekhar for this remark.

THE INTERNAL STRUCTURE OF RED DWARF STARS

DONALD E. OSTERBROCK*
Princeton University Observatory
Received May 10, 1953

ABSTRACT

Models are computed for red dwarf stars, with the hydrogen convection zone taken into account. The calculations show that in red dwarfs this outer convection zone extends inward for a distance of about 30 per cent of the radius of the star. The central temperatures of these models are found to be much lower than the central temperatures of models computed under the assumption of radiative equilbrium throughout the star. Thus the earlier difficulty of an overproduction of energy by the proton-proton reaction does not appear in these models.

The observed luminosities, masses, and radii of red dwarf stars such as Castor C and α Cen B can be understood in terms of these models and lead to normal abundances of the elements. For very late-type dwarfs, such as Kr 60 A, other physical effects appear to become important, and the models of the present paper probably are no longer applicable.

I. INTRODUCTION

The problem of the internal structure of red dwarf stars has attracted considerable attention in recent years. The first work on this problem[1, 2, 3] led to the conclusion that the proton-proton reaction, if it is an allowed nuclear transition, is the main mechanism of energy production in these stars. It is now clear that the proton-proton reaction is allowed,[4, 5] but models incorporating this effect and computed under the usual assumption of radiative equilibrium always give, with any reasonable chemical composition, a computed luminosity much higher than the observed luminosity.[4, 6]

A possible reason for this discrepancy has been suggested by Strömgren,[7] who has pointed out that in the red dwarfs the hydrogen convection zone may be expected to extend down deep into the interior. The reason for this is that the lower temperatures and higher densities in these stars favor the convective transport of energy. Models computed by Biermann[8] show that the central temperature is smaller in a star with a large outer convection zone than in a star with no outer convection zone. The reason for this is that in a convective region the temperature gradient is lower than the radiative temperature gradient, so an extensive outer convection zone will reduce the central temperature and hence also the luminosity. These considerations show that a star with a deep hydrogen convection zone may have a quite different structure from a model computed under the assumption of radiative equilibrium throughout, and that the differences in structure are in the right direction to explain the difficulty quoted above. Detailed calculations of models with the effects of convection taken into account are necessary to see whether the red dwarf stars can be understood in these terms. Biermann[8] has dis-

* This work was supported in part by funds of the Eugene Higgins Trust allocated to Princeton Observatory.

[1] H. A. Bethe and C. L. Critchfield, *Phys. Rev.*, **54**, 248, 1938.

[2] R. E. Williamson and G. F. D. Duff, *M.N.*, **109**, 55, 1949.

[3] J. B. Oke, *J.R.A.S. Canada*, **44**, 135, 1950.

[4] L. H. Aller, *Ap. J.*, **111**, 173, 1950.

[5] E. E. Salpeter, *Phys. Rev.*, **88**, 547, 1952.

[6] L. H. Aller, J. W. Chamberlain, E. M. Lewis, W. C. Liller, J. K. McDonald, W. H. Potter, and N. E. Weber, *Ap. J.*, **115**, 328, 1952.

[7] *A.J.*, **57**, 65, 1952.

[8] *A.N.*, **264**, 361, 1938, and references given there.

cussed stellar models with large hydrogen convection zones, and Öpik[9] has computed several series of models with outer convective regions. However, it was felt that a series of models specifically computed with the opacity, energy production, and chemical abundances to be expected in red dwarf stars was needed, and the present investigation was undertaken along these lines.

Now it is well known that in computing the structure of a star in radiative equilibrium it is a very good approximation to take the boundary conditions at the outer surface as given by $T = 0$ and $P = 0$. Actually, the correct physical condition is that the temperature has a specified value at some given pressure in the atmosphere, but changes in this temperature have no appreciable effect on the internal structure[10] so long as the outer layers are in radiative equilibrium. However, as Biermann[11] has shown, for stars in convective equilibrium in the envelope, the conditions in the outermost region do play a role in determining the internal structure. The reason is that in convective equilibrium there is an adiabatic relation between temperature and pressure similar to the monatomic gas relation,

$$P = KT^{\gamma/(\gamma-1)}\,, \tag{1}$$

and at any rate the temperature and pressure go to zero together. Thus for stars in convective equilibrium, one cannot simply take $T = 0$ and $P = 0$ as the boundary conditions at the surface of the star, because this would leave K undetermined, while, in fact, K is determined by the atmosphere.[12] Therefore, in the next section a rough model is computed of the outermost layers of a typical red dwarf star, for the purpose of obtaining an estimate of the approximate value of K.

II. THE ATMOSPHERE AND HYDROGEN IONIZATION ZONE

The atmosphere of a late-type dwarf is in radiative equilibrium at the surface, but at some depth the radiative temperature gradient becomes unstable against convection. We wish to discuss the structure of this hydrogen convection zone in later-type dwarfs in order to find the proper boundary condition for the interior. Only relatively crude models of the outer layers of the stars are necessary for our purposes.

We take the average of the two components of Castor C as a typical red dwarf with well-determined mass, radius, and luminosity. Starting from the surface, a model atmosphere[13] is integrated inward to the point at which convective instability sets in. This calculation gives the values of the pressure and temperature at the upper edge of the hydrogen convection zone. From this point an approximate model of the hydrogen convection zone is integrated inward to the region in which the ionization of hydrogen is essentially complete. The approximations made in this model convection zone are then tested and found satisfactory. Finally, the approximation used in the remainder of this paper for describing this zone is discussed. The details of these computations are as follows.

The model atmosphere is computed in the gray-body approximation, taking the opacity as due to H^- only and using a constant opacity per H^- ion. Such a model atmosphere which neglects the effects of the many absorption lines and the frequency variation of κ_ν is quite inaccurate but can be used to find the orders of magnitude of the pressure and temperature at which convection sets in. The equations describing this model atmosphere are:

$$\frac{dP}{d\tau} = \frac{g}{\kappa}\,, \tag{2}$$

[9] *Pub. Obs. Tartu*, Vol. **30**, No. 4, 1938.

[10] H. N. Russell, *M.N.*, **98**, 199, 1938.

[11] *A.N.*, **257**, 269, 1935.

[12] *Ibid.*; T. G. Cowling, *M.N.*, **98**, 528, 1938.

[13] B. Strömgren, *Festschrift für Elis Strömgren* (Copenhagen: E. Munksgaard, 1940), p. 218.

$$\kappa = \frac{1 - x_H}{m_H} P_e a_\tau (H^-) \tag{3}$$

$$= (1 - x_H) P_e 8.87 \times 10^{-3} \theta^{5/2} 10^{0.75\theta} ,$$

$$T^4 = \tfrac{3}{4} T_e^4 \rho (\tau) . \tag{4}$$

Here the number in equation (3) is a mean absorption coefficient of H^- taken from the table given by Münch;[14] $\rho(\tau)$ in equation (4) is the solution of the gray-body problem and is tabulated by Mark;[15] and the other symbols have their usual meanings. In addition to these equations, the relation between P_e and P and T is needed. Since the tables of Strömgren[16] do not cover the range of temperatures relevant to red dwarfs, new tables were constructed for this purpose, using the relative abundances among the metals as given in Kuiper's new compilation.[17] The mass, radius, luminosity, and effective temperature of the average component of Castor C used throughout this investigation are listed in Table 1; they were taken from Kuiper's[18] list and differ only slightly from those

TABLE 1

PHYSICAL PARAMETERS OF TYPICAL RED DWARF STARS

Star	Spectrum	log $L/L_\odot$	log $M/M_\odot$	log $R/R_\odot$	T_e
α Cen B.....	K1	−0.44	−0.05	−0.08	4860
Castor C av..	M0	−1.20	− .22	− .20	3600
Kr 60 A.....	M4+	−1.74	−0.58	−0.29	2940

of the newer determination by Kron,[19] which was not available when this work was begun.

Model atmospheres were computed for two assumed values of A, the ratio of number of hydrogen atoms to number of metal atoms. Condensed results of these integrations are presented in Table 2. The condition for stability against convection is

$$(n+1)_{\text{rad}} = \left(\frac{d \log P}{d \log T}\right)_{\text{rad}} \geqslant \left(\frac{d \log P}{d \log T}\right)_{\text{ad}} = (n+1)_{\text{ad}} , \tag{5}$$

the subscripts "rad" and "ad" denoting radiative and adiabatic, respectively. Hydrogen is essentially not ionized, even at the highest temperature in Table 2; so $(n+1)_{\text{ad}} = 2.5$, and it may be seen that instability sets in at approximately $\tau = 1.5$ and at a temperature and pressure that do not vary rapidly with the metal abundance.

From this point inward the star is unstable against convection, and we shall assume that it is, in fact, in convective equilibrium. Furthermore, we shall assume that the temperature gradient is the adiabatic gradient. These two assumptions may be regarded as giving a first approximation to the structure of the convective region; after computing the structure in this approximation, the assumptions will be checked, and, as will be seen below, it turns out that they are satisfactory.

[14] *Ap. J.*, **106**, 217, 1947.

[15] *Phys. Rev.*, **72**, 558, 1947.

[16] *Pub. mind. Med. Kobenhavens Obs.*, No. 138, 1944.

[17] G. P. Kuiper (ed.), *The Atmospheres of the Earth and Planets* (rev. ed.; Chicago: University of Chicago Press, 1952), chap. xii.

[18] *Ap. J.*, **88**, 472, 1938.

[19] *Ap. J.*, **115**, 301, 1952.

The pressure gradient in the convective region is given by the usual equation,

$$\frac{dP}{dr} = -\frac{GM_r\rho}{r^2}, \tag{6}$$

while the temperature variation is given by the adiabatic relation. The computation has been carried out in the way suggested by Unsöld,[20] using directly the condition that the entropy per unit mass be constant to compute the adiabatic P, T relationship. The

TABLE 2

MODEL STELLAR ATMOSPHERES FOR CASTOR C AV

τ	log T	log $A = 3.8$		log $A = 4.2$	
		log P	$(d \log P)/(d \log T)$	log P	$(d \log P)/(d \log T)$
0.00	3.466	.....	.....	.....	.....
0.05	3.480	4.60	.....	4.79	.....
0.10	3.491	4.77	.....	4.95	.....
0.2	3.508	4.94	.....	5.11	.....
0.3	3.521	5.03	.....	5.20	.....
0.4	3.533	5.10	.....	5.27	.....
0.5	3.543	5.15	.....	5.32	.....
0.6	3.553	5.19	.....	5.36	.....
0.8	3.569	5.26	.....	5.43	.....
1.0	3.583	5.30	3.3	5.47	3.2
1.2	3.595	5.34	2.9	5.51	2.8
1.4	3.606	5.37	2.7	5.54	2.6
1.6	3.616	5.40	2.4	5.57	2.4
1.8	3.625	5.42	2.3	5.59	2.2

model convection zone was computed for a composition of pure hydrogen. This neglects the presence of other less abundant elements, in particular, helium; but, as Biermann[8] has pointed out, these have only minor effects. We thus have

$$\frac{S}{k} = 2 \ln \frac{x_H}{1 - x_H} + (1 + x_H)\left(\frac{\chi}{kT} + \frac{5}{2}\right) = \text{Const.}, \tag{7}$$

$$\frac{x_H^2}{1 - x_H} N = \frac{(2\pi m kT)^{3/2}}{h^3} e^{-\chi/kT}, \tag{8}$$

$$P = N(1 + x_H) kT \tag{9}$$

$$\rho = NH, \tag{10}$$

together with equation (6), where S = entropy per hydrogen nucleus, apart from an additive constant, N = number of hydrogen nuclei per unit volume, χ = ionization potential of hydrogen, and the other symbols have their usual meanings. The departure of M_r from its surface value M is negligible.

As starting values we have taken from Table 2 log $T = 3.60$ and log $P = 5.56$ as the temperature and pressure at the top of the convection zone. The integration is then carried out by solving equation (7) for x_H as a function of T with $S/k = 9.3224$, the entropy per nucleus fixed by the starting values of T and P at the top of the convective

[20] *Zs. f. Ap.*, **25**, 11, 1948.

zone. Equations (8), (9), and (10) then give P and ρ as functions of T; and, finally, equation (6) is integrated to give r as a function of T. The results of this integration of the structure of the model convection zone are presented in condensed form in Table 3.

Next, the accuracy of this first approximation for the structure of the convection zone may be checked. To make this check, the departure of the temperature gradient from the adiabatic gradient may be computed by using the equations given by Biermann[8] and by Öpik[21] for the convective transport of energy. Taking the mean free path of the turbulent elements as given by the scale height, we find that at the level log $T = 4.00$ the true temperature gradient differs from the adiabatic temperature gradient by only 4 per cent

TABLE 3

MODEL HYDROGEN CONVECTION ZONE FOR CASTOR C AV

log T	log x_H	log P	$-\log \rho$	$(d \log P)/(d \log T)$	r/R
3.6	−7.124	5.560	5.960	2.500	1.000
3.7	−5.354	5.810	5.810	2.502	1.000
3.8	−3.949	6.061	5.658	2.538	1.000
3.9	−2.839	6.325	5.495	2.817	1.000
4.0	−1.990	6.650	5.274	3.842	1.000
4.1	−1.391	7.111	4.926	5.337	0.998
4.2	−0.998	7.691	4.470	6.084	0.997
4.3	−0.737	8.299	3.994	5.962	0.995
4.4	−0.555	8.870	3.556	5.444	0.993
4.5	−0.423	9.384	3.174	4.836	0.991
4.6	−0.324	9.839	2.849	4.268	0.988
4.7	−0.250	10.241	2.572	3.791	0.984
4.8	−0.195	10.601	2.333	3.415	0.981
4.9	−0.155	10.928	2.123	3.136	0.976
5.0	−0.125	11.231	1.932	2.937	0.970
5.1	−0.104	11.517	1.755	2.800	0.963
5.2	−0.088	11.792	1.587	2.707	0.955
5.3	−0.077	12.059	1.425	2.645	0.945
5.4	−0.069	12.322	1.266	2.603	0.932
5.5	−0.063	12.580	1.110	2.574	0.916
5.6	−0.058	12.837	0.956	2.554	0.898
5.7	−0.054	13.091	0.803	2.540	0.876
5.8	−0.052	13.345	0.651	2.530	0.849
5.9	−0.050	13.598	0.499	2.522	0.820
6.0	−0.048	13.850	0.348	2.518	.....

of its value. This justifies the approximation used above. This same calculation also shows that at this level the flux transported by radiation is less than one one-hundredth of that transported by convection, and it also gives $v \simeq 1.4$ km/sec for the mean velocity of turbulence.

Finally, it may be seen from Table 3 that at log $T = 6.0$ hydrogen is nearly completely ionized and that $n + 1$ has very nearly reached the monatomic gas value, 2.5, so that from this point inward the adiabatic relation (1) holds with $\gamma/(\gamma - 1) = n + 1 = 2.5$. Furthermore, the constant K in this equation may be determined from the last values of P and T in Table 3, log $P = 13.85$, log $T = 6.00$, which give log $K = -1.15$.

III. THE CONVECTIVE ENVELOPE

In the previous section it was seen how a model convection zone can be integrated inward through the region of ionization of hydrogen. This process can be continued further inward as far as desired; but, once the region in which the ionization is nearly

[21] *M.N.*, **110**, 559, 1950.

complete has been reached, a simpler procedure is available. For in the interior regions hydrogen is practically completely ionized, and the adiabatic relation is that of a monatomic gas, i.e., $n + 1 = 2.5$. We then have, with the substitutions

$$P = p\,\frac{GM^2}{4\pi R^4}, \qquad T = t\,\frac{\mu H}{k}\,\frac{GM}{R}, \qquad M_r = qM, \qquad r = xR, \tag{11}$$

the equations

$$p = Et^{2.5}, \tag{12}$$

$$\frac{dp}{dx} = -\frac{pq}{tx^2}, \tag{13}$$

$$\frac{dq}{dx} = \frac{px^2}{t}. \tag{14}$$

The value of the constant E is fixed by comparing equation (12) with equation (1), with $\gamma/(\gamma - 1) = 2.5$, which gives

$$E = 4\pi K \left(\frac{\mu H}{k}\right)^{2.5} G^{1.5} M^{0.5} R^{1.5}. \tag{15}$$

For the model convection zone computed in the previous section for Castor C av, the value of this quantity is $E = 13.6$.

However, this value for Castor C av is only approximate, since it depends upon the opacity in the atmosphere and upon the detailed theory of turbulence, neither of which is accurately known. It appears that the theory of stellar interiors is sufficiently advanced that we can find the conditions in the interior to a good approximation; we must allow for our uncertainty of the structure of the outermost parts of the star by permitting the model of the envelope to vary, using the model computed in the previous section only as a guide. Furthermore, other red dwarfs will differ from Castor C av in their E values. For these reasons we shall not restrict ourselves to constructing one model with the computed E for Castor C av, but rather shall compute a series of models corresponding to a series of values of E which bracket the value for Castor C. We shall finally fix the value of E by the condition that the over-all model of a star fits the observational data, but we expect that the value of E will agree with that of the computed model convection zone within its uncertainties, which means within a factor of about 2 or 3.

For computational purposes we shall take the monatomic gas region as extending to the surface, that is, we shall take as boundary conditions

$$q = 1, \qquad p = 0, \qquad \text{at} \qquad x = 1. \tag{16}$$

This means that we shall make an error of a few per cent in the computed radius of the star; for, once the region of ionization of hydrogen is reached, the temperature gradient is somewhat less steep than that given by $n + 1 = 2.5$. This is illustrated in Figure 1, which shows the variation of t with x for the model convection zone tabulated in Table 3 and for the solution with $E = 13.6$ and the boundary conditions of equation (16). The scales of x are shifted by 0.025, to make the two curves coincide for high temperatures, and therefore the computed radius of the simplified model is incorrect by 2.5 per cent.

Thus, to describe the structure of the outer convective zone, integrations are needed of equations (12)–(14) with boundary conditions (16). A series of 24 such solutions was computed by numerical integration,[22] covering the range[23] $E = 8$ to $E = 46$. These integrations were performed on the electronic computer of the Institute for Advanced

[22] To be published in a forthcoming *Princeton U. Obs. Contr.*

[23] The value of E for the solution regular at the center, which is tabulated in *Brit. Assoc. Adv. Sci., Math. Tables*, Vol. 2 (1932), may be shown to be $E = 45.48$ in the notation used in the present paper.

Study.[24] The form in which the equations were used in the machine integration was suggested by Dr. von Neumann, the basic coding was laid out by Dr. Goldstine, while Mrs. Selberg performed the final coding and supervised the actual computations. In addition to the variables x, p, t, and q, the homology invariants,

$$U = \frac{d \log M_r}{d \log r} = \frac{px^3}{qt}, \qquad V = -\frac{d \log P}{d \log r} = \frac{q}{tx}, \tag{17}$$

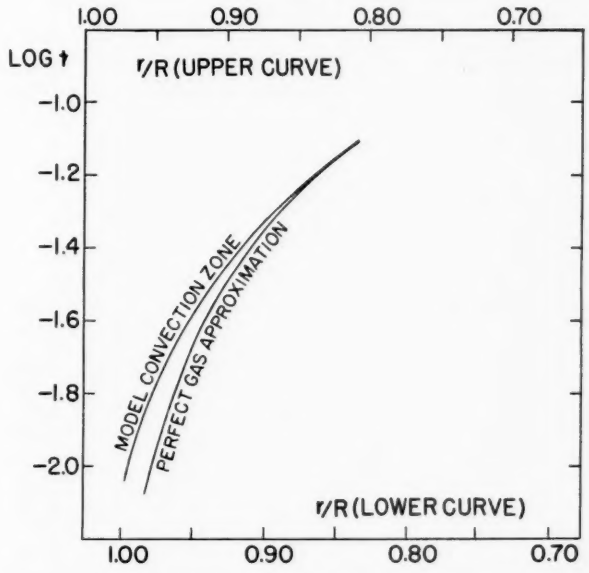

FIG. 1.—Temperature as a function of depth in the model convection zone and in the monatomic gas approximation.

were also computed for each point of each solution. A few of these numerical solutions are plotted in the U, V plane in Figure 2.

IV. THE CENTRAL RADIATIVE REGION

Red dwarf stars have been shown[25] to be in radiative equilibrium at their centers; they do not have convective cores. Hence the equations of radiative equilibrium may be integrated from the center outward to the point at which they become convectively unstable according to criterion (5). From this point outward the structure is convective and is described by the equations in the preceding section.

We assume that the energy production is completely due to the proton-proton reac-

[24] This portion of the work was sponsored by the Office of Naval Research under Contract No. N-7-ONR-388, Task Order I, and by the Ordnance Corps of the United States Army under Contract No. DA-36-034-ORD-1023-RD.

[25] P. Naur and D. E. Osterbrock, *Ap. J.*, **117**, 306, 1953.

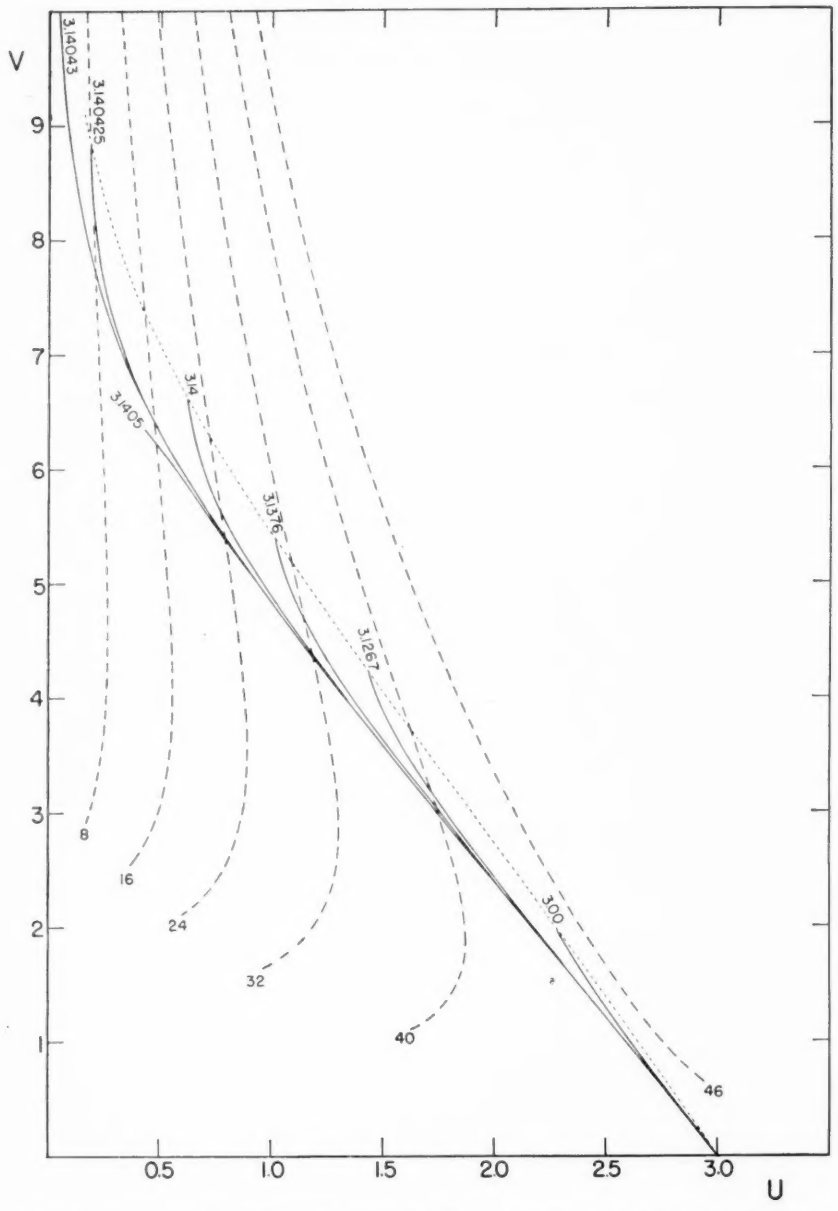

FIG. 2.—Representations of models in terms of the homology invariants U and V. Full lines are radiative-core solutions, each labeled with the value of $(n + 1)_c$; long dashed lines are convective envelopes, each labeled with the value of E. Each model is constructed from a radiative-core solution, together with an interpolated convective-envelope solution. The short dashed line is the locus along which the radiative solutions become convective, that is, along which $(n + 1) = 2.5$.

tion, which may be represented over the temperature range in which we are interested by the interpolation formula

$$\epsilon = \epsilon_0 \rho T^{4.5} \tag{18}$$

with

$$\epsilon_0 = \frac{0.0903}{(10^7)^{4.5}} X^2 . \tag{19}$$[26]

The opacity is assumed to be due to photoionization of metals, present in the Russell mixture proportions, as given in the tables of Morse.[27] In his paper the opacity is written

$$\kappa = \frac{4.34 \times 10^{25} Z}{T^{3.5}} \rho (1 + X) \left(\frac{g}{l}\right), \tag{20}$$

and the guillotine factor (l/g) is tabulated. For the red dwarf models we shall approximate the guillotine factor by the interpolation formula

$$\log \left(\frac{l}{g}\right) = 0.38 + 0.5 \log \rho (1 + X) , \tag{21}$$

which gives

$$\kappa = \kappa_0 \rho^{0.5} T^{-3.5} \tag{22}$$

with

$$\kappa_0 = 1.81 \times 10^{25} Z (1 + X)^{0.5} . \tag{23}$$

Under these assumptions the equations describing the structure in the radiative region can be reduced as follows:

Dimensionless variables:

Equations (11) and

$$L_r = fL . \tag{24}$$

Basic equations:

Equations (13), (14), and

$$\frac{dt}{dx} = -C \frac{p^{1.5} f}{t^8 x^2} , \tag{25}$$

$$\frac{df}{dx} = D p^2 t^{2.5} x^2 , \tag{26}$$

with

$$C = \frac{3 \kappa_0}{4 a c} \left(\frac{1}{4\pi}\right)^{2.5} \left(\frac{k}{\mu H G}\right)^{7.5} \frac{L R^2}{M^6} , \tag{27}$$

$$D = \frac{\epsilon_0}{4\pi} \left(\frac{\mu H G}{k}\right)^{4.5} \frac{M^{6.5}}{L R^{7.5}} . \tag{28}$$

Logarithmic variables:

$$\lambda = \log \frac{p}{p_0} , \qquad \psi = \log \frac{q}{q_0} ,$$

$$\tau = \log \frac{t}{t_0} , \qquad \phi = \log \frac{f}{f_0} , \qquad y = \log \frac{x}{x_0} , \tag{29}$$

[26] The numerical value comes from the value of the energy production by the proton-proton reaction given by Salpeter (*op. cit.*).

[27] *Ap. J.*, **92**, 27, 1940.

with

$$\frac{q_0}{t_0 x_0} = 1\,, \qquad \frac{p_0 x_0^{\,3}}{t_0 q_0} = 1\,,$$
$$C\,\frac{p_0^{1.5} f_0}{t_0^{9.0} x_0} = 1\,, \qquad D\,\frac{p_0^2 t_0^{2.5} x_0^3}{f_0} = 1\,. \tag{30}$$

Logarithmic equations:

$$\log\left(-\frac{d\lambda}{dy}\right) = \psi - \tau - y\,,$$
$$\log\left(+\frac{d\psi}{dy}\right) = \lambda - \psi - \tau + 3y\,,$$
$$\log\left(-\frac{d\tau}{dy}\right) = 1.5\lambda - 9.0\tau + \phi - y\,, \tag{31}$$
$$\log\left(+\frac{d\phi}{dy}\right) = 2\lambda + 2.5\tau - \phi + 3y\,.$$

Conditions at the center:

$$f = q = 0\,, \qquad \tau = 0\,, \qquad \text{at} \qquad x = 0\,. \tag{32}$$

Homology invariants:

Equations (17) and

$$U = \frac{d\psi}{dy}\,, \qquad V = -\frac{d\lambda}{dy}\,,$$
$$W = \frac{d\,\log L_r}{d\,\log r} = \frac{d\phi}{dy}\,, \tag{33}$$
$$n+1 = \frac{d\,\log P}{d\,\log T} = \frac{d\lambda/dy}{d\tau/dy}\,.$$

It may be noted that we have chosen the five constants p_0, q_0, t_0, f_0, and x_0 to fulfil the four requirements (30). This leaves one constant still at our disposal, which we may therefore choose at will without restricting the physical solution. We have fixed this constant by setting t_0 equal to the value of t at $x = 0$, a procedure which gives the boundary condition (32), $\tau = 0$ at $x = 0$. This leaves only one arbitrary choice to be made, the value of λ at $x = 0$, which we write λ_c; and the radiative interiors thus form a one-parameter series of models which may be classified by the value of λ_c or, alternatively, by the value of the polytropic index at $x = 0$,

$$\log\,(n+1)_c = -2.5\lambda_c\,. \tag{34}$$

This relation follows from equation (33), noting that $q/f = dq/df$ at $x = 0$ and using conditions (31).

Starting values for the integrations were found by power-series expansions valid near $x = 0$. Eleven numerical solutions[22] of these equations were integrated outward from the center to the point at which $n + 1$ fell to 2.5. From this point outward a convective envelope must be fitted to construct a complete stellar model.

Several of these solutions are plotted in the U, V plane in Figure 2, together with the solution radiative to the surface, discussed in the next section, and also a solution that asymptotically becomes isothermal, with $n + 1$ increasing steadily outward.

V. CONSTRUCTION OF COMPLETE MODELS

A complete model consists of a central radiative region, described by the integrations of Section IV, together with a convective envelope, described by the integrations of Section III. At the interface between these regions, x, p, q, t, and f and therefore also U, V, W, and $n + 1$ must be continuous. A series of models has been constructed using these conditions by fitting an interpolated convective exterior to each computed radiative interior. The fitting procedure is as follows:

From an integration of a radiative interior, read off values U_1, V_1, and W_1 for the point at which $n + 1 = 2.5$, and the values of y_1, λ_1, τ_1, ψ_1, and ϕ_1 at this point. Interpolate in the U, V plane between the convective exterior solutions to find the solution which passes through the point $U = U_1$ and $V = V_1$, and from this convective solution find the values x_1, p_1, t_1, and q_1 at this point. Then, solving the equations

$$y_1 = \log \frac{x_1}{x_0}, \qquad \lambda_1 = \log \frac{p_1}{p_0},$$
$$\tau_1 = \log \frac{t_1}{t_0}, \qquad \psi_1 = \log \frac{q_1}{q_0}, \tag{35}$$

gives the four quantities x_0, p_0, t_0, and q_0. In addition, in the convective exterior, by integrating equation (26), with the boundary condition that at the outer surface of the star $L_r = L$, or in our notation $f = 1$ at $x = 1$, we find

$$f_1 = 1 - D \int_{x_1}^{1} p^2 t^{2.5} x^2 dx . \tag{36}$$

This integration can be carried out for each convective solution and interpolated between solutions. Equation (36), together with the relation

$$\phi_1 = \log \frac{f_1}{f_0} \tag{37}$$

and the last of equations (30), may be solved for the three unknowns D, f_1, and f_0. The procedure used was to assume a rough value of D, compute the corresponding f_1 by equation (36), then the corresponding f_0 by equation (37), and, finally, a new value of D by equation (30). This iteration method converges very rapidly to the correct values of D, f_1, and f_0.

It may be noted that we have been able to carry out the fitting for f directly, without using the homology invariant W defined by equation (32), as a consequence of the fact that the structure of the convection zone does not depend on the distribution of energy sources in it.

Next the value of C may be computed from the third of conditions (30), and, finally, with p_0 and t_0 known, the central values p_c and t_c can be computed from the values λ_c and τ_c ($= 0$). The mathematical characteristics of the models computed in this way are listed in Table 4.

Although attention has been confined to models that would fit red dwarf stars, for purposes of comparison one additional model has been constructed which is in radiative equilibrium to the surface. To construct this model, a radiative solution[22] was integrated from the outer boundary inward according to equations (13), (14), (25), and (26) with the boundary conditions $q = f = 1$ and $t = p = 0$ at $x = 1$. The parameters C and D were varied to fulfil the conditions of fitting this radiative envelope to a radiative interior. The mathematical characteristics of this model are also listed in Table 4 as model XII of that table. In addition, Table 5 presents a comparison of this model with

TABLE 4

MATHEMATICAL PROPERTIES OF RED DWARF MODELS

	I	II	III	IV	V	VI	VII	VIII	IX	X	XI	XII
$(n+1)_c$	3.00	3.10	3.1133	3.1267	3.134	3.1376	3.14	3.1403	3.14036	3.14041	3.140425	3.14043
E	44.65	41.71	40.39	37.67	34.29	30.65	21.43	16.82	14.69	11.05	8.02	.....
$\log x_0$	− 0.885	− 0.928	− 0.941	− 0.966	− 0.993	− 1.020	− 1.090	− 1.129	− 1.149	− 1.187	−1.225	−1.537
$\log p_0$	+ 1.209	+ 1.296	+ 1.328	+ 1.393	+ 1.471	+ 1.556	+ 1.794	+ 1.936	+ 2.009	+ 2.153	+2.299	+3.541
$\log q_0$	− 1.166	− 1.208	− 1.218	− 1.235	− 1.250	− 1.262	− 1.283	− 1.291	− 1.293	− 1.297	−1.300	−1.303
$\log f_0$	− 0.054	− 0.082	− 0.087	− 0.093	− 0.096	− 0.098	− 0.099	− 0.100	− 0.100	− 0.100	−0.100	−0.100
U_1	2.260	1.786	1.653	1.432	1.214	1.017	0.620	0.455	0.385	0.272	0.184	.....
V_1	2.037	3.302	3.655	4.247	4.845	5.403	6.650	7.280	7.592	8.205	8.860	.....
W_1	0.681	0.199	0.133	0.063	0.027	0.010	0.000	0.000	0.000	0.000	0.000	.....
x_1	0.412	0.506	0.527	0.558	0.586	0.610	0.655	0.676	0.686	0.705	0.723	.....
q_1	0.309	0.508	0.558	0.636	0.707	0.766	0.873	0.913	0.930	0.953	0.971	.....
$\log p_1$	+ 0.567	+ 0.329	+ 0.262	+ 0.148	+ 0.025	− 0.097	− 0.415	− 0.603	− 0.705	− 0.913	−1.144	.....
$\log l_1$	− 0.433	− 0.516	− 0.538	− 0.571	− 0.604	− 0.633	− 0.698	− 0.732	− 0.749	− 0.783	−0.819	.....
f_1	0.889	0.980	0.987	0.996	0.998	0.999	1.000	1.000	1.000	1.000	1.000	.....
$\log p_e$	+ 1.018	+ 1.099	+ 1.131	+ 1.195	+ 1.272	+ 1.358	+ 1.595	+ 1.737	+ 1.810	+ 1.954	+2.100	+3.342
$\log l_e$	− 0.281	− 0.280	− 0.277	− 0.269	− 0.257	− 0.242	− 0.193	− 0.161	− 0.144	− 0.110	−0.075	+0.234
$\log C$	− 5.172	− 5.308	− 5.340	− 5.385	− 5.418	− 5.435	− 5.420	− 5.385	− 5.361	− 5.309	−5.248	−4.645
$\log D$	+ 0.886	+ 0.810	+ 0.773	+ 0.691	+ 0.583	+ 0.456	+ 0.066	− 0.180	− 0.310	− 0.570	−0.836	−3.156

the model computed by Williamson and Duff,[28] using the same opacity law ($a = 0.5$ in their notation) but with a convective core, that is, with a very high temperature dependence of the energy generation. This comparison gives some insight into the effects arising from the concentration of energy sources toward the center of the star.

To summarize, a series of models has been computed, each consisting of a radiative core and a convective envelope. These models form a one-parameter series, each member of which may be labeled by the value of $(n + 1)_c$. All the other quantities are determined from the fitting conditions, and so, for instance, one may alternatively use E as the single parameter which describes a model. Thus the value of E determines the model and in turn determines the other mathematical properties of the model, including x_1, the radius of the interface, and C and D.

VI. PHYSICAL RESULTS

We shall now use the models described in the previous sections to determine the physical conditions in red dwarf stars. Let us confine our attention to a particular star, say Castor C av, for which the observations give the values of M, R, and L. Suppose, now, that we know the correct model which describes this star, that is, we know the value of

TABLE 5

COMPARISON OF RADIATIVE MODELS WITH $\kappa \propto \rho^{0.5} T^{-3.5}$

	$\epsilon \propto \rho T^{4.5}$ No Convective Core	$\epsilon \propto \rho T^{n}$ n Large with Convective Core
log C	−4.645	−4.744
log p_c	+3.3422	+3.1950
log t_c	+0.2337	+0.2273

E, having determined it from the structure of the atmosphere. Then the values of C and D are determined. With these values, equations (27) and (28) give two conditions on the chemical composition. Now the composition is determined by three parameters, X, Y, and Z, but there is one relation between them, namely, $X + Y + Z = 1$, so we may regard two of these parameters—say, X and Z—as the two independent parameters which describe the composition. Thus the above two conditions just determine the two parameters of the composition. This is essentially the procedure used in finding the composition of, say, the sun from its internal structure.[29]

In the present case, however, the correct model is not known because the value of E found in Section III cannot be regarded as an accurate determination. We therefore do not have a single model but a one-parameter series of models, classified by the values of E. We must determine not only the composition but also the model, so we have three quantities, E, X, and Z, to be determined by only two conditions, equations (27) and (28). It is apparent that we cannot determine a unique solution but can rather determine a series of possible sets of solutions. The procedure followed was to assume a value of hydrogen content X and then solve for the other two unknowns, E and Z. The solutions were carried out graphically, as shown in Figure 3, in which the solid curve is a plot of C against D for the series of models. Each dot represents a computed model; the curve has been sketched through these dots. For a given star, such as Castor C av, we choose a

[28] *M.N.*, **109**, 46, 1949.

[29] M. Schwarzschild, *Ap. J.*, **104**, 203, 1946; I. Epstein, *Ap. J.*, **114**, 428, 1951.

value of X—say $X = 0.90$—and compute as a function of Z the values of C and D for this hydrogen content by equations (27) and (28). These values of C and D are indicated by the dashed line; the point where this dashed line intersects the solid curve gives the model (value of E along the solid curve) and the value of Z (along the dashed line) corresponding to this value of X. Then the values x_1, l_1, p_1, q_1, l_c, p_c, etc., can be determined for this model by interpolation with E as argument, and finally the values of the physical quantities, such as T_1, the temperature at the interface, and ρ_c and T_c, the central temperature, and the density may be found. This whole process may be repeated

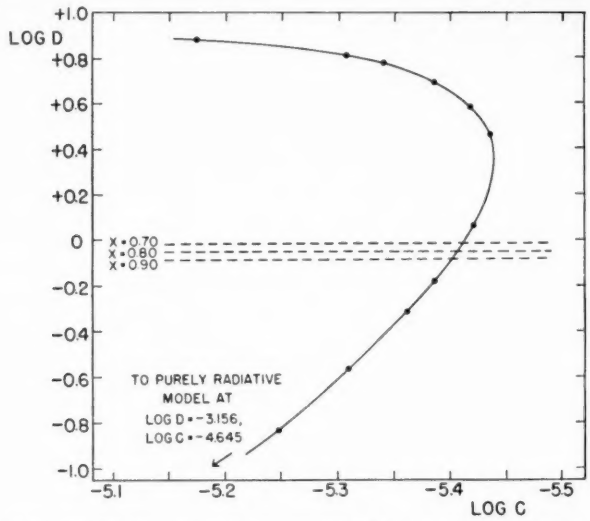

FIG. 3.—The relation between the parameters C and D for the models of this paper (*solid line*). Each dot represents a computed model. Dashed curves are possible values of C and D for Castor C av, for different assumed hydrogen abundances.

for any assumed value of X. We thus determine a table of possible compositions of Castor C av, together with the possible central temperatures, depths of convection zone, and so on, corresponding to each possible composition. This information is summarized in Table 6.

This same procedure may be applied to any red dwarf star for which observed values of M, R, and L are available. We have taken as two typical examples the stars α Cen B and Kr 60 A, whose spectral types are K1 and M4+, respectively. The values of mass, luminosity, and spectral type listed in Table 1 for these two stars are from an unpublished table of the best-determined stellar masses, compiled by Dr. K. Aa. Strand and Dr. R. G. Hall at Yerkes Observatory.[30] The effective temperatures are from Kuiper's tabulation,[14] and the radii then follow immediately. The possible abundances determined for α Cen B are listed in Table 6 also, and it may be seen that they agree well with those determined for Castor C av. There are a few other stars in the list of Strand and Hall intermediate in spectral type between α Cen B and Castor C av, and they likewise may be fitted with reasonable abundances. It must be noted that no claim is made for the detailed accuracy of these derived abundances, because the approximations used in con-

[30] Private communication. I am indebted to Drs. Strand and Hall for giving me permission to quote this table.

structing the models introduce some errors. As shown in the next section, however, these errors are small.

The star Kr 60 A, which has the latest spectral type, M4+, of all stars considered here, cannot be fitted to one of these models with any reasonable abundances; it would require a very low hydrogen content. We shall return to a discussion of this star in the next section.

We have seen, however, that red dwarfs of spectral type M0 or earlier can be fitted by the models of this paper. In deriving possible sets of abundances, we have not assumed values of X smaller than 0.70 because we expect the abundances to be similar to those that occur in the sun, the atmospheres of early-type stars, planetary nebulae, etc.[31]

TABLE 6

POSSIBLE ABUNDANCES OF ELEMENTS AND CORRESPONDING PHYSICAL QUANTITIES

X	Y	Z	E	x_1	q_1	T_1	T_c	ρ_c
	Castor C av							
0.90.....	0.091	0.009	18.7	0.669	0.900	2.2×10^6	7.8×10^6	81 gm/cm^3
.80.....	.184	.016	19.4	.666	.894	2.4×10^6	8.3×10^6	79
.70.....	0.271	0.029	19.9	0.663	0.888	2.6×10^6	8.9×10^6	76
	α Cen B							
.90.....	0.087	0.013	10.2	0.710	0.959	2.1×10^6	10.3×10^6	90
.80.....	.178	.022	10.6	.707	.956	2.3×10^6	11.0×10^6	87
0.70.....	0.261	0.039	10.9	0.705	0.954	2.5×10^6	11.8×10^6	85

It should be noted not only that the fitting can be carried out but also that the resulting value of Z is small. This means that red dwarf stars can be understood in terms of normal abundances, consisting mainly of hydrogen and with helium much more abundant than the metals. Furthermore, as shown by Table 6, over the range of values of X considered likely, that is, $X \geqslant 0.70$, the values of central temperature, depth of the convection zone, and temperature at the bottom of the convection zone do not change much with the assumed value of the hydrogen content.

VII. CHECKS OF ASSUMPTIONS

Finally, we shall turn our attention to a check of the assumptions made in computing the structure of the red dwarf models. First of all, we consider the parameter E, which describes the outer convection zone. From the model convection zone for Castor C av, the value of this quantity is $E \simeq 13.6$, while the determination from the interior of the same star gives E in the range of 18.7 to 19.9. These values therefore agree within the uncertainty of the determination of the atmospheric value of E. It appears that the determination from the interior structure is relatively firm, so that future work should attempt to explain the structure of the atmosphere, using the value of E derived from the interior. As we have not computed a model convection zone for α Cen B, we cannot apply the same check to this star.

Similarly, we shall apply our other checks to the Castor C av model, and we shall use as a definite case the model with $X = 0.80$ to compute the run of temperature and den-

[31] See, e.g., *Trans. I.A.U.*, **7**, Part IV, 1950.

sity. A condensed table of the physical variables in this model is presented in Table 7. The interface between the radiative center and the convective exterior is at $r/R = 0.67$.

With these values of ρ and T, the guillotine factors may be read off from Morse's tables[27] and compared with the interpolation formula (21). Only the values of the guil-

TABLE 7

PHYSICAL VARIABLES FOR CASTOR C AV MODEL
($X = 0.80$)

r/R	M_r/M	L_r/L	log T	log ρ
0.00	0.000	0.000	6.919	+1.896
0.10	0.020	0.161	6.896	+1.846
0.20	0.134	0.642	6.835	+1.697
0.30	0.334	0.918	6.752	+1.463
0.40	0.546	0.988	6.662	+1.166
0.50	0.717	0.998	6.572	+0.840
0.60	0.837	1.000	6.477	+0.512
0.70	0.915	1.000	6.326	+0.220
0.80	0.969	1.000	6.101	−0.118
0.90	0.997	1.000	5.753	−0.640
1.00	1.000	1.000	.....	.....

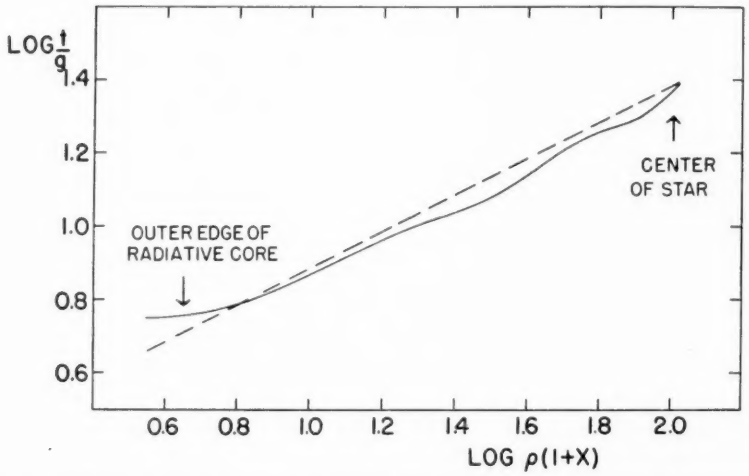

FIG. 4.—Guillotine factor as a function of density. The solid line shows the values determined for Castor C av, while the dashed line represents the interpolation formula (25).

lotine factor in the radiative region up to its boundary are needed, and these are plotted in Figure 4 against log $\rho(1 + X)$. It may be seen that the straight-line approximation of equation (21) is sufficient for our purposes. The opacity at the center is 2.7 cm^2/gm, and the electron-scattering opacity, 0.20 $(1 + X) = 0.4$ cm^2/gm, is small enough to be neglected in comparison with this.

The relative contribution of the free-free transitions[2, 6, 32] in hydrogen and helium to

[32] F. Hoyle, *Trans. I.A.U.*, **7**, 481, 1950.

the opacity must also be estimated. If this opacity is expressed in the form of equation (20), then the free-free opacity in hydrogen and helium corresponds to a guillotine factor[27]

$$\left(\frac{t}{g_{ff}}\right)=\frac{1179Z}{g_{ff}}. \tag{38}$$

The appearance of Z in this equation comes from the fact that we are expressing the free-free opacity as proportional to Z by using equation (25), and we must again divide out this dependence in the guillotine factor. The usual procedure is to assume $g_{ff}=1$, but, according to calculations of Zirin,[33] the effective g factors for free-free transitions at $T\simeq 8\times 10^6$ and $\rho(1+X)\simeq 135$ gm/cm^3 (the central conditions for the Castor C av model) are 0.30 for hydrogen and 0.35 for helium, the reduction from the value $g_{ff}=1$ being due to shielding effects. If we take a mean value $g_{ff}=\frac{1}{3}$, we find

$$\log\left(\frac{t}{g_{ff}}\right)=3.55+\log Z\,, \tag{39}$$

which makes this guillotine factor larger than the guillotine factor of the metals opacity, even at $Z=0.01$. Since the opacity is inversely proportional to the guillotine factor, the conclusion may be drawn that the opacity is determined mainly by the metals and that the interpolation formula (21) is sufficient for our present purposes.

One further check is necessary to test the effect of the thermal conductivity on the flux of energy. In terms of the conductivity, a conductive opacity[34] may be defined which may be compared directly with the radiative opacity. This conductivity may be evaluated by means of the tables of Mestel,[35] and the result is that at the center of the Castor C av model the radiative opacity is about a hundred times more important than the conductive opacity; so the latter may safely be neglected. We thus see that the various approximations used in computing the red dwarf models are justified for dwarfs of spectral type M0 or earlier.

In the case of Kr 60 A, the red dwarf with the smallest well-determined mass, it may be that conduction and incipient degeneracy begin to affect the structure, as suggested by Williamson and Duff[2] and by Aller.[4] It is clear from Section VI that the models of the present paper, which seem to take most of the other physical effects into account, do not fit Kr 60 A with any reasonable abundances of the elements. However, it should also be mentioned that there is some uncertainty in the bolometric correction for Kr 60 A.

VIII. SUMMARY

In this paper models of red dwarf stars have been constructed in which the presence of the outer convection zone has been taken into account. These models show that the red dwarf stars can be understood as stars with normal abundances of the elements, similar to those in other astronomical objects. Values of the helium content Y and the metal content Z for various assumed hydrogen contents X are summarized in Table 6.

The essential feature of red dwarf stars in which they differ from early-type stars is that in the red dwarfs the convection zone extends deep down into the interior of the star. For the two stars considered—α Cen B, spectral type K1, and Castor C av, spectral type M0—the depth of the convection zone is of the order of 30 per cent of the radius of the star.

The various physical quantities listed in Table 6 are relatively well determined in each star, in spite of the uncertainty in the exact hydrogen content. Furthermore, it may be

[33] Private communication. I am very grateful to Dr. Zirin for informing me of the results of his work prior to publication.

[34] T. D. Lee, *Ap. J.*, **111**, 625, 1950.

[35] *Proc. Cambridge Phil. Soc.*, **46**, 331, 1950.

noted that the temperature at the bottom of the convection zone is in the general range of 2.0–2.5 million degrees in both stars, although their spectral types are quite different. In this connection it may furthermore be noted that Strömgren[36] has found 2.5 million degrees as the temperature at the bottom of the outer convective zone in the sun, a still earlier-type dwarf.

In conclusion, I wish to thank all those who have helped me in the course of this investigation: Professor Bengt Strömgren, who suggested this problem to me and first discussed it with me; Professor Martin Schwarzschild, who gave generously of his time for discussions and advice; Mrs. Reeves, Mr. Skumanich, Mr. Rogerson, and especially Mr. Härm, who did much of the numerical work; and Dr. von Neumann, Dr. Goldstine, and Mrs. Selberg, at the Institute for Advanced Study, who advised and coded and carried out the numerical solutions for the convective exteriors with the electronic computer.

[36] *Mat. Tidsskr.* (Copenhagen), Sec. B, p. 96, 1950.

THERMAL EFFECTS OF COLLISIONAL LINE EXCITATION IN GASEOUS NEBULAE

LAWRENCE H. ALLER
University of Michigan Observatory
Received May 18, 1953; revised July 9, 1953

ABSTRACT

The cooling effects of ions of oxygen, neon, nitrogen, and other light elements may be estimated from the observed intensities of all the relevant forbidden lines. The electron temperatures in nebulae such as IC 418, with relatively weak forbidden lines (as compared with the Balmer lines), must be substantially greater than in nebulae with relatively strong forbidden lines. Thus the electron temperatures in high-excitation planetaries are not necessarily higher than those in low-excitation planetaries but may even be relatively low. The electron temperature cannot rise substantially above 25,000° or 30,000° K in a planetary nebula because of the dissipation of energy in the excitation of the hydrogen lines, unless the hydrogen is substantially all ionized.

Many years ago, Bowen[1] pointed out that the forbidden lines in the gaseous nebulae were produced by the collisional excitation of metastable levels in ions of oxygen, nitrogen, neon, etc., in various stages of ionization. The atoms returned to the ground level with the emission of forbidden lines. The emitted quantum simply escaped from the nebula without further absorption. This process removes kinetic energy from the gas and serves to lower the electron temperature below the values it would have for a pure hydrogen nebula in radiative equilibrium with a hot central star.

Some years ago[2] the electron temperatures of gaseous nebulae were estimated from the relative intensities of the green nebular lines and λ 4363 of doubly ionized oxygen with the aid of target areas for collisional excitation calculated by Hebb and Menzel.[3] The resulting temperatures came out mostly in the neighborhood of 10,000° K. Adopting these temperatures as valid, it was shown that the observed intensities of the forbidden lines would account for a lowering of the temperature from the earlier predicted values[4] obtained for a pure hydrogen nebula (e.g., of the order of 34,000° K for a central star of temperature 40,000° K) to a value near 10,000° K.[5] T. L. Page's[6] measures of the intensity distribution in the Balmer continuum favored an electron temperature near 10,000° K. This latter estimate, however, supposes that the background continuum which must be subtracted is constant in intensity with wave length.

More recently, doubts have been cast on the reality of an electron temperature of 10,000° K. The theory from which the target areas of collisional excitation were computed was shown to be inexact by Bates, Fundaminsky, Leech, and Massey.[7] They concluded that the target areas were systematically too large; furthermore, even the relative cross-sections may be in error. Menzel has asserted that the target areas computed by Hebb and himself are not necessarily too large and that they do not violate the conservation theorem of Bohr, Peierls, and Placzek. He has not, however, demonstrated that the other objections raised against this calculation of target areas can be disre-

[1] *Ap. J.*, **67**, 1, 1928.

[2] D. H. Menzel, L. H. Aller, and M. H. Hebb, *Ap. J.*, **93**, 240, 1941.

[3] *Ap. J.*, **92**, 408, 1940.

[4] J. G. Baker, D. H. Menzel, and L. H. Aller, *Ap. J.*, **88**, 422, 1938.

[5] D. H. Menzel and L. H. Aller, *Ap. J.*, **94**, 30, 1941.

[6] *Ap. J.*, **96**, 78, 1942.

[7] *Phil. Trans. R. Soc., London*, **243**, 93, 1950.

garded. Furthermore, Minkowski[8] finds that the observed value of the Balmer discontinuity in IC 418, interpreted with the aid of Spitzer and Greenstein's[9] calculations on the continuum produced by double-photon emissions, cannot be reconciled with an electron temperature as low as 10,000° K.

Therefore, it becomes important to re-examine the hypothesis that the collisional excitation of the nebular lines will necessarily lower the electron temperature to about 10,000° K. The temperature of the electron gas is controlled by the condition that in each unit volume the total amount of energy brought into the continuum by photoionizations is equal to that dissipated in free-free transitions and in collisional excitations of forbidden lines. We suppose, for the moment, that the electron temperature will not be so high that collisional excitation of the hydrogen lines will be important. The effect of possible hydrogen-line excitation will be discussed later. The equation of conservation of energy for the continuum may be written, in the symbolic notation of Menzel, Baker, and the writer, in the following form:[10]

$$\sum_{1}^{\infty}\int_{\nu_n}^{\infty} F_{\kappa n} h\nu_{\kappa n}\,d\nu + \sum_{2}^{\infty}\int_{\nu_n}^{\infty} F_{\kappa n} h\nu_{n1}\,d\nu + \int_0^{\infty}\int_0^{\infty} F_{\kappa\kappa'} h\nu_{\kappa\kappa'}\,d\nu_\kappa\,d\nu_{\kappa'} + \Sigma E_i = \int_{\nu_1}^{\infty} F_{1\kappa} h\nu_{1\kappa}\,d\nu\,, \tag{1}$$

where the left-hand terms represent, respectively, the energy liberated by the free electrons upon recapture and subsequent cascade to the lower levels, the free-free emissions, and the energy dissipated in the excitation of forbidden lines of various ions. The summation is carried out over the forbidden emissions of all different ions. The right-hand side of the equation represents the energy brought into the continuum by photoionizations.

The quantities E_i are related to the intensities of the forbidden lines as measured by various observers. Neglecting, for the moment, the fact that the different forbidden-line emissions have different spatial distributions in the nebula, we may set

$$E_i = E(H\beta)\frac{I_i}{I(H\beta)}\,, \tag{2}$$

where the ratio of the forbidden-line intensity I_i to the intensity of $H\beta$ has been measured by a number of observers.[11] Now $E(H\beta)$, the emission per unit volume in $H\beta$, is given by[12]

$$E(H\beta) = b_4 N_i N_e \frac{2hRKZ^6}{T_e^{3/2}}\frac{g\,e^{X_4}}{512}\,, \tag{3}$$

where

$$X_4 = \frac{hRZ^2}{4^2 kT_e} = \frac{9800}{T_e}\,, \tag{4}$$

[8] *Pub. A.S.P.*, **65**, 161, 1953. I am grateful to Dr. Minkowski for communicating this result to me in advance of publication.

[9] *Ap. J.*, **114**, 407, 1951.

[10] *Ap. J.*, **88**, 313, 1938, eq. (9).

[11] See, e.g., Louis Berman, *Lick Obs. Bull.*, **15**, 86, 1930; *M.N.*, **96**, 893, 1936; A. B. Wyse, *Ap. J.*, **95**, 350, 1942; and L. H. Aller, *Ap. J.*, **93**, 236, 1941; **113**, 125, 1951. M. L. White (*Ap. J.*, **115**, 71, 1952) has measured the relative intensities of the [N II] lines and $H\alpha$ in a number of nebulae.

[12] D. H. Menzel, *Ap. J.*, **85**, 330, 1937; see esp. eqs. (4), (9), (14), (25), and (30).

$K = 3.260 \times 10^{-6}$, and the Gaunt factor, g, is equal to 0.822. Here b_4 is a measure of the deviation of the population of the fourth level from the values appropriate to thermodynamic equilibrium at T_e. The actual numerical value of b_4 depends on the electron temperature. We may make an estimate of it from the calculations of the Balmer decrement by Baker and Menzel.[13] Observation shows that their "case B" appears to be followed for most planetary nebulae, so we shall take b_4 from their tables as a function of temperature. If explicit expressions[12] for the $F_{n\kappa}$'s, $F_{\kappa n}$'s, etc., are now substituted in equation (1), use is made of equations (2) and (3), and the common factor $N_i N_e 2hRZ^6 T_e^{-3/2}$ is canceled from both sides of the equation, we obtain

$$b_1 e^{X_1}\left(\frac{k}{2hRZ^2}\right) T_1 \int_{\nu_1}^{\infty} W_{1\kappa}\,\frac{d\nu}{e^{\nu}-1} = \left(\frac{k}{2hRZ^2}\right)^2 T_e^2 + \left(\frac{k}{2hRZ^2}\right) aT_e + \tfrac{1}{2} G_{T_e} - \frac{1}{2}\sum_1^{\infty}\frac{S_n}{n^5} + \sum_i E(H\beta)\,\frac{I_i}{I(H\beta)}\,. \tag{5}$$

The factor b_1 is eliminated with the aid of the equation[14]

$$b_1 e^{X_1}\int_{\nu_1}^{\infty} W_{1\kappa}\,\frac{d\nu}{\nu\,(e^{\nu}-1)} = \sum_1^{\infty}\frac{S_n}{n^3} = G_{T_e}\,. \tag{6}$$

Here $W_{1\kappa}$ is the dilution factor of the radiation, while G_{T_e} may be calculated as a function of the electron temperature. We then obtain[15]

$$\frac{(k/2hRZ^2)\,T_1\displaystyle\int_{\nu_1}^{\infty}[W_{1\kappa}\,d\nu/(e^{\nu}-1)]}{\displaystyle\int_{\nu_1}^{\infty} W_{1\kappa}\,[d\nu/\nu\,(e^{\nu}-1)]} = \frac{(k/2hRZ^2)^2 T_e^2 + a\,(k/2hRZ^2)\,T_e + \tfrac{1}{2}G_{T_e} - \dfrac{1}{2}\displaystyle\sum_1^{\infty}\dfrac{S_n}{n^5}}{G_{T_e}} + 1.61\times 10^{-3}\,\frac{b_4(T_e)}{G_{T_e}}\,e^{X_4}\sum_i\frac{I_i}{I(H\beta)}\,. \tag{7}$$

The left-hand side of the equation depends only on the temperature T_1 of the central star and the dilution factor $W_{1\kappa}$, which varies so slowly with frequency that it may be canceled out in most instances of practical interest. The right-hand side of the equation depends only on T_e. The last term differs from that given previously[4] by Menzel and the writer, in that observed quantities are introduced directly. Equation (7) may be written symbolically as [14]

$$f_1(T_1) = f_2(T_e) + C(T_e)\,. \tag{8}$$

The correction term $C(T_e)$ may be written as

$$C(T_e) = A(T_e)\,\Sigma\,\frac{I_i}{I(H\beta)}\,, \tag{9}$$

[13] *Ap. J.*, **86**, 70, 1937; **88**, 52, 1938.

[14] J. G. Baker, D. H. Menzel, and L. H. Aller, *Ap. J.*, **88**, 423, 1938.

[15] Compare with *ibid.*, eq. (5).

where the coefficient $A(T_e)$ may be tabulated as shown in Table 1. Notice that the function $A(T_e)$ varies slowly with the temperature.

For a given value of T_1, T_e may be estimated by calculating f_1 as a function of T and calculating f_2 as a function of T, and reading from the resultant tabulation the value of T_e that makes both sides of the equation equal. For purposes of the present illustration, however, I shall assume a series of values of T_e, calculate T_1 with the aid of the

TABLE 1

VALUES OF $A(T_e)$

T_e	$A(T_e)$	T_e	$A(T_e)$	T_e	$A(T_e)$
8000	5.54×10^{-3}	14,000	5.00×10^{-3}	20,000	4.68×10^{-3}
10,000	5.33	16,000	4.86	25,000	4.49
12,000	5.14	18,000	4.76	30,000	4.36

TABLE 2

THEORETICAL RELATION BETWEEN ELECTRON TEMPERATURES AND CENTRAL-STAR TEMPERATURES FOR PLANETARY NEBULAE

	IC 418	NGC 2149	IC 4593	NGC 6210	NGC 6543	NGC 6826	NGC 7662
Assumed electron temperature (° K):							
8000	17,000	22,000	26,000	36,000	26,000	31,000	62,000
10,000	19,000	24,000	28,000	38,000	28,000	33,000	65,000
12,000	22,000	26,000	30,000	40,000	30,000	35,000	65,000
14,000	24,000	28,000	32,000	42,000	32,000	37,000	70,000
16,000	26,000	30,000	34,000	44,000	35,000	40,000	72,000
18,000	28,000	33,000	36,000	46,000	38,000	42,000	74,000
20,000	31,000	36,000	39,000	48,000	40,000	44,000	77,000
25,000	37,000	41,000	44,000	56,000	46,000	52,000	86,000
30,000	46,000	52,000	55,000	68,000	57,000	62,000	98,000
$\Sigma I_i/I(H\beta)$	3.5	7.0	8.7	13.6	9.1	11.5	24
T_1	33,200	32,500	33,400	32,900	35,000*	34,600	55,000*
Suggested T_e	22,000	18,000	16,000	8000	17,000	11,000	.....

* Temperatures obtained by Zanstra method.

observed quantity $\Sigma[I_i/I(H\beta)]$ and equation (7), and compare the resulting series of values of T_1 with various estimates of the central-star temperature.

The body of Table 2 gives the central-star temperatures for a number of planetary nebulae as evaluated from equation (7) for a series of values of the electron temperature T_e. The row labeled $\Sigma[I_i/I(H\beta)]$ gives the sum of the intensities of the forbidden lines in terms of that of $H\beta$. The values of the central-star temperature, T_1, are taken from their spectral classes,[16] except that the entries marked with an asterisk (*) refer to Zanstra temperatures.[17] The row labeled "Suggested T_e" gives a value of T_e consistent with the theoretical T_1-T_e relationship.

Notice that there is a considerable range in the suggested electron temperatures, from

[16] *Ap. J.*, **108**, 462, 1948; temperatures for the nuclei of IC 418 and NGC 2149 were obtained by O. C. Wilson and the writer, *Ap. J.* (in press).

[17] See L. Berman, *Lick Obs., Bull.*, **18**, 73, 1937.

8000° to 25,000° K. The nebulae with relatively weak forbidden lines would tend to have the highest electron temperatures, and there would not necessarily be any close connection between the central-star temperature and the electron temperature. The state of ionization in the nebula which determines the number and kinds of ions present would play a big role in fixing T_e. Clearly the preceding calculation does not permit the determination of the electron temperature. All it shows is that the observed intensities of the forbidden lines are consistent with electron temperature between 8000° and 25,000° K for accepted values of the central-star temperatures. In particular, there is no difficulty in reconciling the cooling mechanism with an electron temperature in IC 418 of the order of 22,000° K or even higher. We cannot give more precise estimates because we do not know the ultraviolet energy distribution in the spectra of the central stars. Calculations by A. Underhill,[18] by Jean McDonald,[19] by William Liller,[20] by James Milligan and the writer, and by others indicate that for stars in this temperature range, the energy distribution beyond the Lyman limit may correspond to a color temperature very different from the effective temperature or the Zanstra temperature for the same star. Qualitatively, the effect is that the flux, F_ν, is cut down far below that of a black body of the same effective temperature but that the blocking of the outgoing radiation is greatest near the Lyman limit and falls off to higher frequencies. Hence, F_ν may fall off more slowly with increasing ν than it would for a black body of the same effective temperature, so that a greater proportion of high-energy electrons would be photo-ejected. The effect is as though the central star had a much higher temperature.

Preliminary calculations show that the theoretical T_1-T_e relation is extremely sensitive to the exact energy distribution in the far ultraviolet. For example, the H/He ratio enters in a fundamental way. Comparison of model atmospheres of pure hydrogen with atmospheres in which an H/He ratio of 5 is introduced show that the effect of the *He* I absorption limit at λ 504 is very marked. The depletion of high-frequency quanta appreciably lowers the theoretical electron temperature.

Furthermore, the energy distribution in the Lyman continuum is modified in an optically thick nebula. Some calculations carried out long ago by Baker, Menzel, and the writer[21] indicated that the theoretical electron temperature would tend to increase near the outer boundary of the ionized zone. The radiation field throughout the main luminous body of the planetary, however, would correspond to that appropriate to small optical depths, in accordance with Strömgren's theory of the ionized hydrogen zone.[22] At these small optical depths the older calculations indicated that W could be canceled on the left-hand side of equation (7) without much loss in accuracy. At the present time a more elaborate study would not appear to be worth while.

The electron temperatures of many nebulae implied by these considerations may be compared with those obtained with the aid of new target areas recently calculated by M. J. Seaton.[23] In Table 3, I list the adopted intensities of $N_1 + N_2$ and λ 4363 and of T_e as computed from Seaton's cross-sections and Garstang's A-values.[24] The nebular-line intensities are approximately corrected for space absorption by assuming that $I(H\gamma)/I(H\beta) = 0.55$, as implied by measures of the Balmer decrement.[25] For IC 418, the intensity of λ 4363 with respect to $H\gamma$ is taken from the work of Wyse. The intensities

[18] *Pub. Copenhagen Obs.*, No. 151, 1950; *Pub. Dom. Ap. Obs. Victoria*, **8**, 357, 1951.

[19] Unpublished thesis, University of Michigan, 1952.

[20] Unpublished thesis, University of Michigan, 1953.

[21] *Ap. J.*, **90**, 271, 601, 1939.

[22] *Ap. J.*, **87**, 526, 1939.

[23] *Proc. R. Soc., London, A*, **218**, 400, 1953. I am indebted to Dr. Seaton for communicating his results to me in advance of publication.

[24] *M.N.*, **111**, 115, 1951.

[25] See L. H. Aller, *Ap. J.*, **113**, 138, 1951.

of the green nebular lines are taken from photometric measures made in 1938–1939[26] and 1943–1945[25] at the Lick Observatory. For IC 4593, NGC 6210, NGC 6543, and NGC 6826, the intensity of λ 4363 with respect to $H\gamma$ was measured on slit spectrograms secured at the McDonald Observatory.[27] The electron temperature is very sensitive to small errors in the $(N_1 + N_2)/4363$ ratio unless this quantity is very large. Unfortunately, the great strength of the green nebular lines in most planetaries renders very difficult the accurate measurement of this ratio by photographic photometry. Photoelectric measures of the $(N_1 + N_2)/H\beta$ ratio in a number of planetaries are planned by William Liller and the writer as a check on the photographic work.

A comparison of the last rows of Tables 2 and 3 is of some interest. Usually the theoretical temperature is higher than the "nebular-line" temperature, the one covering a range from 8000° K to 22,000° K, the other a range from 6700° K to about 20,000° K. Some of the differences might be eliminated by an adjustment of T_1 or perhaps by improved photometric measures, or by a more accurate theoretical treatment of the ultraviolet radiation field in the nebula.

Andrillat[28] has published electron temperatures based on the older cross-sections for a

TABLE 3

ELECTRON TEMPERATURES OBTAINED FROM NEBULAR LINE INTENSITIES

	IC 418	NGC 2149	IC 4593	NGC 6210	NGC 6543	NGC 6826	NGC 7662
$I(N_1+N_2)$	15.7	55	75	116	76	100	198
$I(4363)$	0.33	0.60	0.12	0.8	0.32	0.55	2.7
T_e	19,500	14,000	7600	12,000	10,000	10,700	15,700

number of planetaries. Seaton points out that these temperatures should be greatly increased on the basis of the new cross-sections. If the nebula has pronounced density concentrations, the $I(4363)/I(N_1 + N_2)$ ratio will be increased, as appears to be true for IC 4997.

Unless hydrogen is almost completely ionized, it would appear unlikely that the electron temperatures can be much higher than 25,000° K or 30,000° K. Otherwise, collisional excitation of the hydrogen lines would be important, and the Balmer decrement should be markedly steepened. This effect has been considered by S. Miyamoto[29] and more recently by J. W. Chamberlain.[30] The fact that the observed Balmer decrement appears to agree with the purely radiative theory of the hydrogen-line formation suggests that collisional excitations of the Balmer lines cannot be significant in most planetaries and therefore that the electron temperature cannot be too high.

As an example, we may consider a nebula such as IC 418, for which we may adopt the following tentative values: $T_1 = 30{,}000°$ K, $R = 3R_\odot$, $N_e \sim 15 \times 10^3$ electrons/cm^3, radius of shell $= 1.6 \times 10^{17}$ cm. If $T_e = 20{,}000°$ K, we find with the aid of Chamberlain's tables that the Balmer decrement will not be affected by an observable amount. On the other hand, for an electron temperature as high as 30,000° K, deviations from the purely radiative Balmer decrement can become important. At a temperature well

[26] *Ibid.*, **93**, 236, 1941.

[27] *Ap. J.*, **108**, 462, 1948. The plates were obtained primarily for the planetary nuclei but may be used for nebular lines also.

[28] *C.R.*, **231**, 1432, 1940; **234**, 62, 1952. The intensities actually measured are not given in these brief reports.

[29] *Mem. Coll. Sci., Kyoto Imperial U.*, **A21**, No. 26, 173, 1938.

[30] *Ap. J.*, **117**, 387, 1953.

below that at which the Balmer decrement would be observably altered from the radiative model, the cooling effect of collisional excitation of the hydrogen levels could become important. Suppose that only 2 per cent of the atoms in the third level of hydrogen were excited there by electron collisions. Then about 2 per cent of the intensity of $H\alpha$ is to be attributed to collisional excitations. On the other hand, about eight times as much energy is radiated in Lyman β as in $H\alpha$, so that the amount of energy actually dissipated in the excitation of $H\alpha$ is closer to 18 per cent of the intensity of $H\alpha$ than it is to 2 per cent. As soon as collisionally excited atoms become numerous, the b-factors expressing the deviation from thermodynamic equilibrium increase, and the decrement approaches that of "case C" considered by Menzel, Baker, and the writer,[31] as Chamberlain has pointed out. Detailed consideration of the influence of the hydrogen-line excitation on the conservation-of-energy equation will be reserved for a later paper.

Within the luminous shells of certain planetaries, where the emission per unit volume in the hydrogen and forbidden lines may become very small, the electron temperature

TABLE 4

THEORETICAL ELECTRON TEMPERATURE DISTRIBUTION IN IC 418

Distance from Center (Seconds of Arc)	$\Sigma E_\lambda / E(H\beta)$	T_e (° K)	Distance from Center (Seconds of Arc)	$\Sigma E_\lambda / E(H\beta)$	T_e (° K)
0.0	5.6	21,000	4.82	7.0	19,000
0.96	5.7	21,000	5.78	3.8	23,000
1.93	5.6	21,000	6.75	4.3	22,000
2.90	5.8	21,000	7.72	5.9	20,000
3.86	7.3	18,000			

may approach the theoretical values given in Paper V of the Harvard nebular series.[31] Such high electron temperatures would require so complete an ionization of hydrogen that the collisional excitation of the higher levels would be unimportant.

One important consequence of a relation of the type of equation (7) is that, since the relative emissions in the forbidden and in $H\beta$ (per unit volume) vary from point to point in the nebula, the electron temperature will also vary. We may illustrate the nature of the effect by an application to IC 418, where O. C. Wilson and the writer attempted to analyze the structure of the nebula to determine the relative emission of the various characteristic radiations per unit volume.[32] If the intensity distribution across the monochromatic nebular images is analyzed on the assumption that the nebula is spherically symmetrical, it is found that hydrogen is concentrated in the ring but that there is also a rise in density toward the center, as is shown also by the [O III] and [Ne III] images. On the other hand, the [O II] and [N II] images indicate essentially hollow shells. The published hydrogen and O^{++} distributions are substantiated, at least qualitatively, by more recent observations.

Table 4 gives the emission in the forbidden lines expressed in terms of the emission in $H\beta$ as a function of distance in seconds of arc from the central star, and finally the theoretical electron temperature, T_e. In the central portions of the nebula, T_e is controlled mainly by the excitation of [O III], whereas O^+ becomes important only in the outer portions. The temperature is predicted to be highest in the bright ring, where the relative emission in the forbidden lines is lowest. We neglect the modification of the radiation field by the nebula itself, but this influence of the continuous absorption is presumed to become important only near the outer edge of the luminous zone.

[31] *Ap. J.*, **88**, 422, 1938; **89**, 587, 1939.

[32] *Ap. J.*, **114**, 421, 1951.

The refinements required by the nongray character of the radiation of the central star and by the excitation of the hydrogen lines will be presented in a later paper, in which application will be made to specific models of nebulae that represent the observed objects as closely as possible.

I am indebted to Dr. R. Minkowski for calling my attention to the observational objections to the lower electron temperatures previously assigned. Dr. M. J. Seaton kindly informed me of his results on the target areas for the collisional excitation of the forbidden lines in advance of publication. Dr. D. H. Menzel and Dr. David Layzer have made interesting suggestions and comments concerning the theoretical target areas.

THE PHYSICAL THEORY OF METEORS. IV. INQUIRY INTO THE RADIATION PROBLEM—A LABORATORY MODEL*

RICHARD N. THOMAS AND WILLIAM C. WHITE
University of Utah, Harvard College Observatory, and U.S. Naval Ordnance Test Station, Inyokern, California

Received March 18, 1953; revised June 11, 1953

ABSTRACT

The similarity in atomic spectrum between meteor and artificial meteor (ultra-speed pellet) is discussed. The meteor is equivalent to a mono-energetic atomic beam; the pellet, to a high-temperature furnace in a highly transient and probably nonequilibrium state. The excitation mechanism is probably atom-atom inelastic collision in both cases. A consideration of the pellet molecular spectrum strengthens these conclusions. The pellet molecular spectrum appears to provide information on diffusion processes in the wake. Present spectrophotometric data on both meteor and pellet are very incomplete.

I. INTRODUCTION

The re-examination of various aspects of the physical theory of meteors projected for this series[1] of papers depends heavily upon terrestrial laboratory observations of high-speed objects. We have hoped to gain greater insight into the meteor problem by broadening the scope of the investigation to include the whole astroballistic regime rather than that part defined by the meteors alone. The laboratory (ballistic) investigations span a relatively narrow range of physical conditions but rest upon a fairly solid experimental basis. The meteor investigations span a wide range of physical conditions but have the limitations inherent in a purely observational—as contrasted to experimental—approach. Nevertheless, the progress of the present investigation finds on occasion as much difficulty with the interpretation of the laboratory experiments as with that of the meteor observations. A case in point is the difficulty with the air-density dependence of the heat transfer, found in Paper II. The use of the various types of "artificial" meteors, suggested[2] in various places over the last few years to investigate luminosity questions, provides another example. Little quantitative work[3, 4] on the interpretation of the "artificial" meteor spectrum seems to be available, making its use as a calibration somewhat difficult. Consequently, we present in the present paper a comparison of meteor spectra with those of ultra-speed pellets, remarking on the probable excitation conditions. In subsequent papers we propose to investigate these excitation conditions quantitatively.

II. SUMMARY OF THE EMPIRICAL DATA

In a comparison of the published material on meteor and ultra-speed pellet spectra, five aspects stand out—three referring to the observed spectra, and two to the conditions under which the spectra were produced. In aspect (A-1) the atomic spectrum of the ultra-speed pellet resembles very closely that of meteors, both in general level of excitation and in actual lines present. In aspect (A-2) the most pronounced difference in the spectra lies in the presence of molecular bands of metallic oxides in that of the pellet.

* Work supported in part by ONR.

[1] M. A. Cook, H. Erying, and R. N. Thomas, *Ap. J.*, **113**, 475, 1951; R. N. Thomas and F. L. Whipple, *Ap. J.*, **114**, 448, 1951; R. N. Thomas, *Ap. J.*, **116**, 203, 1952. Hereafter called "Papers I, II, and III," respectively.

[2] First, to our knowledge, by R. W. Wood when he obtained the first spectrum of a lined shaped charge at Aberdeen early in the last war.

[3] W. A. Allen, J. S. Rinehart, and W. C. White, *J. Appl. Phys.*, **23**, 2, 198, 1952.

[4] E. B. Mayfield, *Phys. Rev.*, **85**, 769, 1952 (abstr.).

In aspect (A-3) time-resolved spectra[4] of the pellet show that the molecular bands do not appear abruptly near the "nose" of the pellet, as do the atomic lines, but gradually build up to maximum intensity along the wake, or trail, of the pellet. In aspect (A-4) the kinetic energy per atom[5] of the meteor exceeds that of the pellet by factors up to 500. In aspect (A-5) the atmospheric density for the region of the pellet exceeds that of the meteor by factors up to 10^6.

Of these five aspects, (A-1) and (A-4) probably stand in most startling contrast in a comparison of meteor and pellet spectra. In a center-of-mass system (meteor or pellet atom and atmospheric atom) the energy ranges from 3 to 530 e.v. for the meteor and 0.6 to 2.6 e.v. for the pellets. These values correspond to a velocity range of 8–70 km/sec for meteors, 2.5–6.0 km/sec for pellets, and collisions with oxygen and nitrogen. Yet, of the multiplets listed by Millman[6] as occurring in meteor spectra, presented in Table 1 to-

TABLE 1

MULTIPLETS OBSERVED IN METEOR SPECTRA

Element	Range of E	Element	Range of E	Element	Range of E
Fe I	2.4–5.6 e.v.	*Ca* I	2.9 e.v.	*Mg* I	5.1–5.9 e.v.
Ni I	3.6–3.8	*Ca* II	9.2	*Mn* I	3.1
Al I	3.1	*Na* I	2.1–4.3	*Cr* I	2.9–3.4

TABLE 2

LINES COMMON TO METEOR AND ULTRA-SPEED PELLET SPECTRA

Observed	Source	Range of E	Observed	Source	Range of E
3720	*Fe*	3.4–4.2 e.v.	3962		
3837	*Mg*	5.9	5162	*Mg*	5.1 e.v.
	*Fe**	3.2–4.8		*Fe*†	2.4
3944	*Al*	3.1			

* Previously, *Fe* was not felt to be a source of this line in pellet spectra (see W.A. Allen *et al.*, *J. Appl. Phys.*, **23**, 2, 198, 1952; and E. B. Mayfield, *Phys. Rev.*, **85**, 769, 1952.

† Iron lines do not appreciably contribute to λ 5162 in pellet spectra, we believe.

gether with the excitation energy of the upper level of the transition, lines of *Fe* I, *Al* I, *Na* I, *Mg* I, and *Mn* I have been observed[3] in pellet spectra. The various pellets considered were constructed from Al, Mg, Mg-Li-Al alloy, and Ti. Consequently, the absence of *Ni*, *Ca*, and *Cr* may reflect only the lack of these materials in the pellets. Only the strongest meteor *Fe* I lines were observed in pellet spectra. We note, however, that *Fe* appears as an impurity in the pellet, while it is presumably a major constituent of some meteors. Table 2 exhibits the comparison explicitly by listing lines definitely present in both meteor and pellet spectra, again with the range of excitation of the upper level.

Other lines of *Mg*, *Mn*, and *Na* may also be present in both spectra, but we have listed only the stronger lines definitely identified. We have remarked on the absence of *Ca* II from the pellet spectra. If the absence stems, indeed, only from a difference in composition and not from excitation, we might expect lints of *Mg* II and *Al* II, since the ionization potentials of *Mg* and *Al*, 7.6 and 6.0 e.v., are near *Ca*, 6.1 e.v. However, no lines due to ionized elements have been observed in the pellet spectra. Any conclusion drawn from

[5] Hereafter the term "kinetic energy" of meteor or pellet refers to the energy per atom.

[6] *Harvard Obs. Ann.*, **82**, No. 7, 160, 1937.

these statements must be qualified by the fact that the most observable lines of *Mg* II and *Al* II occur in the ultraviolet with a higher excitation potential than that for the H and K lines of calcium. We note that not all meteors show lines of *Ca* II. Indeed, in his early work[6] Millman divided the meteor spectra into three rough classes:

Y—Spectra in which the H and K lines of ionized calcium are the most prominent feature.
Z—Spectra in which almost all the lines are due to iron, ionized calcium being markedly absent.
X—Refers to a single spectrum where the magnesium lines at 3830 are stronger than the H and K lines.

The pellet spectra are then most similar to those of the meteors, class Z, considering the low concentration of *Fe* in the pellet.

In this comparison of pellet and class Z meteor spectra, which is motivated by the absence of lines from ionized atoms in each, there stands a certain implication of classification according to energy. Such implication is possibly justified if the "energy" refers to the spectral excitation level, but not obviously so if the "energy" refers to the energy of pellet or meteor alone. On the one hand, the interesting aspect of this similarity between meteor and pellet spectra is just the small value of pellet energy with respect to both that of the slowest meteors and that of the excitation level of the spectra. On the other hand, while it is tempting to regard the Y–Z spectral class change as reflecting a decrease in meteor velocity (energy), such a conclusion does not seem universally valid. True, Millman's earlier conclusion[6] favored class Y as characterizing meteors appearing higher in the atmosphere, hence presumably faster. Furthermore, the recent studies of spectra of various meteor showers state the typical Perseid spectrum ($v \sim 60$ km/sec) to show strong ionized *Ca* lines, while the typical Giacobinid ($v \sim 20$ km/sec) shows a neutral spectrum. However, Millman's recent results[7] seem to show a (statistical) shift in color toward the blue, downward along the trajectory. Moreover, Russell has photographed[8] a meteor whose spectrum changed from Z through X to Y as it moved downward into the atmosphere. Consequently, we require an interpretation that permits a similarity in spectrum, in spite of large energy difference, between meteor and pellet and yet allows a considerable difference in spectrum, in spite of small energy difference, between meteor and meteor. In aspect (A-5) above, the comparison of atmospheric density at the particle path, we already note a possible procedural basis for such an interpretation. We proceed to a discussion of the excitation conditions.

We defer discussion on aspects (A-3) and (A-4), concerning the molecular spectrum of the pellet, until—by considering the atomic spectrum—we have a better picture of the physical conditions near pellet and meteor.

III. DISCUSSION OF EXCITATION CONDITIONS AND MECHANISM FOR THE ATOMIC SPECTRUM

We recognize at once that the discussion here of a change in spectrum resulting from a change in atmospheric density must differ from that usually encountered in astrophysical problems. In the latter, one usually proceeds from the assumption of an equilibrium state, and a decrease in density results in an increase in ionization level (other things being equal). Such a change in ionization is opposite in direction to that discussed above. We require, then, a discussion based on the details of the excitation mechanisms for meteor and pellet.

The physical theory of meteor radiation in current use, due to Öpik,[9] views the radiation process as one of collisional excitation of meteor atoms by atmospheric atoms. Because of the low atmospheric densities, the possible formation of any compressed gas cap

[7] *A.J.*, **54**, 177, 1949 (abstr.).

[8] *Pop. Astr.*, **57**, 187, 1949.

[9] *Tartu Obs. Pub.*, Vol. **29**, 1937.

at the nose is ignored in its influence on the excitation process. So only—and all—the kinetic energy of the meteor is available for collisional excitation. We note that the last part of the picture could not hold for the pellet, on the one hand, because the excitation level of the spectrum exceeds the kinetic energy of the pellet and, on the other, because a shock wave must certainly form at these sea-level densities. Accompanying this shock wave will be a rise in kinetic temperature, providing at least some atoms with energies considerably greater than that of the pellet. It has been suggested[3] that the pellet excitation is partially supplied by the oxidation energy of the ablated metal. The later observations summarized in aspect (A-3), however, establish the existence of the metal atomic spectrum at the nose of the pellet, where the oxide has not formed in significant quantity. Quite apart, then, from the details of the excitation process, the environment of the pellet is such as to produce a number of atoms with energies considerably greater than those corresponding to the pellet speed. Moreover, the lower the height a meteor reaches in the atmosphere, the greater the likelihood of a similar energy—"partitioning" effect among the gas atoms in its environment to give greater energies to some atoms. Thus, in a superficial way, the effect of atmospheric density on the spectral-excitation level in the present type of problem is clear.

To obtain a quantitative representation of the comparison between meteor and pellet and meteor and meteor spectra, we inquire precisely how this "energy partitioning," or establishment of a kinetic temperature, acts in the excitation process. Several alternatives exist. First, the relaxation processes accompanying the shock wave may be extremely rapid, and a system of complete thermodynamic equilibrium may be established at some temperature. Then it suffices to compute the temperature ("rapid" must be defined with respect to a time given by some dimension of the body divided by its velocity). Second, only the translational degrees of freedom may be appreciably affected in this characteristic time; hence the spectrum must be determined by the frequency and type of inelastic collision. We denote these first and second possibilities by the "equilibrium" and "nonequilibrium" processes, respectively. The nonequilibrium process again presents two possibilities, according as the essential inelastic collision process occurs via electron or atom collision with the to-be-excited atom. If the process is the latter—atomic—alternative, we have the mechanism discussed by Öpik for meteor radiation. Kantrowitz has recently[10] discussed the former—electronic—mechanism in connection with shock-tube studies. We consider these two possibilities in turn.

a) THE NONEQUILIBRIUM CONFIGURATION

1. *Atomic inelastic collision process.*—Consider, first, the nonequilibrium possibility and that in which the inelastic collisional excitation is atom-atom, as lying closer to the current meteor model. We note, first, that there exists no theory of the low-energy, inelastic collision process between atoms that commands any degree of confidence. Öpik's representation of the meteor radiation process by a semiempirical theory was admittedly an attempt to make the best of a bad situation. Because it is fairly easy to show that the Öpik theory does not represent the well-known resonance effects[11] in low-energy, inelastic collisions and because of certain other internal contradictions of the theory, it is only surprising that the theory has worked as well as it has in Whipple's extensive investigation of upper-atmospheric densities from meteor data. The (1927) summary[12] by Loeb is probably still as good as any in describing these low-energy, inelastic collisions from a physical standpoint. The essential aspect seems to be the coupling of the motion of the nuclei with that of the electrons; consequently, the standard approxi-

[10] Paper presented at Salt Lake City meeting of Fluid Dynamics Section of American Physical Society, June, 1952.

[11] E.g., cf. O. Beeck, *Proc. Nat. Acad. Sci.*, **18**, 311, 1932.

[12] *Science*, **66**, 627, 1927.

mation procedures[13] are useless. All comments, then, must proceed from an ignorance of cross-sections.

In an attempt to by-pass this basic ignorance, we might inquire simply as to the relative number of comparably energetic collisions between atmospheric atom and ablated atom in the cases of meteor and pellet. In this inquiry we note a basic difference between meteor and pellet cases, in the circumstances of the collisions. In the meteor case we inject a high-velocity atom into a static, low-temperature atmosphere and ask the number of inelastic collisions involving a certain transfer of energy to internal degrees of freedom before the atom loses its energy by elastic collision. In the pellet case we inject an atom into a high-temperature gas stream, essentially at rest relative to the atom, but moving and changing its thermodynamic state at high speed. Then we ask the number of inelastic collisions before the local kinetic temperature of the gas drops too low. In either case the rate of radiation from a *single* ablated atom depends upon the atmospheric density (upon the atmospheric density itself, for the meteor, and upon the number of atmospheric atoms with thermal energies exceeding some value, for the pellet). For the meteor the *total* rate of radiation is independent of the atmospheric density, since the "range" of the meteor atom is defined by the total number of collisions and the continuous ablation provides a constant flow of radiating atoms through the region defined by the "range." For the pellet the total rate of radiation depends upon the density, since the dimension of the region of high kinetic temperature depends upon the hydrodynamic-flow pattern as well as upon the relaxation time to bring about thermodynamic equilibrium.

Define, then, dn/dt as the rate of ablating atoms; $\sigma_1(E, I)$, the cross-section for inelastic collision with relative energy E and producing excitation to give radiation I; $\sigma_2(E, \Delta E)$, the cross-section for any collision with relative energy E and mean energy transfer ΔE; N_a, the number of atmospheric atoms per cubic centimeter; N and X, the "range" of the meteor atom in units of total number of collisions and distance, respectively; v, u, and V, the velocity due to thermal motion, the hydrodynamic-flow velocity, and the object velocity, respectively; L, the dimension of the region of significantly high kinetic temperature, T_k; $f(v, T_k)$, the Maxwellian distribution function. Subscripts p and m denote pellet and meteor, respectively. Then, for the rate of radiation-producing collisions, we have

$$\text{Collision rate}_m = \left(\frac{dn}{dt}\right)_m \int_0^X N_{am}\sigma_1(E, I)\, dx\,; \tag{1}$$

but

$$N = \int_0^X N_{am}\sigma_2(E, \Delta E)\, dx\,; \tag{2}$$

so

$$\text{Collision rate}_m = \left(\frac{dn}{dt}\right)_m N\left[\int_0^X \sigma_1 dx\right]\left[\int_0^X \sigma_2 dx\right]^{-1}; \tag{1a}$$

also

$$\text{Collision rate}_p = \left(\frac{dn}{dt}\right)_p \int_0^L \frac{dx}{u}\, N_{ap} \int_{E_0}^{\infty} f(v, T_k)\, v\sigma_1 dv\,, \tag{3}$$

where E_0 is the lowest energy for which $\sigma_1(E, I) \neq 0$. We note that the first factor in each of equations (1*a*) and (3) may be written as

$$\frac{dn}{dt} = \frac{\Lambda}{2\zeta}\, \rho_a V^3 (\mu_a m_H)^{-1} \tag{4}$$

[13] Cf. N. F. Mott and H. S. W. Massey, *Theory of Atomic Collisions* (2d ed.; Oxford: Clarendon Press, 1949).

and has been discussed in Papers II and III. The quantity Λ is a (dimensionless) heat-transfer coefficient, of value $\sim 10^{-2}$; ζ is the ablation energy per gram; a and s refer to atmosphere and solid; and μ is the molecular weight. The first and last sets of factors are probably nearly the same for meteor and pellet. (We have assumed pellet and meteor to have the same projected area; we will choose data to satisfy this.)

Thus we recognize that an exact use of equations (1*a*) and (3) prohibits an estimate of the ratio of number of inelastic collisions—hence of relative radiation—without a knowledge of the cross-sections. We might, however, inquire into the order of magnitude for the ratio, seeking some plausible simplification of equations (1*a*) and (3), since we note that the integral over the inelastic cross-section, $\sigma_1(E, I)$, covers effectively the same energy range in each case. For the meteor the σ_1 integral runs from the initial velocity of an ablated meteor atom, the meteor velocity, down to the minimum velocity at which σ_1 differs significantly from zero. For the pellet the σ_1 integral runs from this same minimum velocity to ∞; but, because of the presence of the Boltzmann factor, f, and the small value of kT relative to the meteor (atom) energy, the upper limit might as well be the meteor velocity. Since the usual behavior of an inelastic cross-section is a rather rapid rise, at the energy at which it first becomes nonzero, to a value from which it decreases relatively slowly, we take the cross-sections as constant over the limited energy range involved here. Making similar approximations on the remaining integrals, we approximate the ratio of equation (1*a*) to equation (3):

$$R(m:p) \sim \frac{(\rho_a V^3)_m}{(\rho_a V^3)_p}\left[\frac{X_2}{X_1} N^{-1}\overline{\sigma_2}\tau \overline{N_{ap} v f_1}(E, T_k)\right]^{-1}, \qquad (5)^{14}$$

where X_2/X_1 represents the ratio of "ranges" for elastic and inelastic collisions and τ is a measure of the time taken for an ablated pellet atom to "flow" out (with the gas stream) of the region of high kinetic temperature. Mayfield's observations[4] on the duration of the initial atomic spectrum suggest $\tau \sim 10$ μsec, a reasonable value, since the pellet is ~ 1 cm in dimension. We assume a $\overline{\sigma_2}$ corresponding to the kinetic theory radius of 1 A for the atom. If we assign thermal velocities of $\sim \frac{1}{3}$ km/sec in the neighborhood of the meteor and estimate an energy loss of 50 per cent per collision, $N \sim 10$ for a 30-km/sec meteor. An estimate of the minimum velocity, v_0, at which $\sigma_1 \neq 0$ is most difficult because of the above-mentioned lack of knowledge of σ_1 and because this velocity enters exponentially in R through f. (Indeed, the preferable procedure would be a determination of v_0 through observations on R, thus indicating the use of combined pellet and meteor observations to supplement the difficult direct study of σ_1.) However, we attempt an estimate by noting that 8–10 km/sec seems to be the lower limit observed on meteors, so we take $v_0 = 10$ km/sec. Also, then, X_2/X_1 becomes ~ 3. The value of $\overline{N_{ap} f}$ has the largest element of uncertainty. The collision mechanism is presumably *Fe-O*, *N* or *Al-O*, *N*; so N_a refers to *O* and *N* rather than O_2 and N_2. Near the shock front, T and hence f are highest; but the dissociation is essentially zero. As the air flows past the shock, T decreases, and dissociation increases. Final, thermodynamic-equilibrium values for strong shocks have been tabulated by Davies.[15] For 5 km/sec, the equilibrium values give $T \sim 7000°$, the gas density ~ 10 standard atmospheric, and dissociation essentially complete for O_2 and trivial for N_2. These values contrast with $\sim 1.3 \times 10^4$ and 6 for temperature value and density ratio just at the shock front, from an application of the usual shock equation, assuming no internal degrees of freedom activated ($\gamma = 1.4$).

[14] We note that, defining

$$y = \frac{m v^2}{2kT}, \qquad \int_{v_0}^{\infty} v f(v)\, dv = \int_{y_0}^{\infty} v f_1(y)\, dy \sim v_0 f_1(y_0) \qquad \text{for} \qquad y_0 \gg 1.$$

[15] *Proc. Phil. Soc. London*, **61**, 105, 1948.

Consequently, with this range of T and dissociation, it would appear that the maximum of $N_{ap}f$ in the region between shock front and onset of equilibrium will be assumed at this equilibrium point. If we use this maximum value—the only value we know, even approximately, for $N_{ap}f$—in equation (5), we set a lower limit for R. Since we consider a 30-km/sec meteor, a mean height of ~80 km is reasonable, corresponding to log $\rho_{am} \sim -7.7$. Thus, with these values,

$$R_e(m:p) > \sim 10^{-2}\,. \tag{6}$$

We are indebted to F. L. Whipple for the remark that some of his recent results indicate a rapid change in excitation efficiency in the velocity range 8–20 km/sec. Since, e.g., a choice of $v_0 = 15$ km/sec changes the value in inequality (6) to $\sim 10^5$, the following remarks on an observed value for R indicate that we are probably not far from the correct picture.

As mentioned, the best use of equation (5) would probably be to infer, from an observed value of R, something about the atomic processes involved; i.e., the value of v_0 and the degree of dissociation. Here, however, we attempt some decision on the particular process, atom-atom or electron-atom collision, and so require an observed R for comparison with the computed. Unfortunately, such does not exist. As mentioned, spectrophotometric observations of neither pellet nor meteor are available, although attempts toward both sets of data are in progress. If we neglect the difference between iron and aluminum preponderance, we may try to obtain a rough idea of R from existing observations. From Whipple's work,[16] we find that the emission from a meteor in the range λλ 4500–5700 is

$$\log E_m\,(\text{erg sec}^{-1}) = 9.84 - 0.4\boldsymbol{m}\,, \tag{7}$$

with -2.0 a good estimate for the apparent magnitude, $\boldsymbol{m}$, of a 30-km/sec meteor.[17] On the other hand, Allen, Rinehart, and White suggest[3] that the mean surface brightness of the pellet[17] (integrated light) is about 0.06 that of the sun. A visual inspection of Mayfield's *uncalibrated* spectrophotometric data[4, 18] suggests that from 1 to 10 per cent of the pellet radiation comes from the atomic spectrum. This atomic spectrum lasts about 10 μsec, as used above for τ, and the intensity decreases nearly linearly over this time, making an average luminous region 5 μsec, or 2.5 cm, in length. The pellet diameter is about 1 cm. Thus an estimate of a cylinder 1 cm in radius and 2.5 cm long is probably a fair one for the region of production of the atomic spectrum. We then have, for the emission,

$$E_p\,(\text{erg sec}^{-1}) \sim 2\pi \cdot 1 \cdot [1 + 2.5] \cdot [0.01\text{–}0.1] \cdot 0.06\,\sigma_S T_\odot^4\,, \tag{8}$$

where σ_S is Stefan's constant and $T_\odot$ is the solar temperature, taken as 6000° K. Thus

$$R_0(m:p) = \frac{E_m}{E_p} \sim 5\text{–}50\,. \tag{9}$$

Comparing equations (6) and (9), we see that (6) is indeed a lower limit, and the difference lies between 10^2 and 10^3. Clearly, such a factor is not prohibited by the uncertainty in the degree of dissociation. Equally clearly, the factor indicates the uncertainty in any conclusion drawn here. We note, however, that the above represents the best data currently available. Experiments at the Naval Ordnance Test Station are currently under way to improve the result.

2. *Electronic inelastic collision processes.*—The suggestion has been advanced by Kantrowitz,[19] in connection with the interpretation of shock-tube experiments, that the

[16] *Rev. Mod. Phys.*, **15**, 246, 1943.

[17] Choosing pellet and meteor of ~1 cm² cross-section.

[18] Private communication from Mayfield, who kindly showed us his basic data.

mechanism of inelastic collision behind strong shocks is electron-atom rather than atom-atom. Kantrowitz proposed that radiation from the high-pressure side of the shock partially ionizes the gas ahead of the shock, as well as behind the shock, and that the electrons assume a high kinetic temperature just behind the shock. Then the excitation process should proceed as in § 1, with, however, σ and N_{ap} in equation (3) referring to the electrons. Actually, Kantrowitz' discussion of his observations was carried through on the basis of the assumption of a Boltzmann distribution over the excited states at the electron temperature, and so more properly belongs in § *b*. No photometric results on the shock-tube observations were presented, however; so no check on the assumption was possible. We consider the possibility of electron collision here.

The big change in (5) in the case of electron-atom collision lies in the N_{ap} and f values, the latter through E_0. We do not expect the maximum value of the inelastic collision cross-section, σ_1, to differ greatly in the two cases of electron-atom and atom-atom collisions. It lies near the dimension of the "struck" atom in each case. However, E_0 differs considerably. The rough, rule-of-thumb value, based simply on the efficiency of momentum transfer, gives the values of E_0 to be in the ratio of the masses. The actual experimental values are not so extreme, particularly under resonance conditions (similar electronic configurations of colliding atoms), but the ratio is still large, 10–100 or more.

We note that had we used even the smaller value, 10, for the ratio, we would have used a considerably higher v_0 in § 1, since the lowest-excitation *Fe* line is 2.4 e.v. Then the exponent in f would have been larger by a factor of 3; f, smaller by a factor of 10^{12}; and R, larger by this same last factor. One becomes forced, then, to admit the presence of considerable reduction in the E_0 ratio, or to look for other mechanisms in the meteor case. One, of course, is that these slow meteors have reached an altitude where a shock wave can form. Another is that electron-atom collisions form the mechanism in the slow meteors. Several years ago, one of us attempted [unfruitfully, unpublished] to consider the possibility that electronic excitation was responsible for the meteor radiation mechanism, motivated by the above-mentioned change of meteor excitation along the trail and the coincidence[19] between the zone of the *E* layer and several meteor phenomena (maximum of radio reflection, etc.). Consequently, the possibility of electron excitation for some meteor phenomena must not be overlooked, but a decision cannot be made until more spectrophotometric data on both meteor and pellets are available.

Consider the value of R to be computed from (5), assuming electron-atom collisions as the mechanism for the pellet. With $E_0 = 3.1$ e.v. (corresponding to *Al*), the electron density, N_e, which replaces N_{ap}, must become 10^{-6} times the N_{ap} in the atom-atom case for the same T value (any larger T, the direction of Kantrowitz' suggestion, increases the figure by a factor of 10) if the same R is to result. This gives $N_e \sim 10^{14}$. The value seems low for this T, about 1 per cent of the equilibrium value. (Any change toward the observed value [9] makes the situation worse—i.e., N_e smaller.) If, however, we depend upon atom-atom collision to ionize behind the shock, such low N_e is not surprising; for the relaxation time for ionization in this way is very long indeed. If, however, we expect preionization by radiation and hence have already an appreciable supply of energetic electrons at the shock front (certainly, if we have enough to give a Boltzmann distribution over the excitation levels!), $N_e = 10^{14}$ seems low. Thus, although we recognize the inadequacy of the data on hand, we conclude that the electron-atom mechanism seems less probable than the atom-atom, when we look for a nonequilibrium, even a nonsteady, state model.

b) THE EQUILIBRIUM CONFIGURATION

We note at the outset that the only completely satisfactory investigation of the equilibrium alternative is through a consideration of spectrophotometric line intensities. Such work, as mentioned above, is currently in progress at NOTS. Earlier work[3] on band

[19] F. L. Whipple, *Advances in Geophysics* (New York: Academic Press, 1952), pp. 119–154.

intensities refers to the molecular spectrum and suffers from lack of photometric calibration. In the next section we consider the question of the time lag in appearance of the molecular bands. Here, however, we can make a few remarks on the possibility of the equilibrium configuration to the same precision as those in § *a*.

We note that, were the gas near the pellet in equilibrium, the quantity corresponding to the collision rate, given by equation (3), would be the transition rate from upper to lower level. Consequently, while equation (3) gives, roughly,

$$\text{Collision rate} \sim \frac{dn}{dt}\,\tau\,\overline{N_{ap} f \sigma_1}\,, \tag{10}$$

we would expect

$$\text{Transition rate} \sim \frac{dn}{dt}\,\tau A\, e^{-E/kT}\,, \tag{11}$$

where A is the transition probability (dimension, time^{-1}). Thus, using the $\overline{N_{ap} f}$ value of § *a* and setting an upper limit of 10^{-16} for σ_1, we have

$$\text{Collision rate} \sim \frac{dn}{dt}\,\tau 3 \times 10^4\,. \tag{10a}$$

In equation (11), we take $E = 3.1$ e.v., corresponding to the observed *Al* I lines of Table 2 (which dominate the spectrum), and $A \sim 10^8$. Then

$$\text{Transition rate} \sim \frac{dn}{dt}\,\tau 6 \times 10^5\,. \tag{11a}$$

Thus the predicted value of R (eq. [6]), corresponding to this increased emission from the pellet, widens the difference already present between equations (6) and (9) by a factor of 20. Again, then, while the data are certainly inadequate, the nonequilibrium atom-atom picture seems preferable.

IV. COMMENT ON THE MOLECULAR SPECTRUM

As already mentioned, the major portion of the pellet luminosity comes from the molecular spectrum, which represents the "burning" of the *Al* ablated from the pellet. In connection with the pellet's use as an "artificial meteor," two questions arise: (1) What information on the excitation problems considered in § III can the molecular spectrum add? and (2) Why is any metallic molecular spectrum so insignificant in the case of the meteor? We consider the questions in turn.

We base the discussion upon the following data,[4] an elaboration of aspect (A-3) of § II. Lines of *Al* corresponding to an (upper) excited level of 3.1 e.v. appear within 1–2 μsec of the onset of luminosity, rising abruptly to maximum intensity, then slowly decreasing, lasting about 20 μsec. The total pellet luminosity reaches a minimum near 100 μsec. *AlO* bands first appear near 200 μsec and increase in strength, the total luminosity reaching a maximum near 350 μsec. The *Al* lines reappear, considerably intensified, in this region of the molecular spectrum. These data refer to an *Al* pellet, with speed ~5 km/sec.

To describe the delay in appearance of the *AlO*, we have two extreme alternatives. First, the high kinetic temperature in the region near the shock wave may prohibit the *AlO* formation. Second, the delay in formation of *AlO* may be simply an activation time for the reaction to occur in the strict chemical sense. The first alternative may also be viewed as a reaction—or pseudo-reaction— for the formation of *AlO* from *Al*. The difference here lies in the true chemical reaction rate being assumed to be so much faster than the rate of change of thermodynamic parameters that the reaction has actually

reached completion to that degree permitted by these thermodynamic parameters at each point. (Such an assumption is, indeed, the one customarily made in aerodynamic-flow problems; it is one form of the "local thermodynamic equilibrium" concept.) Thus the reaction rate from the first process is directly the cooling rate, while the reaction rate from the second process is fixed by the temperature itself; hence the cooling rate represents the change in reaction rate.

a) THE INHIBITION REACTION

Consider the first process, the "inhibition" reaction. If the extreme assumption of a complete equilibrium state having been reached at each point is true, we need consider only the reaction

$$Al+O \longleftrightarrow AlO \tag{12}$$

to obtain the relative concentrations $[Al]$ and $[AlO]$:

$$\frac{[AlO]}{[Al]} = [O]\,\frac{f_{AlO}}{f_{Al}f_O}\exp\left(\frac{X_{AlO}}{kT}\right), \tag{13}$$

where the f's are the partition functions and X is the dissociation energy. As discussed in § III, however, it is not clear whether such equilibrium has been reached or not, and so reaction (12) must be considered in conjunction with the reactions

$$O_2 \longleftrightarrow 2O\,, \tag{14}$$

$$Al+O_2 \longleftrightarrow AlO+O\,. \tag{15}$$

Each of reactions (12) and (14) is two-body. There is also the direct three-body reaction:

$$2Al+O_2 \longleftrightarrow 2AlO\,, \tag{16}$$

which should be slower than the two-body. Since, however, the processes involving the dissociation of O_2, that part of the reaction requiring an activation energy, are exothermic in reactions (15) plus (12), and (16), these are probably the alternative reactions. That is, we would expect the O_2 to dissociate more rapidly in the presence of the ablated Al than otherwise. We may make one estimate of equation (13) from the equilibrium values[15] already used in § III.[20] Assuming that the electronic partition function ratio in equation (13) is unity, we have

$$f_{\text{rib}} = \left(1-\exp\left[-\frac{h\nu}{kT}\right]\right)^{-1} \sim \frac{kT}{h\nu} \tag{17}$$

at these temperatures, where ν is the fundamental vibration frequency. Also

$$f_{\text{rot}} = \frac{8\pi^2 IkT}{h^2}\,,$$

where I is the moment of inertia. With the values[21]

$$\begin{aligned} X_{AlO} &= 3.75 \text{ e.v.}, \quad & \nu_{AlO} &= 2.9\times 10^{13}\,, \quad & I_{AlO} &= 4.4\times 10^{-39}\,; \\ X_{O_2} &= 5.08 \text{ e.v.}, \quad & \nu_{O_2} &= 2.1\times 10^{13}\,, \quad & I_{O_2} &= 3.4\times 10^{-39}\,, \end{aligned} \tag{18}$$

[20] Davies' computations do not include the heat source provided by the ablated Al. This Al is only ~0.1 per cent of the atoms present; and the oxidation is far from complete; so the perturbation is not large.

[21] Gerhard Herzberg, *Molecular Spectra and Molecular Structure* (2d ed.; New York: D. van Nostrand Co., Inc., 1950).

we obtain

$$\frac{[AlO]}{[Al]} = 1.3 \times 10^{-25}\,[O]\,T^{1/2} \exp\left(\frac{X_{AlO}}{kT}\right); \tag{13a}$$

and, with the equilibrium values used in § III, $T = 7 \times 10^3$, $[O] = 9 \times 10^{19}$,

$$\frac{[AlO]}{[Al]} \sim 5 \times 10^{-1}. \tag{13b}$$

On this basis we find difficulty in explaining the presence of Al^* and the absence of AlO. We note, however, that, dropping the assumption of equilibrium, we raise T and lower $[O]$; that is, for $T = 1.34 \times 10^4$, the temperature just behind the shock, (13b) becomes 3×10^{-2}, even with no change in $[O]$. Thus we have no difficulty in interpreting the observations on this "inhibition" model so long as we drop the requirement of strict equilibrium. Physically, the result is obvious. Doubling the temperature increases Al^*, since the formation is by collision, and more sufficiently energetic atoms are then present by the "hot-region" argument of § III. And more energetic collisions hinder the formation of AlO. Thus, if this alternative (*a*) be correct, we find support for the picture formed in § III of a high kinetic temperature, nonequilibrium region just behind the shock wave.

b) THE ACTIVATION MODEL

Considering the various processes leading to the formation of AlO, we may use the 200 μsec observed lag to evaluate the activation energy for the process, and so form an estimate of the "reasonableness" of this alternative. With reaction (12), we have, for the rate of formation of AlO,[22]

$$\frac{d\,[AlO]}{at} = k'\,[Al]\,[O]\,, \tag{19}$$

where

$$k' = \frac{kT}{h}\left(\frac{h^2}{2\pi M kT}\right)^{3/2} \frac{8\pi^2 I_{AlO} kT}{h^2} \exp\left(-\frac{E}{kT}\right), \tag{20}$$

where M is $M_{Al}M_O/M_{AlO}$ and E is the activation energy. (Note that the vibrational degree of freedom of the activated complex, $[AlO]^*$, is replaced in the partition function by the frequency, kT/h, along the reaction co-ordinate.) Thus, setting a lower limit on E by taking $d[AlO] = [Al]$ and with $dt = 200$ μsec, we have

$$E = 0.86 \times 10^{-4} T \ln\{7.8 \times 10^{-16} T^{1/2}\,[O]\}\,\text{e.v.} \tag{21}$$

Whence, for the values earlier discussed:

$$\begin{aligned} &(1)\quad T = 7 \times 10^3\,, \qquad [O] = 9 \times 10^{19} \rightarrow E = 9.4\ \text{e.v.};\\ &(2)\quad T = 1.34 \times 10^4\,, \qquad [O] = 9 \times 10^{19} \rightarrow E = 18\ \text{e.v.} \end{aligned} \tag{22}$$

All these values are much too high. The only activation process would seem to be the breaking of the O_2 band, and the above values are far too great for this. The $[O]$ value used is certainly too great, but we note that E must be reduced by about a factor of 10 and $\ln[O]$ by the same factor, and hence $[O]$ by 10^4. We note, however, that a factor of 10^2 in $[O]$ will prohibit the reaction according to process *a*, without much helping the situation here, so we favor process *a*.

[22] Cf. H. Eyring, S. Glasstone, and K. J. Laidler, *Theory of Rate Processes* (New York: McGraw-Hill Book Co., Inc., 1941).

As already mentioned, process (15) is more likely the slow process than (12), so we should substitute $[O_2]$ for $[O]$ in equation (19) and consider $(AlO_2)^*$ as the activated complex. The partition functions of this complex are difficult to estimate, so we proceed schematically, writing:

$$k' = \frac{kT}{h}\left(\frac{h^2}{2\pi MkT}\right)^{3/2} \frac{(1 \text{ vib} \times 2 \text{ rot})_{AlO_2}}{(1 \text{ vib} \times 1 \text{ rot})_{O_2}} \exp\left(-\frac{E}{kT}\right). \tag{23}$$

Thus the third term becomes essentially one rotational partition function, whose moment of inertia is probably larger than that for O_2. Thus, if we use equations (20) and (21) for equation (23), replacing $[O]$ by $[O_2]$, we obtain a lower limit for the activation energy from equation (23). Thus there is no significant change in the activation-energy values given in equations (22).

There is one final perturbation possible. The air flows around the body very rapidly, then expands, and the temperature drops. It is possible that the activation process occurs in this low-temperature region. However, we note from equations (19) and (20) and the results in equation (22) that so long as the "suppression time" for the appearance of AlO is greater than $\sim 10^{-4} \times 200$ μsec, no reasonable activation energy will result. And the compressed, high-temperature region certainly has dimension larger than that ($\sim 10^{-2}$ cm) traversed in 2×10^{-2} μsec.

Thus we consider that the inhibition process provides more nearly the correct description of the delay in appearance of the molecular spectrum. Also we answer the first question of this section: the molecular spectrum seems to confirm the nonequilibrium picture of the excitation mechanism discussed in § III.

We note that the above conclusions may be checked experimentally by firing pellets at several velocities. If the inhibition mechanism is correct, higher velocities (hence higher temperatures) should give greater delays in the oxide spectrum, and conversely. Such experiments are in progress, and preliminary results do indeed confirm the above conclusion.

c) OXIDATION AND THE METEOR MOLECULAR SPECTRUM

Consider the second question raised, that of a meteor metallic molecular spectrum. From the discussion of the preceding section, we would expect the AlO spectrum to form in the pellet case when the gas had cooled upon expansion around the pellet. The 200 μsec lag, corresponding to ~ 1 meter behind the pellet nose, seems large for a pellet of dimension ~ 1 cm. We expect the air to reach atmospheric pressure in a length several times that of the pellet. Noting values of 1.34×10^4° K and six times standard atmospheric value for temperature and density just behind the shock, adiabatic expansion with $\gamma = 1.4$ would drop these values to 2.73×10^3° K and $\frac{1}{9}$ standard atmospheric. Under these conditions, oxygen is ~ 0.1 per cent dissociated. Thus $[O] \sim 5 \times 10^{14}$. From equation (13a) we obtain, then,

$$\frac{[AlO]}{[Al]} \sim 3 \times 10^{-2}. \tag{24}$$

Thus conditions still do not permit appreciable AlO to form when the pressure has dropped to the atmospheric value. The temperature must drop farther, and the density must rise. This process can occur only by thermal and turbulent diffusion. Thus we understand the long time lag.

From this result, we can remark on the molecular (oxidation) spectrum for faster objects. As the velocity increases, the amount of cooling that must occur by thermal and turbulent diffusion increases. However, such diffusion also permits diffusion of the Al and so reduces the Al concentration. Such reduction decreases the luminous intensity produced by the eventual reaction. Also, of course, faster objects produce a higher initial

concentration of *Al*. Depending upon the balance of these two factors, the relative importance of the molecular spectrum can change. For sufficient importance of the diffusion, we expect the molecular spectrum to become far less important than the atomic. The investigation of such effects should produce knowledge of the diffusion processes occurring in the wake of high-velocity bodies. Clearly, these results may be taken over directly to the meteor case. We enter, then, into the problems of the meteor train, or wake, whichever of the terms seems preferable.

NOTES

THE NEBULAR SPECTRUM OF NOVA PUPPIS 1942

The spectrum of Nova Puppis 1942 in its nebular stage was obtained on several occasions by E. Gaviola and R. Platzeck at the Observatory of Bosque Alegre (Argentina) from 1943 to 1947. The same spectrograph was used throughout (40 A/mm, grating), but widely different emulsions (plates or films) were employed. The available region extends from λ 3400 to approximately λ 5000. The quality of the plates is rather poor, many having been taken during the adjustment of the spectrograph and others when the nova was very faint. However, they give valuable information about the spectrum of Nova Puppis in this stage; as they are almost the only existing observations of the spectrum of this nova after 1943, it seems worth while to give a short description of the plates.

The spectrum of Nova Puppis near maximum was described by H. F. Weaver[1] and R. F. Sanford,[2] who both reached the conclusion that the development of the spectrum followed the general pattern of that of fast novae, but with some peculiarities; among others, Nova Puppis showed strong lines of [*Fe* II], a most unusual feature in fast novae. The last plates measured by Sanford already belong to the nebular stage. Two plates taken on March 15, 1946, and January 9, 1947, have been described by Sanford.[3]

Our plates begin with September 22, 1943; the strongest lines at that time were N_1, N_2, and 4363 [*O* III], followed by the Balmer lines, 3869 [*Ne* III], 4686 *He* II, 4640 *N* III, 3426 [*Ne* V]; a faint feature near λ 3760, outside the region covered by Sanford's spectra, is identified as [*Fe* VII]. No trace of continuous spectrum was visible; neither was it possible to observe the lines 4068 [*S* II] and 4605 *N* V, which, according to Sanford, were present at this time. Doubtless this is due to insufficient exposure.

From the opposition of 1943–1944 to that of 1944–1945 we note various changes. The [*O* III] lines are still the strongest, but they are much fainter than in the previous year relative to the Balmer lines. The ultraviolet line of [*Ne* V] is now very strong, and 3760 [*Fe* VII] is about as strong as 3869 [*Ne* III]. The continuous spectrum in the ultraviolet is well visible, while it is impossible to decide whether the features observed between λ 4400 and λ 4600 are due to a faint continuum or to several adjacent emissions. An appendix to λ 4640 extending to the violet is almost certainly to be identified with 4605 *N* V.

In the successive opposition no major changes could be observed except the strong increase of the continuum relative to the emission spectrum. Indeed, on an exposure just sufficient to show the emission bands λλ 4605, 4640, and 4686, the ultraviolet continuum was conspicuous (see Fig. 1, *a*, *b*, *c*).

The last plate was taken on January 7, 1947; only N_1 and N_2 are visible on it, owing to insufficient exposure.

During all the time, the emission bands showed a rather complicated structure (see Fig. 1, *d*, *e*, *f*) with various maxima, whose relative intensity and (probably) wave length showed some changes. Table 1 gives the radial velocity corresponding to the different maxima, measured on several occasions for the lines N_1 and N_2; only the best plates have been selected for measurement.

Owing to the difference in photographic density from one plate to another, not much significance must be attached to the fact that a given maximum was not observed for

[1] *Ap. J.*, **99**, 280, 1944.

[2] *Ap. J.*, **102**, 357, 1945.

[3] *Pub. A.S.P.*, **59**, 334, 1947.

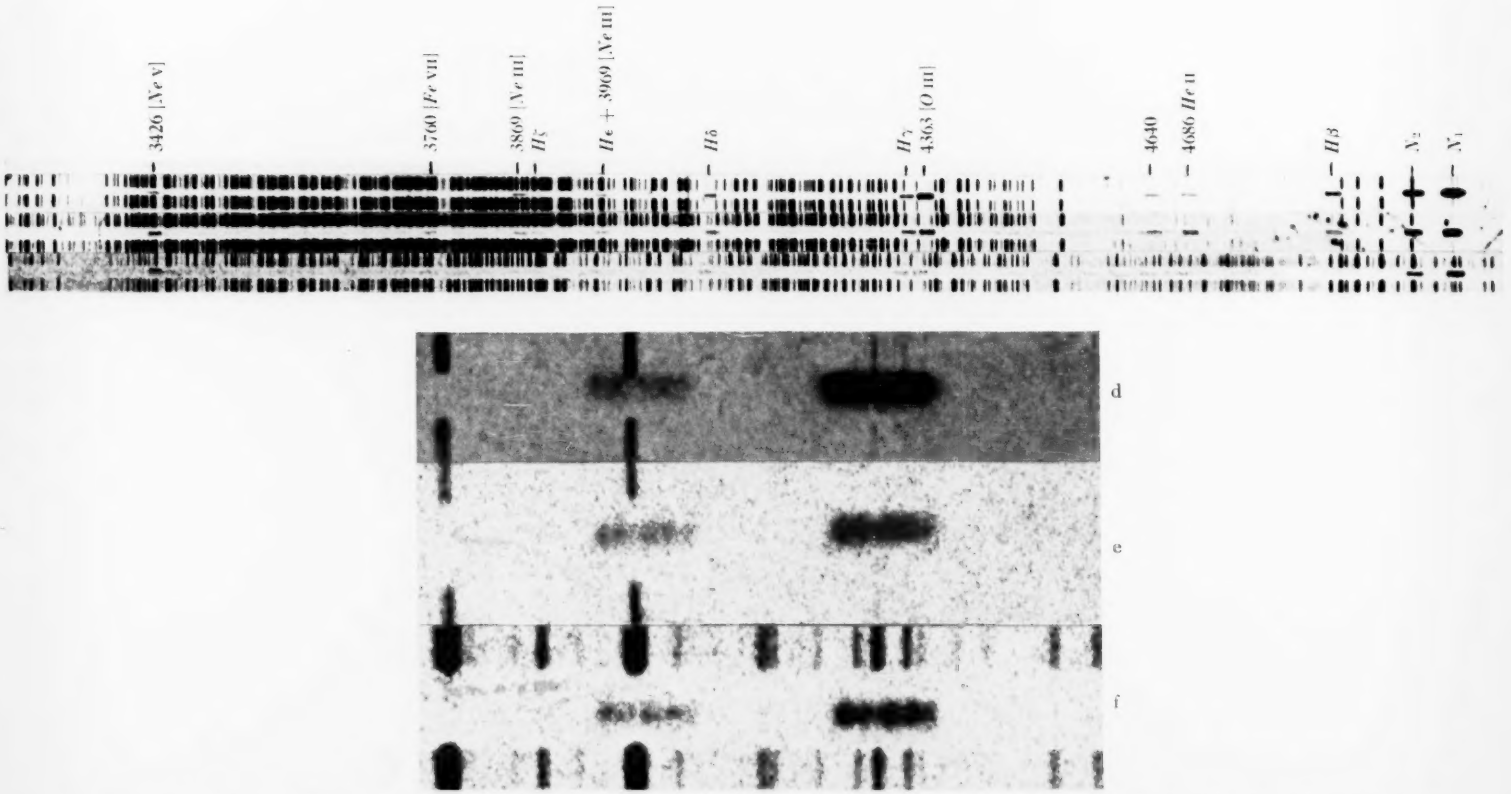

FIG. 1.—*a*, October 16, 1943; *b*, March 4, 1945; *c*, February 5, 1946; *d*, N_1 and N_2, November 17, 1943; *e*, N_1 and N_2, March 5, 1945; *f*, N_1 and N_2, February 22, 1946

some plates or for some bands. However, some changes are undoubtedly real. To describe these, we shall distinguish five main emission components (see also Sanford, *Pub. A.S.P.*, **59**, 334, Table 4, 1947) in the following order: emission component *a* centered at about −480 km/sec; *b*, at −220 km/sec; *c*, at +80 km/sec; *d*, at +400 km/sec; and *e*, at +590 km/sec.

On the first spectra, component *b* is the strongest, followed by *a*, *c*, and *d*; component *e* is not well separated from *d*. Shortly afterward, however, *a* becomes the strongest, while *b* decreases slowly until it becomes barely visible in 1946 and 1947. Components *b*, *c*,

TABLE 1

RADIAL VELOCITIES OF MAXIMA OF THE EMISSION LINES

	Component	1943 Sept. 22	1943 Oct. 10	1943 Dec. 12	1944 Jan. 21	1944 Feb. 19	1944 May 8	1944 Nov. 27	1945 Nov. 15	1946 Feb. 5	1946 Feb. 22	1947 Jan. 7
N_1	violet edge	−650	.....	−680	−590	−640	−610	−590	−530	−560	−540	−550
	a_1	−490	−420	−490	−470	−500	−460	−480	−480	−510	−440	−510
	a_2	.....	.....	.....	.....	.....	.....	.....	−400	−410	.....	−410
	b_1	−210	−240	−250	−210	−260	−240	−250	−260	−320 −230	−280	−310 −260
	b_2	.....	.....	−150	−110	−130	−120	−180	−150	−150	−180	−170
	c_1	+ 90	+110	+ 90	+100	+ 70	+ 50	+ 50	+ 60	+ 50	+ 40	+ 80
	c_2	.....	.....	.....	.....	+230	+220	+220	+180	+190	+210	+190
	d_1	+400	+400	+350 +470	+310 +440	+380	+400	+350 +420	+360 +490	+320 +420	+320 +410	+370 +440
	d_2	.....	.....	.....	.....	+510	.....	.....	.....	+520	+540	.....
	e	.....	.....	+600	+600	+620	+630	+590	+580	+600	+620	+590
	red edge	+730	.....	+700	+680	+710	+720	+670	+640	+660	+650	+660
N_2	violet edge	−580	−670	−610	.....	−570	−600	−550	−540	−560	−550	.....
	a_1	−470	−510	−470	−470	−470	−450	−470	−470	−460	−460	.....
	a_2	.....	.....	.....	.....	.....	.....	.....	.....	.....	−400	.....
	b_1	−220	−230	−270	−250	−260	−190	−250	−260	−280	−270	.....
	b_2	.....	.....	−190	− 90	.....	−110	−150	−150	−160	−120	.....
	c_1	+ 90	+ 90	+100	+ 70	+ 70	+ 80	+ 30	+ 40	+ 70	+ 60	.....
	c_2	.....	.....	+240	+230	+230	+200	+210	+160	+210	+180	.....
	d_1	+400	+400	+420	.....	+320 +450	+340	+380	+410	+390	+320 +410	.....
					+490	.....						
	d_2	.....	.....	.....	.....	.....	.....	.....	.....	+500	.....	.....
	e	.....	.....	+570	+630	+590	+580	+570	.....	+600	+570	.....
	red edge	+580	+690	+650	+700	+680	+690	+640	+650	+650	+700	.....

and *d* most of the time show a complex structure with two or three maxima, but it must be remarked that the separation between *c* and *d* is not clearly defined, because of another component with velocity about +210 km/sec, which soon fills the gap between them. Owing to this fact, they often appear as a unique very broad and complex component. Of course, this separation in components is merely conventional and does not reflect any physical model; the interpretation in terms of expanding shells or (according to an idea put forward by Baade for Nova Aquilae 1918) rings is not possible with the present material. Finally, it may be remarked that component *e* looks relatively much stronger in the line 4363 than in any other line.

I am under deep obligation to Drs. E. Gaviola and R. Platzeck for turning over to me for study their plates of Nova Puppis 1942.

LIVIO GRATTON

OBSERVATORIO ASTRONÓMICO
EVA PERÓN (*formerly* LA PLATA)
March, 1953

NOTE ON THE SPECTRUM OF β DORADUS

The bright southern cepheid ($m_{Max} = 4.5$; $m_{Min} = 5.7$; pg, $P = 9.84$ days) was put into our observing program because Pingsdorf[1] suspected its light-curve to be variable; its period is in the neighborhood of a minimum of frequency of the periods of galactic cepheids.

Table 1 shows the observations which have been secured so far, with the grating

TABLE 1

Plate	J.D. 243+	Phase (Days)	Sp.	$V_a \pm$ p.e.	V_{em}
1047	3306.60	9.27	F6–7	$+2.8 \pm 1.3$	.....
1060	307.67	0.50	F7	-0.6 ± 1.2	+97
1066	308.60	1.43	F7	-7.2 ± 1.6	.....
1071	310.54	3.37	G5	.....	.....
1949	4406.53	6.86	F9	$+4.5 \pm 1.2$	−40
1950	406.55	6.88	F9	$+4.8 \pm 1.4$	−40

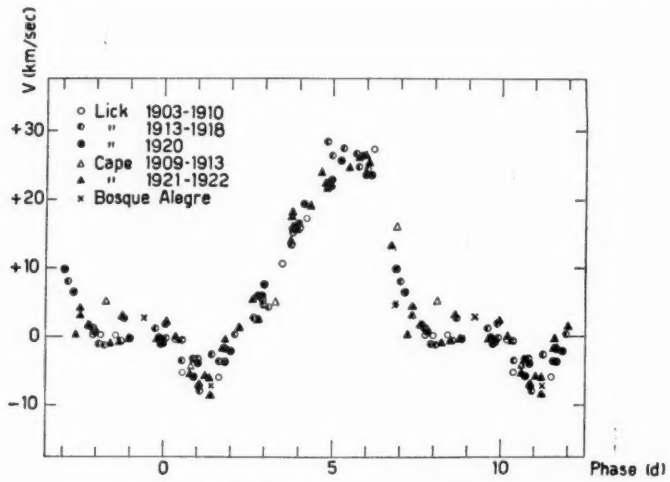

FIG. 1.—Radial-velocity-curve of β Doradus

spectrograph attached to the 60-inch telescope of the Observatory of Bosque Alegre. Plate 1071 was slightly out of focus; it was not measured for radial velocity. The radial velocities fit very well in a general radial-velocity-curve, which can be obtained from old Lick[2] and Cape[3] observations, if a small correction to the period previously obtained from spectrographic observations[2] is adopted. The corrected period is $P = 2.84235$ days, with

[1] *Pub. Obs. La Plata*, ser. astr., Vol. **26**, 1950.

[2] D. Applegate, *Lick Obs. Bull.*, No. 386, 1927.

[3] J. Lunt, *Ann. Cape Obs.*, Vol. **10**, Part 7, 1924.

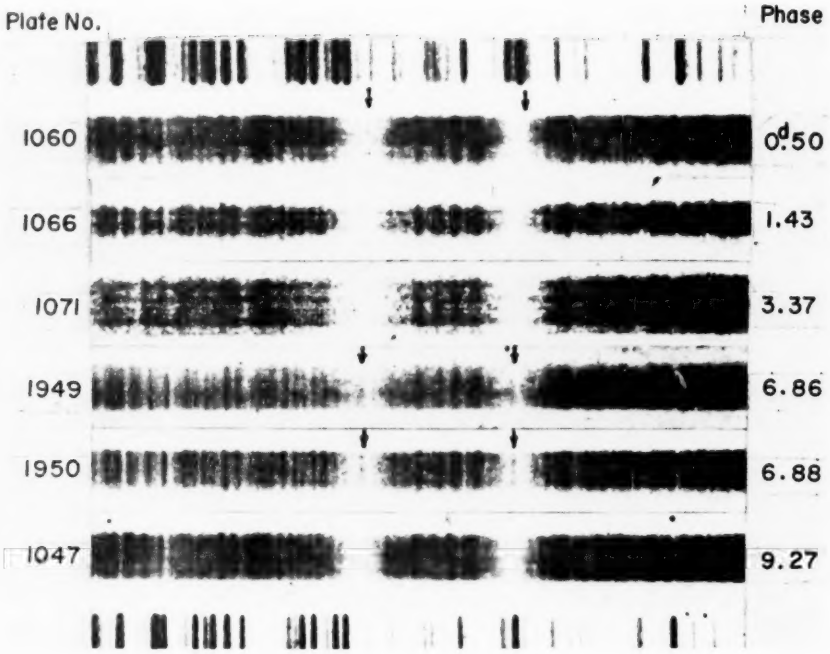

FIG. 2.—Representative spectra of β Doradus

an uncertainty of, say, ± 0.00010 day. Pingsdorf's period from visual observations extending over three years is 2.842603 days; the spectrographic observations extend over an interval of 50 years. The phases of Table 1 have been computed with the following elements:

$$t_{\text{Max}} = 2422431.37 + 9.84235E,$$

which are probably better than Pingsdorf's element contained in Kukarkin and Parenago's *Catalogue of Variable Stars*.

From all existing radial-velocity observations we get the very well-determined radial-velocity-curve shown in Figure 1; slight corrections have been applied to the different series of observations. The very good agreement of these observations, which extend over scores of cycles, makes it very unlikely that the above-mentioned variations of the light-curve are real. An examination of Pingsdorf's published data shows that his observations of this star are less accurate than for other objects. Shapley's photographic observations,[4] although somewhat more accurate, are also insufficient to show a variation in the light-curve. We may thus safely conclude that if these variations are present, they cannot be very large; probably only photoelectric observations will settle this point. The form of the radial-velocity-curve makes it almost certain that the light-curve is of the type with a hump shortly before principal maximum. This fits very well with the general pattern of the relation between period and form of the light-curves of cepheids.[5]

Bright H and K lines were detected on two plates taken in January, 1953; faint traces of emission are also present on a plate taken in 1950 (Fig. 2). β Doradus is the sixth classical cepheid in which *Ca* II emission has been discovered;[6] apparently, this phenomenon is thus fairly common among cepheids.

In this case, three days before maximum light—that is, near the middle of the ascending branch of the light-curve—the emission lines are fairly strong and displaced to the violet; but shortly after maximum they are faint and *displaced to the red*. Owing to the faintness of the features observed, there might be some doubt that this last observation refers to spurious lines produced by chance alignment of the silver grain in the emulsion; I feel, however, that the observed lines are real. If confirmed, apparently this is the only case in which a positive displacement of the emission lines was observed in cepheids, although in several cases double lines were reported, the shortward components being always the stronger.

The present material does not warrant a discussion of the emission lines, their origin, and their bearing on the theory of cepheid pulsation. Further observations, both spectrographic and photometric, are planned in the near future.

Addendum.—Dr. G. H. Herbig called my attention to the fact that Jacobsen (*Pub. A.S.P.*, **64**, 308, 1952) observed faint redward emissions in H and K of η Aql just after light-maximum, much like those found in β Doradus. A reconnaissance of bright cepheids with low dispersion (*Pub. A.S.P.*, **64**, 302, 1952) resulted in the discovery of bright *Ca* II lines in seven more stars. Neither of these papers has yet arrived at Eva Perón.

LIVIO GRATTON

OBSERVATORIO ASTRONÓMICO
EVA PERÓN (*formerly* LA PLATA)
May 18, 1953

[4] H. Shapley and M. L. Walton, *Harvard Circ.*, No. 316, 1927.

[5] C. P. and S. Gaposchkin, *Variable Stars* (Cambridge: At the University Press, 1938), p. 162.

[6] G. Herbig, *Ap. J.*, **116**, 369, 1952.

NOTE ON SPECTRA OF COOL STARS IN THE 1μ REGION

Recent improvement of the I-Z emulsion by the Eastman Kodak Company makes possible the photography of stellar spectra through the atmospheric window near 1μ. The combined 4° and 6° objective prisms of the Curtis Schmidt give the rather low dispersion of 1300 A/mm at 1μ, but offer the usual compensating advantages inherent in objective-prism spectroscopy. The performance of the two-prism combination has been described elsewhere.[1]

The present note is the result of a reconnaissance, undertaken to evaluate the utility of the two-prism combination for research on the 1μ region photographed on ammonia-hypersensitized I-Z(2) plates. Useful experience in handling this emulsion was also acquired. The chief lesson was the necessity for compressing the sequence hypersensitization-exposure-development into the smallest feasible interval, if background fog is to be suppressed.

The plates were found to have adequate speed for the study of the brighter stars. Reduced to visual magnitude 3.0, the exposure times required to obtain well-exposed infrared spectra $\frac{1}{3}$ mm wide varied from approximately 30 minutes in classes F5 through K0, to less than 1 minute for classes M6 and later. The curve of exposure time as a function of effective temperature agrees very well with that predicted by the Planck function, when the effective wave lengths of visual magnitudes and the infrared region covered by the I-Z(2) plates are taken as 5400 and 10,000 A, respectively.

The first plates confirmed the opinion of Kuiper, Wilson, and Cashman[2] that very prominent features in this wave-length region are found in the spectra of the cooler stars. Attention was therefore concentrated on the later spectral classes. Emission spectra of P Cygni and Wolf-Rayet stars have been obtained but are reserved for discussion in a later contribution.

Thirty-minute exposures did not bring out numerous infrared spectra, and it was clear that the investigation should be confined to a few bright stars. Absorption features near the limit of detection cannot, therefore, be verified statistically by examination of large numbers of spectra, and it was found desirable to base conclusions on at least three plates of each star or of similar stars.

The objective-prism material is summarized in Table 1. The star ϵ Aurigae was included with a view to eventual study of the infrared companion postulated by Kuiper, Struve, and Strömgren.[3]

The wave-length system was established initially with the standard Hartmann formula, used, in this instance, to extrapolate to longward of the short-wave-length edge of the ρ and σ telluric band at λ 9300. The results were naturally viewed with suspicion. After the reductions were completed, a 7.5-hour exposure of Y Canum Venaticorum was obtained by McLaughlin and Boggess with the 37-inch reflector, two-prism spectrograph, and 12-inch camera. The dispersion at 1μ is 540 A/mm. This yielded a satisfactory spectrogram, on which comparison lines could be identified to 9660 A. The transmission of the spectrograph decreases rapidly to longward of 10,400 A, which limits its usefulness in the present program.

Wave lengths of stellar features common to the objective-prism plates and the slit spectrogram agreed within the anticipated limits of error. Three wave lengths measured on the slit spectrogram were then used for an improved reduction of the Schmidt spectra. The dispersion in the latter increases slowly near 1μ, and a relation of the form

$$\lambda = \lambda_0 + aR + bR^2$$

was found to be more satisfactory than the standard Hartmann formula.

[1] *A.J.*, **58**, 44, 1953.

[2] *Ap. J.*, **106**, 243, 1947.

[3] *Ap. J.*, **86**, 570, 1937.

All wave lengths were derived from measures on tracings taken with the microdensitometer of the McMath-Hulbert Observatory at a magnification of 35.4×. The internal error of the Schmidt wave lengths, as derived from five to ten determinations for each of eight features common to the four N stars, is of the order of ±25 A. In view of the uncertainty of the final wave-length scale, the mean error is probably more nearly ±75 A but is difficult to assess with precision.

The most conspicuous feature seen in any of the spectra listed in Table 1 is a deep absorption band in that of R Aurigae. The width on the tracings is 300 A, centered at λ 10,660. This is undoubtedly the feature observed with the lead sulphide cell by Kuiper *et al.*[2] in the spectra of Mira and R Leonis. The approximate wave length, measured on their published tracings, is 10,600 A, and the wave-length system adopted for the Schmidt spectra is confirmed.

No trace of this band is found in the spectrum of Z Ursae Majoris, nor has it been noted in any of the faint infrared spectra which appear on the Schmidt plates, with the exception of that of BD+24°1538, for which a spectral classification is not available.

TABLE 1

Star	Type	No. Spectra	Remarks
Z UMa	M6e	3	Observed three months before predicted maximum
R Aur	M7e	4	Observed two months after predicted maximum
U Hya	N2, $C7_3$	4	
X Cnc	N3, $C5_4$	2	
Y Cyn	N3, $C5_4$	3	
RY Dra	N4p, $C4_4$	1	Below-average quality
R Gem	S3	1	Below-average quality; observed 15 days before predicted maximum
ε Aur	F0	1	High quality, wide spectrum

The possibility that this band may be due to the combined 0–1, 1–2, and 2–3 bands of the F-X system of *FeO* recently reported by Bass and Benedict[4] was suggested to the writer by Dr. Goldberg. The evidence is inconclusive. The broad maximum of emission in the published tracing of the *FeO* spectrum at λ 9900 cannot be identified on the writer's tracings. Another broad emission feature in the *FeO* spectrum near 11,900 may correspond to a feature seen in the tracings by Kuiper *et al.*[2] of R Leonis, but it does not appear in their tracing of the spectrum of Mira.

The obvious presence of a number of bands in the spectrum of U Hydrae led to concentration on class N in this preliminary program. The most conspicuous characteristic of these spectra is a broad, complex absorption feature overlying the ρ and σ telluric band. Another absorption feature intrudes on the long-wave-length limit of the spectra; apparently, only the short-wave-length portion of this band is visible, the remainder being hidden by the telluric φ band. Several less conspicuous bands are also seen.

The wave lengths of all features common to the four N stars of the program are presented in Table 2. Short-wave-length edges were measured in all cases except that of *h;* the tabulated wave length for this feature probably corresponds roughly to the middle of the band.

The final entry in Table 2 is for the short-wave-length limit of the telluric ρ and σ band, which is well separated from the stellar feature *b* on the 37-inch spectrogram but is blended with it on the Schmidt plates.

The second column gives an indication of the visibility of the bands on the tracings of the Schmidt spectra, *A* being conspicuous, *D* probably present. Wave lengths of *a*

[4] *Ap. J.*, **116**, 652, 1952.

through *e* were obtained from the slit spectrogram of Y CVn. Points *a*, *c*, and *e* were then used as standards for the calibration of the Schmidt plates, on which *f*, *g*, and *h* were measured.

The fourth and fifth columns list the bands of the infrared cyanogen system which most nearly coincide with the observed wave lengths. In each case except *h*, these are wave lengths of R_2 heads, computed from the constants given by Herzberg and Phillips.[5] For *h*, the *CN* wave length is that observed by them for the R_1 band head, which lies between the R_2 and Q_1 heads and about 60 A from each.

The agreement between wave lengths observed in class N and those computed for the *CN* spectrum is indicated by the last column of Table 2. For features *a* through *e* and *h* the agreement is as close as could be anticipated, and the identification of these bands with those of cyanogen is indicated. The band *e* is markedly stronger than *d* on all plates (ten) of the four class N stars. If the suggested identification with cyanogen is correct, this feature may be a blend with an additional absorption band.

The wave lengths of *f* and *g* disagree significantly with those of the corresponding *CN* band heads. The comparison of the wave length of the strong feature in the spectrum of

TABLE 2

Feature	Visibility	λ_{obs}	λ *CN*	Band	O−C
a	A	9120	9145	1–0	− 25
b	A	9411	9385	2–1	+ 26
c	B	9639	9637	3–2	+ 2
d	C	9930	9903	4–3	+ 27
e	B	10,169	10,184	5–4	− 15
f	C	10,395	10,480	6–5	− 85
g	D	10,655	10,793	7–6	−138
h	B	11,013	10,970	0–0	+ 43
ρ, σ	.....	9304	(Telluric)	.....	.....

R Aurigae with that observed by Kuiper *et al.* indicates that the adopted Schmidt wave lengths are too large at 10,600 A, and this would increase the values of O−C for *f* and *g*. No suggestion can be made at present for their identifications.

The Schmidt spectrograms of the four class N stars differ greatly in density, width, and background fog; and it is difficult to compare the band intensities from star to star. The impression is strong, nevertheless, that the intensities of *d*, *e*, and *f* decrease with decreasing temperature, as indicated by the classification of Keenan and Morgan,[6] or alternatively, that the intensities increase with advancing subclass within class N, for which Shane's data have been adopted.[7]

In addition to the material discussed above, one plate each was obtained of R Geminorum (S3) and of ϵ Aurigae. The former is of less than average quality. Three absorption bands centered at $\lambda\lambda$ 9790, 9960, and 10,190 appear to be present, but additional plates are needed.

The plate of ϵ Aurigae was intended to serve as a control for comparison with spectrograms taken when the current eclipse is further advanced. The present plate is of high quality and wide enough to permit two independent tracings. These tracings agree in exhibiting rudimentary absorption features centered at $\lambda\lambda$ 9810, 10,120, and 10,300. These bands, like those discussed above, do not appear attributable to telluric absorption or to the sensitivity-curve of the emulsion. Spectra of the sky and of an incandescent lamp photographed with the 37-inch reflector by Dr. McLaughlin confirm this opinion.

[5] *Ap. J.*, **108**, 163, 1948.

[6] *Ap. J.*, **94**, 501, 1941.

[7] *Lick Obs. Bull.*, No. 396, 1928.

Since Struve[8] suspects that the atmospheric eclipse of ϵ Aurigae was in progress on the date of the Schmidt spectrogram (March 4, 1953), it is possible that the features observed are due to the infrared companion. Observations during the next observing season will be of great interest.

The writer is indebted to Dr. D. B. McLaughlin for obtaining the spectra with the 37-inch reflector and for numerous helpful discussions on long-period variables. Dr. Leo Goldberg contributed a number of interesting suggestions on possible molecular identifications of the observed bands.

FREEMAN D. MILLER

UNIVERSITY OF MICHIGAN OBSERVATORY
May 28, 1953

[8] *Sky and Telescope*, **12**, 99, 1953.

INTERSTELLAR POLARIZATION AND MAGNETIC FIELDS

Recently Chandrasekhar and Fermi[1] have shown by three independent arguments that if a galactic magnetic field exists, the strength of the field must be approximately 7×10^{-6} gauss. It is of interest to determine the effect of this result on theories which have been put forward to explain the observed interstellar polarization of starlight.[2, 3] The theory of Spitzer and Tukey[2] is based on the alignment of ferromagnetic grains in a magnetic field, and a minimum field of about 10^{-4} gauss is needed by them for this mechanism to be effective. In order to explain the observed polarization, a field of 2×10^{-3} gauss is necessary. This latter field is so much greater than that estimated by Chandrasekhar and Fermi that we shall not discuss this theory further.

The theory of Davis and Greenstein[3] attempts to explain the polarization of starlight by means of the scattering and absorption by elongated dust grains which are partially aligned, owing to the small nonconservative torque due to paramagnetic relaxation in material containing a few per cent iron or other metallic atoms. The torque due to paramagnetic relaxation tends to make the short axis of the grain the axis of rotation and sets the long axis perpendicular to the magnetic field. The efficiency of this aligning process is described by the distribution parameter F. For complete alignment, with the long axes perpendicular to the field,

$$F = \tfrac{1}{3} . \tag{1}$$

The orientation due to the paramagnetic relaxation is countered by the tendency of the grains to take up random orientation through collisions with interstellar atoms. An expression for the degree of alignment given by Davis and Greenstein is

$$F_l = \frac{6.3 \times 10^6 H^2}{aT^{1/2} n_H T_g} , \tag{2}$$

where

$$F = F_l \quad \text{if} \quad |F_l| \ll \tfrac{1}{3} ,$$

and

$$F = \tfrac{1}{3} \quad \text{if} \quad |F_l| \gg \tfrac{1}{3} .$$

In equation (2) a is the mean radius of the grain, T the temperature of the interstellar medium, n_H the number density of hydrogen atoms in the interstellar medium, and T_g

[1] *Ap. J.* **118**, 113, 116, 1953.
[2] L. Spitzer and J. W. Tukey, *Ap. J.*, **114**, 187, 1951.
[3] L. Davies and J. L. Greenstein, *Ap. J.*, **114**, 206, 1951.

the temperature of the grain. For intermediate values of F we can use, approximately, equation (1) for $F_l > \frac{1}{3}$ and equation (2) for $F_l < \frac{1}{3}$. For $F \sim \frac{1}{3}$, and $H = 7 \times 10^{-6}$,

$$aT^{1/2}n_H T_g = 9.26 \times 10^{-4} .$$

Let us consider the alignment of the grains in an H I region. In the recent Russell lecture, Oort[4] discussed the temperatures in H I regions as determined from measurements of the 21-cm. line. Spitzer and Savedoff[5] have estimated from theoretical considerations that $T \sim 60°$ K. Oort states that the recent measurements in Holland and Australia give values of T near to 100° but that the uncertainty in Spitzer and Savedoff's result is larger than the difference from 100° found from the 21-cm. line. As a lower limit, therefore, we shall put $T = 60°$. For the density of the H I region we shall put $n_H = 8$, following Strömgren[6] and Spitzer and Savedoff.[5] Substituting in the equation above, we find that

$$aT_g = 1.49 \times 10^{-5} .$$

If $a \geqslant 10^{-5}$ cm, then $T_g \leqslant 1°.5$. However, van de Hulst[7] has shown that for a smooth dielectric sphere with some impurity it is extremely improbable that the grain temperature could be less than 5° K. In this case $a \leqslant 3 \times 10^{-6}$ cm. Thus we see that, for complete alignment in a magnetic field of 7×10^{-6} gauss, the average grain size would have to be considerably smaller than has usually been supposed. There is considerable objection to this conclusion, however, since with such small grains the dependence of the degree of polarization on wave length would be large, and this is in disagreement with the observational evidence. But in order to explain the observed polarization, it is not necessary that all the grains be aligned. Davis and Greenstein have shown that if all of the grain sizes are equal, then the ratio of the polarization to the total absorption is given by

$$\frac{p}{A_{pg}} = 2.07F \cos^2 \nu \, \frac{(\sigma_A/\sigma_T - 1)}{(\sigma_A/\sigma_T + 2)} . \tag{3}$$

In this equation $(\pi/2 - \nu)$ is the angle between the magnetic field and the beam of light, and σ_A and σ_T are the extinction cross-sections of a spheroidal grain whose long axis is parallel and at right angles to the electric vector in the light, respectively. Tables have been given by Davis and Greenstein for σ_A/σ_T for prolate spheroids for a_A/a_T varying between 1 and 5.025. (The calculations have been carried out by the theory of Gans,[8] which strictly is applicable only for grains much smaller than the wave length of the light being scattered.) For this range of values of a_A/a_T $(\sigma_A/\sigma_T - 1)/(\sigma_A/\sigma_T + 2)$ lies in the range 0–0.24 for the dielectric case.

It is found observationally that $p/A_{pg} \leqslant 0.02$. Thus, in order to explain the maximum polarization/absorption ratio observed, with elongated grains such that $a_A/a_T = 5.025$, we have, from equation (3),

$$0.02 = 2.07 \times 0.24 \times F \cos^2 \nu ,$$

so that

$$F \simeq \frac{1}{25} \sec^2 \nu .$$

For $\nu = 0$ this would mean that only about one-eighth of the grains would need to be aligned. In this case we would have, from equation (2),

$$\frac{1}{25} = \frac{6.3 \times 10^6 H^2}{aT^{1/2}n_H T_g} ,$$

[4] *Ap. J.*, **116**, 233, 1952.
[5] *Ap. J.*, **111**, 593, 1950.
[6] *Ap. J.*, **108**, 242, 1948.
[7] *Rech. Ap. Obs., Utrecht*, Vol. **11**, Part 1, 1946.
[8] *Ann. d. Phys.*, **37**, 881, 1912.

and so

$$aT_g = 1.245 \times 10^{-4} .$$

In this case if $T_g = 10°$, $a = 1.25 \times 10^{-5}$ cm, and this is in satisfactory agreement with previous estimates of grain size.

We conclude that under favorable conditions, i.e., $\nu = 0$, and for grains which have a large value of a_A/a_T, an interstellar magnetic field of 7×10^{-6} gauss would be sufficient to orient a fraction of the grains which are responsible for the interstellar polarization according to the theory of Davis and Greenstein. It must be emphasized, however, that it is probable that the "mean" value of ν is not equal to zero and that there will be a considerable distribution of grain shapes, so that the "mean" value of a_A/a_T may not be so large as 5.

I am indebted to Dr. S. Chandrasekhar for suggestions and discussions on this topic.

G. R. BURBIDGE*

YERKES OBSERVATORY
June 17, 1953

* Now at the Cavendish Laboratory, Cambridge, England.

SIRIUS AND THE CARBON CYCLE

The rate of energy production by the carbon cycle depends on the rate of that reaction which has the longest mean lifetime. It has been generally assumed that the mean life of the N^{14} (p, γ) reaction is longer than that of any other reaction of the carbon cycle; however, the experimental data on this process are uncertain.[1] If a low-energy resonance exists for this process, the effect would be to decrease the mean life. If the resonance were effective enough to reduce the mean life below that of the C^{12} (p, γ) reaction, the latter would determine the energy production by the carbon cycle. Let ϵ_n be the energy production per gram per second if this resonance does not exist, and ϵ_c the energy production assuming that the C^{12} (p, γ) reaction has the longest mean life; then ϵ_c and ϵ_n represent the upper and lower limits, respectively, for energy production by the carbon cycle.

Models of Sirius were constructed in order to determine whether both values of the energy production predict resonable values of the composition parameters. The point-source model was used in all cases. The opacity law was determined as follows:

Models of Sirius were determined for the compqsition $X = 0.80$, $Z = 0.01$, and for the opacity given by Kramers' law and the law $\kappa =$ Constant. From the resulting values of the density and temperature, the opacity was recomputed, taking free-free transitions of hydrogen and helium and electron scattering into account. If the opacity is given by

$$\kappa = \kappa_0 \rho^d T^{-s} ,$$

then the best law is given by those values of d and s which make the quantity $\kappa\rho^{-d} T^s$ most nearly constant throughout the star. The results show that Kramers' law, $d = 1$, $s = 3.5$, is a very good approximation, and it was used in the calculations. Values of the quantity $\kappa\rho^{-1} T^{3.5}$ for the Cowling model with the above composition are given in Table 1.

The first model considered was the Cowling model with the energy production given by ϵ_c. The cross-sections used are those given by E. E. Salpeter,[2] and the resulting values

[1] Perry and Duncan, *Phys. Rev.*, **82**, 809, 1951; Bondi and Salpeter, *Nature*, **169**, 304, 1952.

[2] *Ann. Rev. Nuclear Sci.*, **2**, 41, 1953.

of the energy production are given in Table 2, ν being the value of the temperature exponent. The resulting composition parameters are shown in Table 3, where α is the relative abundance of carbon plus nitrogen to all of the other elements except hydrogen and helium. These results are not unreasonable, and so this method does not eliminate the possibility that the energy production of the carbon cycle is represented by ϵ_c.

Table 3 indicates that, for the energy production given by ϵ_n, the molecular weight would probably be rather high on the uniform composition model; therefore, the generalized Cowling model was used in this case, with the molecular weight in the core being arbitrarily chosen as unity. The quantities needed to construct this model were taken

TABLE 1

r/R	0.169	0.228	0.342	0.455	0.569	0.683	0.797
$10^{-23}\times\kappa\rho^{-1}T^{3.5}$.....	3.3	2.9	2.8	3.9	4.8	4.1	4.0

TABLE 2

$T\times10^{-6}$	$\log(\epsilon_c/\rho XZ\alpha)$	ν	$T\times10^{-6}$	$\log(\epsilon_c/\rho XZ\alpha)$	ν
10.....	9.43	21	22.....	5.59	16
12.....	1.00	19	24.....	6.18	15
14.....	2.28	18	26.....	6.70	15
16.....	3.30	17	28.....	7.18	14
18.....	4.18	17	30.....	7.59	14
20.....	4.94	16	32.....	7.98	14

TABLE 3

α	Z	X	Y	μ	T_c
0.25.....	0.02	0.59	0.39	0.68	19×10^6
.20.....	.02	.59	.39	.68	19
.15.....	.02	.57	.40	.69	19
.10.....	.03	.55	.42	.70	19
0.05.....	0.04	0.53	0.43	0.71	19

from the paper by M. H. Harrison.[3] The modifications needed to eliminate the discontinuity in the molecular weight, as shown by P. Ledoux,[4] are small and were not taken into account. The results are shown in Table 4. Apparently this model is also compatible with the composition requirements.

The lower value of the energy production, for a given composition, requires a later stage of evolution of Sirius than the higher value. Thus, if one assumes that the original composition was such that the molecular weight was 0.6, then the lower limits of the ages of Sirius are 1.7×10^8 years and 3×10^8 years for the energy production given by ϵ_c and ϵ_n, respectively. In deriving these figures the luminosity was assumed constant, and the change in the size of the convective core was neglected. Although the difference be-

[3] *Ap. J.*, **100**, 343, 1944.

[4] *Ap. J.*, **105**, 305, 1947.

tween these two values would be somewhat larger if these effects were taken into account, it would still probably be too small to be of importance in deciding between the two values of the energy production. It must be concluded that both values of the energy production are compatible with the requirements imposed on models of Sirius.

TABLE 4

α	Z	X	Y	μ	T_c
0.25.....	0.013	0.73	0.26	0.61	24×10^6
.20.....	.015	.71	.27	.61	24
.15.....	.020	.68	.30	.62	24
.10.....	.025	.65	.32	.64	24
0.05.....	0.044	0.60	0.36	0.67	24

I would like to thank Dr. B. Strömgren for suggesting the problem and offering valuable advice, and Mr. Peter Naur for many helpful suggestions. I would also like to express my appreciation to the National Science Foundation for the predoctoral fellowship which made this work possible.

THOMAS L. SWIHART

YERKES OBSERVATORY
July 13, 1953

Fills a Long-standing Need

Astrophysics

THE ATMOSPHERES OF THE SUN AND STARS

by LAWRENCE H. ALLER

Associate Professor of Astronomy, University of Michigan

THIS PIONEERING WORK offers a comprehensive study of the stellar atmospheres. Thoroughly up-to-date, it covers the fundamentals and major modern developments concerning the atmospheres of the sun and stars and solar-terrestrial relationships. A brief astronomical introduction is followed by a presentation of the background in physics necessary for a study of interstellar relationships—including atomic structure and spectra; gas laws and velocity distribution; ionization; excitation; dissociation of atoms and molecules; and selected aspects of radiation theory. In subsequent chapters these astrophysical principles are applied to the radiation of the sun and stars, to their continuous and dark-line spectra, to solar phenomena, and to solar-terrestrial relationships.

The book shows how each principle or important formula is put to use in solving some definite numerical problem concerned with the interpretation of the stars and nebulae.

"It is hard to overemphasize the importance of this book, presenting as it does the subject of stellar atmospheres as it is known and accepted today"—**Publications of the Astronomical Society of the Pacific.**

"No question as to the significance of this book for astrophysics, its usefulness in physics, and the competence of the author"—**DR. HARLOW SHAPLEY, Harvard University.**

CONTENTS:

SURVEY OF BASIC DATA — ATOMIC AND MOLECULAR SPECTRA — GAS LAWS AND EQUATIONS OF STATE, TURBULENCE — EXCITATION, IONIZATION, AND DISSOCIATION — EMISSION AND ABSORPTION OF RADIATION — RADIATION OF STARS — CONTINUOUS SPECTRA OF SUN AND STARS — THE FRAUNHOFER SPECTRUM — SOLAR PHENOMENA

412 Pages, 118 Illustrations, 44 Tables. $12

At your bookstore or direct from . . .

THE RONALD PRESS COMPANY 15 E. 26th St., New York 10, N. Y.

ANNOUNCING

THE ASTROPHYSICAL JOURNAL SUPPLEMENT SERIES

These *Supplements* are intended to provide a medium for the publication of extensive investigations, such as wave-length lists of stars of special interest, photometric data, results of numerical integrations pertaining to stellar interiors, model stellar atmosphere calculations, and theoretical investigations not immediately related to astronomical problems.

Supplement No. 1

"Chromospheric Structure of the K-type Component of Zeta Aurigae." O. C. WILSON and HELMUT A. ABT.

Spectrograms of 10 A/mm dispersion taken during the 1947–48 eclipse have been measured for line intensities and for radial velocities, and the results are compared with those obtained previously for the 1939–40 eclipse.

(Ready January, 1954. Price, $1.25)

Supplement No. 2

"Spectroscopic Observations of Mira Ceti, 1934–1952." ALFRED H. JOY.

This is a detailed discussion of two decades of observations of this interesting star. The results of Coudé spectrograms with dispersions up to 2.3 A/mm permits a more critical study of the spectroscopic behavior of Mira Ceti than was possible with lower dispersions.

(Ready March, 1954. Price $1.25)

Supplement No. 3

"An Analysis of W Virginis." HELMUT A. ABT.

This is a study of the population II Cepheid, W Virginis, from high dispersion spectra obtained by Sanford and Abt and from photoelectric colors and magnitudes obtained by Whitford and Code, Eggen, and Gordon and Kron.

(Ready March, 1954. Price, $1.25)

An abstract of each supplement will be published in THE ASTROPHYSICAL JOURNAL. The Supplements will appear irregularly, and may be purchased separately or by subscription. Each volume of Supplements will consist of approximately 500 pages.

Subscriptions

$8.00 per volume

Canada, $8.75. Foreign, $9.50.

To members of the American Astronomical Society, $6.00 per volume.

Orders now accepted.

THE UNIVERSITY OF CHICAGO PRESS

5750 ELLIS AVENUE CHICAGO 37, ILLINOIS

THIS PUBLICATION IS REPRODUCED BY AGREEMENT WITH THE COPYRIGHT OWNER. EXTENSIVE DUPLICATION OR RESALE WITHOUT PERMISSION IS PROHIBITED.